UNIVERSIDADE DE LISBOA
INSTITUTO SUPERIOR TÉCNICO

NONLINEAR DYNAMICS AND STABILITY OF COMPACT OBJECTS

ZHEN ZHONG

Supervisor : Doctor Vítor Manuel dos Santos Cardoso

Thesis approved in public session to obtain the PhD degree in
PHYSICS

Jury final classification: DRAFT V1

2025

TÉCNICO LISBOA

UNIVERSIDADE DE LISBOA
INSTITUTO SUPERIOR TÉCNICO

NONLINEAR DYNAMICS AND STABILITY OF COMPACT OBJECTS

ZHEN ZHONG

Supervisor : Doctor Vitor Manuel dos Santos Cardoso

Thesis approved in public session to obtain the PhD degree in
PHYSICS

Jury final classification: DRAFT V1

JURY

CHAIRPERSON:

Doctor Ilídio Pereira Lopes, Instituto Superior Técnico da Universidade de Lisboa

MEMBERS OF THE COMMITTEE:

Doctor William Edward East, Perimeter Institute for Theoretical Physics

Doctor Ilídio Pereira Lopes, Instituto Superior Técnico da Universidade de Lisboa

Doctor Vítor Manuel dos Santos Cardoso, Niels Bohr Institute & Instituto Superior Técnico da Universidade de Lisboa

Doctor David Matthew Hilditch, Instituto Superior Técnico da Universidade de Lisboa

Doctor Yifan Chen, Niels Bohr Institute

FUNDING INSTITUTION:
China Scholarship Council

2025

NONLINEAR DYNAMICS AND STABILITY OF COMPACT OBJECTS

ZHEN ZHONG

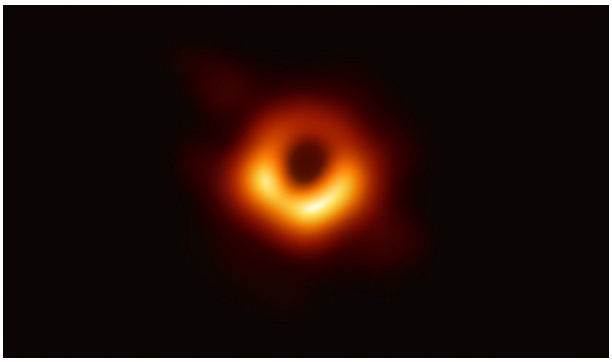

JULY 2025

ABSTRACT

This thesis explores the complex dynamics, stability, and observational signatures of compact objects within General Relativity, leveraging analytical, perturbative, and numerical relativity techniques. Motivated by theoretical challenges to the classical black hole paradigm, the dark matter puzzle, and the advent of gravitational-wave astronomy, we investigate fundamental questions at the intersection of strong gravity, field theory, and astrophysics.

We first examine the stability and potential for energy extraction in horizonless geometries. By analyzing truncated Kerr spacetimes, we precisely determine the threshold for the ergoregion instability, finding it coincides with the equatorial ergosurface for large multipoles, while finding no evidence for linear instabilities driven solely by light rings on relevant timescales. Furthermore, we uncover potent energy extraction mechanisms beyond standard superradiance, demonstrating significant energy amplification via blueshift instabilities in dynamic bouncing geometries and a "blueshift-like" energy exchange between scattering states in time-periodic solitons like Q-balls.

Second, we investigate the interactions between black holes and boson stars through fully nonlinear simulations. Simulating a black hole piercing both mini-boson stars and solitonic boson stars reveals the dominant role of tidal capture, often leading to the near-total accretion of the boson star, even for disparate scales. A consistent outcome is the formation of quasi-bound scalar field remnants—"gravitational atoms"—around the final black hole, linking interaction dynamics to fundamental scalar field properties in strong gravity and potentially constraining bosonic dark matter models.

Third, we study novel observational probes using gravitational waves and related phenomena. We characterize the late-time decay of gravitational perturbations, identifying source-dominated tails generated by matter or nonlinearities that can dominate over the standard inverse-power-law decay, impacting our understanding of late-time signals. We also demonstrate that dynamical gravitational lensing during black hole ringdown encodes quasinormal mode oscillations in the light deflection angle, presenting a new multi-messenger avenue to probe strong-field dynamics.

These interconnected studies refine our understanding of compact object stability, reveal complex dynamics in black hole-boson star interactions, and identify new gravitational-wave and multi-messenger signatures, offering pathways to test General Relativity, probe dark matter candidates, and guide future observational strategies in the era of precision gravitational-wave astronomy.

KEY-WORDS: general relativity; black holes; boson stars; gravitational waves; stability; energy extraction; numerical relativity; dark matter; gravitational lensing; quasinormal modes; late-time tails.

PUBLICATIONS

Most of this doctoral thesis is based on the following publications:

V. Cardoso, T. Ikeda, Z. Zhong, M. Zilhão, *Piercing of a boson star by a black hole*, Phys. Rev. D 106 (2022) 4, 044030; arXiv:2206.00021 [gr-qc]

Z. Zhong, V. Cardoso, E. Maggio, *Instability of ultracompact horizonless spacetimes*, Phys. Rev. D 107 (2023) 4, 044035; arXiv:2211.16526 [gr-qc]

V. Cardoso, J. L. Costa, J. Natário, Z. Zhong, *Energy extraction from bouncing geometries*, Phys. Rev. D 108 (2023) 2, 024071; arXiv:2304.08520 [gr-qc]

Z. Zhong, V. Cardoso, T. Ikeda, M. Zilhão, *Piercing of a solitonic boson star by a black hole*, Phys. Rev. D 108 (2023) 8, 084051; arXiv:2307.02548 [gr-qc]

V. Cardoso, R. Vicente, Z. Zhong, *Energy Extraction from Q-balls and Other Fundamental Solitons*, Phys. Rev. Lett. 131 (2023) 11, 111602; arXiv:2307.13734 [hep-th]

V. Cardoso, G. Carullo, M. De Amicis, F. Duque, T. Katagiri, D. Pereniguez, J. Redondo-Yuste, T. F. M. Spieksma, Z. Zhong, *Hushing black holes: Tails in dynamical spacetimes*, Phys. Rev. D 109 (2024) 12, L121502; arXiv:2405.12290 [gr-qc]

Z. Zhong, V. Cardoso, Y. Chen, *Dynamical Lensing Tomography of Black Hole Ringdown*, (2024); arXiv:2408.10303 [gr-qc]

During the years of my doctoral program, I also coauthored the following works (not discussed in this thesis):

L. Zhou, Z. Zhong, Y. Chen, V. Cardoso, *Forward ray tracing and hot spots in Kerr spacetime*, Phys. Rev. D 111 (2025) 6, 064075; arXiv:2408.16049 [gr-qc]

ACKNOWLEDGMENTS

As my four-year doctoral journey at Instituto Superior Técnico (IST) in Lisbon draws to a close, I am filled with immense gratitude. The completion of this dissertation would not have been possible without the steadfast support and invaluable assistance of numerous mentors, colleagues, friends, and family members. To everyone who has offered their care, support, and help along the way, I extend my most sincere thanks.

First and foremost, I wish to express my sincere gratitude to the China Scholarship Council (CSC) for the full scholarship (No. 202106040037). This generous funding provided the essential financial security for my doctoral studies and research, enabling me to pursue my academic aspirations far from home in the beautiful city of Lisbon, Portugal.

My heartfelt thanks go to my colleagues within the GRIT (Gravitation in Técnico) group at IST. It has been a privilege to be part of such a vibrant and intellectually stimulating team. Over the past four years, I have learned immensely from our interactions and collaborations. While the group is large, and I cannot list everyone by name, I cherish the memory of every friendly exchange with colleagues such as Christian Peterson, Masato Minamitsuji, Tiago Vasques and many others. Collectively, you fostered a remarkably positive, supportive, and collaborative research environment.

Specifically regarding my research, I am grateful to David Hilditch and Hannes Rüter for their insightful discussions and inspiration concerning numerical relativity. I thank Richard Brito for sharing his expertise in the field of massive spin-2 theories, and Yuan Chen for engaging in fruitful discussions on gravitational waves. These valuable conversations were a frequent occurrence, too numerous to list exhaustively, and were crucial for deepening my understanding of these complex subjects.

Beyond the scientific realm, I owe a significant debt of gratitude to Ms. Rita Sousa. Navigating life and administrative procedures as an international student presented numerous challenges, and Rita's patient and meticulous assistance resolved many concerns, allowing me to focus more effectively on my research. My thanks also go to João Vasconcelos for his timely help whenever computer issues arose. Your support in these practical matters brought warmth and ease to my daily life outside of research.

I owe my deepest gratitude to my supervisor, Vitor Cardoso, who has been a constant source of brilliant and insightful ideas. I vividly recall his frequent "Any update?" messages, sometimes arriving twice daily. Though demanding, this consistent engagement served as a powerful catalyst, continually pushing me forward. Our contrasting work schedules also created a unique dynamic, often requiring me to join his early morning meetings immediately after a late night of work—like

an academic relay across time zones. Vitor, thank you for consistently pushing me beyond my comfort zone and challenging the limits of my understanding. Your guidance and brilliant insights have been a lighthouse these past four years, illuminating my path through inevitable moments of confusion and uncertainty.

I would also like to extend special thanks to William East of the Perimeter Institute (PI). Thank you for your warm hospitality and the invaluable opportunity to collaborate during my visit to PI. Our in-depth discussions were not only instrumental in learning cutting-edge knowledge but, more importantly, they sparked new ways of thinking. Our collaboration on massive spin-2 theories was particularly meaningful; it represented my first real opportunity to engage with and attempt to tackle the kind of challenging, fundamental physics problems I had always aspired to address. Will, you were instrumental in helping me take that crucial first step.

Last, but certainly not least, my deepest gratitude goes to my family. Thank you for granting me the freedom to choose my own path in life and research; your trust has been the bedrock of my determination. Thank you for your unwavering financial support throughout my studies, which allowed me to dedicate myself fully to learning and research without distraction. Your unconditional love and support have been my warmest sanctuary while living abroad, sustaining me through every challenge.

The companionship of friends in Lisbon was equally indispensable during this time. Special thanks to Diogo Silva, also from GRIT; our chats in the office helped dispel the isolation that research can sometimes bring, and your insights into local life greatly eased my integration into Lisbon, making me feel welcome and well-supported. I am also grateful to my groupmates Yuan Chen and Xu Qixuan; sharing meals and conversations with you provided precious moments of respite and relaxation away from the intense pressures of research. Those shared laughs were a vital and memorable part of my PhD experience. To all my friends, too many to name individually, thank you. Your companionship enriched my life immeasurably and offered valuable new perspectives.

Once again, thank you to everyone who provided guidance, assistance, and support throughout my doctoral studies!

CONTENTS

LIST OF TABLES

CONVENTIONS, NOTATION AND UNITS

In this thesis, I adhere to the conventions outlined in Ref. [1]. Unless specified otherwise, I use the natural units where the speed of light and Newton's constant are set to unity ($c = G = 1$), and the *mostly positive* metric signature $(-,+,+,+)$ is used throughout. I follow the abstract index notation, where Latin letters from the beginning of the alphabet

denote abstract indices and Greek letters denote coordinate indices. Specifically, Latin letters from a to d are used for abstract spacetime indices, while those from i to n are reserved for abstract spatial indices. The following table summarizes the most relevant conventions and notation used in this work:

$a, b, c, \ldots$	abstract indices (coordinate-independent)
$\alpha, \beta, \gamma, \ldots$	coordinate indices (specific basis-dependent)
$V^a W_a$	Einstein summation convention (implied contraction over repeated indices)
$T_{(ab)} \equiv \frac{1}{2}(T_{ab} + T_{ba})$	symmetrization over indices a and b
$g_{ab}\,, \eta_{ab}$	spacetime metric (curved and flat, respectively) in abstract index notation
$(\,\cdot\,)_{,a} = \partial_a(\cdot)$	partial derivative with respect to coordinate x^a in abstract notation
$(\,\cdot\,)_{;a} = \nabla_a(\cdot)$	covariant derivative (Levi-Civita connection) in abstract notation
$\Box(\cdot) = \nabla^a \nabla_a(\cdot)$	d'Alembertian operator in abstract index notation
$\Psi^* = \overline{\Psi}$	complex conjugate of Ψ

ACRONYMS

ADM	Arnowitt–Deser–Misner
BH	black hole
BHEX	Black Hole Explorer
BL	Boyer-Lindquist
BS	boson star
CCK	Cohen, Chrzanowski, and Kegeles
DM	dark matter
EFEs	Einstein Field Equations
EHT	Event Horizon Telescope
ELT	Extremely Large Telescope
EM	electromagnetic

EMRI	extreme mass-ratio inspiral
EOM	equation(s) of motion
GMT	Giant Magellan Telescope
GR	General Relativity
GW	gravitational wave
IDT	initial data-led tail
IRG	ingoing radiation gauge
KAGRA	Kamioka Gravitational Wave Detector
KS	Kerr–Schild
LIGO	Laser Interferometer Gravitational-Wave Observatory
LISA	Laser Interferometer Space Antenna
LVK	LIGO-Virgo-KAGRA
ngEHT	next generation Event Horizon Telescope
NP	Newman-Penrose
ORG	outgoing radiation gauge
PTA	pulsar timing array
QCD	quantum chromodynamics
QNM	quasinormal mode
SBS	solitonic boson star
SMBH	supermassive black hole
SMBHB	supermassive black hole binary
SoDT	source-driven tail
TMT	Thirty Meter Telescope
UCO	ultracompact object
VLBI	very long baseline interferometry

ZAMO	zero angular momentum observer

Part I

NONLINEAR DYNAMICS AND STABILITY OF COMPACT OBJECTS

1

INTRODUCTION

1.1 THE ENIGMA OF COMPACT OBJECTS: BLACK HOLES AND BEYOND

General Relativity (GR), our leading theory of gravity, describes the gravitational force as a consequence of spacetime geometry dynamically shaped by the distribution of mass and energy [1]. Among the most profound predictions of GR are black holes (BHs) [2], objects whose intense gravity warps spacetime to such an extent that not even light can escape from within their event horizons. These enigmatic entities serve as unique laboratories for testing GR in the strong-field regime, leveraging increasingly precise gravitational-wave and electromagnetic observations [3, 4]. Their astrophysical significance is undeniable; they play critical roles in phenomena such as the evolution of galaxies, powering active galactic nuclei, and serving as primary sources for gravitational waves (GWs) detected by observatories like Laser Interferometer Gravitational-Wave Observatory (LIGO), Virgo, and Kamioka Gravitational Wave Detector (KAGRA) [3, 5]. The study of BHs pushes the boundaries of our understanding, connecting to fundamental questions surrounding spacetime singularities, the information paradox [6, 7], and the ultimate quest for a theory of quantum gravity.

However, the classical picture of BHs, while remarkably successful in explaining observations across vast mass scales [8, 9], faces theoretical challenges, most notably the presence of singularities where GR breaks down and the information loss paradox associated with Hawking radiation [10]. Furthermore, the defining feature of a BH—the event horizon—remains largely untested observationally. These issues motivate the study of BH mimickers: horizonless ultracompact objects (UCOs) arising from physics beyond classical GR, incorporating quantum effects, or considering alternative compact object models [11]. Quantum gravity phenomenology suggests that BHs might not be eternal structures; collapse could be halted before a singularity forms, or evaporation might leave behind a regular spacetime remnant. This leads to the consideration of regular BHs or horizonless alternatives, such as particle-like configurations of a complex scalar field. Such objects can exhibit distinct general relativistic features not typically found in standard BH spacetimes, such as stable light rings, isolated ergoregions, or super-extremal spins [11–14]. These features can lead to unique observational signatures: the absence of a perfectly absorbing horizon can modify the late-time GW ringdown signal [15]; the presence of an ergoregion without a horizon can trigger instabilities potentially leading

to GW emission [16]; and super-spinning objects can alter binary inspiral dynamics. The stability of these alternatives, particularly against mechanisms like the ergoregion instability (whose threshold is precisely located in Chapter 3), and the potential for novel energy extraction processes in dynamic scenarios like bouncing geometries (shown to exhibit significant energy amplification in Chapter 4), are central themes explored in this thesis. These investigations, detailed in Part II, address the implications of moving beyond classical BH descriptions and probe potential quantum gravity effects.

1.2 THE DARK MATTER PUZZLE AND BOSONIC CANDIDATES

Parallel to the mysteries of strong gravity lies one of the most significant puzzles in modern cosmology: the nature of dark matter (DM) [17]. Overwhelming astrophysical and cosmological evidence indicates that the majority of matter in the Universe is non-luminous and interacts primarily through gravity. While the Standard Model of particle physics provides no suitable candidate, numerous theoretical extensions propose new fundamental particles. Among the most compelling candidates, particularly motivated by solutions to outstanding problems in particle physics and cosmology, are new ultralight bosonic particles with masses $\lesssim 10^{-10}$eV. For instance, pseudo-scalar axion-like particles can solve the strong CP problem of quantum chromodynamics (QCD) while simultaneously constituting a significant fraction of DM [18, 19].

A fascinating possibility is that these ultralight bosonic fields condense and form macroscopic, self-gravitating structures through gravitational dynamics. Such objects, generically known as boson stars (BSs) (when formed from scalar fields) [20] or Proca stars (when formed from vector fields) [21], could potentially constitute a significant fraction of the Universe's dark matter content, perhaps seeding structure formation or residing in galactic halos. Depending on the specifics of the boson's potential (mass term and self-interactions), different types of solitonic objects can exist. The simplest models involve a massive complex scalar field with no self-interactions, leading to "mini-BSs". Introducing self-interactions, such as a solitonic potential, gives rise to solitonic boson stars (SBSs), which can exhibit different structures and achieve higher compactness.

Among the various theoretical models for BH mimickers, BSs have emerged as particularly useful testbeds [20, 22]. These are regular, asymptotically flat, horizonless solutions sourced by self-gravitating complex scalar fields. Crucially, certain classes of BSs can possess features like ergoregions, stable light rings, super-extremal spins, and high compactness, mimicking BHs [12–14]. Unlike many other exotic object proposals, BSs arise from a well-defined evolution system (the Einstein-Klein-Gordon equations), making them amenable to study using established numerical relativity techniques [11]. This allows for detailed investigation of their dynamics in isolation and in binaries, providing insights into the potential phenomenology of horizonless objects in the

strong-field, nonlinear regime and setting the stage for considering their observational signatures.

These objects can exist even in flat spacetime as Q-balls [23]. The potential existence of these bosonic structures as astrophysical objects, possibly linked to the DM puzzle, opens exciting avenues for probing fundamental physics through gravitational interactions. Understanding the interactions between these exotic objects and standard BHs, specifically the dynamics of a BH piercing through a BS (which, as shown in Part III, can lead to surprising tidal capture and near-total accretion, potentially generating unique GW signatures), is crucial for assessing their astrophysical relevance. Furthermore, the unique properties of time-periodic solitons like Q-balls motivate the investigation of novel energy extraction mechanisms (explored in Chapter 5), connecting the DM puzzle to fundamental questions about energy conservation and extraction in GR.

1.3 GRAVITATIONAL WAVES AND MULTI-MESSENGER ASTRONOMY

The dawn of gravitational-wave astronomy, initiated by the groundbreaking detections of the LIGO-Virgo-KAGRA (LVK) collaboration, has provided an entirely new window onto the cosmos [3, 5]. GWs, ripples in spacetime itself, carry direct information about the most violent and energetic events in the Universe, such as the mergers of BHs and neutron stars. These observations allow us to probe gravity in its most extreme regimes – highly dynamical, strong-field scenarios inaccessible through traditional electromagnetic (EM) astronomy alone. The field was revolutionized by the first direct detection of GWs from a binary BH merger (GW150914) by LIGO [24]. Since then, the global network, the LVK collaboration, has observed numerous events, revealing a diverse population of sources including binary neutron stars (some with electromagnetic counterparts [25]), neutron star-BH binaries [26], and even intermediate-mass BHs [27]. These observations provide unprecedented tests of GR and insights into astrophysics [28]. The future promises even greater discovery potential with upgrades to current detectors, next-generation ground-based observatories like the Einstein Telescope [29] and Cosmic Explorer [30], the space-based Laser Interferometer Space Antenna (LISA) mission targeting lower frequencies and sources like extreme mass-ratio inspirals (EMRIs) [31], and pulsar timing arrays (PTAs) probing nanohertz waves [32].

Furthermore, the synergy between GW observations and EM counterparts, such as radio observations by the Event Horizon Telescope (EHT) or timing observations from pulsars, marks the era of multi-messenger astronomy. Combining information from different cosmic messengers allows for a much richer understanding of astrophysical phenomena and provides powerful tests of fundamental physics. For instance, observing the EM counterpart of a GW event can help localize the source and probe the environment surrounding the merging objects. Conversely,

GWs can reveal details about the dynamics and nature of compact objects that are otherwise hidden from EM view.

Other potential multi-messenger signatures include the lensing of light by dynamically changing gravitational fields, particularly during BH ringdown (shown in Chapter 9 to imprint quasinormal mode (QNM) signatures on deflection angles), which presents another potential avenue for probing strong gravity. Moreover, the precise nature of the late-time decay of gravitational perturbations following merger events, which can deviate from simple models due to source effects (leading to the source-driven tails (SoDTs) identified in Chapter 8) and potentially reveal subtle aspects of strong-field dynamics, also warrants detailed investigation. These observational frontiers, combined with the theoretical puzzles surrounding quantum gravity alternatives and DM candidates, provide the direct context and motivation for the specific research questions addressed in this thesis.

1.4 RESEARCH QUESTIONS AND OBJECTIVES

The confluence of theoretical puzzles surrounding compact objects and DM, coupled with the new observational capabilities offered by GWs and multi-messenger astronomy, motivates the central research questions addressed in this thesis. We aim to explore the nonlinear dynamics, stability, and observational signatures of BHs and alternative compact objects, particularly those arising from scalar field theories, within the framework of GR. The primary objectives are:

1.4.1 *Exploring Stability and Energy Extraction*

What determines the stability of horizonless compact objects or spacetimes mimicking them? We investigate the linear stability of UCOs modeled as truncated Kerr spacetimes [33], focusing on the ergoregion instability [34–36] and establishing its threshold precisely at the equatorial ergosurface for large multipoles using a truncated Kerr model. Can energy be extracted from non-rotating, non-translating objects? We explore energy extraction mechanisms in dynamic, horizonless scenarios, such as bouncing geometries exhibiting blueshift instability at the inner apparent horizon [37, 38] and time-periodic fundamental solitons like Q-balls via mode-mixing effects [23, 39].

1.4.2 *Investigating Interactions*

How do BHs interact with extended scalar field structures like mini-BSs and SBSs? This involves simulating the "piercing" of a BS by a BH [40, 41] to understand the key dynamical outcomes, including the efficiency of accretion, the role of dynamical friction, the possibility of tidal capture, and the characteristics of the emitted GWs. Does the presence of self-interaction in solitonic BSs significantly alter these interaction dy-

namics compared to mini-BSs? Can remnants like "gravitational atoms" form, and what are their properties [36, 42, 43]?

1.4.3 *Characterizing Dynamics and Signatures*

How do perturbations evolve in realistic, dynamic spacetimes? Specifically, what governs the late-time decay of waves? We investigate deviations from the standard Price's law decay [44, 45], identifying and characterizing SoDTs generated by point-like matter or nonlinear gravitational self-interactions, and determining when they might dominate over initial data-led tails (IDTs) [46]. Can novel observational signatures arise from strong-gravity dynamics? We examine dynamical gravitational lensing during the ringdown phase of a BH merger [47, 48], assessing whether the time-dependent deflection of light, mimicking the QNM oscillations, can provide a new observational probe of the QNM structure and late-time behavior.

1.5 THESIS SCOPE AND STRUCTURE

This thesis delves into the complex and fascinating realm of nonlinear dynamics and stability concerning compact objects, with a particular focus on interactions involving BHs and scalar field configurations, as well as the unique phenomena exhibited by horizonless geometries and their potential observational signatures through GWs.

- **Part I:** Introduction to the theoretical concepts of GR and scalar field dynamics, establishing the mathematical and numerical framework used throughout the thesis (**Chapter 2**). This includes the Einstein Field Equations (EFEs), Kerr spacetime properties, scalar field descriptions, and numerical relativity techniques.
- **Part II:** Exploration of the stability of compact objects and mechanisms for energy extraction beyond standard superradiance. This involves examining the linear stability of horizonless UCOs using a truncated Kerr model (**Chapter 3**, based on [33]) and investigating energy extraction from dynamic, horizonless configurations like bouncing geometries (**Chapter 4**, based on [38]) and time-periodic Q-balls (**Chapter 5**, based on [39]).
- **Part III:** Investigation of the interactions and dynamics between BSs and BHs through fully nonlinear numerical simulations. This covers a BH piercing mini-BSs (**Chapter 6**, based on [40]) and solitonic BSs (**Chapter 7**, based on [41]), analyzing accretion, dynamical friction, tidal capture, remnant formation ("gravitational atoms"), and GW emission.
- **Part IV:** Focus on potential observational probes using GWs and related phenomena. This includes studying the late-time decay of perturbations in sourced spacetimes, identifying SoDTs

(**Chapter 8**, based on [46]), and exploring dynamical gravitational lensing during BH ringdown as a novel observational signature (**Chapter 9**, based on [48]).

- **Part V:** Provides concluding remarks (**Chapter 10**), summarizing the key findings of the research, discussing their broader implications for astrophysics and fundamental physics, and outlining potential avenues for future investigation.

Through these interconnected studies, this thesis aims to contribute to our understanding of the fundamental physics governing compact objects in the strong gravity regime, bridging theoretical modeling with potential observational consequences in the era of gravitational-wave and multi-messenger astronomy.

2

THEORETICAL AND NUMERICAL FRAMEWORK

In this chapter, we present the theoretical and numerical framework needed for the rest of the thesis.

2.1 GENERAL RELATIVITY ESSENTIALS

2.1.1 *Einstein Field Equations*

GR describes gravity as a manifestation of spacetime geometry, determined dynamically by the distribution of matter and energy. The fundamental equations governing this interaction can be derived from the principle of least action applied to the total action of gravity coupled with matter fields.

The total action S is the sum of the Einstein-Hilbert action $S_{\rm EH}$ for the gravitational field and the action $S_{\rm matter}$ for the matter content within the spacetime $\mathcal{M}$:

$$S = S_{\rm EH} + S_{\rm matter}\,, \tag{2.1}$$

The Einstein-Hilbert action $S_{\rm EH}$, describing the dynamics of spacetime geometry itself, is given by [1]

$$S_{\rm EH} = \frac{1}{16\pi}\int_M \mathrm{d}^4x\sqrt{-g}R\,, \tag{2.2}$$

where g is the determinant of the metric g_{ab}, R is the Ricci scalar curvature constructed from the metric and its derivatives, and the integral is taken over the 4-dimensional spacetime manifold $\mathcal{M}$.

The matter action $S_{\rm matter}$ depends on the specific types of matter and energy present. Generally, it can be written as

$$S_{\rm matter} = \int_M \mathrm{d}^4x\sqrt{-g}\,\mathcal{L}_{\rm matter}\,, \tag{2.3}$$

where $\mathcal{L}_{\rm matter}$ is the Lagrangian density for the matter fields. This density typically depends on the matter fields, their derivatives, the metric g_{ab} and its derivatives.

The equations of motion for the gravitational field are obtained by varying the total action S with respect to the inverse metric g^{ab} (or equivalently, g_{ab}) and demanding that the variation vanishes, $\delta S/\delta g^{ab} = 0$. The variation of the Einstein-Hilbert action yields

$$\frac{\delta S_{\rm EH}}{\delta g^{ab}} = -\frac{1}{16\pi}\sqrt{-g}G_{ab}\,, \tag{2.4}$$

where $G_{ab} \equiv R_{ab} - \frac{1}{2} R g_{ab}$ is the Einstein tensor.

The variation of the matter action S_{matter} with respect to the metric g_{ab} defines the energy-momentum tensor T^{ab} of the matter fields:

$$T^{ab} \equiv -\frac{2}{\sqrt{-g}} \frac{\delta S_{\text{matter}}}{\delta g_{ab}} \,. \tag{2.5}$$

Setting the total variation $\delta S = \delta S_{\text{EH}} + \delta S_{\text{matter}}$ to zero yields the EFEs

$$G_{ab} = 8\pi T_{ab} \,. \tag{2.6}$$

These equations elegantly relate the curvature of spacetime, encoded in the Einstein tensor G_{ab}, to the distribution of matter and energy, encoded in the energy-momentum tensor T_{ab}.

A crucial property of the Einstein tensor is that it is automatically divergence-free due to the contracted Bianchi identities:

$$\nabla_a G^{ab} = 0 \,. \tag{2.7}$$

Substituting the EFEs (2.6) into this identity immediately implies the local conservation of energy and momentum for the matter fields:

$$\nabla_a T^{ab} = 0 \,. \tag{2.8}$$

2.1.2 *Kerr Spacetimes*

While the Schwarzschild solution describes the spacetime geometry outside a static, spherically symmetric mass distribution, astrophysical objects such as stars and BHs typically possess intrinsic angular momentum. The Kerr spacetime, derived by Roy Kerr in 1963 [2], represents the unique asymptotically flat, stationary, and axisymmetric vacuum solution to the EFEs that characterises the exterior geometry of a rotating, uncharged BH [49]. This solution is paramount for understanding astrophysical BHs, as gravitational collapse is expected to preserve angular momentum. Consequently, the Kerr metric underpins theoretical models of phenomena intimately associated with rotating compact objects, including accretion disks, relativistic jets, and the gravitational wave signals emitted during binary BH mergers.

Departing from the spherical symmetry of the Schwarzschild case, the Kerr spacetime's inherent rotation introduces axial symmetry around the rotation axis while retaining stationarity. This geometry is uniquely defined by two parameters: the gravitational mass M and the specific angular momentum $a = J/M$, where J denotes the total angular momentum. The weak cosmic censorship conjecture generally imposes the constraint $0 \leq a/M \leq 1$ to preclude the formation of a naked singularity, ensuring the singularity remains hidden behind an event horizon [50].

The Kerr metric is most commonly expressed using Boyer-Lindquist (BL) coordinates (t, r, θ, ϕ), which adapt naturally to the spacetime's symmetries [51, 52]. The line element in these coordinates is given by:

$$\begin{aligned} ds^2 = &- \left(1 - \frac{2Mr}{\Sigma}\right) dt^2 - \frac{4aMr\sin^2\theta}{\Sigma} dt d\phi \\ &+ \frac{\Sigma}{\Delta} dr^2 + \Sigma d\theta^2 \\ &+ \left(r^2 + a^2 + \frac{2Ma^2 r \sin^2\theta}{\Sigma}\right) \sin^2\theta d\phi^2 \,, \end{aligned} \tag{2.9}$$

where the auxiliary functions Σ and Δ are defined as

$$\Sigma \equiv r^2 + a^2 \cos^2\theta \,, \tag{2.10}$$

$$\Delta \equiv r^2 - 2Mr + a^2 \,. \tag{2.11}$$

The Kerr spacetime manifests several distinctive features absent in its non-rotating counterpart. Central to its structure is the nature of the curvature singularity, which is not point-like but forms a ring located at $r = 0$ within the equatorial plane ($\theta = \pi/2$). This is confirmed by the divergence of curvature invariants, such as the Kretschmann scalar $R_{abcd}R^{abcd}$, as $\Sigma \to 0$.

Furthermore, the Kerr geometry possesses distinct horizon structures. Coordinate singularities arising from the divergence of the g_{rr} component occur where $\Delta = 0$. This quadratic equation yields two solutions:

$$r_\pm = M \pm \sqrt{M^2 - a^2} \,, \tag{2.12}$$

provided $a \leq M$. These correspond to the outer event horizon (r_+) and the inner Cauchy horizon (r_-). While the event horizon is a stable feature, the Cauchy horizon is generally considered unstable under generic perturbations, potentially collapsing into a curvature singularity, thus limiting its physical relevance within realistic astrophysical scenarios [53, 54].

A region unique to rotating spacetimes, the ergosphere, exists between the outer event horizon and the ergosurface. The ergosurface is defined as the surface where the stationary Killing vector ξ^a becomes null ($g_{ab}\xi^a\xi^b = 0$). In the Boyer-Lindquist coordinates, the ergosurface is given by

$$r_E^\pm(\theta) = M \pm \sqrt{M^2 - a^2\cos^2\theta} \,. \tag{2.13}$$

The ergosphere occupies the space $r_+ < r < r_E^+(\theta)$. Within this region, the dragging of inertial frames by the BH's rotation is so extreme that no observer can remain static relative to observers at infinity; all trajectories are inevitably forced into co-rotation with the BH. Despite this, particles entering the ergosphere can still escape to infinity. This property enables mechanisms like the Penrose process, theoretically allowing for the extraction of rotational energy from the BH [50]. The outer

boundary $r_E^+(\theta)$ touches the event horizon r_+ at the poles ($\theta = 0, \pi$) and extends furthest in the equatorial plane ($\theta = \pi/2$).

Finally, the Kerr spacetime features unstable spherical photon orbits. In contrast to the singular photon sphere found in Schwarzschild spacetime, these orbits occupy a range of radii determined by the photon's angular momentum and the BH's spin parameter a. The collection of all such unstable orbits constitutes a "photon shell". Light rays that complete multiple orbits within this shell before escaping to infinity are responsible for the characteristic photon ring structure observed in theoretical images of BHs [55, 56]. Within the equatorial plane, two specific circular photon orbits exist: a prograde orbit and a retrograde orbit. Their radii are given by

$$r_\pm^\circ = r_+ \left[1 + \cos\left(\frac{2}{3}\arccos\frac{\pm|a|}{M}\right)\right] . \tag{2.14}$$

2.2 SCALAR FIELDS IN CURVED SPACETIME

Scalar fields represent a fundamental type of matter source frequently considered in cosmological models and theoretical physics. The notation adopted in this section will be Φ for real scalar fields and Ψ for complex scalar fields. Their dynamics play a crucial role in several topics explored later in this thesis.

2.2.1 *Real Scalar Field*

The dynamics of a real scalar field Φ minimally coupled to gravity and governed by a potential $V(\Phi)$ are described by the Lagrangian density:

$$\mathcal{L}_\Phi = -\frac{1}{2} g^{ab}\nabla_a\Phi\nabla_b\Phi - V(\Phi) . \tag{2.15}$$

The equation(s) of motion (EOM) for the scalar field is derived using the principle of least action, by varying the corresponding action $S_\Phi = \int d^4x\sqrt{-g}\mathcal{L}_\Phi$ with respect to Φ and setting the variation to zero ($\delta S_\Phi/\delta\Phi = 0$). This yields the Klein-Gordon equation in curved spacetime:

$$\nabla^a\nabla_a\Phi - V'(\Phi) = 0 , \tag{2.16}$$

where $\nabla^a\nabla_a \equiv g^{ab}\nabla_a\nabla_b$ is the d'Alembert operator. The energy-momentum tensor T^{ab}, which sources the gravitational field via Einstein's field equations, is obtained by varying the scalar field action S_Φ with respect to the metric g_{ab}:

$$T^{ab} = \nabla^a\Phi\nabla^b\Phi - g^{ab}\left(\frac{1}{2}g^{cd}\nabla_c\Phi\nabla_d\Phi + V(\Phi)\right) . \tag{2.17}$$

This tensor describes the energy density, pressure, and momentum flux associated with the scalar field configuration.

2.2.2 *Complex Scalar Field*

Similarly, a complex scalar field Ψ with a potential $V(|\Psi|^2)$ that depends only on the modulus squared $|\Psi|^2 = \Psi^*\Psi$ is described by the Lagrangian density:

$$\mathcal{L}_\Psi = -\frac{1}{2} g^{ab} \nabla_a \Psi^* \nabla_b \Psi - V(|\Psi|^2) \,. \tag{2.18}$$

Note the factor of $1/2$ is conventional and sometimes omitted as here, depending on the field normalization. Varying the action $S_\Psi = \int d^4x \sqrt{-g} \mathcal{L}_\Psi$ with respect to Ψ^* (or Ψ) yields the EOM:

$$\nabla^a \nabla_a \Psi - V'(|\Psi|^2)\Psi = 0 \,. \tag{2.19}$$

It is important to note that the prime in $V'(|\Psi|^2)$ denotes the derivative with respect to $|\Psi|^2$. The energy-momentum tensor for the complex scalar field is:

$$T^{ab} = \nabla^{(a} \Psi^* \nabla^{b)} \Psi - g^{ab} \left(\frac{1}{2} g^{cd} \nabla_c \Psi^* \nabla_d \Psi + V(|\Psi|^2) \right) . \tag{2.20}$$

Complex scalar fields admit a conserved Noether current $J^a = \frac{i}{2}(\Psi^* \nabla^a \Psi - \Psi \nabla^a \Psi^*)$ associated with the global $U(1)$ symmetry $\Psi \to e^{i\alpha}\Psi$, satisfying $\nabla_a J^a = 0$. The associated conserved charge $Q = \int d^3x \sqrt{-g} J^0$ plays a crucial role in the stability of configurations like BSs and Q-balls.

Part II

STABILITY AND ENERGY EXTRACTION MECHANISMS

3

INSTABILITIES OF HORIZONLESS ULTRACOMPACT OBJECTS

3.1 INTRODUCTION

The special properties of BH horizons, and the failure of classical GR in their interior calls for outstanding observational evidence for BHs [11, 57]. In parallel, theoretical arguments constraining the universe of alternatives are welcome. Stability arguments are a robust indicator for the feasibility of the equilibrium solutions of a given theory. In fact, the very existence of structure – galaxies, planets, stars – is due to a wide array of instability mechanisms, such as Jeans' [58, 59]. In the context of the gravitational physics of very compact objects, two mechanisms can play a role, and they are tied to the distinctive features of horizons, or the absence thereof. These mechanisms hinge on fundamental aspects of GR, specifically the existence of ergoregions and regions of the spacetime where lensing is so strong that photon orbits can "close," and which therefore work as trapping regions.

The vacuum Kerr spacetime possesses an *ergoregion*, a region within which static timelike observers don't exist and "negative energy" states are allowed. The existence of the ergoregion allows for efficient extraction of energy from spinning BHs [36, 60–63]. In the absence of horizons, ergoregions give rise to a linear instability: any small negative-energy fluctuation within the ergoregion must trigger a positive-energy state upon traveling to the exterior of the ergoregion (where only positive-energy states are allowed). Energy conservation then implies that the negative energy states inside must grow in amplitude, triggering an exponentially growing cascade [34, 36, 64–67]. This mechanism was shown to be effective for spinning compact objects, with timescales which are astrophysically relevant [35, 68–76]. Thus, spinning objects whose exterior is close to Kerr, but which do not have horizons should be spinning down and emitting copious amounts of gravitational waves. A stochastic gravitational-wave background from spin loss has not been detected yet, thus excluding classes of horizonless compact objects via observations [16].

In addition to the ergoregion instability, it was argued that even non-spinning objects should be unstable, if compact enough to develop light rings, against a nonlinear mechanism. Schwarzschild BHs have a single, unstable photon surface. However, in the absence of horizons, stable photon surfaces necessarily appear [77–79]. In these spacetimes,

linearized fluctuations decay extremely slowly, leading to the conjecture that nonlinear effects might cause either a collapse to a BH or dispersion of star material [77, 78]. Unlike the ergoregion instability, this "trapping instability" is nonlinear in nature. Therefore, estimation of timescales or even the verification that the instability is present is a formidable problem.

Nevertheless, it was recently reported that the trapping instability was observed in two different classes of objects made of fundamental fields, i.e. boson and Proca stars [80]. The objects all were spinning stars and the instability timescale was always relatively short, raising the possibility that the mechanism observed is not a trapping instability in nature, and possibly not even nonlinear, but rather something else (for example, as we discuss in the main text, the stiffness of the system under study could introduce artificial effects). The work reported in Ref. [80] motivated us to understand in finer detail the ergoregion instability of Kerr-like objects, studied in the literature but not exhaustively [11, 35, 75, 76]. In particular, Refs. [75, 76] studied the instability when the surface sits deep in the gravitational well (in fact, close to the horizon). A study on the ergoregion instability threshold was done in a fluid setup [81], where strong evidence was found that the critical surface is indeed the ergosurface (see also Ref. [82] where zero modes – a property of special interest in Kerr-like geometries, as we will show – were investigated).

Here, we aim to explore further the ergoregion instability in the exterior Kerr spacetime (truncated at a finite radius outside the horizon), and to understand at which surface the instability is quenched (do we find numerical evidence that it coincides with the ergosurface?) and whether new (linear) instabilities – related to the presence of light rings – set in even when the surface sits outside the ergosurface. We note that the interplay between ergoregions and light rings is made all the more interesting since stationary, axisymmetric, and asymptotically flat spacetime in $3+1$ dimensions with an ergoregion must have at least one light ring on its exterior [83].

3.2 SETUP

3.2.1 *The spacetime, coordinates and dynamical equations*

In BL coordinates, the metric of Kerr spacetime can be written as

$$\begin{aligned} ds^2 &= -\left(1-\frac{2Mr}{\Upsilon^2}\right)dt^2 - \frac{4aMr\sin^2\theta}{\Upsilon^2}dtd\varphi \\ &+ \left[\left(r^2+a^2\right)\sin^2\theta + \frac{2Mr}{\Upsilon^2}a^2\sin^4\theta\right]d\varphi^2 \\ &+ \frac{\Upsilon^2}{\Delta}dr^2 + \Upsilon^2 d\theta^2\,. \end{aligned} \tag{3.1}$$

where

$$\Delta = r^2 - 2Mr + a^2\,, \qquad \Upsilon^2 = r^2 + a^2\cos^2\theta\,. \tag{3.2}$$

The horizons of this geometry are located at $r_\pm = M \pm \sqrt{M^2 - a^2}$, i.e. the outer event and Cauchy horizons, respectively. These will be absent in our construction. The ergosurface is defined by the zeros of g_{tt}, which is the torus $r_{\rm ergo} = M + \sqrt{M^2 - a^2 \cos^2\theta}$. On the equator and the poles, $r_{\rm ergo} = 2M$, $M + \sqrt{M^2 - a^2}$, respectively. The ergoregion is the chief responsible for a linear instability, which is governed by the angular velocity

$$\Omega = \frac{a}{2Mr_+}\,. \tag{3.3}$$

The spacetime also has unstable light rings at $r_{\rm LR} = 2M\left(1 + \cos\left(\frac{2}{3}\arccos(\mp a/M)\right)\right)$. When $a = \sqrt{2}M/2 \sim 0.707$, the co-rotating light ring sits at the same radius than the ergoregion, in the equatorial plane ($r = 2M$).

On the Kerr background, a single master equation governs perturbations of massless fields Ψ [47]

$$\begin{aligned}&\left[\frac{\left(r^2+a^2\right)^2}{\Delta} - a^2\sin^2\theta\right]\partial_t^2\Psi - \Delta^{-s}\partial_r\left(\Delta^{s+1}\partial_r\Psi\right)\\ &+\frac{4Mar}{\Delta}\partial_t\partial_\varphi\Psi + \frac{a^2}{\Delta}\partial_\varphi^2\Psi - \mathcal{D}_s\Psi - 2s\frac{a(r-M)}{\Delta}\partial_\varphi\Psi\\ &\quad -2s\left[\frac{M\left(r^2-a^2\right)}{\Delta} - r - ia\cos\theta\right]\partial_t\Psi = 0\,,\end{aligned} \tag{3.4}$$

where Ψ is a field with spin s, $\mathcal{D}_s$ is the spin-weighted spherical Laplacian given by

$$\mathcal{D}_s \equiv \frac{1}{\sin\theta}\frac{\partial}{\partial\theta}\left(\sin\theta\frac{\partial}{\partial\theta}\right) + \left(s - \frac{\left(-i\partial_\varphi + s\cos\theta\right)^2}{\sin^2\theta}\right)\,.$$

We will focus for simplicity on scalar fields, $s = 0$. We find no reason why scalars should have special properties in this context, so we expect similar results for other massless fields. Following Ref. [84], we briefly review and introduce the horizon penetrating, hyperboloidally compactified coordinates $\{\tau, \rho, \theta, \phi\}$, which is a natural choice for studying BH perturbations [85]. First of all, the ingoing coordinates $\{v, r, \theta, \phi\}$ are given by

$$dv = dt + \frac{2Mr}{\Delta}dr, \quad d\phi = d\varphi + \frac{a}{\Delta}dr\,. \tag{3.5}$$

The hyperboloidal time variable τ is defined as

$$\mathrm{d}\tau \equiv \mathrm{d}v - \left(1 + \frac{4M}{r}\right)\mathrm{d}r\ , \tag{3.6}$$

and the compactified radial coordinate ρ as

$$\rho \equiv \frac{1}{r}\,. \tag{3.7}$$

By applying the separation of variables, setting

$$\Psi(\tau, \rho, \theta, \phi) = e^{-i\omega\tau}e^{im\phi}S(\theta)R(\rho)\,, \tag{3.8}$$

Eq. (3.4) is separated into two equations

$$\mathcal{C}_2 R''(\rho) + \mathcal{C}_1 R'(\rho) + (\mathcal{C}_0 - {}_0\mathcal{A}_{\ell m}(c))\, R = 0\,, \tag{3.9}$$

$$\frac{1}{\sin\theta}\frac{d}{d\theta}\left(\sin\theta\frac{dS}{d\theta}\right) + \left(a^2\omega^2\cos^2\theta - \frac{m^2}{\sin^2\theta} + {}_0\mathcal{A}_{\ell m}(c)\right) S = 0\,, \tag{3.10}$$

where $c = a\omega$ is the oblateness parameter, ${}_0\mathcal{A}_{\ell m}(c)$ is the angular separation constant and

$$\mathcal{C}_2 = -\rho^2(1 - 2M\rho + a^2\rho^2)\,, \tag{3.11}$$

$$\mathcal{C}_1 = 2i\omega - 2\rho + 2i\left[am + a^2\omega - M(3i + 8M\omega)\right]\rho^2 + 4a^2(2i\omega M - 1)\rho^3\,, \tag{3.12}$$

$$\mathcal{C}_0 = \omega(2am + a^2\omega - 16M^2\omega) + 2(i + 4\omega M)(am + a^2\omega - M(i + 4M\omega))\rho + 2a^2(i + 2\omega M)(i + 4\omega M)\rho^2\,. \tag{3.13}$$

Notice that in the zero-rotation limit, ${}_0\mathcal{A}_{\ell m}(c) = \ell(\ell+1)$ where ℓ is the angular integer number used to label the harmonics. In this limit, scalar spheroidal harmonics are simply the standard spherical harmonics [86].

3.2.2 *Boundary conditions*

We will deal only with the exterior Kerr spacetime, by imposing boundary conditions at the surface of the ultracompact object, which we parametrize as

$$r_0 = r_+(1 + \epsilon)\,. \tag{3.14}$$

In particular, we enforce Dirichlet boundary conditions on the radial function,

$$R(1/r_0) = 0\,, \tag{3.15}$$

which means that Ψ also vanishes at the surface.

We will not deal with the interior region, and instead assume that it is composed of a material where condition (3.15) holds. Our main goal is to understand the ergoregion instability and possible linear instability mechanisms associated with the existence of light rings. Therefore, we assume that the matter content of the object is such that scalar waves are totally reflected [1]. Dirichlet boundary conditions are also intended

1 This procedure is akin to studying reflection of electromagnetic waves off a perfect conductor [87]. In reality, a formal analysis would require one to provide the conductivity and permeability of the material, but the correct calculation in the perfect conductor limit allows one to simply impose boundary conditions at the surface of the conductor and to forget about the conductor itself.

to mimic the regularity conditions in the interior of the object. We do not expect any new qualitative feature to arise from the introduction of the interior itself, but parameters describing the interior (e.g., the equation of state of matter, etc.) could possibly mask the physics we want to explore and bring in new unwanted complications. The physics we want to understand is related to features that are found in the exterior vacuum spacetime already.

The above setup has two necessary ingredients that we require: an ergoregion and a trapping region. There is no stable light ring, instead the trapping is caused by the Dirichlet conditions at the boundary, which confine perturbations in the region between the surface and the unstable light ring. This feature can be more easily seen in non-spinning geometries, which are governed by a wavelike equation with a potential peaked at close to the $r = 3M$ surface [88]. We have confirmed numerically that large ℓ modes are extremely long-lived when $a = 0$, as in Ref. [78]. Note also that the non-spinning geometry of compact stars is stable, hence putative new features – if there are any at the linear order – should be associated with *rotation and trapping*, both present in our setup.

3.2.3 *Toy model justification for boundary conditions*

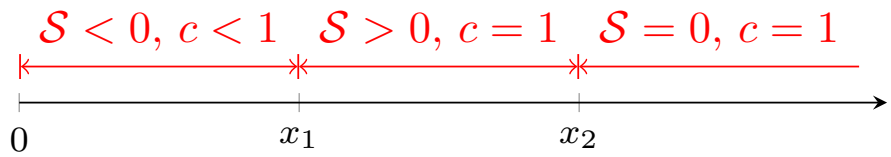

Figure 3.1: Two-dimensional star model with different sound speed, c, and Lorentz-violating factor, $\mathcal{S}$, in different intervals. $x < x_1$ is the interior of the star, $x_1 < x < x_2$ is the ergoregion mimicker, and $x > x_2$ is the vacuum case.

To understand the effects of allowing the scalar wave to probe the interior, we discuss a simple two-dimensional toy model, where we implement superradiance via a Lorentz-violating term in the Klein-Gordon equation (following the original work by Zel'dovich [61, 62]) and we mimic the star interior assigning a sound speed different from unity in its interior. To be specific, we consider the second order partial differential equation

$$\left(-\frac{1}{c^2}\frac{\partial^2}{\partial t^2} + \frac{\partial^2}{\partial x^2} + \mathcal{S}\frac{\partial}{\partial t}\right)\Phi(t,x) = 0\,, \tag{3.16}$$

in the half-line $x > 0$, where $x = 0$ stands for the star center. The speed of propagation is $c < 1$ in the interior of the star $x < x_1$, and we assume that the star is an absorber, with $\mathcal{S} < 0$. Between $x_1 < x < x_2$ there is an ergoregion, which we model by adding a Lorentz-violating

parameter $\mathcal{S} > 0$. For $x > x_2$ we have vacuum and $c = 1, \mathcal{S} = 0$. By assuming an harmonic ansatz,

$$\Phi(t, x) = \chi(x) e^{-i\omega t}\,, \tag{3.17}$$

we can get

$$\chi''(x) + \left(\frac{\omega^2}{c^2} - i\mathcal{S}\omega\right)\chi(x) = 0\,. \tag{3.18}$$

The generic solution is

$$\begin{aligned}\chi =& c_1^{(i)} \exp\left(\frac{(-1)^{\frac{1}{4}} x\sqrt{i\omega + c^2\mathcal{S}}\sqrt{\omega}}{c}\right) \\ &+ c_2^{(i)} \exp\left(-\frac{(-1)^{\frac{1}{4}} x\sqrt{i\omega + c^2\mathcal{S}}\sqrt{\omega}}{c}\right),\end{aligned} \tag{3.19}$$

where $c_1^{(i)}$ and $c_2^{(i)}$ are constants in i-th interval, which is determined by the boundary condition $\chi(0) = 0$, the outgoing boundary condition $\chi(x > x_2) \sim \exp(i\omega x)$ and connection conditions ($\chi(x)$ and $\chi'(x)$ is continuous) at x_1 and x_2.

Results are summarized in Fig. 3.2, where for now we let $\mathcal{S} = 0$ in the star interior, i.e., the star is not absorbing. The top panel shows the dependence of the characteristic ringing frequency and the instability timescale on the speed of waves inside the star. We show the first 10 most unstable modes, labeled by different colors. The star material in this model is slowing the back-and-forth process of negative-energy waves, thus delaying the growth. This explains why the frequency decreases when c decreases inside the star, and also why $M\omega_I$ decreases too. The only exception concerns purely imaginary modes, the instability rate of which remains roughly constant when the sound speed changes. These are modes which damp out very quickly inside the star and therefore are not affected by sound speed. In fact, and because of this property, we will see below that such modes reduce to modes calculated with Dirichlet conditions at the surface. There is no new feature appearing when the sound speed varies, the structure of the modes only changes at the qualitative level. The bottom panel on the other hand, shows the dependence of the instability on the location of the surface of the star. There are two noteworthy features here: when x_1 – the location of the surface – varies, the main features of the instability remain, lending support to our procedure of simply imposing Dirichlet conditions at the surface. The second noteworthy feature is that when $x_1 \to x_2$ the instability disappears, since there is no ergoregion anymore.

Let us now turn the absorption on, in the star interior. In parallel with conducting materials in electromagnetism, one could infer that dealing with the star interior is equivalent to simply imposing Dirichlet conditions at its surface. This is also the underlying rationale behind the simple model in the main text. To understand if this is true, we

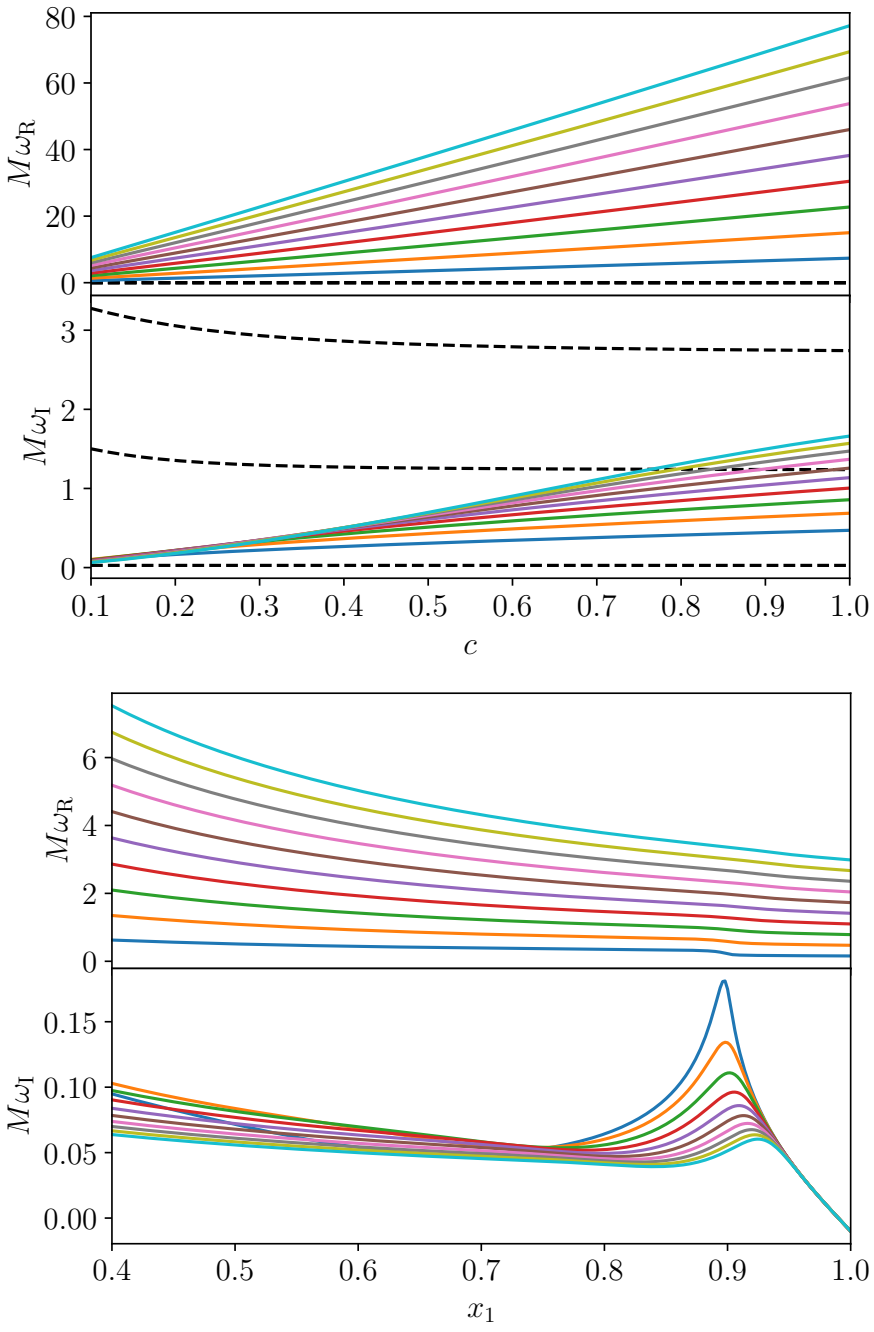

Figure 3.2: QNMs of the two-dimensional model with $x_2 = 1$ and $\mathcal{S} = 100$ for $x_1 < x < x_2$. The star is not absorbing, so we set $\mathcal{S} = 0$ in its interior $x < x_1$. We show the 10 most unstable modes, labeled by different colors. **Top panel:** QNM frequencies as a function of the sound speed c with $x_1 = 0.4$. The black dashed lines are purely imaginary QNMs. **Bottom panel:** QNM frequencies as a function of the surface location x_1 when $c = 0.1$. Notice that when x_1 approaches x_2, the instability vanishes. Although not included in this bottom panel, the instability rate of the purely imaginary modes also vanishes when x_1 approaches x_2.

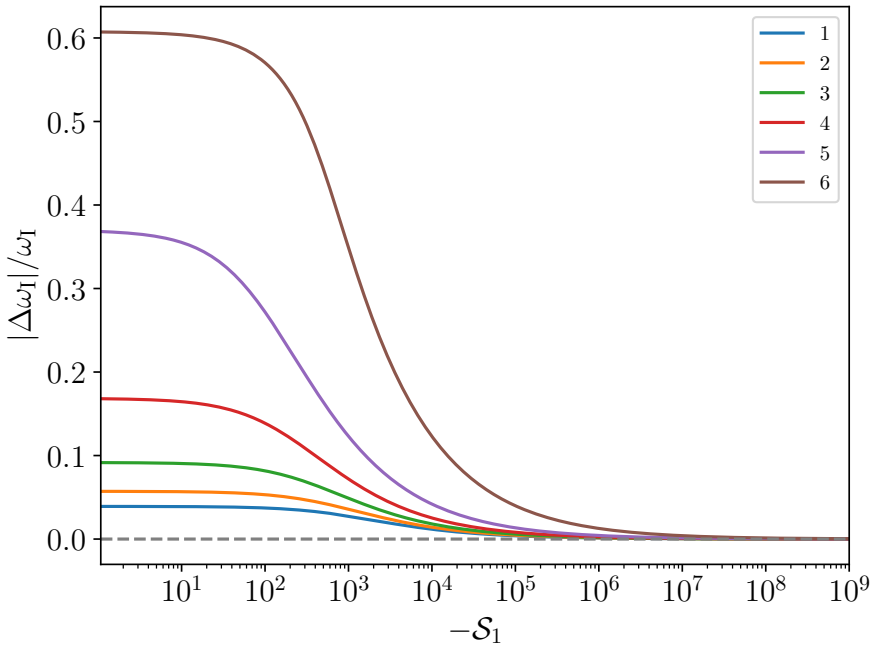

Figure 3.3: QNMs of the two-dimensional model with $x_1 = 0.4$, $x_2 = 1$ and $\mathcal{S} = 100$ for $x_1 < x < x_2$. We vary $\mathcal{S} = \mathcal{S}_1$ in the star interior $x < x_1$. These modes are pure imaginary modes, and the imaginary parts are 9.50, 6.12, 3.61, 1.81, 0.64 and 0.07 in the limit $\mathcal{S}_1 \to -\infty$ for labels 1 to 6, respectively. In this limit, the modes converge to modes obtained by imposing Dirichlet boundary conditions at x_1, $\chi(x_1) = 0$.

calculate the characteristic frequencies imposing boundary conditions at $x = 0$, and compare them with the spacetime with no star, where Dirichlet conditions are imposed instead at the surface, $x = x_1$. Results are summarized in Fig. 3.3. The figure shows the relative difference in ω_I when calculating the modes imposing boundary conditions at the center of the star ($x = 0$) or at its surface ($x = x_1$) for a very absorbing material, as a function of the Lorentz-violating factor in the star interior. The figure shows, in the first place, that no new qualitative feature arises when imposing conditions at the star surface. But it also shows that, in the limit where absorption is very large, $\mathcal{S}_1 \to -\infty$, the QNM frequencies of the two problems *are the same*. This justifies well our usage of the exterior Kerr spacetime in the main body of this work, with Dirichlet conditions at its surface.

3.3 NUMERICAL APPROACH

3.3.1 *Frequency-domain calculations of the spectra*

A robust method to deal with the eigenfrequencies of Kerr BHs – stable, well-tested and widely used in the computation of Kerr QNMs – consists on a continued-fraction representation of the problem, also known as Leaver method [89, 90]. Unfortunately, the method is well suited for BH spacetimes, but not for the problem at hand, where we need to enforce boundary condition (3.15) at a finite radius r_0. We use instead the approach by Ripley [84], which discretizes the radial equation using a Chebyshev pseudospectral method, and use the Cook-Zalutskiy spectral approach [91] to solve the angular sector. The spin-weighted spheroidal harmonics are related to the angular spheroidal function of the first kind when $s = 0$ and $\varphi = 0$, see Refs. [86, 92–94] for an extensive discussion. For $c = 0$, ${}_0\mathcal{A}_{\ell m}(0)$ increases monotonically with ℓ, but for $c \neq 0$, the ℓ-th eigenvalue is not defined uniquely. In Ref. [91], the ℓ-th eigenvalue is identified via continuity along some sequence of solutions connected to the well-defined value of ${}_0\mathcal{A}_{\ell m}(0)$. In our case, since we do not study extreme spin parameters, we find that the ℓ-th smallest eigenvalue is same as previous one. For a more detailed explanation, please refer to Ref. [91].

Furthermore, due to the rapid change of the eigenfunction as the boundary approaches the horizon, we made the following improvements to Ripley's method. First of all, the matrix given by Chebyshev pseudospectral method with Dirichlet boundary condition (3.15) is very ill-conditioned, so we replace the Chebyshev pseudospectral method with ultraspherical or Olver-Townsend spectral method [95], which gives sparser and better conditioned matrices and was incorporated into `chebfun` [96] and `ApproxFun.jl` [97] package. Especially, in one dimensional cases, the condition number of the matrix is bounded by a constant [95].

To further confirm the correctness of our results, we also use a direct integration method to check our results. For given parameters, we

need to search the dominant mode and overtones. To avoid missing the modes we are interested in, we use the global complex root and pole finding algorithm [98–100] to search multiple modes. In addition, we also perform an adaptive sampling in the complex plane region using `adaptive` package [101] to be further sure we are not missing some related modes.

3.3.2 *Time-domain analysis*

To further validate our results in the frequency domain, we also perform a time domain analysis following using the $1+1$ approach of Ref. [102]. Our procedure is almost identical, except that we use Dirichlet boundary condition (3.15) at the left boundary and an outgoing boundary condition at the right boundary (typical $r \sim 1000M$) [103]. The decomposition of the scalar field can be written as

$$\Psi = \sum_{j=|m|}^{\infty} \psi_j(r) Y_{jm}(\theta)\,, \tag{3.20}$$

where $Y_{jm}(\theta)$ is the spherical harmonic of degree j and order m. To specify initial data, we first define a tortoise coordinate as

$$\frac{\mathrm{d}r_*}{\mathrm{d}r} = \frac{r^2+a^2}{\Delta}\,, \tag{3.21}$$

or, after fixing the constant of integration,

$$r_* = r + \frac{2M}{r_+ - r_-}\left(r_+ \ln\left|\frac{r-r_+}{2M}\right| - r_- \ln\left|\frac{r-r_-}{2M}\right|\right)\,. \tag{3.22}$$

Our initial condition is a time-symmetric Gaussian,

$$\psi_{l=m} = \exp\left(-\frac{r_*-r_c}{2\sigma^2}\right)\,, \quad \psi_{l>m} = 0 = \partial_t \psi_l, \tag{3.23}$$

with $r_c = 10M$ and $\sigma = 2M$. We extract the dominant modes from the time series data using the Prony method [104] and compare them with the results in the frequency domain.

STIFFNESS AND NUMERICAL INSTABILITY For some surface locations, the time-domain evolutions can become very challenging: the modes are extremely long-lived and the system becomes stiff, leading to the appearance of numerical instabilities. Unlike physical instabilities, which we find and discuss below when ergoregions are present, numerical instabilities are not robust against grid settings and in particular when the resolution increases. Nevertheless, they are important to identify as they set a limit on the region of the parameter space we are able to probe. We can estimate the stiffness of our system since the signal (as we will see below in more detail) has the late-time form

$$\psi_{\ell=m}(t,r) = \sum_{j=0}^{n} e^{-i\omega_j t} c_j(r)\,, \tag{3.24}$$

where ω_0 is the dominant mode and $\omega_j (j > 0)$ are the j-th overtones. Normally there are infinite terms, but in the following we ignore the terms with $c_j \ll 1$. Then the stiffness ratio at some fixed radius is given by [105]

$$\mathcal{S} = \frac{|\mathrm{Im}(\omega_n)|}{|\mathrm{Im}(\omega_0)|} \,. \tag{3.25}$$

The ratio above is a measure of stiffness of the system; differential equation systems with larger stiffness ratio can be considered more stiff. From the frequency domain data in Table 3.1, we have that $|\mathrm{Im}(\omega_0)| \ll 1$ and decreases as $\ell = m$ increases, thus stiffness becomes more and more important. Accordingly, evolving the system for large timescales is challenging. Thus, in this work we limit ourselves to excluding possible instabilities with timescales $\tau \lesssim 10^5 M$ only.

Table 3.1: QNMs for $a = 0.5M$, $\ell = m$ and a surface at $r_0 = 2M$. Notice that modes with very small imaginary parts may have considerable relative error.

$\ell = m$	$M\omega$	${}_0\mathcal{A}_{\ell m}(c)$
1	$-0.338 - 7.47 \times 10^{-2} i$	$1.98 - 1.02 \times 10^{-2} i$
2	$-0.444 - 2.24 \times 10^{-2} i$	$5.97 - 2.86 \times 10^{-3} i$
3	$-0.532 - 3.44 \times 10^{-3} i$	$12.0 - 4.09 \times 10^{-4} i$
4	$-0.600 - 1.79 \times 10^{-4} i$	$20.0 - 1.96 \times 10^{-5} i$
5	$-0.652 - 4.06 \times 10^{-6} i$	$30.0 - 4.09 \times 10^{-7} i$
6	$-0.696 - 5.62 \times 10^{-8} i$	$42.0 - 5.24 \times 10^{-9} i$
7	$-0.734 - 4.95 \times 10^{-10} i$	$56.0 - 4.29 \times 10^{-11} i$

Table 3.2: Dominant unstable QNMs for $a = 0.99M$ and a surface at $\epsilon = 10^{-3}$.

$\ell = m$	$M\omega$	${}_0\mathcal{A}_{\ell m}(c)$
1	$0.339 + 2.29 \times 10^{-5} i$	$1.64 - 2.61 \times 10^{-6} i$
2	$0.757 + 1.16 \times 10^{-5} i$	$5.91 - 2.55 \times 10^{-6} i$
3	$1.18 + 4.82 \times 10^{-6} i$	$11.8 - 1.29 \times 10^{-6} i$
4	$1.60 + 1.84 \times 10^{-6} i$	$19.8 - 5.52 \times 10^{-7} i$
5	$2.02 + 6.69 \times 10^{-7} i$	$29.7 - 2.17 \times 10^{-7} i$

3.4 RESULTS

We have searched for the complex eigenfrequencies, which we write as

$$\omega = \omega_R + i\omega_I \,, \tag{3.26}$$

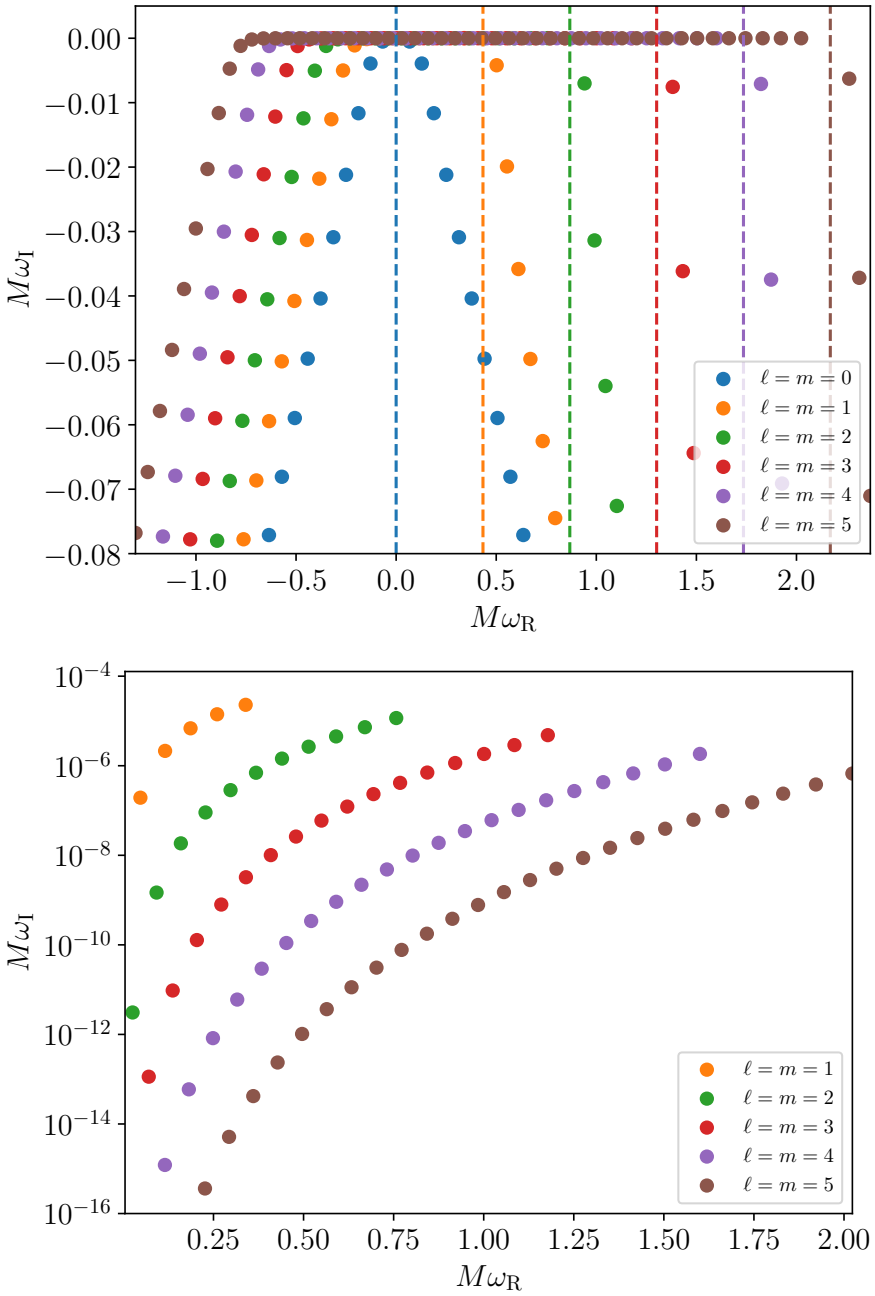

Figure 3.4: QNMs of a spacetime with $a = 0.99$, $\epsilon = 10^{-3}$ for the six lowest multipoles with $\ell = m$. The figure includes both stable and unstable modes. **Top panel:** the dashed lines mark the superradiant condition $\omega_R = m\Omega$, which is the onset of the instability. Unstable modes are barely visible on this scale. **Bottom panel:** zoom of the top panel, showing only unstable modes with positive ω_R. The next mode, with larger ω_R would be stable and would therefore fall below to the negative ω_I plane.

for different spacetime spin parameter a and surface location r_0 (or ϵ). We focus solely on the modes with $\ell = m$, for which there is an infinity of solutions, called overtones. The modes with $\ell = m$ have instability rates higher than the modes with $\ell > m$, so we can proceed focusing only on $\ell = m$ modes, safe since we are concerned with the disappearance of instability.

Fig. 3.5 shows some unstable modes with different m and ℓ. We can see that the $\ell = m$ modes are more unstable than the $\ell > m$ modes since their imaginary part is larger, thus their instability timescale is shorter. Furthermore, the $\ell > m$ modes become stable for smaller values of ϵ, as highlighted by the dashed vertical lines. Fig. 3.6 shows that the surface location of the zero-frequency mode always decreases as ℓ grows with fixed m. This means that modes with $\ell > m$ always become stable before modes with $\ell = m$ as the surface location r_0 increases. This ensures that when considering superradiance instability, we do not need to consider the modes with $\ell > m$.

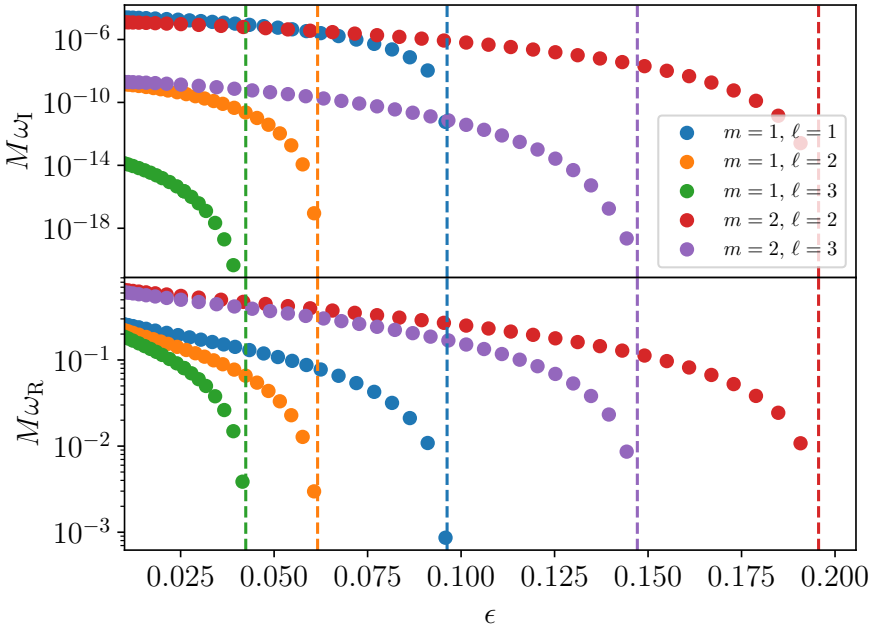

Figure 3.5: Dominant QNMs for $a = 0.99M$ as a function of ϵ. The figure shows that the modes eventually become zero-frequency modes, in this case at $\epsilon = 0.096, 0.062, 0.042, 0.20, 0.15$, marked by dashed lines.

Although not the focus of this work, we also verified that in the spinless $a = 0$ limit, large ℓ modes are extremely long-lived, as in Ref. [78] (but in the latter work boundary conditions are imposed at the origin). In fact, we find that all modes are stable but their lifetime increases exponentially with ℓ. This finding lends support to the claim that the geometry is a trapping geometry as we discussed in the introduction.

Our results are summarized in Figs. 3.4–3.7 and Table 3.2, and are always expressed in units of the spacetime mass, or equivalently, we set $M = 1$. We first focus on r_0 close to r_+ ($\epsilon \ll 1$) so we recover previous

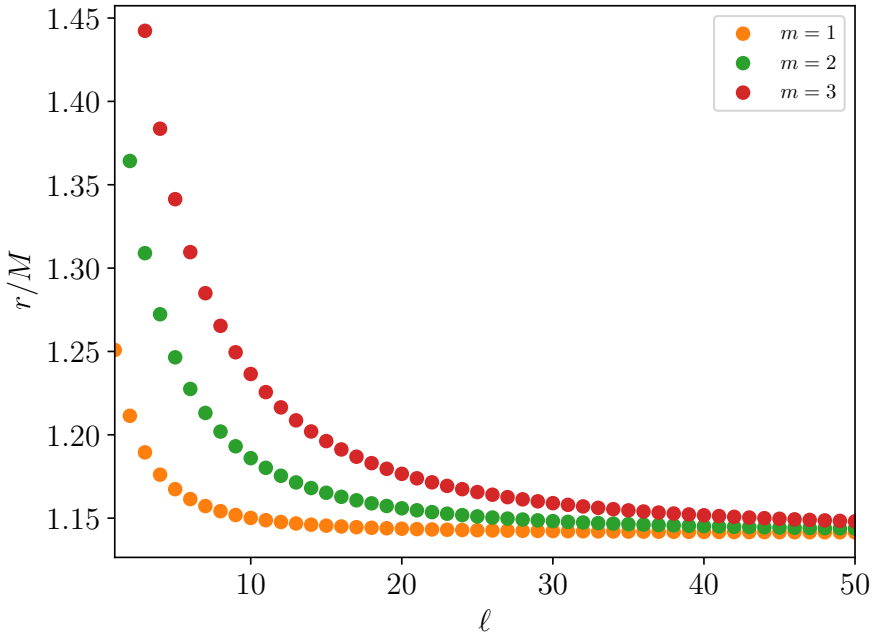

Figure 3.6: The surface locations of zero-frequency modes with $a = 0.99M$ as a function of ℓ for different m.

results in the literature [75, 76]. Fig. 3.4 shows a few tens of modes for the first six multipoles. There are a few aspects worth highlighting. The first is that there are both stable and unstable modes, and that the transition from stability to instability is well marked by the superradiant threshold $\omega_R = m\Omega$: modes for which $|\omega_R| < m\Omega$ are unstable, whereas the other modes are stable. The dominant unstable mode is shown in Table 3.2. Our results are consistent and in excellent agreement with the analytical and numerical results reported in Ref. [76] for $\epsilon \ll 1$.

The threshold varies with r_0 (or ϵ, cf. Eq. (3.14)). Fig. 3.7 illustrates how the unstable modes converge to marginally stable modes when ϵ varies. These results, complementary to those in Refs. [75, 76], indicate that all unstable modes pass through zero frequency modes before they become stable [36, 76]. When $\epsilon \ll 1$, our results are consistent with those of Refs. [75, 76]. We complemented the frequency-domain analysis with the evolution in time of the wave equation subjected to Dirichlet boundary conditions (3.15) at the surface of the object. Figure 3.8 shows the evolution for a rapidly spinning object with $a = 0.99M$ and surface at $\epsilon = 10^{-3}, 10^{-2}$. An initial transient is followed by a rapid exponential growth, with a growth rate which we extracted using Prony techniques. The results of the time-evolution are in very good agreement with the frequency-domain calculation of the dominant mode.

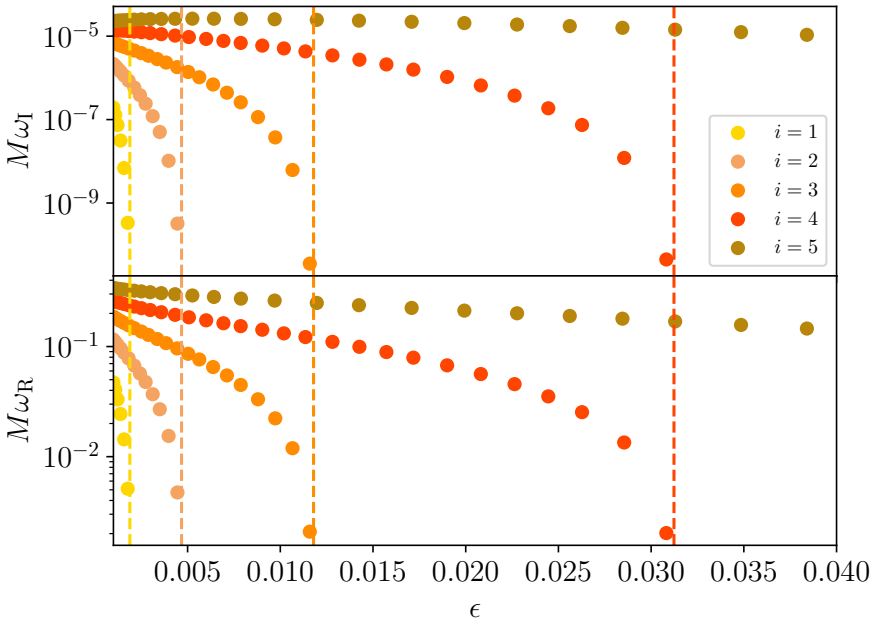

Figure 3.7: QNMs for $a = 0.99M$ and $\ell = m = 1$ as a function of ϵ. We select five unstable modes at $\epsilon = 10^{-3}$ and follow them as ϵ increases. The figure shows that the modes eventually become zero-frequency modes, in this case at $\epsilon = 0.0019,\ 0.0047,\ 0.012,\ 0.031,\ 0.096$, marked by dashed lines. Our results indicate that all the unstable modes pass through zero frequency modes before becoming stable.

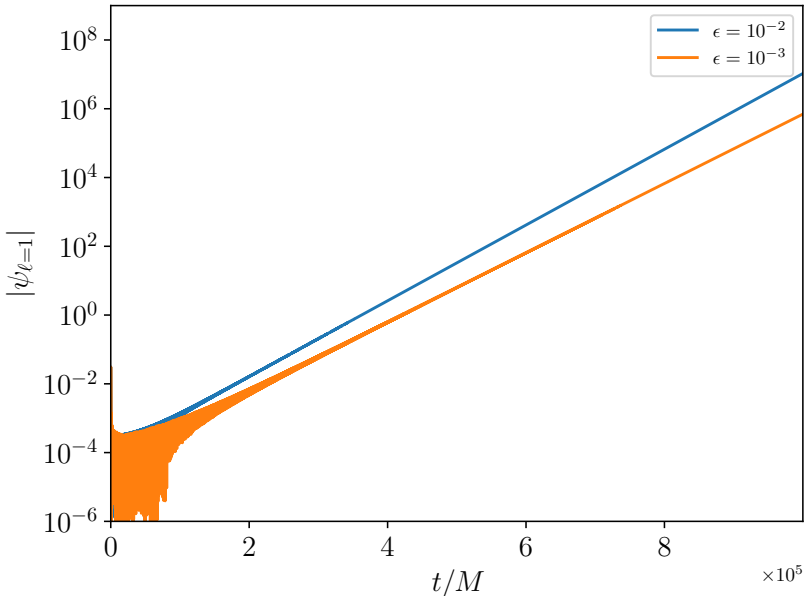

Figure 3.8: Time series data for the evolution of the field for $a = 0.99M$ and $\ell = m = 1$, up to $t = 10^6 M$. The instability rate agrees well with frequency domain predictions. In particular, using a Prony method in the time-domain data we find a dominant unstable mode with $\omega \sim 0.339 + 2.32 \times 10^{-5} i$ for $\epsilon = 10^{-3}$, to be compared with the frequency-domain prediction in Table 3.2. The field is extracted at $r_* = -28.83, -47.25$ for $\epsilon = 10^{-2}, 10^{-3}$, respectively. The instability details are independent on the extraction radii within numerical error.

3.4.1 *The zero-frequency modes*

Our numerical study indicates that, at fixed overtone, the transition from stability to instability occurs via a zero-frequency mode. A similar feature had been observed numerically in analogue fluid geometries [81] and used to explore analytically the transition from stability to instability [82]. The existence of zero-frequency modes is – to our knowledge – far from trivial or obvious. Nevertheless, as we show below, they exist and we find simple analytical expressions requiring regularity at the boundaries. These modes provide a clean discriminator to understand better when our spacetime becomes linearly stable, so they merit a more detailed analysis (see also Ref. [106], where the investigation of zero-modes in this setup was initiated). When $\omega = 0$, ${}_0\mathcal{A}_{\ell m}(0) = \ell(\ell+1)$ and one finds a simple solution to the Klein-Gordon equation, in Boyer-Lindquist coordinates:

$$\begin{aligned} \Psi &= a_1 P_\ell^{-\frac{ima}{\Gamma}}\left(\frac{r-M}{\Gamma}\right) + a_2 Q_\ell^{-\frac{ima}{\Gamma}}\left(\frac{r-M}{\Gamma}\right), \\ \Gamma &= \sqrt{M^2-a^2}\,, \end{aligned} \tag{3.27}$$

where $P_\mu^\nu(z)$ and $Q_\mu^\nu(z)$ are generalized associated Legendre functions (type 2) of first kind and second kind [107]. We will continue with units $M = 1$ and focusing only on $\ell = m$ modes. Requiring regularity at infinity, we find $a_1/a_2 = -\pi/(2i)$. A zero-frequency mode appears when, and if, the surface at r_0 coincides with a zero of the function Ψ. To analyze the zeros of Ψ, we define an auxiliary function

$$\mathcal{F}(\alpha, m, x) = \frac{P_m^{-i\alpha m}(x)}{Q_m^{-i\alpha m}(x)} - \frac{2i}{\pi}\,. \tag{3.28}$$

where $m \in \mathbb{Z}^+$ and

$$\alpha = \frac{a}{\sqrt{1-a^2}}, \quad \alpha \in (0, +\infty)\,. \tag{3.29}$$

$$x = \frac{r-1}{\sqrt{1-a^2}}, \quad x \in (1, +\infty). \tag{3.30}$$

The function $\mathcal{F}(\alpha, m, x)$ has the same zeros as Ψ. Next, we analyze the zeros of the function analytically and numerically. We will keep $\mathcal{F}$ as a function of $x(r)$ although we will impose the boundary condition at r_0.

For convenience of the analysis, we replace m with a continuous variable μ in $\mathcal{F}(\alpha, \mu, x)$ where $\mu \in [1, +\infty)$ is a real number. Fig. 3.9 shows how $\mathcal{F}(a, \mu, x)$ varies with r. We can see that the asymptotic behavior of the function depends on the surface location, namely it separates into three cases, $1 < x < \sqrt{1+\alpha^2}$ ($r_+ < r < 2$) in the top three panels of Fig. 3.9, $x = \sqrt{1+\alpha^2}$ ($r = 2$) in the fourth panel of Fig. 3.9, and $x > \sqrt{1+\alpha^2}$ ($r > 2$) in the last panel of Fig. 3.9. We deal with these cases separately and we use the asymptotic expansion of $\mathcal{F}(\alpha, \mu, x)$ for $\mu \to +\infty$ given in Ref. [108][2].

2 Note that the definition of the generalized associated Legendre function in Ref. [108] is different from ours, as we take into account when expressing asymptotic properties.

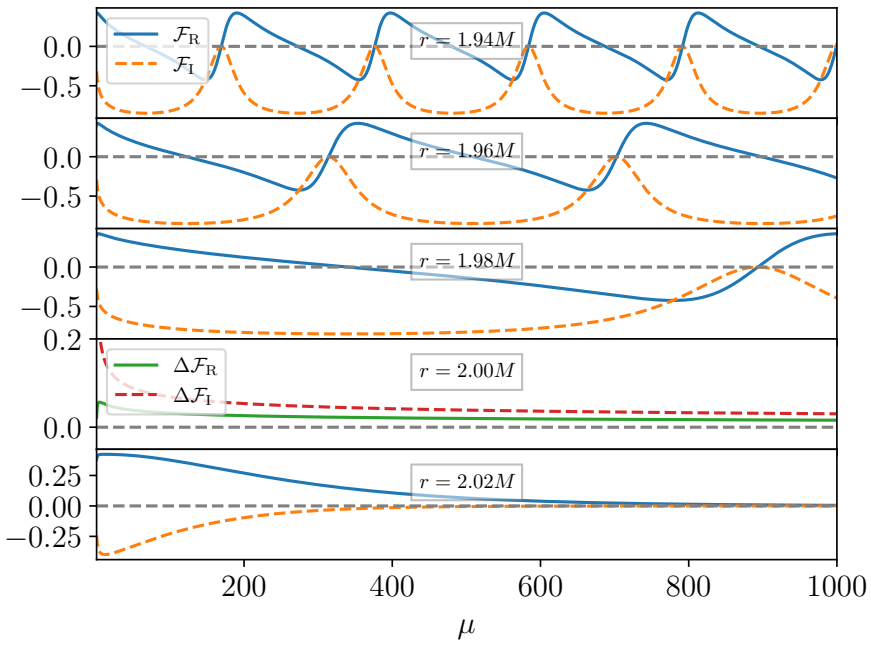

Figure 3.9: The function $\mathcal{F}(a, \mu, x)$ for $a = 0.99$ and fixed r as a function of μ, which is an asymptotically periodic function with period given by Eq. (3.40). We define $\Delta\mathcal{F}_R = \mathrm{Re}\left\{\mathcal{F} - \frac{2}{\sqrt{3}\pi}\right\}$ and $\Delta\mathcal{F}_I = \mathrm{Im}\left\{\mathcal{F} + i\frac{2}{\pi}\right\}$. As r gradually approaches $2M$, the zero points of $\mathcal{F}$ gradually disappear. For $r = 2M$, we derived analytically the result $\lim_{\mu\to+\infty} \mathcal{F}(a, \mu, r) = \frac{2}{\sqrt{3}\pi} - \frac{2i}{\pi}$, see discussion around (3.41). For $r > 2M$, we have $\lim_{\mu\to+\infty} \mathcal{F}(a, \mu, r) = 0$ (except in the neighbourhood of $r = 2M$). Therefore, we conclude that there is no zero point for $r \geq 2M$.

When $1 < x < \sqrt{1+\alpha^2}$ (corresponding to a surface within the ergoregion, $r_+ < r < 2$), we can see that $\mathcal{F}(a,\mu,x)$ is an asymptotically periodic function of μ at fixed a and x. In particular, at large μ

$$\mathcal{F} \sim -\frac{2i}{\pi - 2\pi f_1 f_2 f_3 f_4 f_5} - \frac{2i}{\pi}\,, \tag{3.31}$$

$$f_1 = \left(\alpha^2+1\right)^{-i\alpha\lambda+\lambda-\frac{1}{2}}\,, \tag{3.32}$$

$$f_2 = \left(x^2-1\right)^{-i\alpha\lambda}\,, \tag{3.33}$$

$$f_3 = (x+if_6)^{-2\lambda}\,, \tag{3.34}$$

$$f_4 = f_6 + ix\,, \tag{3.35}$$

$$f_5 = (f_6+\alpha x)^{2i\alpha\lambda}\,, \tag{3.36}$$

$$f_6 = \sqrt{\alpha^2 - x^2 + 1}\,, \tag{3.37}$$

and has infinite zeros

$$\lambda = \frac{\tan^{-1}(\frac{x}{f_6})}{\log p(\alpha,x)} + n\mathcal{P}(\alpha,x)\,, \tag{3.38}$$

where $n \in \mathbb{Z}$,

$$p(\alpha,x) = \left(\frac{(\alpha^2+1)\,(x^2-1)}{(f_6+\alpha x)^2}\right)^{\alpha} e^{2\tan^{-1}\frac{f_6}{x}}\,, \tag{3.39}$$

and its period $\mathcal{P}(\alpha,x)$ is

$$\mathcal{P}(\alpha,x) = -\frac{2\pi}{\log p(\alpha,x)}\,. \tag{3.40}$$

It is easy to verify that $\frac{\partial \mathcal{P}}{\partial x} > 0$, $p > 0$ and $\frac{\partial p}{\partial x} > 0$, so the period $\mathcal{P}$ increases as x increases, consistently with Fig. 3.9.

For $x = 1$, we have $\mathcal{P}(\alpha,1) = 0$. Thus, for surfaces placed close to the horizon at r_+ there are a large number of zeros, and hence a large number of unstable modes. For $x = 1+\delta$ and $\delta \ll 1$, we obtain the asymptotic expansion of $\mathcal{F}(a,\mu,x)$ near the horizon. If we keep only the leading term in δ, then we find a periodic function of $\log(\delta)$ with period $2\pi/(\alpha m)$ and zero points at

$$\begin{aligned} &\log\delta + \frac{2\pi}{\alpha m}n \\ =\;& \frac{i}{am}\log\left(\frac{2^{-i\alpha m}\Gamma(1-i\alpha m)\Gamma(i\alpha m+m+1)}{\Gamma(1+i\alpha m)\Gamma(-i\alpha m+m+1)}\right)\,, \end{aligned}$$

where $n \in \mathbb{Z}$ and $\delta \to 0^+$ corresponds to $n \to +\infty$. Thus, as we bring the Dirichlet condition closer to the horizon, there are more zero frequency modes, i.e. we can get an infinite number of superradiant modes in this way. This result is consistent with the findings in Ref. [106] and Ref. [76] (c.f. Eq. (29) with $q = 2n$ where $n = 1, 2, ...$).

On the other hand, for $x = \sqrt{1+\alpha^2}$, we have $p(\alpha,\sqrt{1+\alpha^2}) = 1$, then we can get $\mathcal{P} \to +\infty$ for $p \to 1^-$. Thus, the number of zero modes

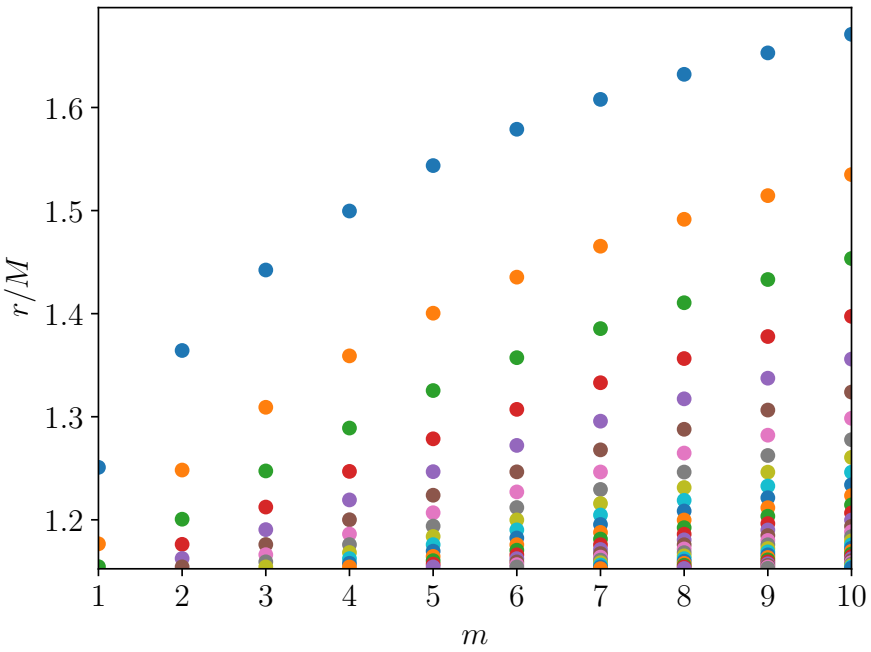

Figure 3.10: The surface location of zero-frequency modes with $a = 0.99M$ as a function of $\ell = m$. As discussed in the main text, the outermost zero mode is always at $r < 2M$ in the limit $m \to \infty$. If we consider $m \in \mathbb{Z}^+$ as $\mu \in [1, +\infty)$, then each zero-mode family is a continuous line as function of μ. We use different colors to distinguish the zero points connected by different lines.

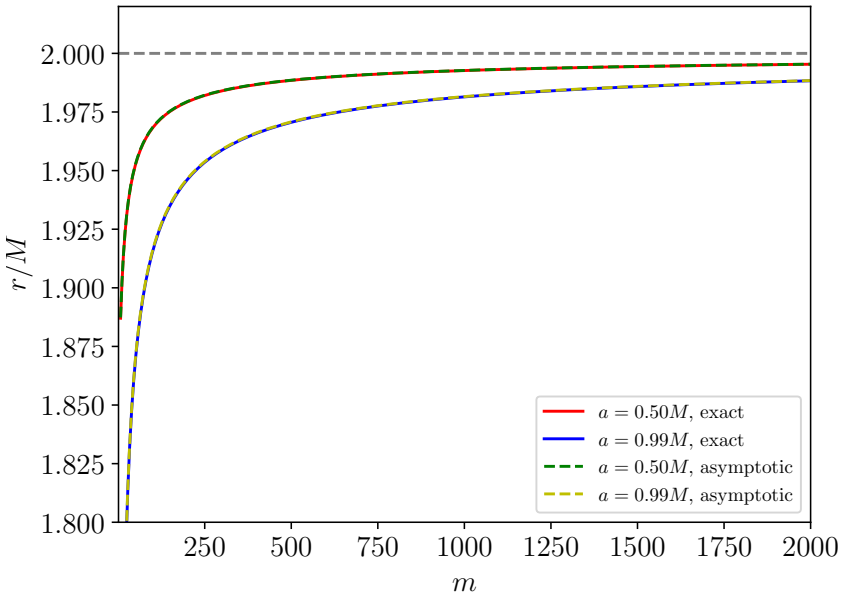

Figure 3.11: Outermost zero-frequency modes as a function of $\ell = m$ for two representative values of the spin, $a/M = 0.50, 0.99$. A polynomial fit indicates that the critical surface lies at $r_{\rm crit} = 1.998M$, $1.999M$ at large m for $a/M = 0.99, 0.5$ respectively, compatible with the location of the equatorial ergosurface. The dashed lines are obatined by using the inverse function of Eq. (3.38) with $n = 1$.

vanishes asymptotically when the surface approaches the equatorial ergoregion boundary at $r_0 = 2M$. This zero-frequency behavior is shown in Fig. 3.9.

In summary, our analytical results show that there exist zero modes for objects with ergoregions – as had also been previously discussed [106] – and their existence is *precisely* delimited by the equatorial ergoregion. An example of this behavior is shown in Figs. 3.10, 3.11. Figure 3.10 shows the surface location of the various zero-modes, for different $\ell = m$ modes. As discussed before, at fixed m there are several solutions sustaining zero modes. The outermost solution (i.e., the largest r_0, blue dots in Fig. 3.10) are shown in Fig. 3.11 but now for the first 2000 multipoles. We also show the corresponding modes for $a = 0.5M$. In other words, these results strongly suggest that as long as the surface is placed within the ergoregion, there will be zero-modes and hence linear instabilities. Thus, our findings are consistent with the generic proofs that asymptotically flat, horizonless spacetimes with ergoregions are unstable [34, 36, 64, 66, 67].

When the surface location is at the outermost boundary of the ergosphere ($x = \sqrt{1+\alpha^2}$ or $r = 2M$), then two saddle points coalescence (i.e. Eq. (4.3) and Eq. (4.4) in Ref. [108]). Then,

$$\lim_{\mu\to+\infty} \mathcal{F}(a,\mu,\sqrt{1+\alpha^2}) = \frac{2}{\sqrt{3}\pi} - \frac{2i}{\pi}\,, \tag{3.41}$$

a limit which is well captured by our numerics at $a = 0.99$ (cf. panel 4 in Fig. 3.9).

The third case where the radius is greater than the outermost boundary of the outer ergosphere ($x > \sqrt{1+\alpha^2}$ or $r > 2$) (except in the neighbourhood of the $\sqrt{1+\alpha^2}$), we have

$$\lim_{\mu\to+\infty} \mathcal{F}(a,\mu,x) = 0\,. \tag{3.42}$$

Combining Fig. 3.9, we conclude that there are no zero-frequency modes when $x \geq \sqrt{1+\alpha^2}$ ($r \geq 2$). Especially, $x = \sqrt{1+\alpha^2}$ ($r = 2$) is not a zero point even in the limit $m \to \infty$. This indicates that all superradiant modes disappear before reaching the outermost boundary of the outer ergosphere. Note that when restricting $\mu \in [1, +\infty)$ to $m \in \mathbb{Z}^+$, the zeros of $\mathcal{F}(a, m, x)$ may even disappear earlier when $x \to \sqrt{1+\alpha^2}$.

3.4.2 *Is there a new family of modes?*

Our results are a strong indication that zero-frequency modes do not exist when $r_0 > 2M$. Thus, the ergoregion family of modes cannot be the explanation for the findings of Ref. [80]. However, we are still left with the possibility that a linearized instability exists, not associated with any zero-frequency mode. In particular, it is possible that a new instability mechanism sets in for spinning spacetimes without ergoregions but with light rings. To investigate this possibility, we did a thorough search of unstable modes in the spectrum of the problem when $r_0 \geq 2M$ and $a = 0.5M$ (as discussed above, for $a < \sqrt{2}M/2$ the

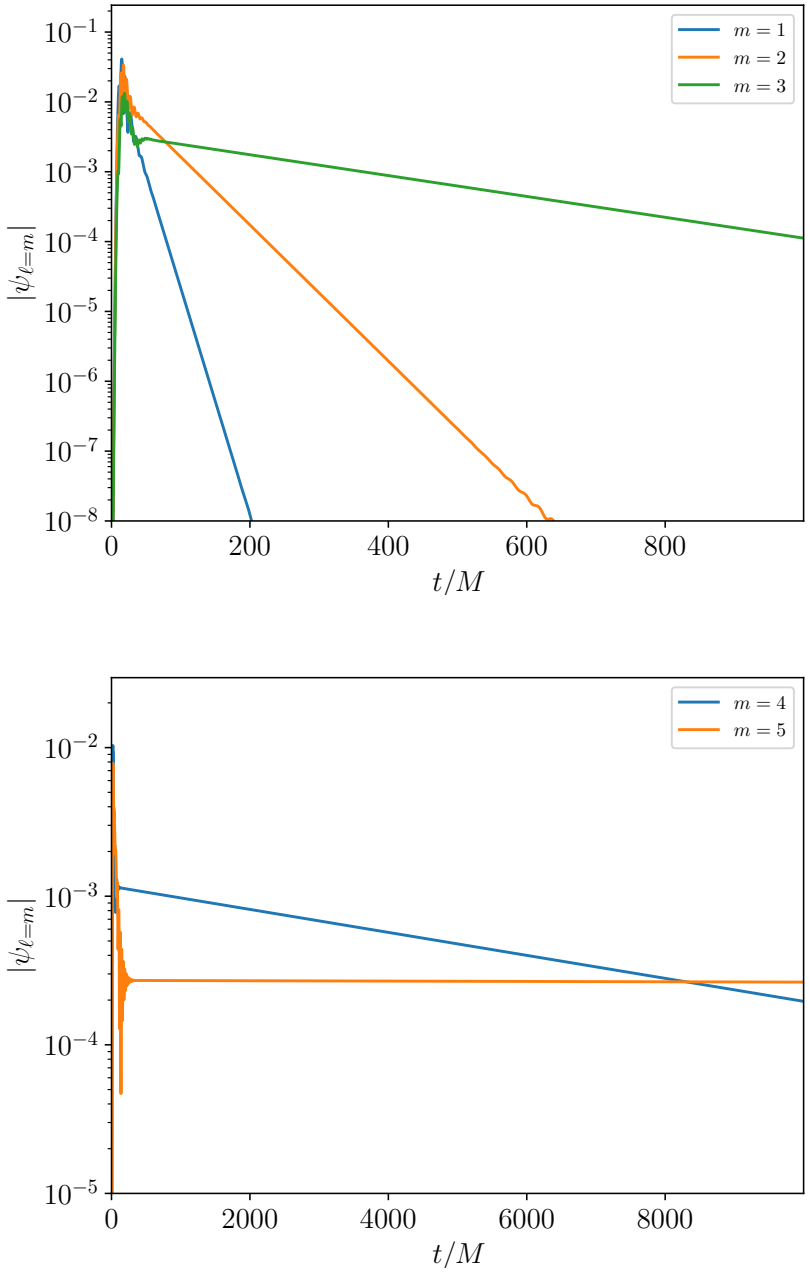

Figure 3.12: Time series data for the evolution of a scalar field in the geometry of an object with $a = 0.5M$ and a surface at $r_0 = 2M$. The field is extracted at $r_* = -3.69$, but the overall behavior is independent of the extraction radii. **Top Panel:** Evolution of the multipoles $m = 1, 2, 3$, up to $t = 10^3 M$. Using a Prony method, we estimate a dominant mode with $M\omega = -0.338 - 7.48 \times 10^{-2} i$, $-0.444 - 2.24 \times 10^{-2} i$ and $-0.532 - 3.44 \times 10^{-3} i$ for $m = 1, 2, 3$ respectively. These estimates compare well with the frequency-domain data in Table 3.1. **Bottom Panel:** Same as top panel, for multipoles $m = 4, 5$ which are longer-lived, up to $t = 10^4 M$. A Prony method now yields $M\omega \sim -0.600 - 1.78 \times 10^{-4} i$ and $-0.652 - 2.65 \times 10^{-6} i$ for $m = 4, 5$, which are still in good agreement with frequency-domain predictions, despite the rather large timescales now involved.

unstable equatorial light ring lies outside the ergoregion). We found no unstable mode. The evolution of initial data, using time-domain methods, also shows no hints of a physical instability, but it does show clearly the dominance of long-lived modes. Typical examples are shown in Fig. 3.12.

3.5 DISCUSSION

Our results establish that there are exponentially growing modes in a horizonless Kerr geometry, when it contains ergoregions. The instability is connected continuously to zero-frequency modes which cease to exist for surface locations outside the ergoregion, i.e., for $r_0 \geq 2M$. An important point for the context at hand is that the ergoregion instability has timescales $\tau \gtrsim 10^5 M$ [3]. One of our main motivations was to understand possible new linear mechanisms in the absence of an ergoregion but when light rings are present, possibly explaining the findings of Ref. [80] and the relatively short timescales reported in that work (possibly too short for a nonlinear mechanism). We found no evidence of new instabilities on timescales $\lesssim 10^5 M$.

3 For $a/M = 0.99$ and $m = 1$, the maximum instability occurs at $\epsilon \sim 0.0056$, for $a/M = 0.99$ and $m = 2$ at $\epsilon \sim 0.0052$, and the relevant timescales are of order $\sim 10^6 M$ [76].

4

ENERGY EXTRACTION FROM BOUNCING GEOMETRIES

Having examined instabilities inherent to horizonless ultracompact objects – systems probing the limits of GR without forming an event horizon – we now transition to a complementary scenario: energy extraction mechanisms driven by the dynamic formation and evaporation of horizons in bouncing geometries. This shift allows us to explore the profound consequences of horizon physics from a different angle. Both phenomena are deeply intertwined with the physics near the would-be horizon scale, often necessitating quantum considerations – whether to explain the potential stability or instability of horizonless objects, or to account for particle creation and energy release during transient horizon phases. We will now delve into these energy extraction processes.

4.1 INTRODUCTION

Hawking radiation and the consequent BH evaporation are among the most remarkable possibilities raised by theoretical physics in the last half century. These are prime examples of quantum gravitational phenomena, but, due to the lack of a fully established theory of quantum gravity, their understanding stems mostly from semiclassical arguments (as the ones that led to their discovery [109]), where gravity is treated classically and matter quantum mechanically. Similar phenomena arise also from somewhat informal pictures developed in the context of candidates to full quantum gravity theories, such as Loop Quantum Gravity [110], and from phenomenological approaches leading to classical metrics that explicitly capture some of the features suggested by the proposals above [37].

Even under this theoretical uncertainty, and without observational evidence, it is widely accepted that some form of radiation and evaporation play an essential role in BH dynamics. It is then natural to try to understand what distinguishes such quantum gravitational objects from their classical counterparts, and, more excitingly, if any of these differences might show up under observational scrutiny.

Here, we consider a simple family of bouncing geometry models, prescribed by classical metrics which are simplified versions of a proposal by Hayward [37], describing fully regular spacetimes containing a "BH" that forms dynamically and later on evaporates. The Penrose diagram of such a dynamical spacetime is depicted in Fig. 4.1. Strictly speaking, these spacetimes don't contain a BH region, since every event can be

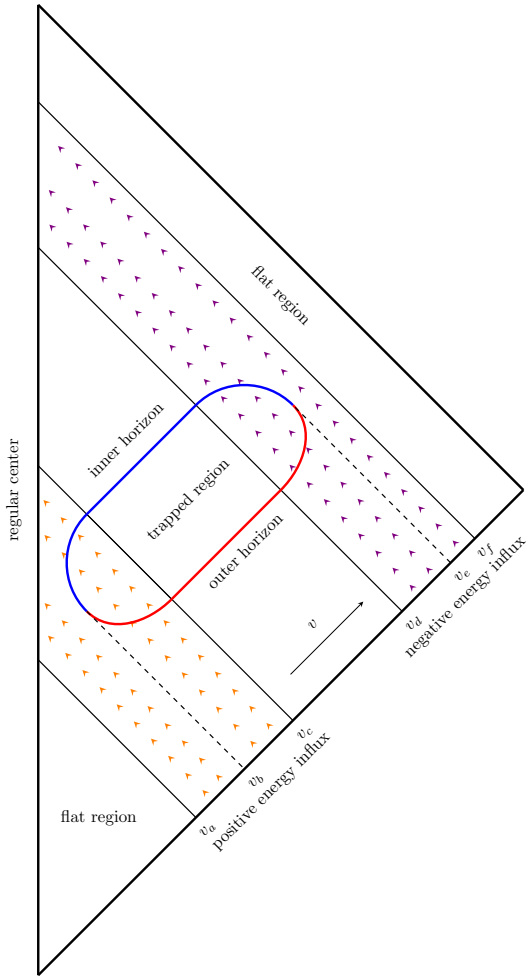

Figure 4.1: Penrose diagram of a (everywhere regular) bouncing geometry. Following the advanced time coordinate v, we start ($v < v_a$) with a flat region; then, an influx ($v_a < v < v_c$) of positive energy leads to the formation ($v = v_b$) of two horizons bounding a region containing trapped surfaces; afterwards, an influx of negative energy ($v_d < v < v_f$) leads to the evaporation of the horizons ($v = v_e$), and to a flat spacetime in the far future region ($v > v_f$).

seen from future null infinity. Nonetheless, they have a trapped region bounded by two apparent horizons, an inner horizon and an outer horizon, which form dynamically and eventually evaporate, leaving behind a flat spacetime in the far future.

Our goal is to understand how these spacetimes respond to perturbations, by re-evaluating the geometric optics approximation and, more importantly, by studying the evolution of (massless) scalar fields. We show that the evaporation and consequent disappearance of the horizons leaves behind a clear signature: a burst of extremely high energy generated at the inner horizon. This burst may lead to detectable observational signals, either in gravitational waves or in the electromagnetic spectrum, that could allow us to gain further insight into the quantum nature of astrophysical horizons.

4.2 A DYNAMICAL "BOUNCING" SPACETIME.

We consider a spherically symmetric metric of the form

$$ds^2 = -F(v,r)dv^2 + 2dvdr + r^2 d\Omega^2 \,, \tag{4.1}$$

where $d\Omega^2$ is the round metric on the unit sphere and

$$F(v,r) = 1 - \frac{2m(v)r^2}{r^3 + 2l^2 m(v)} \,. \tag{4.2}$$

Here, the constant l is assumed to be positive, and the mass function $m(v)$ is assumed to be non-negative. There are two positive real solutions $r_\pm(v)$ of the equation $F(v,r) = 0$ when $m(v) > m_* = \frac{3\sqrt{3}}{4} l$, corresponding to an inner and an outer apparent horizons.

We are interested in describing a spacetime which is flat at early and late times, but has transient horizons. We follow Ref. [37] in choosing $m(v)$ to be a smooth function that (nearly) vanishes in the intervals $(-\infty, v_a)$ and (v_f, ∞), is (nearly) constant equal to $m_0 > m_*$ in the interval (v_c, v_d), is increasing in the interval (v_a, v_c), and is decreasing in the interval $v \in (v_d, v_f)$, where $v_a < v_c < v_d < v_f$ are adjustable parameters. Under these assumptions, the horizons are formed at some advanced time $v_b \in (v_a, v_c)$ and disappear at $v_e \in (v_d, v_f)$, where v_b and v_e are determined by $m(v_b) = m(v_e) = m_*$. Concretely, we choose

$$m(v) = \frac{m_0}{2}\left[\tanh\left(s\frac{v - v_a}{v_c - v_a}\right) - \tanh\left(s\frac{v - v_d}{v_f - v_d}\right)\right] \,, \tag{4.3}$$

which closely resembles Hayward's profile. In particular, for larger values of s, the slope in the transition intervals (v_a, v_c) and (v_d, v_f) becomes steeper. For concreteness, here we take $s = 10$.

4.3 BLUESHIFT OF NULL GEODESICS.

Our main result is a large blueshift of the radiation trapped inside the horizons. This radiation may have been absorbed during horizon

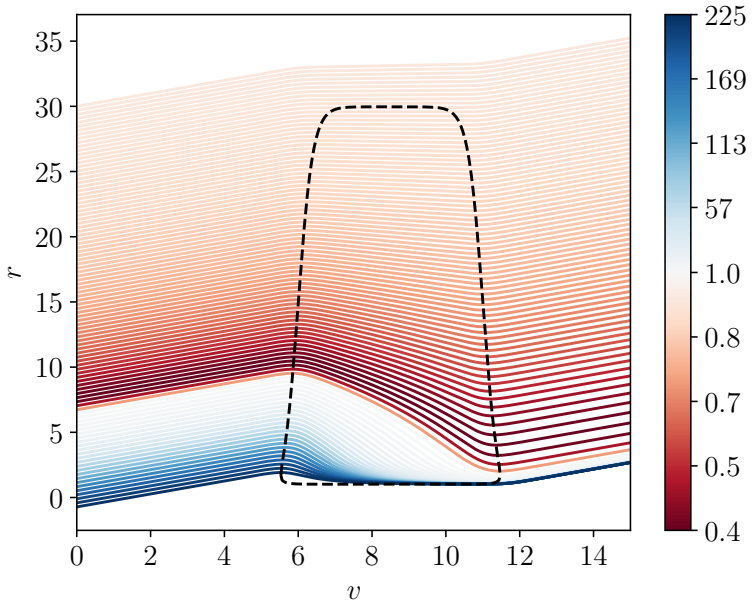

Figure 4.2: Null geodesics for spacetime `IA`. The black dashed line shows the location of the horizons. Notice how null geodesics pile up near the inner horizon, which is ultimately the reason for the high-energy burst of radiation that we see once the spacetime bounces and horizons disappear, cf. Fig. 4.3. The line color indicates the amplification factor, with darker blue lines representing a stronger blueshift and darker red lines indicating a stronger redshift. In regions located far away from the inner horizon, there is only a minimal amount of redshift.

formation, or accreted at later stages. Although our focus is on massless (scalar) fields, we can see the blueshift already at the level of null geodesics, a good description of high-frequency radiation. This geometric optics approximation was previously studied in Ref. [111], although for a different mass function. We quickly revisit this problem for the mass function (4.3), in order to compare with our main result concerning the amplification of scalar waves. Consider a radially outgoing light ray. The energy of the corresponding photon with respect to stationary observers in the flat region, as well as observers at the center $r = 0$ (for whom $F(v, r) = 1$), is simply

$$E = -\frac{\partial L}{\partial \dot{v}} = F(v, r)\dot{v} - \dot{r}\,, \tag{4.4}$$

where

$$L = \frac{1}{2}\left[-F(v, r)\dot{v}^2 + 2\dot{v}\dot{r}\right] \tag{4.5}$$

is the Lagrangian for radial geodesics. This is also a conserved quantity in the static Schwarzschild-like region where m is constant, and so we identify it with the photon's energy. For outgoing null geodesics, we have

$$F(v, r)\dot{v} = 2\dot{r} \quad \Rightarrow \quad \frac{dr}{dv} = \frac{1}{2}F(v, r)\,, \tag{4.6}$$

and also

$$E = \dot{r} = \frac{1}{2}F(v, r)\dot{v}\,. \tag{4.7}$$

Using the Euler-Lagrange equation in r, we find that

$$\ddot{v} = -\frac{1}{2}\frac{\partial F}{\partial r}\dot{v}^2\,, \tag{4.8}$$

and so, assuming $v = v_0$ and $\dot{v} = \dot{v}_0$ for $r = 0$, we have

$$\dot{v} = \dot{v}_0 \exp\left(-\frac{1}{2}\int_{v_0}^{v} \frac{\partial F}{\partial r} dv\right)\,, \tag{4.9}$$

where $r(v)$ in this integral is computed from Eq. (4.6). From Eq. (4.7) we then obtain the ratio between the energies of the photon at $r = 0$ and $r = \infty$:

$$\mathcal{A} \equiv \frac{E_\infty}{E_0} = \exp\left(-\frac{1}{2}\int_{v_0}^{\infty} \frac{\partial F}{\partial r} dv\right)\,. \tag{4.10}$$

We evaluated the integral in (4.10) to compute the largest and smallest amplification factor $\mathcal{A}$ for different spacetimes, shown in Table 4.1 and Fig. 4.2. Notice that the amplification can become arbitrarily large for sufficiently long-lived horizons (when $v_d - v_c$ is very large compared to the other scales in the problem), and stems from geodesics close to the inner horizon, which is in fact an attractor for radial null geodesics, as is easily seen from Eq. (4.6).

Table 4.1: List of simulations for the evolution of the $\ell = 0$ mode of a scalar field in spacetime (4.1)-(4.3). We use $r_G = 8$, $\sigma = 1$ for the initial pulse, with initial energy $E_0 = 0.63$. We also use $s = 10$ for the mass function $m(v)$. We define the amplification $\mathcal{A} \equiv E_\infty/E_0$, the ratio between final and initial energy of the scalar field, cf. Eq. (4.19). The quantities $\mathcal{A}_g^{\max}$, $\mathcal{A}_g^{\min}$, are the corresponding amplification factors for null geodesics which maximize or minimize the energy gain, respectively, cf. Eq. (4.10). We get similar results for $\ell > 0$. To assess whether the effect also is present for longer wavelengths, we incorporated additional test runs, referred to as `IWA`, `IWB`, and `IWC`. We adjusted the parameters as follows: $r_G = 45$, $E_0 = 0.06$ and $\sigma = 1, 5, 10$, respectively.

Run	m_0	v_a	v_c	v_d	v_f	l	κ_-	E_f	$\mathcal{A}$	$\mathcal{A}_g^{\max}$	$\mathcal{A}_g^{\min}$
`IA`	15	6	10	11	15	1	0.9329	4.55	7.26	225	0.38
`IIA`	15.5	6	10	11	15	1	0.9351	5.15	8.22	232	0.38
`IIIA`	16	6	10	11	15	1	0.9371	5.67	9.06	239	0.38
`IVA`	16.5	6	10	11	15	1	0.9390	6.10	9.73	246	0.37
`VA`	17	6	10	11	15	1	0.9408	6.40	10.2	253	0.37
`ILA`	15	6	10	11	15	2	0.4324	0.47	0.747	10.7	0.63
`ILB`	15	6	10	11	15	4	0.1813	0.63	0.998	2.59	0.82
`IMA`	15	6	10	12	16	1	0.9329	11.3	18.1	573	0.34
`IMB`	15	6	10	13	17	1	0.9329	26.5	42.3	1457	0.31
`IMC`	15	6	10	14	18	1	0.9329	69.0	110	3704	0.28
`IMD`	15	6	10	15	19	1	0.9329	178	285	9416	0.26
`IME`	15	6	10	16	20	1	0.9329	459	733	23935	0.24
`IWA`	50	6	10	11	15	1	0.9800	1.31	0.905	640	0.30
`IWB`	50	6	10	11	15	1	0.9800	1.31	2.76	640	0.30
`IWC`	50	6	10	11	15	1	0.9800	1.31	20.9	640	0.30

In the limit $v_a \sim v_c$, $v_d \sim v_f$, and for null geodesics that stay close to the inner horizon, we have the approximate formula

$$\mathcal{A} \sim \exp\left(\kappa_-(v_d - v_c)\right) , \tag{4.11}$$

where

$$\kappa_- = -\frac{m_0 r_-^4 - 4l^2 m_0^2 r_-}{\left(r_-^3 + 2l^2 m_0\right)^2} , \tag{4.12}$$

is the surface gravity of the inner horizon, with r_- the smallest positive root of $r_-^3 - 2m_0 r_-^2 + 2l^2 m_0$. Note that for $l \ll m_0$ we have $r_- \sim l$ and $\kappa_- \sim 1/l$, and so the amplification acquires the simple form $\mathcal{A} \sim \exp\left((v_d - v_c)/l\right)$.

4.4 DYNAMICS OF A MASSLESS SCALAR FIELD

To verify that energy extraction holds also for large wavelength fields, a proper description of radiation is necessary. For simplicity, we follow the dynamics of a massless scalar field on the above background, governed by the wave equation

$$\nabla^a \nabla_a \Phi = 0\,. \tag{4.13}$$

We can expand Φ as a superposition of spherical modes, given in terms of the spherical harmonics $Y_{\ell m}(\theta,\varphi)$ as solutions of the form

$$\Phi(v,r,\theta,\varphi) = \frac{\phi(v,r)}{r} Y_{\ell m}(\theta,\varphi)\,, \tag{4.14}$$

and so we focus on these solutions. The wave equation for the modes can be written explicitly as follows:

$$\partial_v \partial_r \phi + \frac{F}{2}\partial_r^2 \phi + \frac{\partial_r F}{2}\partial_r \phi - \left(\frac{\partial_r F}{2r} + \frac{\ell(\ell+1)}{2r^2}\right)\phi = 0\,. \tag{4.15}$$

In what follows we will solve this equation numerically as a characteristic initial value problem by giving initial data on the characteristic surface $v = v_a$. Specifically, we will take a Gaussian centered at $r = r_G$ with width σ:

$$\phi\,(r, v_a) = e^{-\left(\frac{r-r_G}{\sigma}\right)^2}\,. \tag{4.16}$$

Even though the spacetime is dynamic, it has static regions where one has well-defined notions of energy. The energy of the field on a characteristic surface $\mathcal{N}$ of constant v contained in the static regions can be computed as

$$E = -\int_{\mathcal{N}} T_{\mu\nu}\left(\frac{\partial}{\partial v}\right)^{\mu}\left(\frac{\partial}{\partial r}\right)^{\nu} = -\int_0^\infty\!\!\int_{S^2} T_{vr} r^2 d\Omega dr\,. \tag{4.17}$$

From the usual expression for the massless scalar field energy-momentum tensor, we find

$$T_{vr} = -\frac{1}{2}F(\partial_r\Phi)^2 - \frac{1}{2r^2}|\nabla\!\!\!/\,\Phi|^2\,, \tag{4.18}$$

where $\nabla\!\!\!/$ is the gradient on the unit 2-sphere. Since the spherical harmonics $Y_{\ell m}(\theta,\varphi)$ form an orthonormal basis of eigenfunctions of the Laplacian on the unit 2-sphere with eigenvalues $-\ell(\ell+1)$, we obtain, after integrating by parts,

$$E = \frac{1}{2}\int_0^\infty \left[F r^2\left(\partial_r\left(\frac{\phi}{r}\right)\right)^2 + \frac{\ell(\ell+1)}{r^2}\phi^2\right] dr\,. \tag{4.19}$$

We define the amplification factor $\mathcal{A}$ as we did for the null geodesics, $\mathcal{A} \equiv E_\infty / E_0$.

4.5 NUMERICAL SCHEME

We can proceed to solve Eq. (4.15) by employing numerical methods. Specifically, we apply a 2^{nd} order finite difference method for spatial discretization and a 4^{th} order Runge-Kutta method for time integration. We evolve ϕ and $\partial_r\phi$ using the boundary conditions

$$\begin{cases} \phi(v,0) = 0 & \text{(regularity at the origin)}\,, \\ \phi(v,\infty) = \partial_r\phi(v,\infty) = 0 & \text{(no incoming radiation)}\,, \end{cases}$$

together with the implicit boundary condition obtained by integrating Eq. (4.15):

$$\partial_r\phi(v,0) = -\int_0^\infty \left(\frac{\partial_r F}{r} + \frac{\ell(\ell+1)}{r^2}\right)\phi\, dr\,. \tag{4.20}$$

More precisely, given ϕ and $\partial_r\phi$ on a surface of constant v, we recompute $\partial_r\phi(v,0)$ from Eq. (4.20) (if $\ell > 0$, the convergence of the integral in Eq. (4.20) implies immediately that $\partial_r\phi(v,0) = 0$), which we use to evaluate $\partial_r^2\phi$. We then have $\partial_v\partial_r\phi$ from Eq. (4.15), and $\partial_v\phi$ from

$$\partial_v\phi(v,r) = -\int_r^\infty \partial_v\partial_r\phi\, dr\,, \tag{4.21}$$

which we use to evolve ϕ and $\partial_r\phi$ by the method of lines.

In practice, we use a finite computational domain rather than an infinite one. Furthermore, in order to improve the resolution at the inner horizon, we introduce a new radial coordinate R by stretching r as (see [112])

$$f(R) = A\,(R - R_0) + B\sqrt{1 + (R-R_0)^2/\epsilon}\,, \tag{4.22}$$

$$r = f(R) - f(0)\,. \tag{4.23}$$

By using these coordinates, it is possible to smoothly transition between the two resolutions. These resolutions are determined by the values of the parameters A and B, and the transition takes place in a region with a width of ϵ centered around the value of R_0. To be specific, we use $R_0 = 1000$, $\epsilon = 10$, and obtain the values of A and B by solving $r'(0) = 0.01$ and $\lim_{R\to\infty} r'(R) = 1$. This allows us to resolve sharply shaped waveforms caused by blueshift near the inner horizon. Our numerical results show second-order convergence, consistent with the scheme we use.

4.6 BLUESHIFT OF SCALAR FIELDS.

Our results are summarized in Fig. 4.3 and Table 4.1. A common feature to all our simulations is clear in Fig. 4.3: a sharp spike of radiation, produced close to the inner horizons and released out when the horizons disappear. This is the wave analog of the blueshift seen before in null geodesics, and is responsible for the energy amplification shown in the

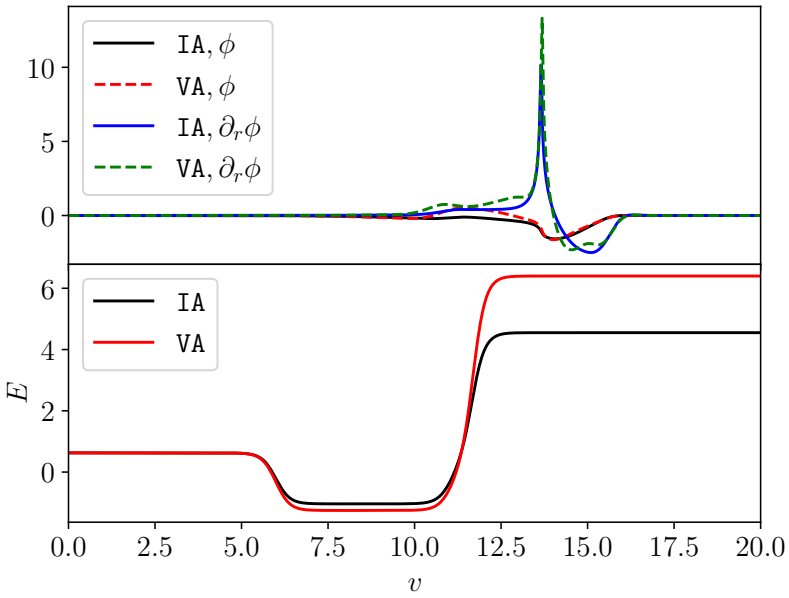

Figure 4.3: Evolution of Gaussian initial data in bouncing spacetimes. **Top panel:** the scalar field measured at $r \approx 2.0$ for spacetimes `IA` and `VA`. Notice a sharp spike in the radial derivative, signalling what we term "blueshift" phenomena. **Bottom panel:** the total energy E in the spacetime, defined in Eq. (4.19). Energy amplification is apparent.

lower panel of the figure and quantified also in Table 4.1. A study of different families of initial data confirms the geodesic estimate (4.11): the amplification $\mathcal{A}$ scales exponentially with the lifetime of the horizons and with the inner horizon surface gravity. It is also reassuring to notice that the amplification $\mathcal{A}$ of the scalar pulse lies between the largest and smallest values of the corresponding amplification factor of null geodesics, i.e. $\mathcal{A}_g^{\min} < \mathcal{A} < \mathcal{A}_g^{\max}$ (cf. Table 4.1). The last row in Table 4.1 shows that no fine tuning of initial data is necessary: even initial data which is spread ($\sigma \gg l$) gives rise to very large amplification factors.

The spacetime also possesses one unstable light ring, which corresponds to the maximum real root of the equation $2F(r) - rF'(r) = 0$ (in the stage where m is constant to a good approximation). Thus, we expect all the physics associated to unstable light rings – for example, quasinormal ringdown [11, 113, 114] – to be shared by our dynamical spacetime. The fractional correction to the light-ring frequency is $\delta\Omega/\Omega = 2l^2/(27m_0^2) + \mathcal{O}(l/m_0)^4$, and thus for microscopic l not accessible to current detectors.

4.7 DISCUSSION

The novel energy amplification mechanism that we have identified here originates from a blueshift instability which is akin, but nonetheless significantly different, from the Cauchy horizon instability discovered by Penrose [115].

Cauchy horizon instabilities have been studied extensively [53, 54, 116–124], in particular in the related context of regular (eternal) BHs [125–127]. In all these cases, the inner horizon is an ingoing Cauchy horizon and the corresponding blueshift mechanism leads to a divergent instability and the blow-up of perturbations, which remain confined to the BH interior. In fact, the global causal structure of these spacetimes is significantly different from the one depicted in Fig. 4.1 (for comparison, see for instance Fig. 1 in [127]), and the infinite blueshift instability can already be foreseen by inspection of the corresponding Penrose diagrams: at the level of geometric optics, it stems from the piling up (at the Cauchy horizon) of an infinite number of ingoing null geodesics emitted at regular time intervals, as measured by an exterior observer.

By contrast, in our framework, the inner horizon *is not* a Cauchy horizon; in particular, spacetime is globally hyperbolic and inextendible. Moreover, the inner horizon is outgoing and, in this case, the blueshift instability leads to a finite amplification, in accordance with the fact that now only a finite number of equally timed outgoing geodesics can pile up near the inner horizon. Most remarkably, these phenomena can be observed from infinity, after the horizons evaporate, leading, in essence, to an energy extraction mechanism.

If indeed collapse is halted and horizons disappear, our results seem to imply that there are high-energy phenomena in the cosmos that could be of quantum origin. These effects could give rise to high energy

photons, neutrinos or GWs. Page has shown that primordial BHs of mass $m_0 \lesssim 5 \times 10^{14}\,\mathrm{g}$ would have evaporated by now [128]. Take therefore, for illustration purposes, an object which is evaporating today, hence with $v_d - v_c \sim 13 \times 10^9\,\mathrm{yr}$. For Planck size cores, $l \sim 10^{-44}\,\mathrm{s}$, we find an amplification $\mathcal{A} \sim e^{10^{61}}$, which means that the outgoing pulse has a significant backreaction in the spacetime, not taken into account in our study. Indeed, a single cosmic microwave background photon would be amplified to a much larger energy than the object itself (and it's challenging if not impossible to concoct an initial fluctuation for which this is not true). Indeed, even for macroscopic l the amplification is tremendous. Note that Hawking radiation would also be present during the process, but it is significantly different from the inner horizon instability effect. In fact, Hawking radiation has a purely quantum origin, and it is thermal. In contrast, the inner horizon amplification identified in this paper is a classical mechanism (acting on model regular spacetime geometries that may result from Hawking evaporation), and it is non-thermal. A deeper understanding of both phenomena would require analyzing the effects of backreaction.

Backreaction in the geometry is an interesting problem, but it requires knowledge of an underlying theory leading to spacetime (4.1)-(4.3). Attempts in this direction can be found in Refs. [129–135].

We did not dwell on more classical phenomena like BH ringdown, but it is clear that for spacetimes for which the horizons linger longer than a light ring timescale, BH ringdown should also be observed [11, 15, 136].

Finally, our results could have experimental verification, beyond the gravitational realm, in the context of analogue gravity [137–140]. For example, sound waves in a nontrivial flow propagate as a scalar field on a curved spacetime. For flows with sonic points (where flow velocity equals local sound speed) horizons appear. Spherically symmetric, or more general time-dependent flows, therefore develop apparent acoustic horizons and no acoustic event horizons [139]. There are indeed acoustic geometries with multiple sonic points [141, 142]. It would be interesting to understand the consequences of our results for those acoustic setups, or even if they have a bearing on collapse of air bubbles leading to sonoluminescence [143].

5

ENERGY EXTRACTION FROM FUNDAMENTAL SOLITONS

The blueshift amplification near the inner horizon presents a potent energy extraction mechanism tied to the specific dynamics of bouncing geometries. In this chapter, we investigate whether similar energy extraction phenomena, potentially driven by different underlying physics such as self-interaction and time-periodicity, can occur in fundamental solitons like Q-balls.

5.1 INTRODUCTION

Energy exchange phenomena play a pivotal role in the small and large scale dynamics of all observed phenomena. A class of these are termed "superradiant" and take place when an object with many internal degrees of freedom – which can internally dissipate energy – is able to amplify certain impinging radiation modes, while increasing its internal energy [144]. In this mechanism the necessary energy to enhance the radiation (and increase the object's internal energy) is usually provided by kinetic energy. For objects in uniform linear motion superradiance requires a velocity larger than the characteristic phase velocity in the medium (e.g., Vavilov-Cherenkov effect), while rotational superradiance requires angular velocities larger than the characteristic (angular) phase velocity in the medium [36, 61, 62, 144]. A different energy exchange mechanism is realised by the interaction of radiation with a time-dependent background. Time-periodic backgrounds tend to induce a coupling between a discrete set of modes, leading to an effective energy exchange with radiation. In particular, the energy of radiation may be enhanced through a blue-shift of incoming modes to higher frequencies (as it happens with oscillating cavity walls and objects [145–148] or moving objects [149]).

Superradiance has attracted a considerable amount of attention in BH physics, since it may be a viable way to power violent phenomena in the cosmos, or even to transfer energy between BHs and new fundamental degrees of freedom [36]. Spinning BHs have two properties which are ideal for superradiance: an ergoregion that effectively couples radiation to spacetime, and an horizon that quenches negative-energy modes, allowing for energy exchange in a stable manner [67]. It was recently claimed that Q-balls – a type of non-topological scalar

field soliton [23, 150] – are also prone to superradiance, not requiring rotation nor any type of motion in real space [151].

Here, we argue that even though the original proof was flawed, energy extraction from Q-balls is indeed possible. It is not of superradiant nature, but it involves rather a blue-shift mechanism powered by the time-periodic background, akin to Doppler shift of radiation in oscillating cavities. Due to Derrick's theorem [152] – showing that there is no stable time-independent solution of finite energy for a wide class of nonlinear wave equations – most fundamental solitons are expected to be time-periodic. This energy extraction mechanism most likely extends to all these objects, since nonlinearites will induce the necessary mode-mixing in impinging radiation. We have explicitly proved that this is the case for (Newtonian) BSs, which have attracted attention in connection with DM physics and BH mimickers [11, 20].

5.2 Q-BALLS AS A TESTBED

Consider a simple U(1)-symmetric theory of a complex scalar field $\bar{\Phi}$ in a three-dimensional flat spacetime $(\mathbb{R}^3, \eta_{\alpha\beta})$ described by the action

$$S = -\tfrac{1}{2}\int \mathrm{d}^3\bar{x}\sqrt{-\eta}\left[\partial^{\bar{\alpha}}\bar{\Phi}^*\partial_{\bar{\alpha}}\bar{\Phi} + V\left(|\bar{\Phi}|\right)\right], \tag{5.1}$$

where $\eta := \det(\eta_{\alpha\beta})$, with the potential $V = \mu^2|\bar{\Phi}|^2 - \lambda|\bar{\Phi}|^4 + \bar{g}|\bar{\Phi}|^6$. We work with the re-scaled the dimensionless quantities $x := \mu\bar{x}$, $\Phi := \sqrt{\lambda}\bar{\Phi}/\mu$ and $g := \mu^2\bar{g}/\lambda^2$, in terms of which the potential reads $V = |\Phi|^2 - |\Phi|^4 + g|\Phi|^6$. We restrict to $g \geq 1/4$ (so that $\Phi = 0$ is the true vacuum). The field satisfies the equation of motion

$$\Box_\eta\Phi - \frac{\partial V}{\partial\Phi^*} = 0, \tag{5.2}$$

and possess the divergenceless Noether current

$$J^\alpha_Q = \mathrm{Im}\left(\Phi^*\partial^\alpha\Phi\right), \tag{5.3}$$

and energy current (as measured by a family of parallel inertial observers with 4-velocity δ^α_t)

$$J^\alpha_E = -\eta^{\alpha\beta}T_{\beta\gamma}\delta^\gamma_t, \tag{5.4}$$

with the (also divergenceless) energy-momentum tensor

$$T_{\alpha\beta} = \partial_{(\alpha}\Phi^*\partial_{\beta)}\Phi - \tfrac{1}{2}\eta_{\alpha\beta}\left[\partial^\gamma\Phi^*\partial_\gamma\Phi + V\left(|\Phi|\right)\right]. \tag{5.5}$$

Using polar coordinates (r, φ) on the hypersurfaces Σ_t orthogonal to δ^α_t, Q-balls are solutions of the form

$$\Phi_Q(t, r, \varphi) = \frac{1}{\sqrt{2}}f(r)e^{-\mathrm{i}\left(\omega_Q t - m_Q\varphi\right)}, \tag{5.6}$$

that are regular at $r = 0$ and $r = +\infty$ (without loss of generality, we consider $\omega_Q > 0$ and $m_Q \in \mathbb{Z}^+_0$). Some radial profiles with different ω_Q are shown in Fig. 5.1. To exist the Q-ball frequency must be $\omega_Q^{\mathrm{thin}} < \omega_Q < 1$, with the lower bound $\omega_Q^{\mathrm{thin}} := \min[2V/|\Phi|^2]$ corresponding to the so-called *thin-wall* limit [23].

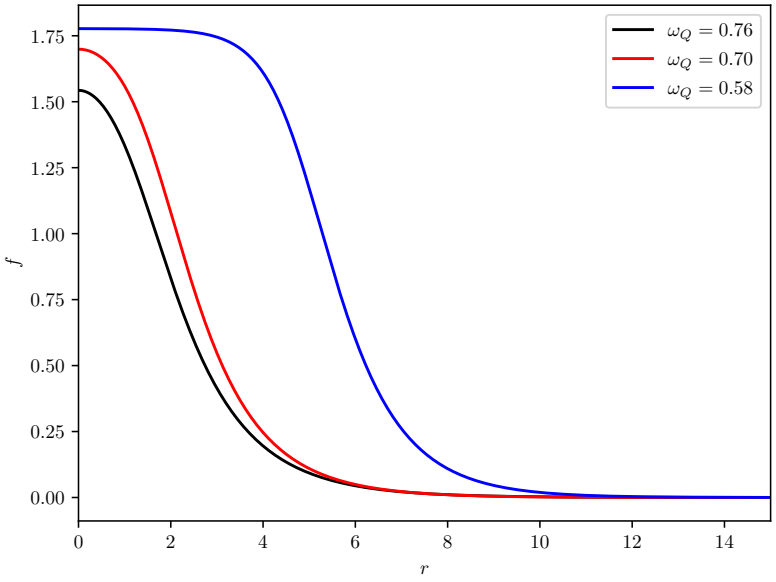

Figure 5.1: Radial profile $f(r)$ of the Q-balls studied in this work, with $\omega_Q = (0.58, 0.70, 0.76)$, $m_Q = 0$ and $g = 1/3$. The values at the origin are, respectively, $f(0) = (1.78, 1.70, 1.54)$, their charge is $Q = \int_\Sigma J^t_Q = (70.77, 13.70, 9.76)$ and energy is $E = \int_\Sigma J^t_E = (47.02, 12.00, 9.14)$. We consider only ground-state (nodeless) Q-ball solutions.

5.3 LINEAR PERTURBATIONS

A sufficiently small perturbation Φ_1 to a Q-ball background solution, $\Phi \approx \Phi_Q + \Phi_1$ with $|\Phi_1| \ll |\Phi_Q|$, satisfies the *linearized* equation of motion

$$\Box_\eta \Phi_1 - U(r)\Phi_1 - e^{-2\mathrm{i}(\omega_Q t - m_Q \varphi)} W(r) \Phi_1^* = 0, \tag{5.7}$$

where $U \coloneqq 1 - 2f^2 + \frac{9}{4} g f^4$ and $W \coloneqq -f^2 + \frac{3}{2} g f^4$. The last term gives rise to mode-mixing and, thus, this equation does not admit monochromatic solutions.

5.4 FREQUENCY-DOMAIN ANALYSIS

The solutions with minimal frequency-content are of the form

$$\Phi_1 = \phi_+(r) e^{-\mathrm{i}(\omega_+ t - m_+ \varphi)} + \phi_-(r) e^{-\mathrm{i}(\omega_- t - m_- \varphi)}, \tag{5.8}$$

where $\omega_\pm = \omega_Q \pm \omega$ and $m_\pm = m_Q \pm m$. The mode functions (ϕ_+, ϕ_-) satisfy the *coupled* system

$$\frac{1}{r} \partial_r \left(r \partial_r \phi_\pm \right) + \left[\omega_\pm^2 - U - \frac{m_\pm^2}{r^2} \right] \phi_\pm - W \phi_\mp^* = 0, \tag{5.9}$$

which clearly shows the mode-mixing between ϕ_+ and ϕ_- introduced by the background Q-ball. At infinity the mode functions are

$$\lim_{r\to\infty}\phi_\pm \approx \tfrac{1}{\sqrt{2\pi|k_\pm|r}}\left(A^{\rm out}_\pm e^{{\rm i}k_\pm r}+A^{\rm in}_\pm e^{-{\rm i}k_\pm r}\right), \tag{5.10}$$

and at the origin

$$\lim_{r\to 0}\phi_\pm \approx C_\pm\left(|k_\pm|r\right)^{|m_\pm|}, \tag{5.11}$$

where $k_\pm \coloneqq \pm s_\omega(\omega_\pm^2-1)^{1/2}$ with $s_\omega \coloneqq \mathrm{sign}(\omega)$. From the scale invariance of the linear perturbations, we can choose $C_+=1$ without loss of generality.

In this work we focus on perturbations satisfying the double condition $|\omega_\pm|>1$, in which case both modes describe propagating waves (i.e., *scattering states*); the waves with amplitude $A^{\rm out}_\pm$ (resp., $A^{\rm in}_\pm$) have radial group velocity $\frac{{\rm d}\omega_\pm}{{\rm d}k_\pm}$ (resp., $-\frac{{\rm d}\omega_\pm}{{\rm d}k_\pm}$). This means that $A^{\rm out}_\pm$ describe outgoing states propagating in the δ^μ_r direction, the opposite to the direction of propagation of incoming $A^{\rm in}_\pm$ states.

The time-averaged flux of Q-charge through a 1-sphere of radius r (with $r\to\infty$) is

$$\begin{aligned}\mathcal{F}_Q &= \lim_{r\to\infty} r\int_0^{2\pi}{\rm d}\varphi\left\langle J^r_Q\right\rangle\\ &\approx s_\omega\sum_{s=+,-} s\left(|A^{\rm out}_s|^2-|A^{\rm in}_s|^2\right),\end{aligned} \tag{5.12}$$

that of of energy is

$$\begin{aligned}\mathcal{F}_E &= \lim_{r\to\infty} r\int_0^{2\pi}{\rm d}\varphi\left\langle J^r_E\right\rangle\\ &\approx s_\omega\sum_{s=+,-} s\,\omega_s\left(|A^{\rm out}_s|^2-|A^{\rm in}_s|^2\right),\end{aligned} \tag{5.13}$$

and of angular momentum is

$$\begin{aligned}\mathcal{F}_L &= \lim_{r\to\infty} r\int_0^{2\pi}{\rm d}\varphi\left\langle T_{r\varphi}\right\rangle\\ &\approx s_\omega\sum_{s=+,-} s\,m_s\left(|A^{\rm out}_s|^2-|A^{\rm in}_s|^2\right).\end{aligned} \tag{5.14}$$

where $\langle\,\cdot\,\rangle \equiv \lim_{T\to\infty}\frac{1}{T}\int_0^T{\rm d}t\,(\,\cdot\,)$.

It is easy to see from Eq. (5.9) that the quantity

$$J_\phi \coloneqq r\,{\rm Im}\left(\phi_+^*\partial_r\phi_+ + \phi_-\partial_r\phi_-^*\right), \tag{5.15}$$

is independent of r on-shell, i.e., $\partial_r J_\phi = 0$ for a solution of Eq. (5.9). Regularity of the linear perturbations at the origin [c.f. Eq. (5.11)] implies then that $J_\phi = 0$. But, since $J_\phi(r\to\infty)\propto\sum_{s=\pm}(|A^{\rm out}_s|^2-|A^{\rm in}_s|^2)$, one finds

$$|A^{\rm out}_-|^2+|A^{\rm out}_+|^2 = |A^{\rm in}_-|^2+|A^{\rm in}_+|^2. \tag{5.16}$$

The time-averaged fluxes can then be written as

$$\mathcal{F}_Q \approx 2s_\omega \left(|A_+^{\rm out}|^2 - |A_+^{\rm in}|^2\right), \tag{5.17}$$

$$\mathcal{F}_E \approx 2s_\omega\omega_Q \left(|A_+^{\rm out}|^2 - |A_+^{\rm in}|^2\right), \tag{5.18}$$

$$\mathcal{F}_L \approx 2s_\omega m_Q \left(|A_+^{\rm out}|^2 - |A_+^{\rm in}|^2\right). \tag{5.19}$$

Thus, both Q-charge, energy and angular momentum can be exchanged with the background (exchange of angular momentum is only possible with a spinning Q-ball). Energy extraction from a spinning Q-ball is necessarily accompanied by angular momentum extraction.

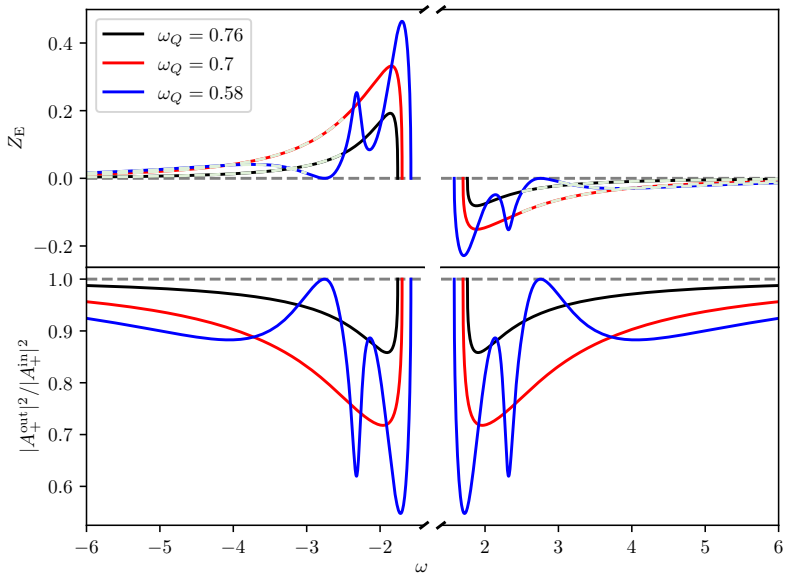

Figure 5.2: *Upper panel:* Relative energy amplification factor, Z_E, of an incoming mode ϕ_+ with $m = 0$ scattering off a non-spinning Q-ball; the coupling is $g = 1/3$. The dashed lines are the results from time-domain simulations. *Lower panel:* Ratio $|A_+^{\rm out}|^2/|A_+^{\rm in}|^2$, which is seen to be ≤ 1 for all ω.

The amplification factors of Q-charge, energy and angular momentum in the scattering process, defined as (the absolute value of) the ratio of the time-averaged outgoing flux to the incoming flux, are respectively

$$1 + Z_Q = \left|\frac{|A_+^{\rm out}|^2 - |A_-^{\rm out}|^2}{|A_+^{\rm in}|^2 - |A_-^{\rm in}|^2}\right|, \tag{5.20}$$

$$1 + Z_E = \left|\frac{\omega_+|A_+^{\rm out}|^2 - \omega_-|A_-^{\rm out}|^2}{\omega_+|A_+^{\rm in}|^2 - \omega_-|A_-^{\rm in}|^2}\right|, \tag{5.21}$$

$$1 + Z_L = \left|\frac{m_+|A_+^{\rm out}|^2 - m_-|A_-^{\rm out}|^2}{m_+|A_+^{\rm in}|^2 - m_-|A_-^{\rm in}|^2}\right|. \tag{5.22}$$

The Z-factors measure the *relative* amplification (or attenuation) in the scattering process: $Z > 0$ for amplification, whereas $Z < 0$ for attenuation.

Note that asymptotic fluxes are the appropriate quantities that allow one to discriminate between amplification and attenuation in a scattering process. In Ref. [151] an alternative criteria for energy amplification was used, based instead on (the absolute value of) the ratio of energy contained in outgoing states to incoming ones in some asymptotic annular region $r_1 < r < r_2$. Given the different propagation speeds of the $\phi_\pm$ modes, this is not an appropriate measure. In fact, in the limit where one mode has arbitrarily small group velocity, its energy density becomes arbitrarily large (c.f. Fig. 2 of [151]), but its energy flux – which determines the rate of energy exchanged with the exterior – may still be small.

From Eq. (5.21) it is clear that energy amplification will occur for any incoming state with $A^{\rm in}_+ = 0$ and $\omega > 0$, or $A^{\rm in}_- = 0$ and $\omega < 0$. On the other hand, there will be energy attenuation ($Z_E < 0$) for any incoming state with $A^{\rm in}_- = 0$ and $\omega > 0$, or $A^{\rm in}_+ = 0$ and $\omega < 0$. These sufficient conditions for energy amplification do *not* agree with the ones found in Ref. [151], due to the different criteria for amplification given there. The outcome of a more general scattering process in which the incoming state contains a mixture of ϕ_+ and ϕ_- modes depends on the details of the process, i.e., on the scattering parameters ω, m and $A^{\rm in}_-/A^{\rm in}_+$. Similarly, one can immediately see from Eq. (5.22) that for a spinning Q-ball ($m_Q > 0$) there is angular momentum amplification for an incoming state with $A^{\rm in}_+ = 0$ and $m \geq m_Q$, or $A^{\rm in}_- = 0$ and $m \leq -m_Q$, and attenuation for an incoming state with $A^{\rm in}_- = 0$ and $m \geq m_Q$, or $A^{\rm in}_+ = 0$ and $m \leq -m_Q$.

The energy extraction mechanism discussed here is *not* of superradiant-type. In fact, enhancement of energy (or Q-charge, or angular momentum) of a single incoming state is never observed, as can be seen by noting that $|A^{\rm out}_s|/|A^{\rm in}_s| \leq 1$, either directly from Eq. (5.16), or from the lower panel of Fig. 5.2. Instead, the energy extraction is accomplished through a "blueshift-like" exchange, where the time-dependent background effectively pumps energy from the lowest energy (i.e., frequency) state to the highest. As we discuss in the next section, the Q-ball will then evolve to a new Q-ball with different parameters as to conserve the total Q-charge, energy, and angular momentum in the process.

The Z_E-factor is shown in the upper panel of Fig. 5.2 for an incoming ϕ_+ mode (i.e., $A^{\rm in}_- = 0$) from solving numerically Eq. (5.9); these results show a remarkable agreement with those from evolving a wavepacket in the time-domain (discussed in the next section). As expected, we find energy amplification of $\omega < 0$ modes for all Q-balls, and attenuation of $\omega > 0$ modes. Note also how energy extraction is more effective for Q-balls closer to the thin-wall limit, for which the field profile is nearly constant in the interior (c.f. Fig. 5.1).

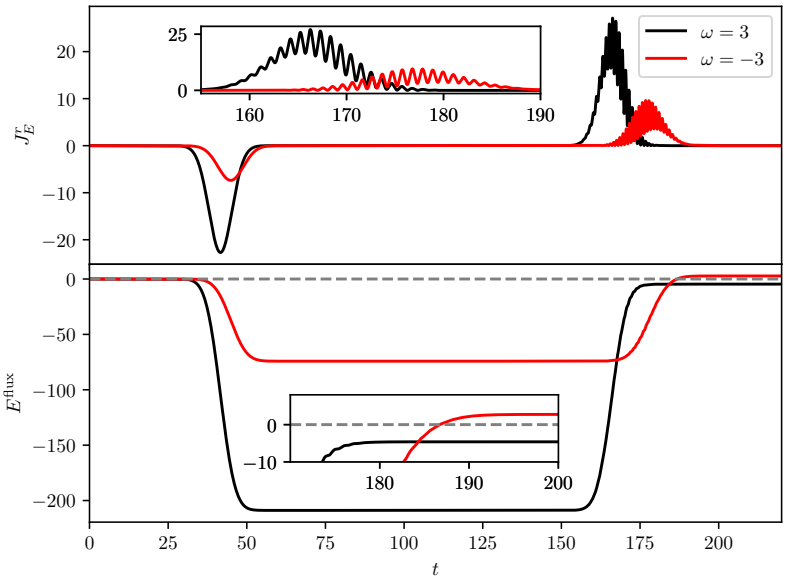

Figure 5.3: Wavepacket scattering off a non-spinning Q-ball with $\omega_Q = 0.76$; the coupling is $g = 1/3$ and we use initial conditions with $\sigma_r = 5$, $r_0 = 100$, and $\omega_0 = \{-2.24, 3.76\}$. *Upper panel:* Energy flux $J^r_E(r = 60)$ as function of time, with the outgoing flux zoomed-in. *Lower panel:* Integrated energy flux $E^{\rm flux} = \int_0^t {\rm d}t J^r_E(r = 60)$, with an inset showing attenuation ($Z_E = -0.022$) for $\omega = 3$ and amplification ($Z_E = 0.037$) for $\omega = -3$. These results are in excellent agreement with the frequency-domain analysis (c.f. Fig. 5.2).

5.5 TIME-DOMAIN ANALYSIS

To verify the consistency of our results, we performed a time-domain evolution of a $m = 0$ wavepacket scattering off a Q-ball, solving Eq. (5.7) with initial conditions appropriate for a Gaussian wavepacket with (average) frequency ω_0 and radial width σ_r,

$$\Phi_1(0,r) = e^{-\frac{(r-r_0)^2}{2\sigma_r^2}} e^{-\mathrm{i}\, s_{\omega_0}\sqrt{\omega_0^2-1}\, r}\,, \tag{5.23}$$

$$\partial_t \Phi_1(0,r) = -\mathrm{i}\,\omega_0 \Phi_1(0,r). \tag{5.24}$$

Additionally, we have also evolved the full *nonlinear* Eq. (5.2) around non-spinning Q-ball solutions, using the initial conditions

$$\Phi(0,r) = \Phi_Q(0,r) + \delta\, e^{-\frac{(r-r_0)^2}{2\sigma_r^2}} e^{-\mathrm{i} s_{\omega_0}\sqrt{\omega_0^2-1}\, r}\,, \tag{5.25}$$

$$\partial_t \Phi(0,r) = -\mathrm{i}\left[\omega_Q \Phi_Q + \omega_0(\Phi - \Phi_Q)\right](0,r). \tag{5.26}$$

For small enough $\delta \ll \Phi_Q(0,0)$ the nonlinear scattering results are consistent with the linearized calculations. We employ a fourth-order finite difference scheme in space and a standard Runge-Kutta 4 algorithm in time. The results are summarized in Figs. 5.2–5.3. Figure 5.3 shows how a smooth nearly monochromatic wavepacket scatters off and acquires extra energy. For an incoming wavepacket with $\omega_0 = 3.76$, a Fourier transform shows that the scattered wavepacket contains the modes $\omega_- \approx -2.24$ and $\omega_+ \approx 3.76$, in agreement with the analysis around Eq. (5.9) for $\omega = 3$. The calculation of the amplification factor Z_E from time-domain data is straightforward, and the results are shown in Fig. 5.2 together with the frequency-domain prediction. The agreement is remarkable.

The fact that the currents J^α_Q and J^α_E are divergenceless, implies the conservation of both Q-charge and energy; so, any change in Q and E of the scattering states, must be accompanied by a symmetric change in the Q-ball. Indeed, our results from full nonlinear evolutions show that, after the scattering takes place, the remnant relaxes to a configuration compatible with a *new* Q-ball with parameters such that charge and energy conservation are verified. This allows us to predict the maximum extractable energy from these Q-balls. We verified numerically that the entire family of Q-balls in our testbed model (with $g = 1/3$) is *absolutely stable* (i.e., have $E/Q < 1$), and their energy decreases monotonically to $E \approx 5.85$ in the limit $\omega \to 1$; this is a qualitative agreement with the analytic approximation of Ref. [153]. Thus, the maximum extractable energy for the Q-balls with $\omega_Q = (0.58, 0.70, 0.76)$ is, respectively, $(88\%, 51\%, 36\%)$ of their initial energy. One can then – in principle – extract more energy from these objects than from spinning BHs [154].

5.6 OTHER FUNDAMENTAL OBJECTS

The simplicity of the energy extraction mechanism discussed in this work indicates that other fundamental objects (like BSs [20], Proca

stars [21], etc) might be prone to the same mechanism. For instance, the extension of the proof to spherically symmetric Newtonian BSs is particularly simple. It goes as follows. Consider a four-dimensional complex scalar field Φ of mass μ minimally coupled to gravity. In the non-relativistic limit the scalar field $\Phi := e^{-\mathrm{i}\mu t}\Psi/\sqrt{\mu}$ satisfies the Schrödinger-Poisson system [155]

$$\mathrm{i}\partial_t\Psi = -\tfrac{1}{2\mu}\nabla_i\nabla^i\Psi + \mu U\Psi, \tag{5.27}$$

$$\nabla_i\nabla^i U = 4\pi\mu|\Psi|^2. \tag{5.28}$$

Newtonian BSs are solutions of the form $\Psi_0 = \psi_0(r)e^{-\mathrm{i}\omega_0 t}$ with $0 < \omega_0 < \mu$, and a static gravitational potential $u_0(r)$, both satisfying regularity at $r = 0$ and $r = +\infty$. Inspired by the Q-ball treatment, it is not hard to see that:

1. The linearized system contains time-periodic coefficients, and all of these are of the form $\propto e^{-2\mathrm{i}\omega_0 t}\Psi_1^*$ and $\propto e^{-\mathrm{i}\omega_0 t}U_1$.

2. This leads to mode-mixing between the states $\omega_- = \omega_0 - \omega_1$ and $\omega_+ = \omega_0 + \omega_1$; so, the minimal frequency-content solutions Ψ_1 must contain these two modes [c.f. Eq. (5.8)], while U_1 is real-valued and has frequencies $\pm\omega_1$. This was also seen, e.g., in Ref. [155, 156].

3. The current

$$J_{\psi,u} := r^2\,\mathrm{Im}\big(\psi_+^*\partial_r\psi_+ + \psi_-\partial_r\psi_-^* - \tfrac{\mu}{2\pi}u_+\partial_r u_+ - \tfrac{\mu}{2\pi}u_-\partial_r u_-\big) \tag{5.29}$$

   satisfies $\partial_r J_{\psi,u} = 0$. Regularity at the origin implies $J_{\psi,u} = 0$, and the asymptotic behaviour gives $J_{\psi,u}(r\to\infty) \propto \sum_{s=\pm}(|A_s^{\mathrm{out}}|^2 - |A_s^{\mathrm{in}}|^2)$.

4. As for the Q-ball, an incoming state with $A_+^{\mathrm{in}} = 0$ and $\omega_1 > 0$, or $A_-^{\mathrm{in}} = 0$ and $\omega_1 < 0$ will necessarily extract energy from the boson star.

5.7 DISCUSSION

Our results establish that energy extraction from Q-balls is allowed by a process that does not require rotation nor any motion in real space, but merely an interaction with a time-periodic background. As we showed, there is no superradiance in this process, since an incoming single state is never enhanced. Instead, this mechanism bears strong similarities to the blue-shift mechanism reported when a wave is trapped within a cavity whose boundaries oscillate periodically [145–148]. In general, an interaction of radiation with a time-periodic background tends to lead to mode-mixing, effectively coupling a discrete set of modes. If initially the radiation has only support in the lowest frequency (i.e., energy) mode, the interaction with the background will then re-distribute radiation over the several coupled modes, leading to an overall energy

amplification of radiation powered by the internal energy of the background. The simplicity of this argument indicates that other types of fundamental solitons – expected to be time-dependent due to Derrick's theorem – might be prone to the same mechanism. We have showed it explicitly for Newtonian BSs.

If a continuous family of (stable) soliton solutions exists (as for Q-balls, boson and Proca stars) the backreaction of the scattering process on the soliton is straightforward. For instance, if we continuously "illuminate" a Q-ball with a single state ϕ_+ of frequency $\omega_+ > 1$, the deposition of energy in the object will drive secularly the soliton through a continuous sequence of Q-balls with increasingly larger energy and charge (i.e., along the thin-wall limit). The process will eventually saturate if $\omega_- = -1$ is attained. Similarly, illuminating a Q-ball with a single state ϕ_+ of frequency $\omega_+ < -1$ will continuously extract energy and charge from the object driving the soliton through a continuous sequence of Q-balls with increasingly smaller energy and charge, which saturates if $\omega_+ = -1$ is attained. The evolution picture drawn here is compatible with our full nonlinear time evolutions of wavepacket scattering. Note however that this evolution may be hindered by the soliton reaching some unstable configuration.

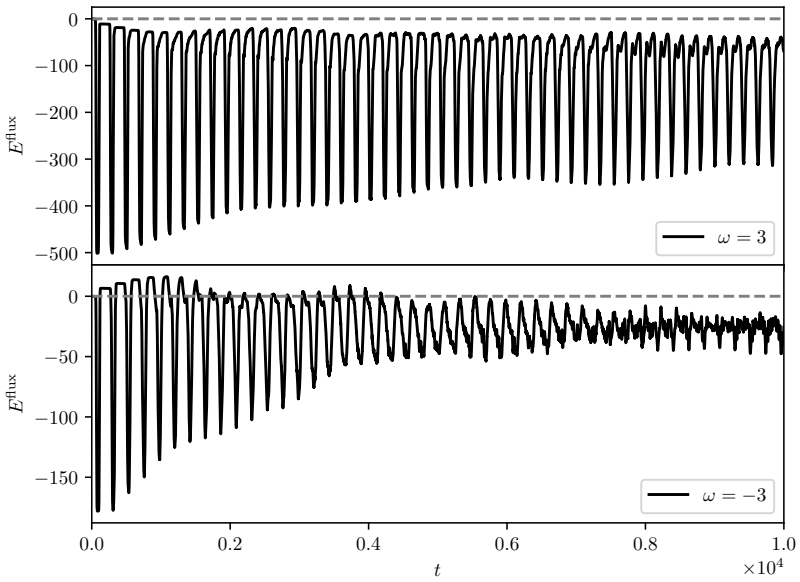

Figure 5.4: Integrated energy flux $E^{\rm flux} = \int_0^t {\rm d}t J_E^r$ at $r = 20$ for a wavepacket scattering off a non-spinning Q-ball with $\omega_Q = 0.76$ inside a cavity; the coupling is $g = 1/3$ and we use initial conditions with $\sigma_r = 5$, $r_0 = 80$, and $\omega_0 = \{-2.24, 3.76\}$. We impose Dirichlet conditions $\Phi_1 = 0$ at $r = 100$ to model the cavity.

In the case of superradiance, energy extraction can also be associated to instabilities when the radiation is confined and forced to repeatedly interact with the amplifying body (the cavity can be artificial, or arse

naturally as part of the geometry) [36, 145–148, 157, 158]. However, for the energy extraction mechanism discussed in this work, it is not as obvious (as it is for superradiance) that confining the radiation should lead to an instability. This is because, even if the initial (incoming) state is chosen so that its energy must be necessarily amplified, the scattered state will be in a mixture of modes whose energy does not need to be enhanced. Although we are unable at this point to provide statements of sufficient generality, we can trap radiation in a cavity with a Q-ball inside and study numerically its evolution. Our results are summarized in Fig. 5.4 for a moderately large cavity. Interestingly, they indicate that the system relaxes to a state with a Q-ball that overall has *absorbed* energy, even when starting with a state that initially extracts energy from the soliton (c.f. lower panel of Fig. 5.4). We have not investigated trapped radiation around fundamental solitons in full generality, neither have we studied them when orbited by a point-like charge, a good proxy for some astrophysical systems. Is it possible for a soliton to loose energy to an orbiting point-like charge, making it out-spiral (something known as floating orbit)? This and other aspects remain open.

Part III

INTERACTIONS AND DYNAMICS BETWEEN BOSON STARS AND BLACK HOLES

6

PIERCING OF A MINI-BOSON STAR BY A BLACK HOLE

6.1 INTRODUCTION

The nature of the matter making up most of the universe is unknown. There is overwhelming evidence for the existence of DM of an unknown nature and properties, which nevertheless interacts gravitationally [159–162]. Efforts to determine the properties of such matter and to place it in a theoretical framework have so far been unsuccessful, but will continue vigorously for years to come [163, 164]. If the standard model of particle physics is a good guide, one can expect new "dark stars" of various types (depending on the number and properties of the putative new elementary particles passing as DM), which can make up a significant fraction of astrophysical environments. The scales at which such new structures will appear depend, in particular on the fundamental scale dictated by the fundamental constituents of the, hitherto invisible, new fields.

Here we entertain the possibility that there are new fundamental, scalar degrees of freedom minimally coupled to gravity, and that these form localized, self-gravitating objects. It is well known that for complex scalar fields—such as the ones we focus on—BSs form rather generically as a consequence of gravitational collapse [20, 165–168]. For real scalars, similar objects exist and form (see Refs. [20, 169] and work cited therein; the extension to vector degrees of freedom can also be considered [21]). In the absence of self-interactions, the maximum mass $M_{\rm max}$ of such configurations is dictated by the mass of the fundamental boson μ, as $M_{\rm max} = 0.8 M_\odot \times (10^{-10}\,{\rm eV}/\mu)$ [170]. For sufficiently light fields, BSs can therefore have stellar masses, or even galactic-scale masses. Indeed, there are indications that such solutions describe well DM cores in halos. These models are often referred to as fuzzy DM models, and require ultralight bosonic fields (we refer the reader to Refs. [155, 171–177], but the literature on the subject is very large and growing).

Dark stars have so far gone undetected, but the advent of gravitational-wave astronomy may also mark the beginning of the illumination of such dark components of our Universe [11, 178–180]. Understanding the behavior of DM when moving perturbers drift by, or when a binary inspirals within a DM medium is crucial for attempts at detecting DM via GWs. In the presence of a nontrivial environment accretion, gravitational drag and the self-gravity of the medium contribute to a small, but potentially observable, change of the GW phase [155, 181–189].

When the length scales between different objects are similar, numerical relativity can be used to extract accurate predictions for the dynamics of the objects and of gravitational waveforms [190–193]. When the scales are too different, one needs to rely on other methods. The tidal deformability of BSs leaves an imprint in gravitational waveforms and was considered recently [191, 194, 195]. Dynamical friction in scalar structures was also studied recently and allows us to understand the slowdown of bodies moving within scalar structures [155, 172, 189, 196]. The evolution of a compact binary within a large scale BS was studied within a pointlike approximation for the binary [155], and it predicts a −6-PN dephasing effect, potentially observable.

Here, we wish to bridge the gap between these two types of results, and consider the motion of a small BH as it "pierces" a large BS structure fully nonlinearly. The small BH will be subjected to friction, it accretes a portion of the scalar material from the BS, and it emits GWs carrying energy and momentum. Likewise, as a consequence of the BH motion, the BS itself will move and be nonlinearly perturbed—or even destroyed entirely.

6.2 BOSON STAR CONSTRUCTION

We consider a minimally coupled, complex scalar field Φ described by the Einstein-Klein-Gordon action,

$$S = \int d^4x\sqrt{-g}\left[\frac{\mathcal{R}}{16\pi} - \left(g^{ab}\nabla_a\Phi\nabla_b\Phi^* + \mu^2\Phi\Phi^*\right)\right] ,$$

where g_{ab} is the spacetime metric, $\mathcal{R}$ is the Ricci scalar, μ is the mass of the scalar field and * denotes complex conjugation. From the action, the equations of motion are

$$\mathcal{R}_{ab} - \frac{1}{2}\mathcal{R}g_{ab} = 8\pi T_{ab} , \tag{6.1}$$

$$g^{ab}\nabla_a\nabla_b\Phi = \mu^2\Phi , \tag{6.2}$$

with the stress-energy tensor

$$T^{ab} = \nabla^a\Phi\nabla^b\Phi^* + \nabla^a\Phi^*\nabla^b\Phi - g^{ab}\left(\nabla^c\Phi\nabla_c\Phi^* + \mu^2\Phi\Phi^*\right) . \tag{6.3}$$

Following Ref. [20], we derive equilibrium equations in spherical symmetry by assuming a harmonic ansatz for the scalar field and a stationary geometry,

$$\Phi(\mathbf{r}, t) = \phi(\mathbf{r})e^{i\omega t} , \tag{6.4}$$

$$ds^2 = -\alpha(r)^2dt^2 + a(r)^2dr^2 + r^2d\Omega_2^2 . \tag{6.5}$$

Then, the spherically symmetric Einstein-Klein-Gordon system can be written as three ordinary differential equations

$$
\begin{aligned}
a' &= \frac{a}{2}\left\{\frac{1-a^2}{r} + 8\pi r\left[\left(\frac{\omega^2}{\alpha^2}+\mu^2\right)a^2\phi^2 + (\phi')^2\right]\right\}, \\
\alpha' &= \frac{\alpha}{2}\left\{\frac{a^2-1}{r} + 8\pi r\left[\left(\frac{\omega^2}{\alpha^2}-\mu^2\right)a^2\phi^2 + (\phi')^2\right]\right\}, \\
\phi'' &= -\left\{1+a^2-8\pi r^2 a^2\mu^2\phi^2\right\}\frac{\phi'}{r} - \left(\frac{\omega^2}{\alpha^2}-\mu^2\right)\phi a^2 ,
\end{aligned}
$$

where primes stand for radial derivatives. In order to obtain a physical solution, the following boundary conditions must be imposed on this system.

$$
\phi(0) = \phi_0 , \qquad \phi'(0) = 0 , \qquad a(0) = 1 , \tag{6.6a}
$$

$$
\lim_{r\to\infty} \phi(r) = 0 , \tag{6.6b}
$$

$$
\lim_{r\to\infty} \alpha(r)a(r) = 1 . \tag{6.6c}
$$

Here, ϕ_0 can be specified arbitrarily, and it roughly determines the mass of the boson star. We can find a simpler system by rescaling the variables in the following manner,

$$
\tilde{\phi} \equiv \sqrt{8\pi}\phi, \quad \tilde{r} \equiv \mu r, \quad \tilde{t} \equiv \omega t, \quad \tilde{\alpha} \equiv (\mu/\omega)\alpha .
$$

Then the equations become

$$
\begin{aligned}
a' &= \frac{a}{2}\left\{\frac{1-a^2}{\tilde{r}} + \tilde{r}\left[\left(\frac{1}{\tilde{\alpha}^2}+1\right)a^2\tilde{\phi}^2 + (\tilde{\phi}')^2\right]\right\}, \\
\tilde{\alpha}' &= \frac{\tilde{\alpha}}{2}\left\{\frac{a^2-1}{\tilde{r}} + \tilde{r}\left[\left(\frac{1}{\tilde{\alpha}^2}-1\right)a^2\tilde{\phi}^2 + (\tilde{\phi}')^2\right]\right\}, \\
\tilde{\phi}'' &= -\left\{1+a^2-\tilde{r}^2 a^2\tilde{\phi}^2\right\}\frac{\tilde{\phi}'}{\tilde{r}} - \left(\frac{1}{\tilde{\alpha}^2}-1\right)\tilde{\phi}a^2 .
\end{aligned} \tag{6.7}
$$

where primes stand for the derivatives with respect to $\tilde{r}$. Note that both μ and ω drop out of the equations. We will use the mass parameter μ as our unit.

To integrate these equations, we need to understand their asymptotic behavior. At the origin, $\tilde{r} = 0$, we can expand all quantities in a Taylor series to find

$$
\begin{aligned}
a(\tilde{r}) &= 1 + \frac{\tilde{r}^2(\tilde{\alpha}_0^2+1)\tilde{\phi}_0^2}{6\tilde{\alpha}_0^2} + \mathcal{O}(\tilde{r}^4) , \\
\tilde{\alpha}(\tilde{r}) &= \tilde{\alpha}_0 - \frac{\tilde{r}^2(\tilde{\alpha}_0^2-2)\tilde{\phi}_0^2}{6\tilde{\alpha}_0} + \mathcal{O}(\tilde{r}^4) , \\
\tilde{\phi}(\tilde{r}) &= \tilde{\phi}_0 + \frac{\tilde{r}^2(\tilde{\alpha}_0^2-1)\tilde{\phi}_0}{6\tilde{\alpha}_0^2} + \mathcal{O}(\tilde{r}^4) ,
\end{aligned}
$$

where $\tilde{\phi}(0) = \tilde{\phi}_0$, $\tilde{\alpha}(0) = \tilde{\alpha}_0$. Notice that the form of the metric in Eq. (6.5) is consistent with the Schwarzschild metric at large distances where

$$a(r) = \left(1 - \frac{2M}{r}\right)^{-\frac{1}{2}} , \tag{6.8}$$

with M the Arnowitt–Deser–Misner (ADM) mass of the spacetime. This allows us to define a more general mass aspect function

$$M(r) = \frac{r}{2}\left(1 - \frac{1}{a^2(r)}\right) , \tag{6.9}$$

which measures the total mass contained in a sphere of radius r. Furthermore, we can use boundary condition Eq. (6.6c) together with Eq. (6.8) to get $\alpha(r)$ at large distances

$$\alpha(r) = \left(1 - \frac{2M}{r}\right)^{\frac{1}{2}} . \tag{6.10}$$

We are now ready to solve for the boson star structure using a shooting method to solve Eqs. (6.7): we fix $\tilde{\phi}_0$ and shoot for $\tilde{\alpha}_0$ using boundary conditions Eqs. (6.6a) and (6.6b), so as to have an asymptotically flat spacetime. There are many possibilities for $\tilde{\alpha}_0$, which correspond to different excited states of the boson star. Once we have solved for a, $\tilde{\alpha}$ and $\tilde{\phi}$ we can recover ω by using Eq. (6.6c). In practice, since we use a finite grid, we use the values of α and a at the last radial grid point of the solution we have (see below for details on how good the agreement is with the Schwarzschild metric at $r \sim 100$).

Finally, to perform numerical evolutions in the absence of symmetries, isotropic coordinates are preferred. In isotropic coordinates, the spherically symmetric metric can be written as [20]

$$ds^2 = -\alpha(R)^2 dt^2 + \psi(R)^4 \left(dR^2 + R^2 d\Omega^2\right) , \tag{6.11}$$

where ψ is the conformal factor. A change of the radial coordinate $R = R(r)$ can transform the solution obtained in Schwarzschild coordinates into isotropic ones, in particular,

$$\frac{dR}{dr} = a\frac{R}{r} . \tag{6.12}$$

In a boson star the scalar field decays exponentially, and therefore the solution quickly asymptotes to a Schwarzschild exterior. We can thus integrate Eq. (6.12) by imposing a Schwarzschild exterior of mass M at large distances, with

$$r(R) = M + \frac{M^2}{4R} + R . \tag{6.13}$$

We perform the coordinate transformation (6.12) numerically where Eq. (6.13) is used when $r > r_{\max}$. We solve this equation via a shooting method, where we integrate outwards; we therefore need to understand

the behavior $R(r)$ for small r. Taylor expanding at $\tilde{r} = 0$, i. e.., $R(r) = \sum_n R^{(n)} r^n / n!$, we find

$$R(r) = cr - \frac{cr^3(1+\alpha_0^2)\phi_0^2}{12\alpha_0^2} + \mathcal{O}(r^5)\,. \tag{6.14}$$

Then, $R'(0) = c$ is a free parameter which we determine by shooting to the exterior solution (6.13). In practice we set $r_{\rm max} \sim 100$ and we can verify that we effectively recover the Schwarzschild metric from this point onward: $|\phi| < 10^{-16}$, $|a(r) - (1-2M/r)^{-\frac{1}{2}}| < 10^{-16}$. Hence, our solution is smoothly connected.

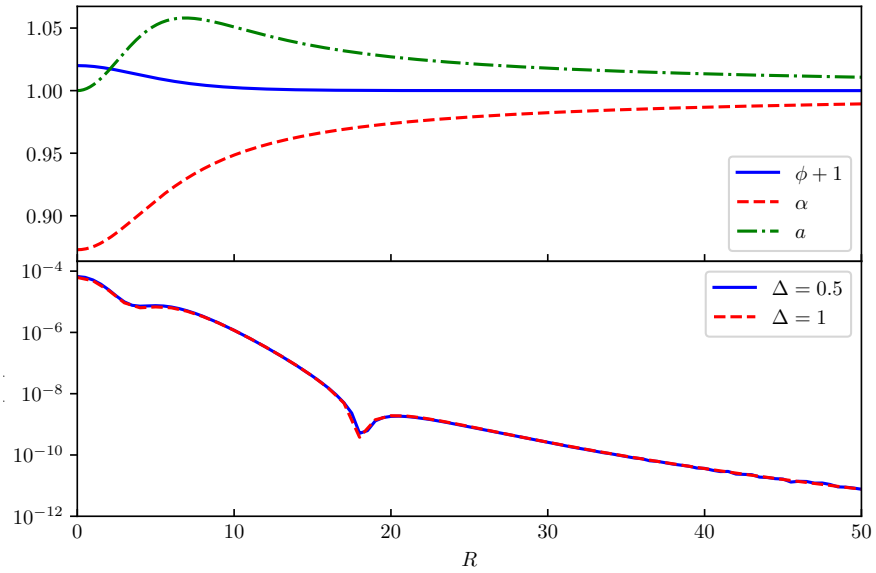

Figure 6.1: Configuration describing an isolated BS with mass $M = 0.53$ in isolation, corresponding to a value of the scalar field at the center $\phi_0 = 0.02$, $\alpha_0 = 0.873$, $\omega = 0.936$. **Top:** scalar field and metric components as a function of the radial coordinate. **Bottom:** Hamiltonian constraint along the R axis. The red curve has been multiplied by 16, the expected factor for fourth-order convergence. We use mesh refinement, and Δ represents $\mathrm{d}x\,, \mathrm{d}y$, and $\mathrm{d}z$ of the coarsest level.

In the following, we use a ground-state BS with mass $M = 0.53$ in isolation, corresponding to BS parameters $\mu = 1$, $\phi_0 = 0.02$, $\alpha_0 = 0.873$, $\omega = 0.936$. The solution is summarized in the top panel of Fig. 6.1. Note that $R_{98} = 12.39$ is the radius of the isolated BS solution which encloses 98% of the BS mass. A measure of the correctness of this solution can be assessed by the violation of the Hamiltonian constraint (introduced in the next section, see Eq. (6.20)), shown in the bottom panel of Fig. 6.1. Notice that when the resolution increases, the constraint violation decreases in accordance with the expected fourth-order convergence of our results (we use fourth-order accurate finite-difference operators throughout).

When the BS is dilute, the relevant equations governing the structure of isolated BSs reduce to the Schrodinger-Poisson equations [155, 197].

In this limit, all BS solutions are related via simple scaling relations, and accurate fits are given by expressions (45)-(50) in Ref. [155]. In this regime, the radius R_{98} (defined by the areal radius containing 98% of the BS mass) can be related to the total mass via $M\mu \simeq 9.1/R_{98}\mu$. The BS that we use as a reference is not fully within the Newtonian regime.

6.3 DYNAMICAL BH-BS SPACETIMES

6.3.1 *3+1 decomposition and evolution procedure*

Our strategy to perform numerical evolutions makes use of the standard 3+1 decomposition [198, 199], whereby a 3-metric γ_{ab} is introduced via

$$\gamma_{ab} = g_{ab} + n_a n_b \,, \tag{6.15}$$

where n^a denotes a unit timelike vector normal to a spacelike hypersurface. The full spacetime metric g_{ab} can then be written in the form

$$\begin{aligned} ds^2 &= g_{ab} dx^a dx^b \\ &= -\left(\alpha^2 - \beta^i \beta_i\right) dt^2 + 2\beta_i \, dt \, dx^i + \gamma_{ij} \, dx^i \, dx^j \,, \end{aligned} \tag{6.16}$$

where α and β are the usual lapse and shift gauge functions, and the indices $i, j, \ldots$ run from 1 to 3.

To write the evolution equations in this formalism we introduce the extrinsic curvature K_{ij},

$$K_{ij} = -\frac{1}{2\alpha} \left(\partial_t - \mathcal{L}_\beta\right) \gamma_{ij} \,, \tag{6.17}$$

and the "conjugate momentum" of the complex scalar field Φ,

$$K_\Phi = -\frac{1}{2\alpha} \left(\partial_t - \mathcal{L}_\beta\right) \Phi \,, \tag{6.18}$$

where $\mathcal{L}$ denotes the Lie derivative. The evolution equations then take the form

$$\partial_t \gamma_{ij} = -2\alpha K_{ij} + \mathcal{L}_\beta \gamma_{ij} \,, \tag{6.19a}$$

$$\begin{aligned} \partial_t K_{ij} = &-D_i \partial_j \alpha + \alpha \left({}^3\mathcal{R}_{ij} - 2K_{ik} K^k{}_j + K K_{ij} \right) \\ &+ \mathcal{L}_\beta K_{ij} + 4\pi\alpha \left[(S - \rho)\gamma_{ij} - 2S_{ij} \right] \,, \end{aligned} \tag{6.19b}$$

$$\partial_t \Phi = -2\alpha K_\Phi + \mathcal{L}_\beta \Phi \,, \tag{6.19c}$$

$$\begin{aligned} \partial_t K_\Phi = &\alpha \left(K K_\Phi - \frac{1}{2} \gamma^{ij} D_i \partial_j \Phi + \frac{1}{2} \mu^2 \Phi \right) \\ &- \frac{1}{2} \gamma^{ij} \partial_i \alpha \partial_j \Phi + \mathcal{L}_\beta K_\Phi \,, \end{aligned} \tag{6.19d}$$

which is subject to the following constraints

$$\mathcal{H} \equiv {}^3\mathcal{R} - K_{ij} K^{ij} + K^2 - 16\pi\rho = 0 \,, \tag{6.20}$$

$$\mathcal{M}_i \equiv D^j K_{ij} - D_i K - 8\pi j_i = 0 \,. \tag{6.21}$$

where $K \equiv \gamma^{ij} K_{ij}$, D_i and ${}^3\mathcal{R}_{ij}$ denote, respectively, the covariant derivative and Ricci tensor with respect to the 3-metric, and the source terms are given by

$$\begin{aligned} \rho &\equiv T^{ab} n_a n_b \,, \\ j_i &\equiv -\gamma_{ia} T^{ab} n_b \,, \\ S_{ij} &\equiv \gamma^a{}_i \gamma^b{}_j T_{ab} \,, \\ S &\equiv \gamma^{ij} S_{ij} \,. \end{aligned} \tag{6.22}$$

For the numerical simulations we rewrite the evolution equations above in the Baumgarte-Shapiro-Shibata-Nakamura form [200–202], as detailed in Ref. [203], and use the Einstein Toolkit infrastructure [204–206] for the evolutions. We use Carpet [207] for mesh refinement capabilities, AHFinderDirect [208, 209] for finding and tracking apparent horizons, and QuasiLocalMeasures [210] for extracting BH mass. The spacetime metric and scalar field variables are evolved in time using the LeanBSSNMoL and ScalarEvolve codes, which are freely available as part of the Canuda library [211].

For our simulations we use two refinement centers, one center corresponding to the location of the BH and the other to the location of the BS, which sits initially at the origin of the numerical domain. We use up to 10 refinement levels for the BH and 3 refinement levels for the BS. We always use at least 25 points to cover the BH, thus ensuring enough grid points for an acceptable resolution. During the evolution, the mesh refinement around the BH moves, and the mesh refinement resolving BSs are fixed at the origin of the numerical domain. To avoid redundant calculations, we assume reflection symmetry on the $x = 0$ and $y = 0$ planes (the collision will always be along the z axis).

Throughout the code, derivatives are approximated using fourth-order-accurate finite-differencing stencils but there are also lower-order elements in the code, such as prolongation operations, which are only second-order accurate in time. We use the method of lines with Runge-Kutta 4 to evolve the equations in time with outgoing (radiative) boundary conditions and the usual 1 + log and Gamma-driver gauge conditions [199].

6.3.2 *Diagnostics*

To understand and characterize some of the physics more precisely, we monitor the scalar field around the moving BH, in a frame comoving with the BH.

We simply consider a sphere with constant coordinate radius $\bar{r}$ around the BH, as measured with the numerical coordinates introduced above, and we extract the multipole mode of the scalar field on the sphere, which is defined as

$$\phi_{lm}(t, \bar{r}) = \int_{S_{\rm BH}} d^2\Omega Y^*_{lm}(\Omega) \Phi(t, \bar{r}, \Omega) \,, \tag{6.23}$$

where $S_{\rm BH}$ is the sphere around the BH with radius $\bar{r}$. For the small Lorentz boosts considered in this work, such a sphere is also a constant-radius sphere in the BH frame.

In addition, we monitor the energy $E^{\rm rad}$ and momentum $P^{\rm rad}$ radiated in GWs, which can be be calculated as [212],

$$\frac{dE^{\rm rad}(t)}{dt} = \lim_{r\to\infty}\left[\frac{r^2}{16\pi}\int_\Omega \left|\int_{-\infty}^{t}\Psi_4 d\tilde{t}\right|^2 d\Omega\right], \tag{6.24}$$

$$\frac{dP_i^{\rm rad}(t)}{dt} = -\lim_{r\to\infty}\left[\frac{r^2}{16\pi}\int_\Omega \ell_i\left|\int_{-\infty}^{t}\Psi_4 d\tilde{t}\right|^2 d\Omega\right], \tag{6.25}$$

where $\ell_i = (-\sin\theta\cos\phi, -\sin\theta\sin\phi, -\cos\theta)$, and Ψ_4 is the Newman-Penrose scalar, which is defined in Appendix C of Ref. [213].

Besides, we also monitor the energy density and momentum flux of the scalar field into the BH horizon. For any vector field, we have

$$Q = \int_\Omega d^3x \alpha\sqrt{\gamma} T_a{}^t \xi^a\,, \tag{6.26}$$

where T_{ab} is the energy-momentum tensor, γ is the determination of the 3-metric, and α is the lapse function. When $\xi^a = (\frac{\partial}{\partial t})^a$ we denote Q by Q_t, and for $\xi^a = (\frac{\partial}{\partial z})^a$ we denote Q by Q_z. Even though ξ is not a Killing vector, the charge defined in Eq. (6.26) is a good measure of the scalar field energy, and it has been adopted by other authors (e.g. Ref. [214]).

6.3.3 *Initial data*

For our evolution procedure, the relevant initial data amount to specifying the spatial profile of the 3-metric, extrinsic curvature, lapse and shift, as well as the scalar field, at a given time slice. We have described in Sec. 6.2 our construction of stationary BS spacetimes. Isolated BH spacetimes are known analytically, and to construct spacetimes containing both objects we superpose these two solutions using a procedure analogous to the one outlined in Ref. [215], which we can summarize as follows. The spacetime is described by

$$K_{ij} = K_{ij}^{\rm (BH)} + K_{ij}^{\rm (BS)} + \delta K_{ij}\,, \tag{6.27a}$$

$$\psi = \psi^{\rm (BH)} + \psi^{\rm (BS)} - 1 + \delta\psi\,, \tag{6.27b}$$

$$\gamma_{ij} = \psi^4\,{\rm diag}(1,1,B^2)\,, \tag{6.27c}$$

$$B^2 = \Gamma^2\left[1 - v^2(3 - \psi^{\rm (BH)} + \psi^{\rm (BS)})^2\psi^{-6}\right], \tag{6.27d}$$

where $\Gamma \equiv 1/\sqrt{1-v^2}$, v is the speed of the BH, $K_{ij}^{\rm (BH)}$ and $K_{ij}^{\rm (BS)}$ are the extrinsic curvatures of the BH and BS respectively, while $\psi^{\rm (BH)}$ and $\psi^{\rm (BS)}$ are the conformal factors of the BH and BS solutions, respectively. In the above system δK_{ij} and $\delta\psi$ are correction terms, which should be solved for by solving the appropriate elliptic system. For simplicity, here we set $\delta K_{ij} = 0$ and $\delta\psi = 0$. This means that these initial data

do not satisfy the constraint equations (6.20) and (6.21). While not ideal, the constraint violation incurred is small for large initial distances, and such a construction has been standard practice in studies of BS binaries [216–218].

One can find explicit expressions for the metric and extrinsic curvature of a boosted BH in Ref. [215]. For the spherically symmetric BS solutions that we consider, $K_{ij}^{(\mathrm{BS})} = 0$ and

$$K_{\Phi}^{(\mathrm{BS})} = -\frac{1}{2\alpha}\partial_t \Phi = -\frac{i\omega\phi}{2\alpha}\,,$$

where α is the lapse function obtained previously for BSs in isolation; ω and ϕ are defined in Eq. (6.4). Finally, we fix the initial conditions for the gauge variables by choosing $\alpha = \psi^{-2}$, and $\beta^i = 0$.

We place the BS at the center of our coordinates, and we keep its parameters fixed in all our simulations: as we discussed above, we consider a BS which in isolation is characterized by a total mass $M = 0.53$, corresponding to a value of the scalar field at the center, $\phi_0 = 0.02$, $\alpha_0 = 0.873$, $\omega = 0.936$, as shown in Fig. 6.1. Hereafter we fix units where $\mu = 1$—all our results will be shown and discussed in these units.

Table 6.1: List of simulations analyzed for collisions between a BH of mass parameter M_{BH} and a BS of mass $M = 0.53$. The BH has initial velocity v_0 along the z axis, and starts from position z_0. The BS is characterized by a frequency $\omega = 0.936$ and values at the origin $\phi_0 = 0.02$, $\alpha_0 = 0.873$. The total energy is $M_{\mathrm{tot}} = \Gamma M_{\mathrm{BH}} + M - \Gamma M_{\mathrm{BH}} M/z_0$ with Γ the Lorentz factor. The total momentum of the boosted BH is $\Gamma M_{\mathrm{BH}} v_0$. We define a mass ratio $q = M/M_{\mathrm{BH}}$ and a length ratio $\mathcal{L} = R_{98}/(2M_{\mathrm{BH}})$. Notice that at the initial time the mass parameter M_{BH} is equal to the irreducible mass M_{irr} within better than 0.5% and the irreducible mass is given by $\mathcal{A} = 16\pi M_{\mathrm{irr}}^2$, where $\mathcal{A}$ is the area of the apparent horizon.

Run	M_{BH}	$\mathcal{L}$	v_0	z_0	M_{tot}	P_{tot}
IA	1	6	10^{-4}	-50	1.52	0
IB	1	6	0.5	-200	1.68	0.577
IIA	0.4	16	10^{-4}	-50	0.93	0
IIB	0.4	16	0.5	-200	0.99	0.231
IIIA	0.2	31	10^{-4}	-50	0.73	0
IIIB	0.2	31	0.5	-200	0.76	0.115
IVA	0.1	62	10^{-4}	-50	0.63	0
IVB	0.1	62	0.5	-200	0.65	0.086

What we vary in the initial data are the BH parameters, in particular, its initial velocity and mass. We have studied a variety of initial conditions, summarized in Table 6.1. Our initial data include a BS-BH mass ratio $q = M/M_{\mathrm{BH}}$ ranging from 0.2 to 2, and a length ratio $\mathcal{L} = R_{98}/(2M_{\mathrm{BH}})$ from 6 to 62. These ratios are far from those expected

for galactic halos [155], but they are the only ones possible with current infrastructure. They could be appropriate to describe the interactions between BHs and DM roaming "lumps," or even as a starting point to understand how to extrapolate to other, more extreme ratios.

We also consider two different initial BH velocities. One describes slow infalls, for which we take an almost static BH with $v_0 = 10^{-4}$ at $z_0 = -50$. We also consider high velocity collisions, for which $v_0 = 0.5$ at $z_0 = -200$. In all cases, the BH is initially well outside the BS, $z_0 \gg R_{98}$.

6.4 SIMULATION RESULTS

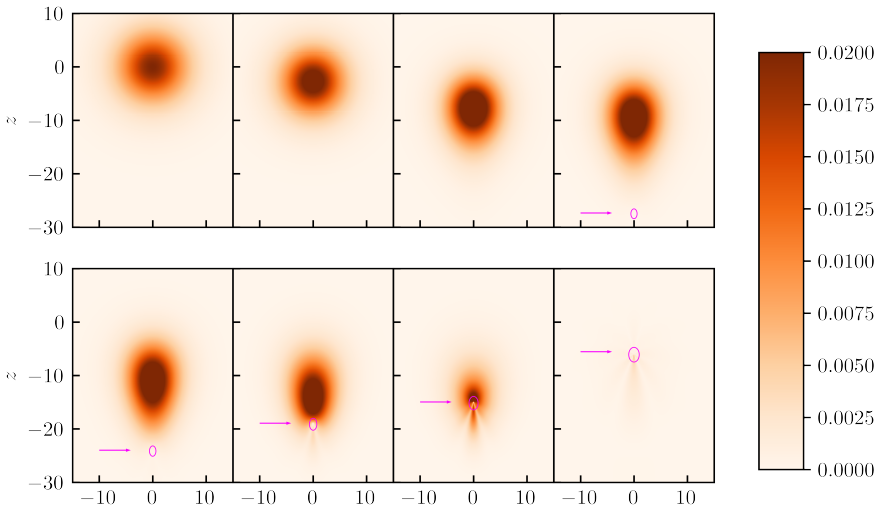

Figure 6.2: Snapshots of evolution, depicting the scalar field absolute value $|\Phi|$ for the initial data `IB` in Table 6.1. From left to right, the snapshots are taken at instants $t = 0.0$, 300.8, 380.8, 390.4 in the top row, and at $t = 396.8$, 406.4, 416.0, 448.0 in the bottom row. Pink lines depict contours of constant lapse function $\alpha = 0.2$, which are a good approximation for the location of the horizon, further indicated by arrows. Notice how the BS is tidally distorted as it approaches the BH and how it eventually is almost totally swallowed up by the BH. Animations are available online [219], and also as ancillary files in this submission.

6.4.1 *Dynamics and accretion during collision process*

We mostly look at results in the "lab frame," where the BS is at rest, and the BH—initially at $(0, 0, z_0)$—is moving along z axis to eventually collide and interact with it.

The numerical convergence of our results is consistent with the discretization scheme we used, as discussed in Section 6.4.5. The outcome

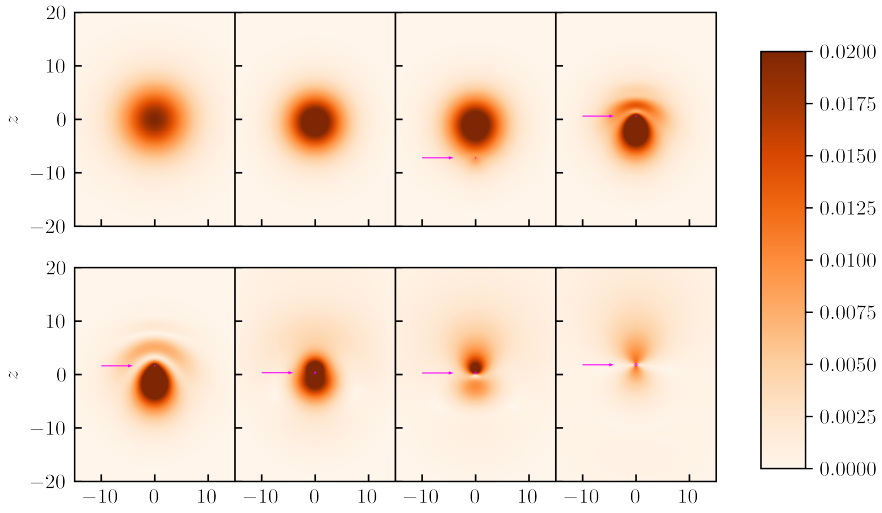

Figure 6.3: Snapshots of evolution, depicting the scalar field absolute value $|\Phi|$ for the initial data `IVB` in Table 6.1. From left to right, the snapshots are taken at instants $t = 0.0$, 349.6, 389.6, 408.8 in the top row, and at $t = 415.2$, 436.8, 450.4, 480.8 in the bottom row. Pink lines depict contours of constant lapse function $\alpha = 0.2$, which, as in the previous figure, indicate the horizon location; this region is much smaller (and difficult to see) than the corresponding one of Fig. 6.2 since the BH is much smaller. Notice how the BS pulls back the BH during the collision process (panels 5 and 6), and eventually is swallowed up by the BH. Animations are available online [219], and also as ancillary files in this submission.

of our numerical simulations are summarized in Figs. 6.2-6.7 and Table 6.2.

Snapshots of the scalar field absolute value $|\Phi| = \sqrt{\Phi\Phi^*}$ are shown in Figs. 6.2–6.3, for initial data `IB` and `IVB`. The contour in pink marks the contour of constant lapse function $\alpha = 0.2$, which is a good indication of the BH apparent horizon location. It is clear from Fig. 6.2 that, in this frame, during the collision the BS moves towards the BH as it approaches. If we define the collision as the instant when the BH crosses R_{98}, it is clear from these snapshots that even prior to collision the BS is tidally distorted. Tidal Love numbers of BSs are positive and relatively large as compared to compact systems [194, 220], hence the deformation is along the BH-BS axis and visible. The tidal deformation is clear for nearly equal mass objects, as the effects are much stronger in this regime. For the purpose of our study, the case `IVB` in Fig. 6.3 is more interesting, for it describes a very small BH plunging through a large BS. Tidal effects are now less obvious on length scales of the boson star; however, they become visible and will play a crucial role once the BH pierces through the BS, as we explain below.

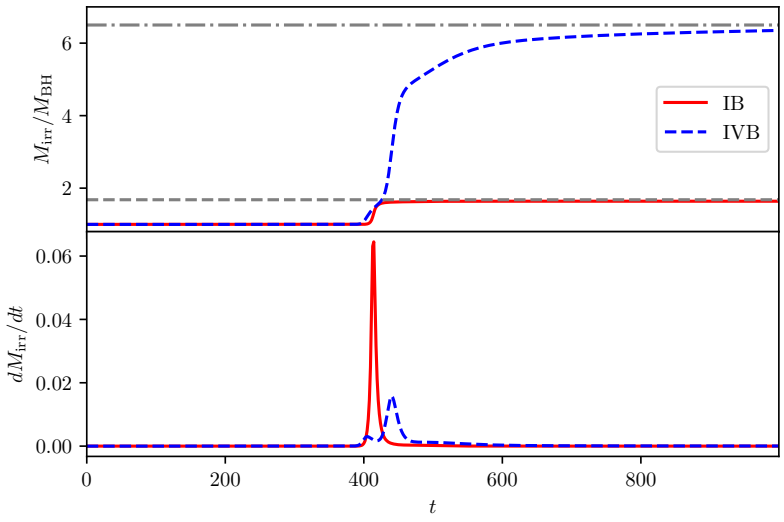

Figure 6.4: Accretion of scalar onto the BH. **Top panel:** normalized BH irreducible mass $M_{\rm irr}/M_{\rm BH}$ for simulations `IB` and `IVB`. The gray lines are the total mass $M_{\rm tot}$ normalized by the initial mass $M_{\rm BH}$ given in Table 6.1. At late times the BH mass approaches $M_{\rm tot}$, thus the BH ends up accreting the entire BS. **Bottom panel:** accretion rate for the two different initial data. Notice that there are two accretion stages for simulation `IVB`, which we argue to be due to tidal effects. The accretion rate is larger than expected for a stationary regime, see main text.

It is also evident from the snapshots that the BS is almost entirely swallowed by the BH, which continues moving—albeit with a smaller velocity by momentum conservation—after the interaction with the BS. We find that the BS is nearly totally accreted for *all* the initial data

in Table 6.1; an extreme example concerns simulation `IVB`: even a BH which is 62 times smaller than the BS and moving at half the speed of light, ends up "eating" all of the BS material. This is seen, in particular, in Fig. 6.4 where we show the BH irreducible mass (estimated with the help of the horizon area) as function of coordinate time. After a relatively short timescale ~ 1000, and after the BH has had time to interact with the BS, the final BH mass is at least 95 % of the total initial energy. We have further quantified accretion by computing the scalar energy in the initial and final spacetime slices [cf. definition (6.26)]; our results are shown in Table 6.2 and are consistent with total or nearly total accretion of the BS onto the BH, even for such length ratios as $\mathcal{L} = 62$ of run `IVB`.

Accretion onto a nonmoving BH placed at the center of a Newtonian BS proceeds at a stationary rate $\dot{M} \sim 8\pi \times 10^{-2}(\mu M_{\rm BH})(\mu M_{\rm BS})^4$ [221]. For simulation `IV` this amounts to $\dot{M} \sim 2 \times 10^{-4}$, roughly 2 orders of magnitude below what we observe numerically. We can estimate the effective absorption cross section σ from our results, letting $\dot{M} = \sigma \rho v_0$. For simulation `IVB` one finds $\sigma \sim 400$ at the peak of accretion, corresponding to an absorbing disk with radius 2 orders of magnitude larger than the BH scale [222]. We do not understand the origin of such large accretion rates, but we suspect they are related to a transient stage. Unfortunately, our setup does not allow us to simulate more extreme length scales; hence, we never see past the transient and into the stationary regime.

For simulations with smaller BH masses, the residual scalar field outside the BH increases by several orders of magnitude as seen in Table 6.2, although it is still but a small fraction of the total energy. One can expect that for even smaller BH masses the BH can pierce through without "eating" the entire BS. Unfortunately, as we said, in order to evolve such a small BH, one would need too large an amount of computational resources.

6.4.2 *Black hole motion and tidal capture*

To interpret our results and to compare them with simple estimates, consider first the motion, in Newtonian dynamics, of two pointlike particles of mass m_1 at $z = z_1(t)$ and m_2 at $z = z_2(t)$. We thus neglect tidal effects (although they are apparent in our results, cf. Fig. 6.2) and relativistic effects. Defining $d = z_2 - z_1$ and using Newtonian dynamics (or equivalently, energy and momentum conservation), one finds

$$\ddot{d} = -\frac{m_1 + m_2}{d^2}\,, \qquad \ddot{z}_1 = \frac{m_2}{d^2}\,. \tag{6.28}$$

For our system, we take $m_1 = M_{\rm BH}$, $m_2 = M$, and we integrate them with initial conditions appropriate for the initial data. For `IB`, $z_1(0) = -200$, $d = 200$. We find that the BH and BS are separated by a distance $d = 5$ when the BS sits at $z_2 = -7.7$, which is consistent with the left bottom panel in Fig. 6.2.

Table 6.2: Summary of the results of the dynamical evolution of the initial data in Table 6.1. Here, M_f is the final BH irreducible mass, and v_f is the final BH velocity as calculated from the puncture trajectory; in parentheses we show the expected value $M_{\rm BH}v_0/M_{\rm tot}$ from momentum conservation, assuming that the entire BS is accreted onto the BH (notice the good agreement between these two estimates). Note that $E^{\rm rad}$ and $P^{\rm rad}$ are the energy and momentum radiated in GWs, respectively. They are calculated from ψ_4 and compared to a Newtonian, quadrupolar approximation which includes no accretion (number in parentheses, see main text for further details). Finally the total momentum and energy flux of the *scalar* field into the BH horizon are the last two entries. The junk radiation exists in all cases and we neglect it.

Run	$M_{\rm BH}$	M_f	v_0	v_f	$10^4 E^{\rm rad}$	$10^4 P_z^{\rm rad}$	$Q_t^{\rm initial}$	$Q_t^{\rm final}$	$Q_z^{\rm initial}$	$Q_z^{\rm final}$
`IA`	1.0	1.56	10^{-4}	-2.9×10^{-4} (0)	2.9 (11.7)	-0.24	0.53	7.7×10^{-5}	0	4.1×10^{-8}
`IB`	1.0	1.64	0.5	0.33 (0.30)	12.5 (35.6)	4.1	0.54	3.9×10^{-4}	0	-7.4×10^{-5}
`IIA`	0.4	0.94	10^{-4}	-1.6×10^{-3} (0)	0.63 (1.9)	6.5×10^{-3}	0.52	2.6×10^{-3}	0	-3.1×10^{-6}
`IIB`	0.4	1.01	0.5	0.20 (0.20)	5.5 (5.7)	1.5	0.54	4.0×10^{-3}	0	-6.4×10^{-4}
`IIIA`	0.2	0.73	10^{-4}	-2.5×10^{-3} (0)	0.20 (0.47)	9.0×10^{-3}	0.51	4.2×10^{-3}	0	-1.6×10^{-4}
`IIIB`	0.2	0.78	0.5	0.12 (0.13)	2.2 (1.4)	0.47	0.54	1.1×10^{-2}	0	-1.3×10^{-3}
`IVA`	0.1	0.61	10^{-4}	-7.1×10^{-3} (0)	0.10 (0.12)	4.7×10^{-3}	0.51	1.5×10^{-2}	0	-1.0×10^{-3}
`IVB`	0.1	0.64	0.5	0.064 (0.077)	0.75 (0.36)	0.11	0.53	2.2×10^{-2}	0	-1.2×10^{-3}

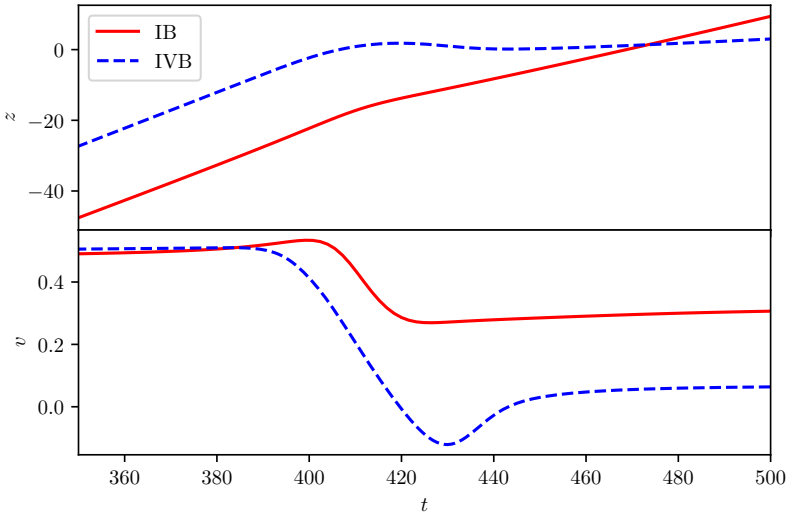

Figure 6.5: Location z and the speed v of the BH for `IB` and `IVB`, as read from the puncture location. The interaction between the BH and the BS is clear from these data, and it translates into a deceleration starting at $t \sim 400$ and lasting for 20, roughly the time taken to cross the bulk of the BS. Notice also that the BH velocity is *negative* for a small amount of time in simulation `IVB`: the BH is tidally captured by the boson star.

The BH velocity can be estimated from our numerical results, using the puncture trajectory. These estimates are shown in Fig. 6.5 for simulations `IB` and `IVB`, and also in Table 6.2. Due to our initial gauge condition $\beta = 0$, the puncture velocity is zero at the initial time, but it will reach v_0 over a period of time (see Fig. 6.6). Notice that the BH velocity after interaction with the BS agrees well with simple momentum-conservation estimates. For extreme length ratios, the agreement is not as good due to the extreme requirements necessary; our simulation is not yet accurate enough, and we would require larger resolutions to fully capture the dynamics to the necessary level of precision.

Nevertheless, there are interesting details in how the asymptotic velocities are achieved, which require a deeper analysis. We find that the BH pierces through the boson star and produces a tidal "stretching," with a significant amount of energy deposited in such a configuration. A point of near-maximum distortion is shown in the lower left panel of Fig. 6.3. At this instant, the velocity of the BH is close to zero, and the tidally distorted cloud is slowly moving in the positive z direction. Thus, the cloud pulls the BH, which then acquires a velocity in the negative z direction, as seen in Fig. 6.5. The pull is significant and can make the BH velocity large, but negative. As the cloud relaxes from this tidal pull, it is accreted by the BH and transfers all its positive momentum to the BH, which then reaches its asymptotic value, consistent with momentum conservation. This momentarily retrograde motion is

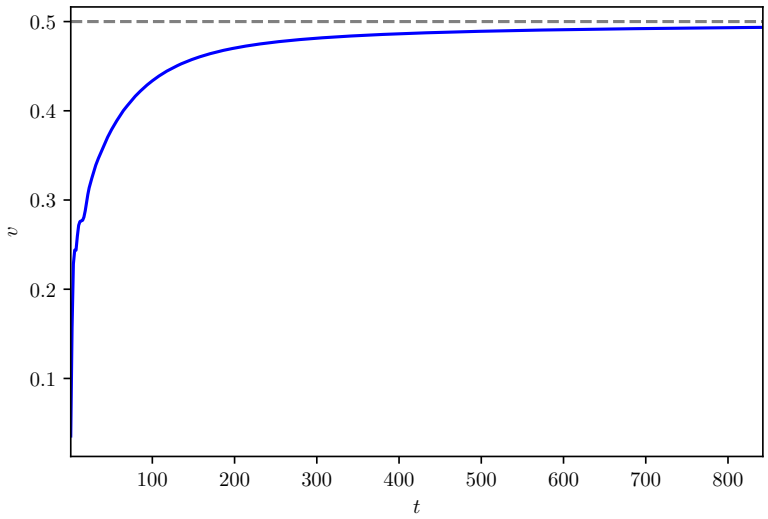

Figure 6.6: Puncture velocity of a single boosted BH with $M = 1$ and $v = 0.5$. The dashed gray line represents $v = 0.5$. Since we set $\beta = 0$ at the initial time, the puncture speed is initially zero. Here we show the effect of this initial gauge condition using a simulation of an isolated boosted BH with $M = 1$ and $v = 0.5$. One can see that the puncture speed (as measured by the zero of the shift vector β) of the boosted BH approaches the BH speed $v = 0.5$ over time and eventually stabilises at $v = 0.5$. This means that the instantaneous puncture speed before the collision can be used to gauge the speed of the BH.

directly responsible for the different accretion peaks in Fig. 6.4, and for the features in GW emission that we discuss below.

In other words, what we find is an extreme example of "tidal capture" [223, 224], which in our setup leads to the subsequent accretion of the entire boson star. As discussed in Ref. [223], the maximum tidal oblateness that can be induced is of order $M_{\rm BH}/M$ for a BH sitting at the BS "radius." The associated tidal energy is $\sim M_{\rm BH}^2/R_{98}$. Since the BH mass grows by the time it reaches the other BS extreme, this quantity can be a sizable fraction of the initial kinetic energy, leading to the stoppage of the BH. To prevent the BH backward motion, smaller BH masses need to be considered, or more dilute BSs. Unfortunately, either choice requires more extreme length ratios, which we are unable to study at this point.

One of our original motivations was to study dynamical friction in a full nonlinear realistic setup. Dynamical friction is of order $4\pi M\rho/v^2$ for a constant density boson star [155, 172, 189, 225]. We can estimate when dynamical friction is dominant with respect to gravitational acceleration; both effects will impart similar accelerations (albeit of different sign) when

$$\frac{4}{3}\pi\rho r \sim \frac{4\pi M_{\rm BH}\rho}{v^2}\,, \tag{6.29}$$

where energy conservation requires that the BH velocity, in the constant-BH-mass approximation, satisfies $v^2 = v_R^2 + 4\pi\rho/3(R_{98}^2 - r^2)$. Here v_R is the BH velocity when it reaches the BS radius. Even in the most favorable situation when the BH starts from rest at infinity, $v_R^2 = 2M/R_{98}$, and therefore we find that dynamical friction dominates only at distances

$$r \lesssim \gamma R_{98}\,, \tag{6.30}$$

where γ is defined by $M_{\rm BH} = \gamma M$. Thus, we see how challenging it is to perform simulations of self-gravitating objects where dynamical friction can be isolated.

6.4.3 *Gravitational-wave emission*

When the BS is Newtonian and the BH velocity is nonrelativistic, we can use the quadrupole approximation to estimate waveforms and radiated fluxes. In addition, when the BH mass $M_{\rm BH}$ is much smaller than that of the BS mass M, one can find simple solutions to the dynamics of the system and consequent GW emission. In such a setup, the BH simply follows a spacetime geodesic parametrized by a radial position $r(t)$, in a background whose geometry is dictated by a BS fixed at the center of coordinates. The quadrupole approximation yields

$$\frac{dE}{dt} = \frac{8}{15}M_{\rm BH}^2\left(3\dot{r}\ddot{r} + r\dddot{r}\right)^2\,. \tag{6.31}$$

We first approximate the BS as a scalar blob of constant density and radius R_{98}, with vacuum outside. In this Newtonian setup the motion of the BH in the exterior can be calculated using energy conservation,

$$\dot{r}^2 - 2M/r = v_0^2\,, \tag{6.32}$$

where v_0 is the asymptotic velocity at large distances. In the interior, one needs an accurate description of the BS gravitational potential. In the approximation of constant density $\rho = 3M/(4\pi R^3)$, one finds

$$\dot{r}^2 + \frac{4}{3}\pi\rho\left(r^2 - R_{98}^2\right) = v_R^2 \tag{6.33}$$

in the interior, where R_{98} is the BS radius and v_R the velocity at R_{98} which can be obtained from (6.32).

Consider first infalls from rest. Integrating the quadrupole formula in the exterior, one then finds (using $dt = dr/\dot{r}$ to perform a radial integration)

$$E_{\rm rad}^{\rm ext} = \frac{16\sqrt{2}}{105}\left(\frac{M}{R_{98}}\right)^{5/2}\frac{M_{\rm BH}^2}{R_{98}}\,. \tag{6.34}$$

In the interior one finds instead

$$E_{\rm rad}^{\rm int} = \left(\frac{63\cot^{-1}\left(\sqrt{2}\right)}{\sqrt{2}} - 7\right)E_{\rm rad}^{\rm ext}\,. \tag{6.35}$$

For finite velocity or realistic matter density, a numerical integration of the equation of motion, along with that of the quadrupole formula is necessary. The result of such an integration is shown in Table 6.2, where we use the fully relativistic boson star solution, and a slow motion approximation. We truncate the integration at the origin when $v_0 = 0$, but we assume that the BH plunges through and emerges on the other side for $v_0 = 0.5$.

Our fully relativistic results for GW emission are shown in Table 6.2 and Fig. 6.7. We compute the energy and momentum flux of GWs at $r = 500$. There is a pulse of "junk" radiation in the initial data, which is easily distinguished from the physical pulse [226]. Hence we are able to discard nonphysical contributions to the total radiated fluxes and energies. As seen in Table 6.2, our Newtonian estimate is in good agreement with the full relativistic results, especially if one considers how simple the Newtonian model is, with no accretion included. The flux of energy in GWs for extreme length ratios, Fig. 6.7, shows three emission peaks, which are caused by the BH tidally induced retrograde motion and accretion and momentum-induced forward motion described above.

Table 6.2 also shows the linear momentum carried by GWs. Since radiation is forward focused, linear momentum in GWs is along the direction of the BH motion, in the positive z direction. The only exception concerns simulation `IA`, for which the collision happens from rest and the BS is less massive than the BH. It is thus expected that this is best described by a BS falling onto a BH, hence a negative total linear momentum radiated. In any case, the linear momentum carried by GWs is too small to influence any of the dynamics of the system.

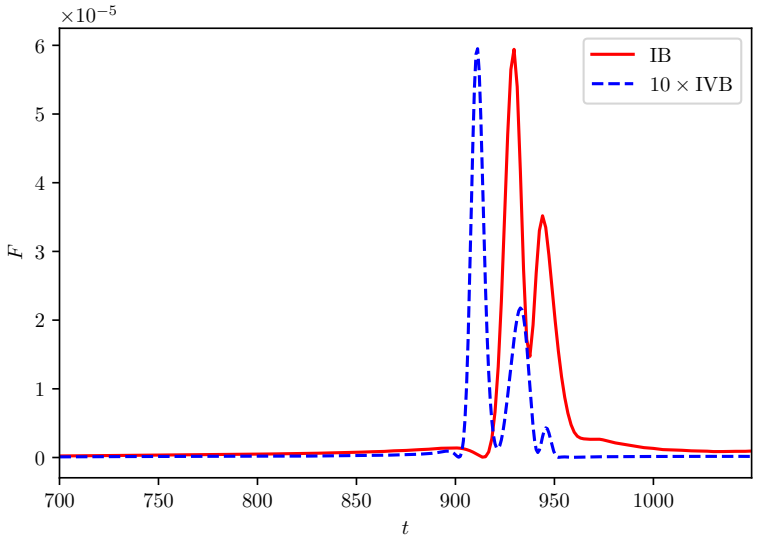

Figure 6.7: Energy flux $F = \frac{dE^{\rm rad}(t)}{dt}$ of the GW, which is the integration of Ψ_4 on the sphere $r = 500$. The blue dashed line is multiplied by 10.

6.4.4 *Late-time decay of the scalar*

The BH accretes most of the BS material in a violent accretion stage, as we saw. However, a small fraction of the BS leftovers linger around the BH in a quasi-bound state co-moving with the BH, as might be expected for massive scalars. To understand if such states correspond to those in perturbation theory [36], we use a spherical harmonic decomposition in the BH frame, as explained in Sec. 6.3.2.

Figure 6.8 shows the monopolar ($l = m = 0$) component of the scalar field on a sphere around the BH extracted close to the BH for simulations `IB` and `IVB`. The field oscillates at a frequency μ, as expected for massive fields. We also see a clear exponential decay of the field after the collision, indicating that the system is relaxing in one of its characteristic modes of vibration, corresponding to the so-called "gravitational atom" (with a BH "nucleus" and the light scalar field as the "electron") [36, 42, 43].

To test this picture and to compare with the decay timescale of a bound state within perturbation theory, we calculate the quasi-bound states of massive scalars in a fixed Schwarzschild geometry, using Leaver's continued fraction method [36, 89]. In other words, the field is assumed to be quasistationary $\phi \sim e^{i\omega t}$ and evolving on a fixed BH background. The characteristic frequencies $\omega = \omega_R + i\omega_I$. For simulation `IA`, for example the final BH mass $M_f \sim 1.56$, and the decay rate seen in the time evolution is close to that predicted by mode calculations, at $\omega_I = -0.13$. For simulations `IB` and `IVB`, we find a similar behavior, although the agreement with linearized mode calculations is not as good, nor as clean, since the BH is still accreting at late times (which changes

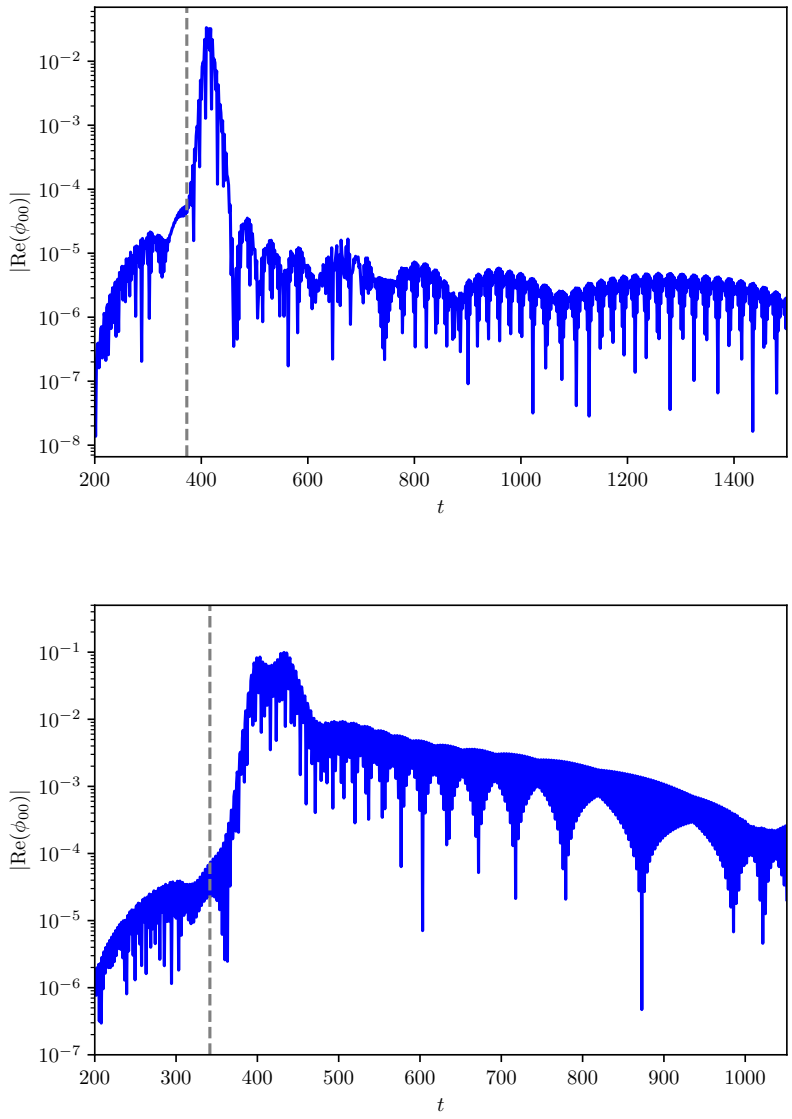

Figure 6.8: Real part of the $l = m = 0$ multipole of the scalar field on sphere $r = r_{\mathrm{BH}} + 1$ around the BH for `IB` and `IVB`, where the origin is the position of the BH and r_{BH} is the BH horizon radius. The dashed gray line indicates a "merger instant," (somewhat arbitrarily) defined as the instant where $|\phi_{00}| > 10^{-2}$ on the sphere $r = r_{\mathrm{BH}} + 1$. The monopolar component grows once the BH plunges into the BS, after which we see an exponentially decaying stage of a rate ($\omega_I \sim -0.15$ for `IB` and $\omega_I \sim -0.075$ for `IVB`, in rough agreement with expectations from the quasi-bound state calculation within a linearized approach). Our calculations indicate that this is the first overtone and that a "gravitational atom" was created. At late times, we see a power-law decay, $\phi_{00} \sim t^{-1.5}$ for simulations `IB`, as expected for massive fields [227, 228]. For simulation `IVB` we do not have clear control on the very-late-time behavior: this would require a longer simulation, which for these extreme values is very challenging to achieve, while keeping precision under control.

its mass, and the quasi-bound state frequencies are very sensitive to the precise value of the BH mass).

The quasi-bound states decay exponentially, and eventually may give way to power-law tails. For massive scalars, the tail stage is dominated at intermediate times by a behavior $\phi_{00} \sim t^{-3/2}$ for spherically symmetric modes [227, 228]. This behavior is independent of the presence of the BH and is already present in Minkowski: it is a characteristic of massive fields. Our results for the late-time behavior, seen for example in Fig. 6.8, are consistent with a decay close to the theoretical power-law tail $t^{-3/2}$, characteristic of intermediate times [227, 228]. We note that this behavior is consistent with what we see in runs `IA`, `IVA`, and `IB`. For simulation `IVB` we do not have any indication that the field settled to its late-time value yet (by the time the simulation finishes, the BH is still accreting). At very late times, one expects a slightly different behavior, $\phi_{00} \sim t^{-5/6}$, for which we have no evidence. There are several possible reasons for this, one of them being that we are not able to evolve the spacetime long enough for this decay to dominate.

6.4.5 *Numerical convergence*

To check the convergence of our numerical results, we define the usual convergence factor

$$Q_n = \frac{f_{\Delta_c} - f_{\Delta_m}}{f_{\Delta_m} - f_{\Delta_h}} = \frac{\Delta_c^n - \Delta_m^n}{\Delta_m^n - \Delta_h^n} \tag{6.36}$$

where n is the order of the finite difference scheme used, and f_{Δ_c}, f_{Δ_m}, and f_{Δ_h} are the numerical solutions obtained for a given function f at resolutions Δ_c, Δ_h and Δ_h, respectively. For these tests we performed simulations for configuration `IB` (see Table 6.1) with resolutions $\Delta_c = 2.4M$, $\Delta_m = 2M$ and $\Delta_h = 1.6M$.

As explained in the main text, we use a simple superposition procedure to build initial data. The Hamiltonian constraint is therefore expected to converge to a small, but nonzero, value. This is shown in Fig. 6.9, where a fourth-order convergence can be seen. We experimented with other methods for the superposition operation, but saw no noticeable advantage. For the future, we intend to try the method of Ref. [229], or a similar method, to check if any improvement is observed.

We also monitor the ℓ^2-norm of the constraint violations during the evolution (see Fig. 6.10) to confirm these do not grow with time.

Finally, we plot in Fig. 6.11 the convergence analysis for the $l = 0$, $m = 2$ multipole of Ψ_4, extracted at $r = 500M$, for configuration `IB`. The results are compatible with a convergence order between third and fourth order.

6.5 CONCLUSION

We have performed some of the most challenging simulations to date involving BHs and BSs, with length ratios as large as ~ 62. Our goal

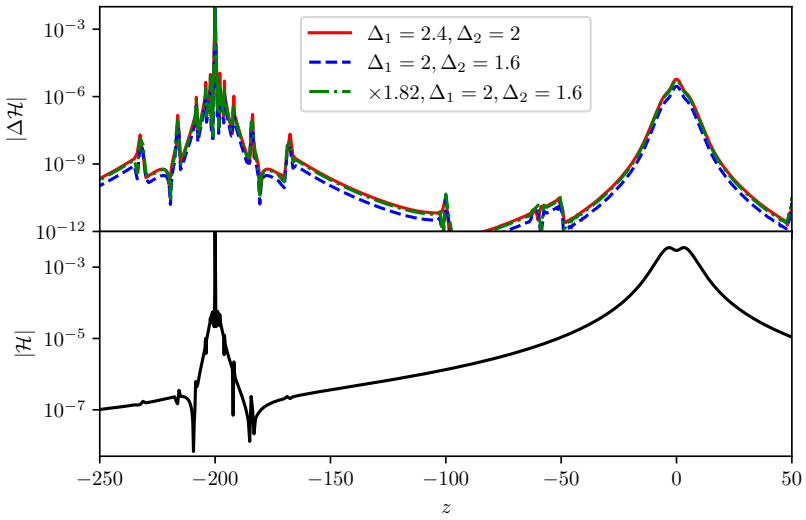

Figure 6.9: **Top:** convergence of the Hamiltonian constraint violation at $t = 0$ for `IB`. The green line is multiplied by $Q_4 = 1.82$, the expected factor for fourth-order convergence. **Bottom:** Richardson extrapolation used to obtain the value of the Hamiltonian constraint as $\Delta \to 0$.

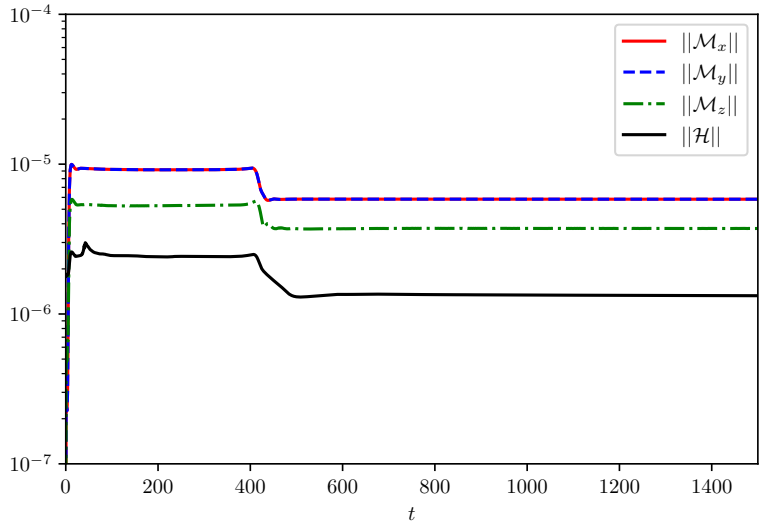

Figure 6.10: Violation of the Hamiltonian and momentum constraints as functions of time for run `IB`.

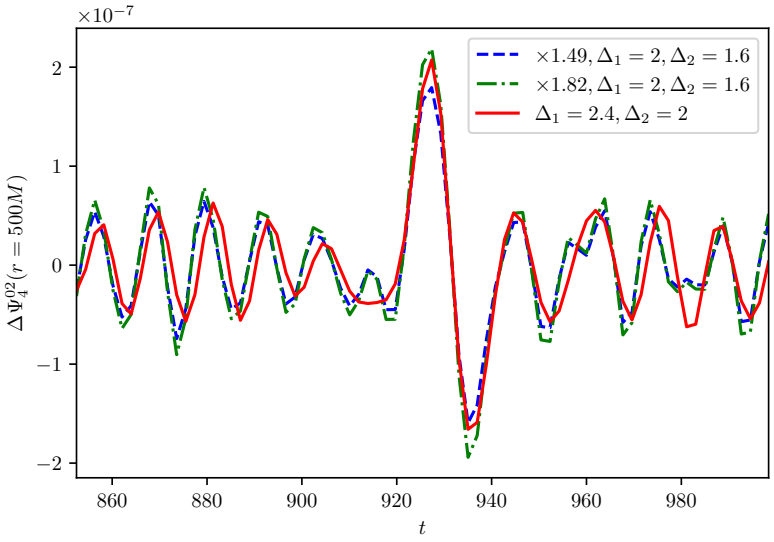

Figure 6.11: Convergence analysis of the $l = 0$, $m = 2$ multipole of Ψ_4, extracted at $r = 500M$. The blue line shows the expected result for third-order convergence ($Q_3 = 1.49$), while the green line shows the expected result for fourth-order convergence ($Q_4 = 1.82$).

was to understand how bosonic structures—which could describe dark matter—interact with BHs, and which dynamical friction or accretion they induce on the BHs. Our fully relativistic results are in good agreement with Newtonian estimates for the motion and asymptotic velocities of the objects, as well as for GW emission. To our surprise, even at the most extreme length ratios we considered, the boson star is entirely accreted by the BH. The reason, we believe, is that the BH is tidally captured by the boson star. This seems to be an extreme case of tidal capture not reported previously. At late times, a "gravitational atom" is formed, where a massive BH is surrounded by a quasi-bound state of the scalar field, the BS remnant.

One of our goals was to see the fate of a boson star which had been pierced by a high-velocity BH, and how dynamical friction on the BH compares to estimates in the literature. Unfortunately, because of tidal capture, the BS is swollen and dynamical friction turns out to be strongly enhanced due to transient accretion. We estimate in Sec. 6.4.2 that very challenging simulations need to be done, if tidal friction is to be identified at the full nonlinear level in self-gravitating structures.

In our configuration, the BS is kept fixed in all scenarios, but we believe the results would be similar for other BS parameters. We focus on spherically symmetric, neutral configurations, but there are obviously new phenomena when one extends the initial data to spinning or charged configurations (see also Ref. [217] for a possible similar end state with spin). We are currently starting these studies.

7

PIERCING OF A SOLITONIC BOSON STAR BY A BLACK HOLE

In this chapter, we generalize Ref. [40] to SBSs. The addition of a repulsive self-interaction term introduces extra resistance to gravitational collapse and may drastically modify the relevant length scales [230]. Moreover, the maximum mass of mini-BSs, $M_{\max} \approx M^2_{\text{Planck}}/\mu$, is significantly smaller than the Chandrasekhar mass, $M_{\text{Ch}} \approx M^3_{\text{Planck}}/\mu^2$, for bosonic particle candidates with typical masses, where μ is the mass of the particle [20, 170, 231]. Dark stars are anticipated to accrete mass from their surroundings, regardless of their initial mass. As a result of this accretion process, their mass can increase by as much as $10^7 M_\odot$ [232]. To extend the limit of the potential to astrophysical masses that are comparable to the Chandrasekhar mass, a self-interaction component has been incorporated into the potential to provide additional pressure to counteract gravitational collapse [233].

As the simplest example of nontopological solitons, an SBS can even exist in the absence of gravity and is referred to as a Q-ball [12, 20, 23, 234]. Mini-BSs attain stability through the balance between gravitational and repulsive pressure forces. On the other hand, the stability mechanism of SBSs differs, with a bubble-like structure emerging in the densest region of the parameter space. Stability arises from the accumulation of energy near the surface, engendering surface tension among distinct vacua [12].

Evidence also suggests that SBSs can describe dark matter cores in sub-halos. A sub-halo is a smaller clump of dark matter that is gravitationally bound within a larger dark matter halo, and is created when smaller halos are accreted and tidally disrupted by larger ones [235]. A solitonic core can be considered as a special type of sub-halo that has a different profile and properties than other sub-halos [236]. However, the variability of the core-halo relation can make the discrepancy between soliton and sub-halo less strong for larger halos [237]. If dark matter is made up of ultralight bosons, it is possible for solitonic cores to form at the centers of dark matter halos [172]. It is worth noting that Ref. [238, 239] provides evidence that the density profiles of different mergers of solitonic cores conform to the SBS profile in ultralight axion dark matter halos. In addition, although the well-known cusp-core problem can be overcome by introducing a quartic term in the self-interaction scalar potential [240, 241], the scaling relation between the dark matter halo radius and central density still contradicts the observations [242]. With

an additional ϕ^6-term in the potential, the problem could be resolved and the cores would have a non-trivial phase structure [242, 243]. In this work, by focusing on SBSs, we aim to gain a comprehensive understanding of how solitonic cores behave in the presence of drifting perturbers. We note, however, that for relativistic fuzzy dark matter models, the boson mass is approximately of the order of 10^{-22} eV, which would correspond to a solitonic core radius of order 1 kpc [177]. Considering the largest known astrophysical BH, `Tonantzintla 618*`, its radius is of the order of 10^{-6} kpc [244], resulting in a length ratio of 10^6 which is impossible to resolve with our current approach. As a model for such systems, we will present the largest ratios that are feasible with our computational infrastructure, and as we will argue later, we do not expect our results to change significantly for larger length ratios that remain within one order of magnitude. Probing length scales much higher than these currently considered would necessitate a fundamentally different approach.

7.1 FRAMEWORK

7.1.1 *Solitonic boson star*

We consider the Lagrangian density of a self-gravitating, complex scalar field Φ with a solitonic potential $V = V(|\Phi|^2)$

$$\mathcal{L}_m = \frac{\mathcal{R}}{16\pi} - \left[g^{ab}\nabla_a\Phi\nabla_b\Phi^* + V\right], \tag{7.1}$$

where g_{ab} is the metric of the spacetime, $\mathcal{R}$ is the Ricci scalar, Φ^* is the complex conjugate of the scalar field and V is the potential

$$V = \mu^2|\Phi|^2\left(1 - 2\frac{|\Phi|^2}{\sigma^2}\right)^2 . \tag{7.2}$$

Here μ is the scalar field mass and σ is a free parameter controlling the self-interaction. The self-interaction potential is chosen to provide configurations that can exist even in flat spacetime [12, 23, 234], and is a standard choice in the literature (e.g. [190, 245]). Variation of the corresponding action with respect to the metric g^{ab} gives the equations of motion

$$\mathcal{R}_{ab} - \frac{1}{2}\mathcal{R}g_{ab} = 8\pi T_{ab}\,, \tag{7.3}$$

$$g^{ab}\nabla_a\nabla_b\Phi = \Phi\frac{dV}{d|\Phi|^2}\,, \tag{7.4}$$

with energy-momentum tensor

$$T^{ab} = \nabla^a\Phi\nabla^b\Phi^* + \nabla^a\Phi^*\nabla^b\Phi - g^{ab}\left(\nabla^c\Phi\nabla_c\Phi^* + V\right). \tag{7.5}$$

Following Refs. [20, 40, 246], we write down equilibrium equations with the general, spherical symmetric metric in Schwarzschild-like coordinates

$$ds^2 = -\alpha^2dt^2 + a^2dr^2 + r^2d\Omega_2^2\,, \tag{7.6}$$

where $\alpha = \alpha(r)$, $a = a(r)$. In addition, to get the time-independent solution, we assume a harmonic ansatz

$$\Phi = \phi(r) e^{i\omega t} \,. \tag{7.7}$$

Then, the Einstein-Klein-Gordon system can be written as three coupled ordinary differential equations

$$\begin{aligned}
\frac{2a'}{a} &= \frac{1-a^2}{r} + 8\pi r \left[\left(\frac{\omega^2}{\alpha^2} + \frac{\mu^2(\sigma^2 - 2\phi^2)^2}{\sigma^4} \right) a^2\phi^2 + (\phi')^2 \right] , \\
\frac{2\alpha'}{\alpha} &= \frac{a^2-1}{r} + 8\pi r \left[\left(\frac{\omega^2}{\alpha^2} - \frac{\mu^2(\sigma^2 - 2\phi^2)^2}{\sigma^4} \right) a^2\phi^2 + (\phi')^2 \right] , \\
\phi'' &= -\left\{ 1 + a^2 - 8\pi r^2 \mu^2 a^2 \phi^2 \frac{(\sigma^2 - 2\phi^2)^2}{\sigma^4} \right\} \frac{\phi'}{r} \\
&\quad - \left\{ \frac{\omega^2}{\alpha^2} - \mu^2 - \frac{4\mu^2\phi^2}{\sigma^4}(3\phi^2 - 2\sigma^2) \right\} \phi a^2 \,,
\end{aligned}$$

where primes stand for radial derivatives ∂_r. To obtain a physical solution, the following boundary conditions must be imposed on this system.

$$\phi(0) = \phi_0 \,, \qquad \phi'(0) = 0 \,, \qquad a(0) = 1 \,, \tag{7.8}$$

$$\lim_{r\to\infty} \phi(r) = 0 \,, \quad \lim_{r\to\infty} \alpha(r)a(r) = 1 \,. \tag{7.9}$$

ϕ_0 can be specified arbitrarily and roughly determines the mass of the BS. We can find a simpler system by rescaling the variables in the following manner,

$$\tilde{\phi} \equiv \frac{\phi}{\sigma}, \quad \tilde{r} \equiv \mu r, \quad \tilde{t} \equiv \omega t, \quad \tilde{\alpha} \equiv (\mu/\omega)\alpha.$$

Then the equations become

$$\begin{aligned}
a' &= \frac{a}{2} \left\{ \frac{1-a^2}{\tilde{r}} + 8\pi\sigma^2\tilde{r} \left[\left(\frac{1}{\tilde{\alpha}^2} + (1-2\tilde{\phi}^2)^2 \right) a^2\tilde{\phi}^2 + (\tilde{\phi}')^2 \right] \right\} , \\
\tilde{\alpha}' &= \frac{\tilde{\alpha}}{2} \left\{ \frac{a^2-1}{\tilde{r}} + 8\pi\sigma^2\tilde{r} \left[\left(\frac{1}{\tilde{\alpha}^2} - (1-2\tilde{\phi}^2)^2 \right) a^2\tilde{\phi}^2 + (\tilde{\phi}')^2 \right] \right\} , \\
\tilde{\phi}'' &= -\left[1 + a^2 - 8\pi\mu^2\sigma^2\tilde{r}^2 a^2 \tilde{\phi}^2 (1-2\tilde{\phi}^2)^2 \right] \frac{\tilde{\phi}'}{\tilde{r}} \\
&\quad - \left[\frac{1}{\tilde{\alpha}^2} - 1 - 4\tilde{\phi}^2(3\tilde{\phi}^2 - 2) \right] \tilde{\phi} a^2 \,,
\end{aligned} \tag{7.10}$$

where primes now stand for derivatives with respect to $\tilde{r}$. To integrate these equations, we need to understand their asymptotic behavior. At the origin, $\tilde{r} = 0$, we can expand all quantities in a Taylor series to find

$$\begin{aligned}
a(\tilde{r}) &= 1 + \frac{4\pi\tilde{r}^2\sigma^2\tilde{\phi}_0^2}{3\tilde{\alpha}_0^2} \left[1 + \tilde{\alpha}_0^2(1-2\tilde{\phi}_0^2)^2 \right] + \mathcal{O}(\tilde{r}^4) \,, \\
\tilde{\alpha}(\tilde{r}) &= \tilde{\alpha}_0 + \frac{4\pi\sigma^2\tilde{r}^2\tilde{\phi}_0^2}{3\tilde{\alpha}_0} \left[2 - \tilde{\alpha}_0^2(1-2\tilde{\phi}_0^2)^2 \right] + \mathcal{O}(\tilde{r}^4) \,, \\
\tilde{\phi}(\tilde{r}) &= \tilde{\phi}_0 + \frac{\tilde{r}^2\tilde{\phi}_0}{6} \left[1 - \frac{1}{\tilde{\alpha}_0^2} - 8\tilde{\phi}_0^2 + 12\tilde{\phi}_0^4 \right] + \mathcal{O}(\tilde{r}^4) \,,
\end{aligned}$$

where $\tilde{\phi}(0) = \tilde{\phi}_0$, $\tilde{\alpha}(0) = \tilde{\alpha}_0$. At large distances, the asymptotic behavior of ϕ is

$$\tilde{\phi}(\tilde{r} \to \infty) \sim \frac{1}{\tilde{r}} \exp\left(-\tilde{r}\sqrt{1-\tilde{\alpha}^{-2}}\right). \tag{7.11}$$

Equation (7.2) results in the potential of mini-BSs in the limit $\sigma \to \infty$ [156]. A SBS is not always dynamically stable against linear fluctuations. An unstable solution evolves on timescales possibly shorter than those of collision processes we aim to study, hence it is crucial to select linearly stable solutions as initial data. The stability of spherically symmetric BSs has been investigated with findings showing that stability changes at a mass extremum, meaning it is marginally stable at a particular value of ϕ_0: $dM/d\phi_0 = 0$ (See II. C in Ref. [247] for details). This result reveals, as indicated in Fig. 2 of Ref. [248], that SBSs possess two stable and two unstable branches for any value of $\sigma \ll 1$ [12, 234, 249, 250].

The first stable branch of SBSs arises from the non-relativistic limit ($\phi_0/\sigma \to 0$) with weak self-interactions, leading us to anticipate that it will yield results similar to those of the mini-BS. In contrast, the second stable branch is situated near ϕ_0/σ and possesses significantly stronger self-interactions. This allows for a more compact configuration of SBSs compared to the first branch.

It is also worth noting that while SBSs may initially form in a dilute state, subsequent interactions and coalescence could lead to more compact configurations [12, 168]. Moving forward, we will standardize units such that $\mu = 1$. All our results will be shown and analyzed using this unit measure. In the following analysis, we will focus on the second branch and utilize a ground-state SBS characterized by $\tilde{\phi}_0 = 0.7$, $\sigma = 0.1$, $M = 0.20$, and $R_{98} = 4.41$, where R_{98} represents the radius that encompasses 98% of the SBS mass. This configuration is depicted in Fig. 7.1.

7.1.2 *BH-BS binary*

To construct initial data of BH-SBS spacetime, we transform radial coordinates of SBS into isotropic coordinates R and superpose this solution with a boosted Schwarzschild BH, the details of which are demonstrated in Ref. [40].

To evolve this system, we employ the Baumgarte-Shapiro-Shibata-Nakamura formulation of Einstein's equations [200–202] for our numerical simulations and rely on the infrastructure of the Einstein Toolkit [204, 205, 251] for the numerical evolutions. Mesh refinement capabilities are facilitated by Carpet [207], apparent horizons are located and tracked using AHFinderDirect [208, 209], and BH mass is extracted using QuasiLocalMeasures [210]. The spacetime metric and scalar field variables are evolved in time using the LeanBSSNMoL and ScalarEvolve codes [203, 211]. We employ the method of lines, coupled with the fourth-order Runge-Kutta technique, to advance our equations over time. In the integration process, we use outgoing (radiative) boundary conditions along-

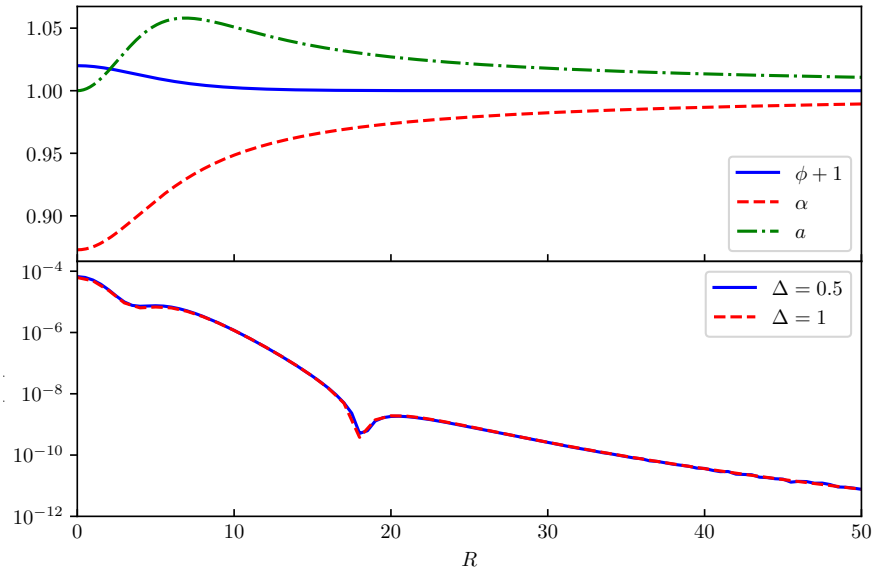

Figure 7.1: Scalar field and metric components as functions of the isotropic radial coordinate R for an isolated SBS with mass $M = 0.20$, $\tilde{\phi}_0 = 0.7$, $\sigma = 0.1$, $\omega = 0.1$, $R_{98} = 4.41$. In this work we focus on this specific SBS.

side the common 1+log and Gamma-driver gauge conditions [199]. For all simulations we use a square numerical domain with $x^i_{\rm min} = -430$, $x^i_{\rm max} = 430$. We tested also with larger domain sizes and it did not change the final results. We consistently employ a minimum of 40 points to cover the BH, thereby guaranteeing sufficient grid points to achieve satisfactory resolution and use the same grid structure as in Ref. [40]. We have run simulation `IVA` until $t \sim 1500$ and simulation `IVB` until $t \sim 800$. The data analysis for this project was performed utilizing the Python package "kuibit" [252].

7.1.3 *Diagnostic tools*

To gain a clearer understanding and more precise characterization of some of the physics involved, we track the following quantities, whose definitions can be found in Ref. [40]:

- The spherical harmonics decomposition of the scalar field $\phi_{lm}(t, r)$ in the vicinity of the moving BH, using a frame that is comoving with the BH. We use a coordinate system where the dynamics is axi-symmetric, hence the only contributing multipoles have azimuthal number $m = 0$.
- The energy $E^{\rm rad}$ and momentum $P^{\rm rad}$ radiated in GWs at large distances.
- The total energy density Q_t of the scalar field into the BH horizon.

7.2 NUMERICAL RESULTS

Table 7.1: List of simulations analyzed for collisions between a BH of mass parameter $M_{\rm BH}$ and an SBS with mass $M = 0.20$. The BH is initially moving along the z-axis with a velocity of v_0 and starting from position $z_0 = -50$. The SBS is characterized by a frequency of $\omega = 0.759$ and values of $\tilde{\phi}_0 = 0.7\,, \sigma = 0.1\,, \alpha_0 = 0.827$ at the origin. The total energy of the system, $M_{\rm tot}$, can be approximated using a Newtonian approach as $M_{\rm tot} = \Gamma M_{\rm BH} + M - \Gamma M_{\rm BH} M/z_0$, where Γ is the Lorentz factor. The total momentum of the boosted BH is $\Gamma M_{\rm BH} v_0$. The simulations use a mass ratio of $q = M/M_{\rm BH}$ and a length ratio of $\mathcal{L} = R_{98}/(2M_{\rm BH})$ as parameters. It should be noted that initially the mass parameter $M_{\rm BH}$ is approximately equal to the irreducible mass $M_{\rm irr}$ to within 0.5%. The irreducible mass can be calculated as $\mathcal{A} = 16\pi M_{\rm irr}^2$, where $\mathcal{A}$ is the area of the apparent horizon. Recall that all results are presented in units where $\mu = 1$.

Run	$M_{\rm BH}$	$\mathcal{L}$	v_0	$M_{\rm tot}$	$P_{\rm tot}$
`IA`	0.5	4	10^{-4}	0.70	0
`IB`	0.5	4	0.5	0.78	0.289
`IIA`	0.25	9	10^{-4}	0.45	0
`IIB`	0.25	9	0.5	0.49	0.144
`IIIA`	0.125	18	10^{-4}	0.33	0
`IIIB`	0.125	18	0.5	0.35	0.072
`IVA`	0.0625	35	10^{-4}	0.26	0
`IVB`	0.0625	35	0.5	0.27	0.036

We conducted a study on a range of initial conditions, varying the initial mass and velocity of the BH. We use coordinates such that the SBS is initially at rest at the origin, and the BH is located along the z axis, initially at $(0, 0, z_0)$ and moving in the positive z-direction. The convergence of our numerical simulations is demonstrated in Section 7.2.4.

The initial conditions are summarized in Table 7.1 and our numerical results and findings are summarized in Table 7.2 and Figs. 7.2–7.7. In the following subsections, we focus on two typical cases, Run `IIIB` and Run `IVB`, as our main interest lies in small BHs. However, to more clearly illustrate tidal deformation, we opt to showcase Run `IB` rather than Run `IIIB` in Section 7.2.1.

7.2.1 *Dynamics and accretion during collision*

Snapshots of the evolution of the scalar field for initial data `IB` and `IVB` are shown in Figs. 7.2 and 7.3, respectively. In both figures the tidal distortion of the BS as the BH approaches is clear, probably due to their large (and positive) tidal Love numbers compared to compact systems [194, 220]. The distortion becomes more visible as the BH

Table 7.2: Summary of the results of the dynamical evolution of the initial data in Table 7.1. Here, M_f represents the final BH irreducible mass, and v_f denotes the final BH velocity, calculated from the puncture trajectory. In parentheses, we display the expected value $M_{\rm BH}v_0/M_{\rm tot}$ based on momentum conservation, assuming that the entire BS is accreted onto the BH (note the strong agreement between these two estimates). $E^{\rm rad}$ and $P^{\rm rad}$ stand for the energy and momentum radiated in GWs, respectively. These values are calculated from ψ_4. Lastly, the total momentum and energy flux of the scalar field into the BH horizon are presented in the final two entries. Junk radiation is present in all cases, but its effect has been excluded.

Run	$M_{\rm BH}$	M_f	v_0	v_f	$10^4 E^{\rm rad}$	$10^4 P_z^{\rm rad}$	$Q_t^{\rm initial}$	$Q_t^{\rm final}$
IA	0.5	0.70	10^{-4}	-3×10^{-3} (0)	2.10	0.26	0.20	2.6×10^{-4}
IB	0.5	0.75	0.5	0.36(0.36)	4.99	-1.72	0.20	6.3×10^{-4}
IIA	0.25	0.45	10^{-4}	-4.8×10^{-3} (0)	1.05	0.08	0.19	2.0×10^{-3}
IIB	0.25	0.48	0.5	0.27(0.26)	3.09	-0.84	0.20	2.0×10^{-3}
IIIA	0.125	0.29	10^{-4}	-1.9×10^{-2} (0)	0.46	9.7×10^{-3}	0.19	2.8×10^{-2}
IIIB	0.125	0.31	0.5	0.17(0.18)	1.35	-0.31	0.20	2.4×10^{-2}
IVA	0.0625	0.24	10^{-4}	1.0×10^{-3}(0)	0.29	0.005	0.19	1.9×10^{-2}
IVB	0.0625	0.25	0.5	0.12(0.12)	0.52	-0.09	0.20	2.9×10^{-2}

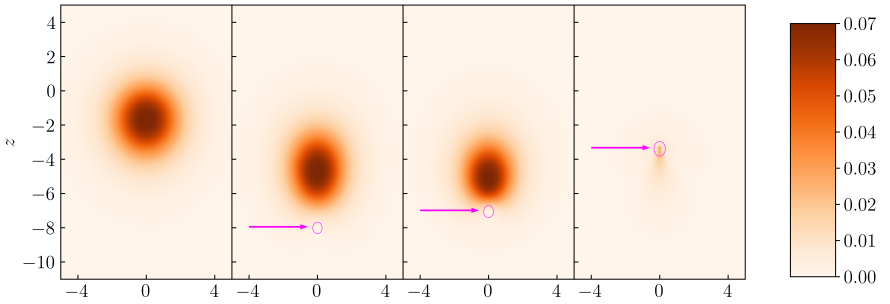

Figure 7.2: Snapshots of evolution for the simulation `IB`, where the BH and SBS are nearly of equal mass. Color intensity depicts scalar field absolute value $|\Phi|$. Snapshots are shown at instants $t = 80$, 100, 102, 112 from left to right. The pink lines depict contours of constant lapse function $\alpha = 0.2$, a rough measure for the location of the apparent horizon. This figure illustrates that the SBS undergoes considerable tidal distortion as it nears the BH, and ultimate near-total accretion by the BH.

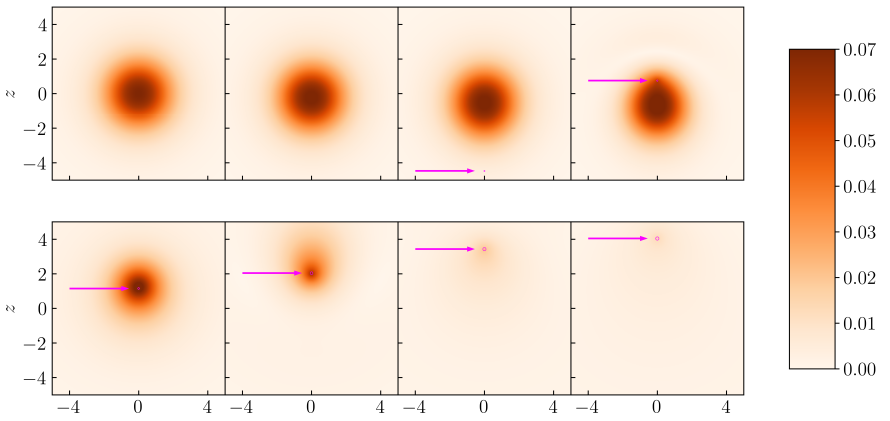

Figure 7.3: Snapshots of evolution, depicting the scalar field absolute value $|\Phi|$ for the simulation `IVB`. The top row displays snapshots taken at instants $t = 0.0\,, 79.36\,, 94.72$, and 107.52 from left to right, while the bottom row shows snapshots taken at $t = 120.32\,, 130.56\,, 140.8$, and 145.92 from left to right. As in the previous case, the pink lines depict contours of constant lapse function $\alpha = 0.2$, indicating the location of the apparent horizon. The pink circle in this figure is much smaller and harder to see compared to the one in Fig. 7.2, due to the significantly smaller size of the BH. In this figure, the SBS pulls back the BH during the collision process, as depicted in panels 5 and 6. Finally, the BH swallows the BS completely. Notice that when the BH first passes through the SBS, the tidal deformation of the SBS is quite inconspicuous. However, as the SBS accretes an increasing amount of the scalar field, the deformation becomes more pronounced.

approaches the BS along the BH-BS axis. Tidal effects become crucial to capture the BH, and this is evident for simulation `IVB`: a much smaller BH, moving at half the speed of light is still captured by the SBS via tidal effects, ending up by accreting almost all of the SBS. The tidal capture is clearly illustrated in bottom panel of Fig. 7.4, where the BH's velocity even becomes negative for a short period.

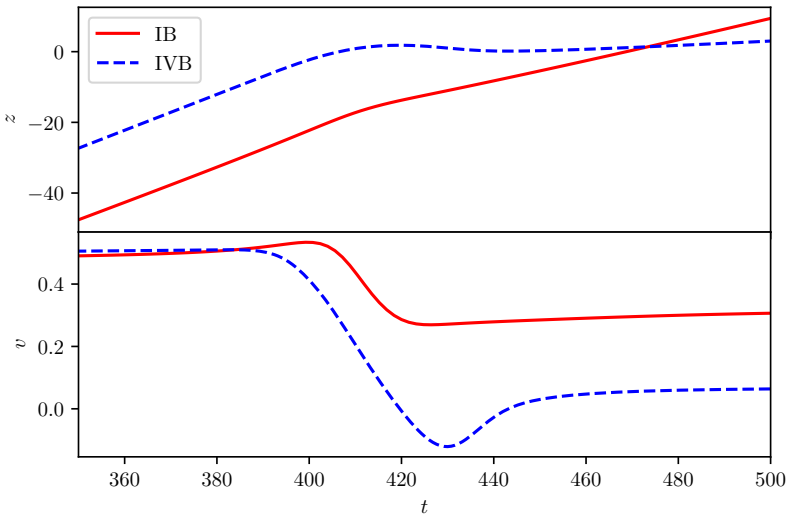

Figure 7.4: The puncture location z and the velocity v of the BH for simulations `IIIB` and `IVB`. They provide good estimates for the location and velocity of the BH, and these results demonstrate a clear interaction between the BH and the BS. Notably, in simulation `IVB`, the BH velocity becomes negative for a brief period as the BH is tidally captured by the SBS.

Some of the main numerical results are reported Table 7.2, which shows a few interesting aspects of this process. For all simulations we performed, across the different mass ratios, the BH ends up accreting the SBS. The reason for this is most likely three-fold: accretion and dynamical friction slows the BH down as the plunges through the SBS material [155, 189, 196], but for the process to be fully effective, tidal capture ensures that the BH remains inside the SBS, eventually accreting it all or almost all. Accordingly, the velocity of the BH at late times is well estimated by simple momentum conservation as can be seen from Table 7.2.

Given the velocity dependence of dynamical friction, it is unlikely that yet higher velocities would allow for the BH to cross the SBS and exit without first accreting it [155, 189, 196], unless of the course one gets to more extreme mass ratios. In fact, the BH absorption cross-section is the main factor that determines whether a BH can pass through a BS without destroying it, and to decrease it one needs to make the BH smaller. Table 7.2 seems to indicate indeed that the residual scalar field increases for smaller BH mass. We can infer that for yet smaller BHs than those simulated here, the BH may pierce through

the SBS, consuming only a small portion of scalar field, thereby leaving a smaller SBS in its wake. However, our numerical simulations would take a prohibitively long time to evolve such cases. As a result, within this theoretical framework, it is very difficult to verify whether a BH can pass through a BS without destroying it.

7.2.2 *The tidal capture and gravitational-wave emission*

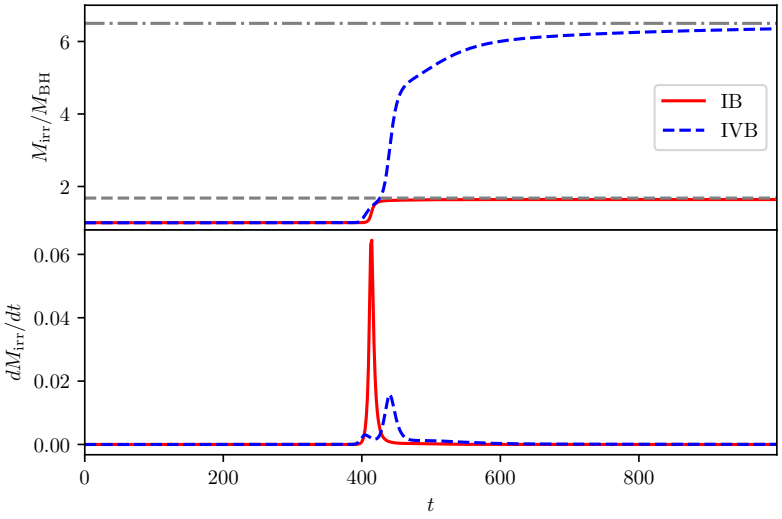

Figure 7.5: Accretion of scalar onto the BH. **Top panel:** normalized BH irreducible mass $M_{\rm irr}/M_{\rm BH}$ for simulations `IIIB` and `IVB`. The gray lines are the normalized total mass $M_{\rm tot}/M_{\rm BH}$ given in Table 7.1. At late times the BH mass approaches $M_{\rm tot}$, thus the BH ends up accreting the entire BS. **Bottom panel:** accretion rate for the two different initial data. It is worth mentioning that for simulation `IVB`, there are two distinct stages of accretion that we believe are caused by tidal effects.

When small BHs are tidally captured, we find that they oscillate around the center of the SBSs like a harmonic oscillator. The phenomenon is clearly observable for `IVB` case in both bottom panel of Fig. 7.5 and upper panel of Fig. 7.6, which features multiple peaks, indicating various stages of oscillation. The peaks depicted in the bottom panel of Fig. 7.5 indicate a high accretion rate, suggesting that the BH is traversing the core of the SBS. Due to the deformation of the SBS, this core is identified as the region where the absolute value of the scalar field $|\Phi|$ reaches its maximum at this stage. Meanwhile, the peaks seen in the upper panel of Fig. 7.6 stem from the acceleration and deceleration of the relative movement between the SBS and the BH. It is worth noting that this oscillatory behavior is not clear in Fig. 7.4, given that the SBS have non-zero velocity in the lab frame.

To estimate the period of this oscillation and determine how close we are to the test particle threshold, we use the test particle approximation.

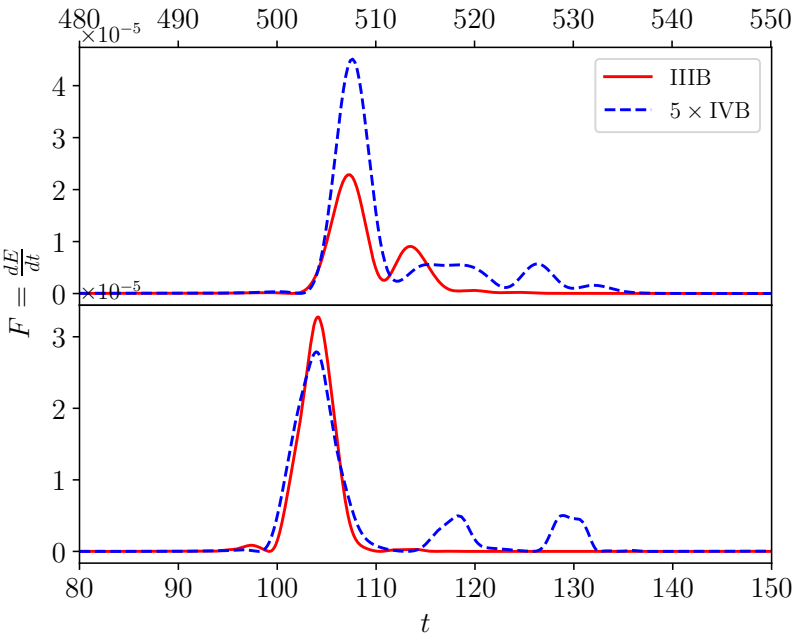

Figure 7.6: Energy flux $F = dE^{\text{rad}}/dt$ of the GW for `IIIB` and `IVB`. **Top:** The energy flux obtained by integrating Ψ_4 over the sphere with radius $r = 400$. **Bottom:** The energy flux is calculated using the quadrupole approximation (7.14), which requires numerical data from the simulation such as the puncture location, puncture velocity, and BH mass.

By assuming this, we can use the lapse function $\alpha(R)$ of non-deformed SBS, which provides a good approximation of the gravitational potential. Therefore this function is also commonly referred to as the Newton potential. When considering a test particle oscillating within this potential, the acceleration it experiences can be determined from

$$\frac{d^2R}{dt^2} = -\frac{d\alpha(r)}{dR}\,. \tag{7.12}$$

The period given by the equation of motion is then

$$T = \frac{2\pi}{\sqrt{\alpha''(0)}} \approx 23.23\,. \tag{7.13}$$

Additionally, the period of the emitted gravitational wave corresponds to half of the motion period T, which for this case is 11.62. This period is consistent with the first peak of gravitational waves observed in case `IVB`, as shown in Fig. 7.6. This suggests that we are very near the test particle threshold for simulation `IVB`. Therefore, it is unlikely that we will observe any new phenomena at length ratios slightly larger but still within one order of magnitude. As we observe subsequent peaks, the oscillation period gradually decreases due to the BH accretion.

Our results for gravitational wave emission, derived using a fully relativistic approach, are presented in Table 7.2. We have selected two typical cases to illustrate the waveform, as depicted in top panel of Fig. 7.6. Following Ref. [40], in the case that the BH mass is much smaller than SBS mass, the quadrupole approximation can be used to estimate the waveforms and radiated fluxes, with the BH moving along a spacetime geodesic defined by a radial position $r(t)$ in a background dictated by the SBS

$$\frac{dE}{dt} = \frac{8}{15} M_{\rm BH}^2 (3\dot{r}\ddot{r} + r\dddot{r})^2. \tag{7.14}$$

Nevertheless, the present scenario differs significantly from the Newtonian case, which is characterized by $\phi/\sigma \to 0$, rendering the methodology in Ref. [40] inapplicable in this context. As an alternative solution, we use the puncture location, puncture veolcity and BH irreducible mass in numerical simulations instead of the original semi-analytic approximation. To reduce the impact of high frequency noise in numerical data of `IIIB` and `IVB`, we utilize a low-pass filter on both the puncture location and puncture velocity with a cutoff frequency $\omega_c = 2.5$ ($T = \frac{2\pi}{\omega_c} \approx 2.51$). From the numerical results, it can be seen that the dominant wavelength of the energy flux exceeds 2.51, indicating that it would not significantly affect the main waveform. However, as depicted in bottom panel of Fig. 7.6, this approximation fails to describe the peaks that follow the initial main peak in both `IIIB` and `IVB`, which emerge from the BS, retaining only specific remnants during the final acceleration phase. This circumstance invalidates our initial assumption in the quadrupolar formula, where the BH mass $M_{\rm BH}$ is significantly smaller than the BS mass and the trajectory of the BH is a geodesic on the SBS background. Ideally, substituting the puncture velocity with

the relative velocity between BHs and SBS could lead to improved results. However, defining and calculating this relative velocity poses significant challenges. The result of quadrupolar approximation is given in bottom panel of Fig. 7.6. However, in all instances, these values are too insignificant to exert any substantial impact on the system.

7.2.3 *Late-time decay of the scalar*

As noted in Ref. [40] and demonstrated in the `IIIB` case in Fig. 7.5, when the mass of the BH is about half that of the BS, the BH enters a violent accretion phase, during which it absorbs most of the material from the BS. However, as shown in the `IVB` case in Fig. 7.5, the scenario deviates slightly. Here, the BH starts significantly smaller than the BS. After the BH is tidally captured and begins to increase in size, the subsequent stage of accretion becomes significantly more violent compared to the initial phase. In any case, a small portion of the BS remnants remains in a quasi-bound state, moving alongside the BH, which is typical for massive scalars. The small portion of BS remnants is expected to be mainly composed of spherical components and large wavelengths due to their lower accretion rate [255, 256]. Therefore, we validate the quasi-bound states for $l = m = 0$ multiple, as predicted by perturbation theory, by using the spherical harmonic decomposition technique in the BH frame [36]. Specifically, we calculate the quasi-bound state spectrum corresponding to the final BH mass using Leaver's method [89, 253, 254]. We find that the imaginary part of these modes align with the fitting result from one of the exponential decay stages. The results are shown in Fig. 7.7. Note that while there are multiple exponential stages, it becomes challenging to compare them with the results of perturbation theory before the BH mass reaches a stable stage, due to the variations in the BH mass during the accretion process.

7.2.4 *Numerical convergence*

We check the convergence of our numerical results by defining the usual convergence factor

$$Q_n = \frac{f_{\Delta_c} - f_{\Delta_m}}{f_{\Delta_m} - f_{\Delta_h}} = \frac{\Delta_c^n - \Delta_m^n}{\Delta_m^n - \Delta_h^n} \tag{7.15}$$

where n denotes the order of the finite difference scheme employed, while f_{Δ_c}, f_{Δ_m}, and f_{Δ_h} represent the corresponding numerical solutions for a specified function f at resolutions of Δ_c, Δ_m, and Δ_h.

We plot in Fig. 7.8 the convergence analysis for the $l = 0$, $m = 2$ multipole of Ψ_4, extracted at $r = 400M$, for configuration `IB`. The results are compatible with a convergence order between second and fourth order for physical waveform between $t = 500$ to $t = 530$.

As illustrated in the bottom panel of Fig. 7.9, the Hamiltonian constraint does not converge to zero, which is attributed to the superposition procedure used in constructing the initial data. To demonstrate

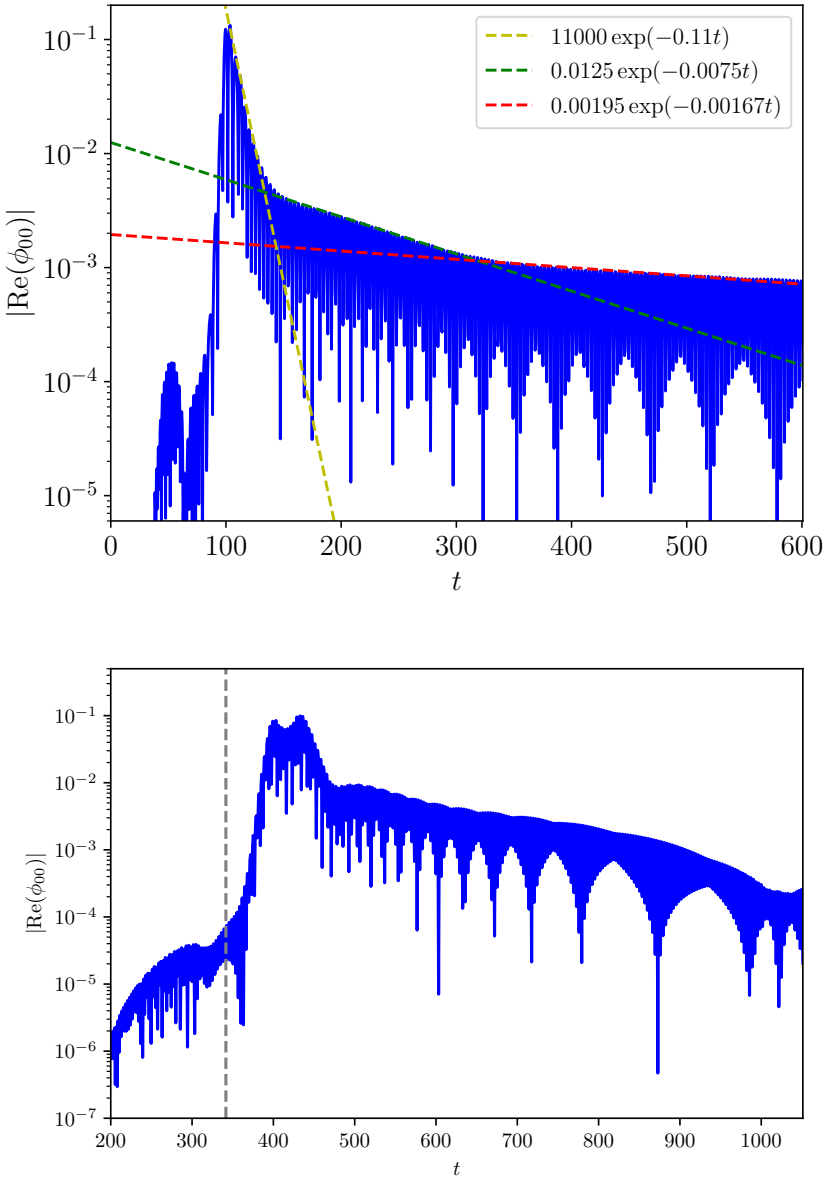

Figure 7.7: Real part of the $l = m = 0$ multipole of the scalar field on sphere $r = r_{\rm BH} + 1$ around the BH, where the left figure (a) is for `IIIB` and the right figure (b) is for `IVB`. The position of the sphere is taken as the position of the BH, and $r_{\rm BH}$ represents the radius of the BH horizon. As indicated by the dashed lines, it is evident that both `IIIB` and `IVB` display exponential decay, with varying rates at distinct stages. The rates of the dashed red lines are roughly consistent with the expectations from the quasi-bound state calculation using Leaver's method [36, 89, 253, 254], which predicts $\omega_{\rm I} \simeq -0.0350, -0.00559, \mathbf{-0.00167}, \ldots$ for `IIIB` ($M_{\rm f} = 0.31$) and $\omega_{\rm I} \simeq \mathbf{-0.018}, -0.0025, -0.00073, \ldots$ for `IVB` ($M_{\rm f} = 0.25$), respectively. The modes are characterized by the principal quantum number n [42]. It is notable that for `IIIB`, the corresponding mode is the $n = 3$ mode $\omega_{\rm I} \simeq -0.00167$, while for `IVB`, the corresponding mode is the $n = 1$ mode $\omega_{\rm I} \simeq -0.018$. This result indicate the existence of a "gravitational atom". The monopolar component experienced two growth phases. The decrease after the first growth is due to passing through the center of the SBS (defined as the place with the highest scalar field density). The second growth is caused by the BH pulling the SBS back and gradually swallowing it. Notice in panel (b) that the monopolar component has two highest peaks near the highest point, which implies that the BH oscillates at the center of the SBS.

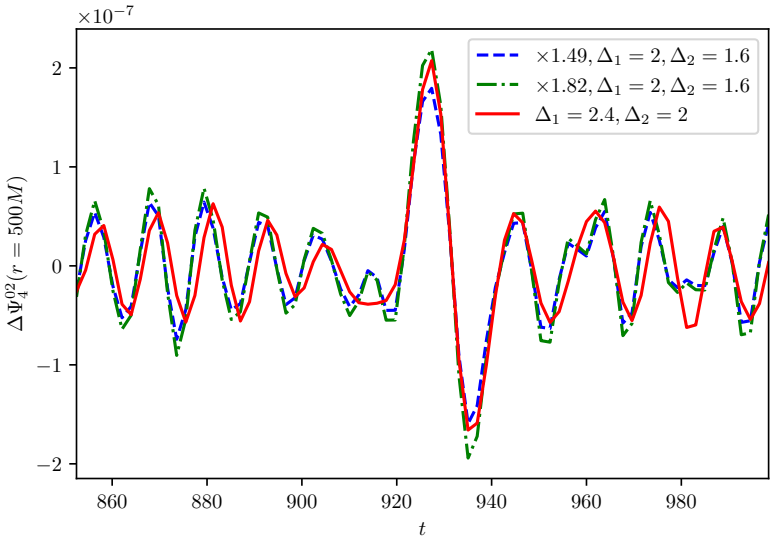

Figure 7.8: **Top:** The analysis of convergence for the $l = 0$, $m = 2$ multipole of Ψ_4, which was extracted at $r = 400M$, is presented. The blue line represents the expected result for a second-order convergence with a value of $Q_2 = 1.15$, while the green line illustrates the expected result for a fourth-order convergence, identified by $Q_4 = 1.53$. **Bottom:** The $l = 0$, $m = 2$ multipole of Ψ_4. The time interpolation order of Carpet is of the 2th order, whereas Multiple Thorn, which we employed to extract Ψ_4^{02}, utilizes a 3rd order interpolation order. Consequently, we anticipate that the convergence order of Ψ_4^{02} will land between these two values—namely, the 2rd and 3th orders.

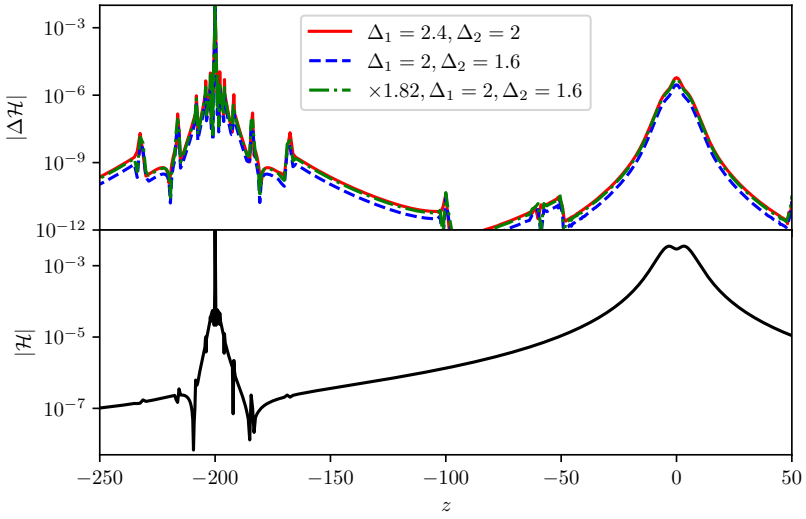

Figure 7.9: **Top:** Convergence of the Hamiltonian constraint violation at $t = 0$ for `IB`. The green line is multiplied by $Q_4 = 1.70$, the expected factor for fourth-order convergence. **Bottom:** We employ a technique known as *Richardson extrapolation* to derive the value of the Hamiltonian constraint as $\Delta \to 0$.

the convergence that aligns with the finite difference scheme that was implemented, the top panel of Fig. 7.9 shows that the violation of the Hamiltonian constraint exhibits fourth-order convergence.

To ensure that constraint violations do not increase over time, we track the evolution of the ℓ^2-norm of these violations, as shown in Fig. 7.10. Fig. 7.11 shows that the apparent horizon is consistently covered by finest level of the grid in Run `IB`, which demonstrates that Carpet tracks the grid structure effectively.

7.3 CONCLUSION

We have performed simulations involving BHs and SBSs, with length ratios as large as ~ 35. Our objective is to investigate the interaction between bosonic structures with self-interaction, which could potentially represent dark matter, and BHs, as well as to determine the dynamical friction or accretion they induce on the BHs. We find that the results are very similar to those obtained in Ref. [40], even for a more compact SBS. The presented results in this study, combined with those in with Ref. [40], suggest that if a scalar field with self-interaction is a good model for describing dark matter, then the emergence of gravitational atoms will be very common in astrophysical environments, and thus possible to be detected by detectors [257]. As we expected, a gravitational atom comes into existence after collision, characterized by a massive BH surrounded by a quasi-bound state of the scalar field, known as the SBS remnant. This differs from the ones in Ref. [258, 259],

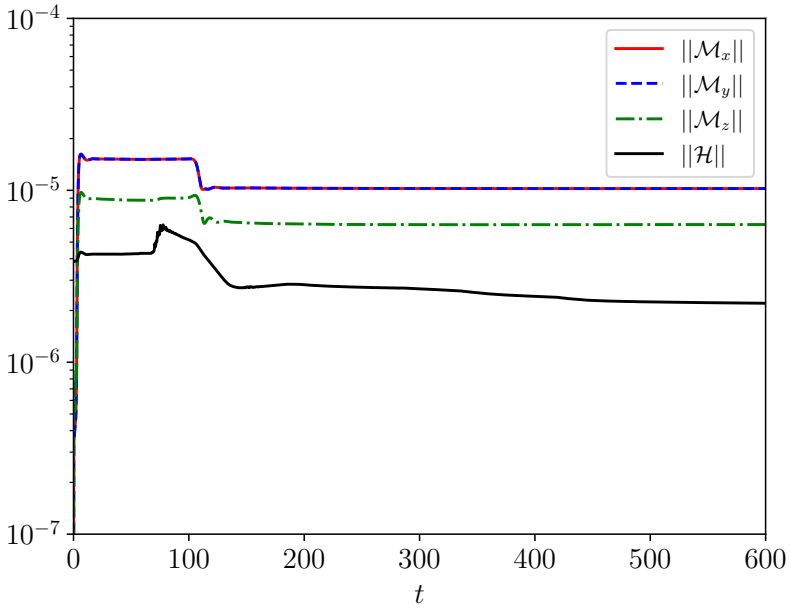

Figure 7.10: Violation of the Hamiltonian and momentum constraints as functions of time for run `IB`.

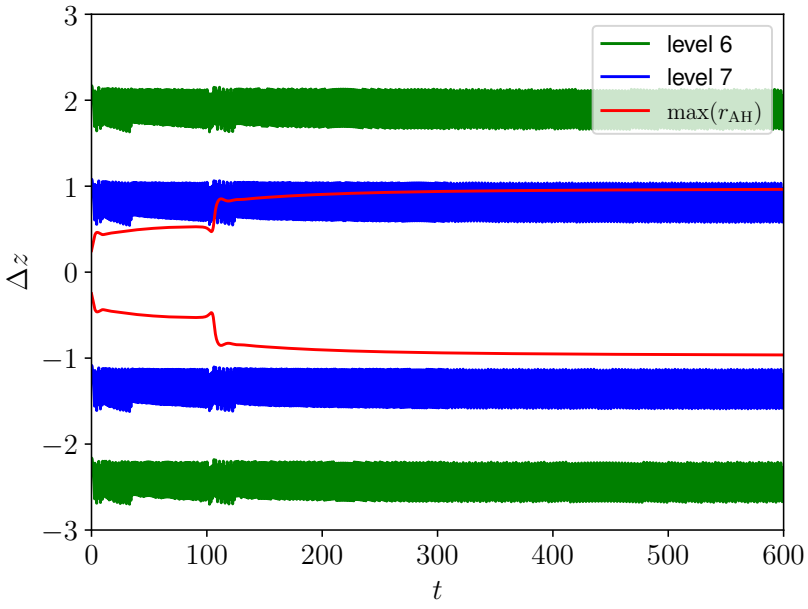

Figure 7.11: Difference in the z direction between the boundary of the two finest refinement levels and the location of the BH puncture. The red line indicates the maximum apparent horizon radius of the BH.

which are primarily mixed-state solutions of the Schrödinger-Poisson system including spherical and dipolar components. Given that the oscillation period of the BH located at the center of the SBS is already close to the test particle limit, we do not expect any new phenomena to emerge until we reach extremely high length ratios, such as intermediate or even extreme mass ratios. However, as we discussed in the introduction, the length ratio of solitonic cores formed by relativistic fuzzy dark matter and astrophysical BHs would be at least on the order of 10^6, representing extreme mass ratio systems. Simulating such systems with our current computational infrastructure is not possible. In all of our scenarios, we focus on a specific SBS, illustrated in Fig. 7.1. However, we anticipate that our findings will be similar for other SBS configurations with similar compactness to our present cases.

Part IV

OBSERVATIONAL PROBES OF GRAVITATIONAL WAVES

8

LATE-TIME TAILS IN DYNAMICAL SPACETIMES

8.1 INTRODUCTION

GR is our ultimate description of the gravitational interaction. It contains, as a mathematical solution, perhaps the most interesting and bizarre object known to humankind: BHs [52, 260, 261]. Two powerful results highlight the role of BHs in our understanding of nature and on their potential to uncover new laws of physics: i. the most general vacuum BH solution belongs to the Kerr family [262–264]; ii. BHs harbour spacetime singularities, where the known laws of physics break down [50, 265]. The assertion that all singularities are hidden from us is so remarkable that any observational evidence for or against it is highly sought for.

The advent of gravitational-wave astronomy harnessed access to information from the coalescence of two BHs, opening new exciting ways to test gravity in its strong-field and dynamical regime. A key aspect involves understanding the full gravitational waveform, including its behavior long after the initial merger burst. One relevant question concerns the approach to the final state: if there is a stationary state and it is well described by the Kerr family, how is it approached? How does the spacetime shed its multipolar structure when approaching a stationary BH state? Insight into this problem was provided by linearizing the field equations. At late times, BHs relax ("ring down") in a series of exponentially damped sinusoids, so-called quasinormal modes [88], followed by an inverse power-law decay with time, Price "tails" [44, 45, 266, 267]. This chapter focuses on these late-time tails as a specific probe derived directly from the gravitational wave signal. For generic initial data of multipolar structure described by a spherical harmonic of angular number ℓ, a massless field in a non-spinning BH background decays at fixed spatial position as $\Phi \sim t^{-p}$, $p = 2\ell + 3$ at very late times [44]. Such behavior arises from a branch-cut in the Green's function, or equivalently from large-radius scattering, and is observed in linearized analysis of scattering experiments, stellar collapse or point particle evolutions in BH backgrounds [45, 268, 269]. We term such decay "Initial Data-led Tails" (IDT). In numerical experiments, power-law tails are suppressed relative to the ringdown stage, hence they are very challenging to observe. Nevertheless, they dictate how fluctuations behave at late times and play a crucial role in foundational issues such as strong cosmic censorship [120, 270–272].

It has recently been observed in linear and nonlinear simulations of eccentric coalescences (see Fig. 19 in Ref. [273] and Fig. 1 in Ref. [274]) that the ringdown stage can be much shorter than previously thought, and very soon dominated by large amplitude transients which decay slower than IDTs (reporting fall-offs at null infinity slower than the asymptotic Price value at intermediate times). This behavior is unexpected, and exciting, as it means that large-amplitude post-ringdown signals might be detected with upcoming experiments, leading to new tests of Einstein equations with gravitational waves. If such a decay really describes the long-term behavior of relaxing BH spacetimes, it also means that our understanding of final state problem (how does one get to the final Kerr state) is incomplete; should such a decay also be present in cosmological backgrounds, then there are also important consequences for strong cosmic censorship.

We see three possibilities to circumvent Price's results: a) the effect is linear but triggered by the motion of sources in the BH vicinity, something not taken into account in all previous asymptotic analyses, which focused on the vacuum (and sourceless) linearized equations. As we will show, source-driven tails—SoDTs—do indeed exist, and depend on the source spatial distribution; b) the effect is nonlinear in nature. Such a possibility was raised in the past in the context of toy models [275]. Here we show, in the context of second-order perturbation theory, that second order tails exist and may dominate over linear ones, yet are weaker than predicted [275]; c) the effect is only a transient, possibly triggered by initial conditions. To understand the context of these potential new signals, we first review the established understanding of late-time behavior.

8.2 KNOWN RESULTS FOR LINEAR FLUCTUATIONS

To place the context, we start by briefly summarizing the main results on the late-time decay (IDTs) of massless fields in BH backgrounds. We focus on non-spinning BHs.

Linearized fluctuations of BH spacetimes seem to be well understood. For a Schwarzschild BH of mass M in standard coordinates, the evolution of these variables is governed by the wave equation [276–280] (x ranges from $]-\infty,+\infty[$)

$$\partial_x^2\Phi - \partial_t^2\Phi - V\Phi = \mathcal{S}\,. \tag{8.1}$$

Here Φ denotes a gauge-invariant combination of metric variables. These are expanded in tensor spherical harmonics of indices ℓ, m and decomposed in two different sets, so-called Regge-Wheeler or axial and Zerilli or polar. The tortoise coordinate is defined as

$$x = r + 2M\log(r/(2M) - 1)\,, \tag{8.2}$$

and the potentials $V = V_{\rm Z}$ or $V = V_{\rm RW}$ are given by

$$\begin{aligned} V_{\rm Z} &= f\left[\frac{\ell(\ell+1)}{r^2} - \frac{6M}{r^3}\frac{r^2\lambda(\lambda+2)+3M(r-M)}{(r\lambda+3M)^2}\right], \\ V_{\rm RW} &= f\left[\frac{\ell(\ell+1)}{r^2} - \frac{6M}{r^3}\right], \end{aligned} \tag{8.3}$$

where $\lambda = (\ell-1)(\ell+2)/2$, and $f = 1-2M/r$. The source term $\mathcal{S}$ encapsulates information about possible matter exciting the fluctuations Φ. For other massless fields, a similar wave equation describes all radiative degrees of freedom, with an effective potential $V_{\rm RW} = f\left[\frac{\ell(\ell+1)}{r^2} - \frac{2(1-s^2)M}{r^3}\right]$, with $s = 0, 1$ for scalar or electromagnetic fields, respectively. We will use scalar fields as toy models in some of our discussions.

In the absence of a source, the late time decay of generic massless fluctuations at fixed spatial position and asymptotically late times, corresponding to solutions of the linear wave equation, is governed by Price's law [44, 45, 266, 267],

$$\Phi \sim t^{-p}\,. \tag{8.4}$$

This behavior is dictated by a branch cut at zero frequency [266, 281, 282]. For generic initial data ($\Phi(t=0) \neq 0, \partial_t\Phi(t=0) \neq 0$) of compact support then $p = 2\ell+3$. If initial data is of compact support and initially static ($\partial_t\Phi(t=0) = 0$) then $p = 2\ell+4$ [283, 284]. For static initial data but non-compact support $p = 2\ell+2$. As a special example, a late-time decay t^{-3}, was proven to describe the asymptotics of a self-gravitating scalar field, with compact-support initial conditions [285].

In the presence of forcing terms, like matter moving in the BH exterior, the source $\mathcal{S}$ in (8.1) is nonzero. Its effect on possible late-time behavior has hardly been explored. However, when the full set of Einstein equations is expanded to second order around a fixed BH background, then second order metric quantities obey a similar equation, sourced by first order quantities. There are arguments suggesting that these lead to nontrivial power-law decay at late times [275]. Thus, here we focus on precisely the class of equations (8.1), in BH spacetimes.

8.3 INITIAL AND SOURCE-DRIVEN TAILS

Building on previous work [283, 284, 286], we develop a two-parameter perturbative expansion to estimate the asymptotic decay of the fields in the presence of sources. Details are given in Supplemental Material of Ref. [46]. Consider the wave-like equation describing massless field evolutions in a spherically symmetric BH spacetime, written in double null coordinates (u, v),

$$-4\partial^2_{uv}\Phi = V\Phi + \alpha\mathcal{S}\,, \tag{8.5}$$

where $V = V(x)$ is an effective potential that depends only on the tortoise coordinate $x \in]-\infty, +\infty[$; α is a book-keeping parameter

that controls the source $\mathcal{S}$. Since the background has a Killing vector $T = (1/2)(\partial_u + \partial_v)$, the potential is a function of $x = (v-u)/2$ [45]. We decompose the potential into a truncated centrifugal potential barrier, V_0, and a perturbation δV,

$$V = V_0 + \varepsilon \delta V \,, \tag{8.6}$$

with

$$V_0 = \begin{cases} \dfrac{\ell(\ell+1)}{x^2} \,, & x \geq x_0 \\ 0 \,, & x < x_0 \end{cases} \,. \tag{8.7}$$

Here, x_0 characterizes wave scattering and is of the order of the light ring radius, whereas ε is a small book-keeping parameter. We consider[1]

$$\delta V = x^{-\rho} \,, \tag{8.8}$$

with $\rho = 3, 4, 5, \cdots$. The correction δV and the source $\mathcal{S}$ are responsible for the appearance of late-time tails, which we now study. It is known that a branch cut in the Green's function in the complex frequency plane is a generic feature if δV tends to zero asymptotically slower than an exponential [281, 282]. Consider Φ in a two-parameter perturbative expansion,

$$\Phi = \Phi^{(0,0)} + \varepsilon \Phi^{(1,0)} + \alpha \Phi^{(0,1)} + \alpha\varepsilon \Phi^{(1,1)} + \dots \,. \tag{8.9}$$

For $\alpha = 0$ this expansion gives a good description of the late-time behavior [284]. Clearly, $\Phi^{(0,0)}$ contains the direct propagation of the initial conditions through the centrifugal barrier (flat space, if $\ell = 0$).

In summary, we find the following. In the absence of a source (see also footnote 2)

$$\Phi^{(1,0)}_{\mathcal{I}^+}(u) \sim u^{1-\rho-\ell} \,, \qquad \Phi^{(1,0)} \sim t^{-\rho-2\ell} \,, \quad t \gg x \,. \tag{8.10}$$

For $\rho = 3$, we recover Price's law [44].[2]

Sources of the form (or their extended version, see Supplemental Material of Ref. [46])

$$\mathcal{S} = \frac{\delta(x - x_s - U_s t)}{x^\beta} \,, \quad \beta \geq 0 \,, \tag{8.11}$$

where U_s ($|U_s| \leq 1$) is a source velocity, are physically interesting, as they describe compact objects moving in the vicinity of BHs, plunging ($U_s < 0$) or moving outwards ($U_s > 0$). Outward motion is a good prototype for gamma-ray bursts [287], or to mimic eccentric motion where long-lived transients have been observed [273, 274]. We find,

1 In a spacetime of mass M, one can expand $r = x - 2M \log x + 4M^2/x(1+\log x) + \dots$. For massless fields, $\rho = 3$. One can extend the analysis to $\delta V = x^{-\rho} \log x$ [281, 282].

2 We are mostly interested in waves at $t \gg r =$ constant and large. One can also use null coordinates and focus on $\mathcal{I}^+$ ($v \to \infty$ at constant u). For $\Phi \sim t^{-m}$ then $\Phi \sim u^{-m+\ell+1}$ at $\mathcal{I}^+$ [44, 286].

i) for outward-directed sources and $\beta \leq \ell + 2$ with $0 < U_s < 1$, SoDTs of the form

$$\Phi^{(0,1)}_{\mathcal{I}^+,0<U_s<1} \sim u^{1-\beta}\,, \quad \Phi^{(0,1)}_{0<U_s<1} \sim t^{-\beta-\ell}, \quad t \gg x\,. \tag{8.12}$$

ii) for outward-directed sources and $\beta \geq \ell + 3$ with $0 < U_s \leq 1$, SoDTs (8.12) are generated but the late-time behavior is dominated by the IDTs, Eq. (8.10).

iii) for outward-directed sources of $\beta = 0, 1$ or $\beta = \ell + 2$ with $U_s = 1$, SoDTs of the form

$$\Phi^{(0,1)}_{\mathcal{I}^+,U_s=1} \sim u^{1-\beta}\,, \quad \Phi^{(0,1)}_{U_s=1} \sim t^{-\beta-\ell}, \quad t \gg x\,, \tag{8.13}$$

but when $2 \leq \beta \leq \ell + 1$ for $\ell \geq 1$,

$$\Phi^{(0,1)}_{\mathcal{I}^+,U_s=1} \sim u^{-\beta}\,, \quad \Phi^{(0,1)}_{U_s=1} \sim t^{-\beta-\ell-1}, \quad t \gg x\,. \tag{8.14}$$

iv) in the presence of the inward-directed sources with $-1 \leq U_s < 0$, no SoDTs appear at late times. The late-time behavior is dominated by IDTs (8.10).

Problem (8.5) can describe a linearized setting with pointlike masses, or a nonlinear problem expanded to second order. Our analytical results therefore predict a nontrivial late-time decay, which can be source-dominated. The following explores the same problem, but from a numerical perspective, confirming our predictions, both for pointlike sources and for sources appropriate for the second-order expansion of the Einstein equations, thus establising our results in the nonlinear regime.

8.4 NUMERICAL PROCEDURE

We used different numerical routines to obtain the results in the main text, as a way to validate our results independently. Our first code is a time-domain solver with a two-step Lax-Wendroff integrator with second-order finite differences, which has been thoroughly described and validated in Refs. [288–292]. To achieve the necessary precision for the study of tails, we employ quadrupole floating point precision. Some of the results are extracted at null infinity, which is achieved by a hyperboloidal compactification of the spatial coordinate, with the outer boundary of the compactified domain corresponding to null infinity $\mathcal{I}^+$.

Another code employs an 8th-order finite difference method for spatial discretization, the canonical Runge-Kutta 4th-order method for time integration and quadruple-precision floating-point. We use the outflow boundary condition as proposed by Ref. [293], placing it distant from the region where we extract the data to mitigate the impact of an imperfect boundary condition.

We will often work with pointlike particles as our radiation source. They are represented by Dirac-delta distributions localized around the spatial location of the particle at a given instant, $x_{\rm p}(t)$. We approximate the Dirac-deltas with narrow Gaussian distributions

$$\delta(x - x_{\rm p}(t)) = \frac{\exp\left[-(x - x_{\rm p}(t))^2/(2\lambda_{\rm p}^2)\right]}{\sqrt{2\pi}\lambda_{\rm p}}\,, \tag{8.15}$$

where $\lambda_{\rm p}$ is sufficiently small to ensure numerical convergence as $\lambda_{\rm p} \to 0$. We take $\lambda_{\rm p} \approx 4{\rm d}x$, where ${\rm d}x$ is the grid discretization step [294]. Typically, we use ${\rm d}x \lesssim 0.05$.

Throughout this work, we use three sets of initial data. (i) Static initial data (s), which corresponds to a Gaussian localized at some initial radius x_I

$$\phi_{\rm s}(0,x) = \exp\left(-\frac{(x-x_I)^2}{2\sigma^2}\right), \quad \partial_t\phi_{\rm s}(0,x) = 0\,, \tag{8.16}$$

where σ controls the width of the pulse. (ii) Non-static/generic (g) initial data of the form

$$\phi_{\rm g}(0,x) = 0\,, \quad \partial_t\phi_{\rm g}(0,x) = \exp\left(-\frac{(x-x_I)^2}{2\sigma^2}\right). \tag{8.17}$$

(iii) Zero initial data for which $\phi(0,x) = \partial_t\phi(0,x) = 0$. We have checked that all types of initial data listed above are in excellent agreement with the analytical predictions for tails of the homogeneous Zerilli equation.

The main quantity extracted from numerical simulations is the local decay rate $p = p(t)$, which we evaluate as

$$p = -t\partial_t \ln|\phi|\,, \tag{8.18}$$

such that p is a constant for a field $\Phi \sim t^{-p}$.

8.5 NUMERICAL RESULTS I: POINTLIKE OBJECTS AROUND A BH

Consider now a $3+1$ problem on a BH background. We focus on a scalar field, sourced by a pointlike charge of the form:

$$\nabla^a\nabla_a\Phi = \sum_{\ell,m}\frac{\delta(x-x_s-U_st)}{r^{\beta+1}}Y_{\ell m}\,, \tag{8.19}$$

where $Y_{\ell m}$ are standard spherical harmonics. We take the ansatz $\Phi = \phi(t,r)Y_{\ell m}/r$ and find,

$$\partial_t^2\phi - \partial_x^2\phi + f\frac{rf'+\ell(\ell+1)}{r^2}\phi + \frac{f\delta(x-x_s-U_st)}{r^\beta} = 0\,, \tag{8.20}$$

with $f = 1-2M/r$ and the tortoise coordinate x defined in terms of the coordinate r via ${\rm d}r/{\rm d}x = f$. The peculiar choice of the power $(\beta+1)$ in (8.19) is made such that β in (8.20) is the curved space analog of the 1+1 source (8.11).

As apparent in Fig. 8.1, inward-moving sources excite BH ringdown, a stage which subsequently gives rise to Price tails (8.10). On the other hand, outward-moving sources give rise to SoDTs (8.12), which are longer lived (for $\beta < \ell+3$) than Price tails. The results concern $U_s = \pm 0.5$, but the outcome is qualitatively the same for other velocities and for Gaussian widths which are orders of magnitude larger. At late times and for $|U_s| < 1$, we obtain at finite radii [295]

$$\begin{aligned} \Phi &\sim t^{-\beta-\ell}, \quad 0 < U_s < 1 \quad \& \quad \beta \leq \ell+2\,, \\ \Phi &\sim t^{-3-2\ell}, \quad \text{otherwise} \end{aligned} \tag{8.21}$$

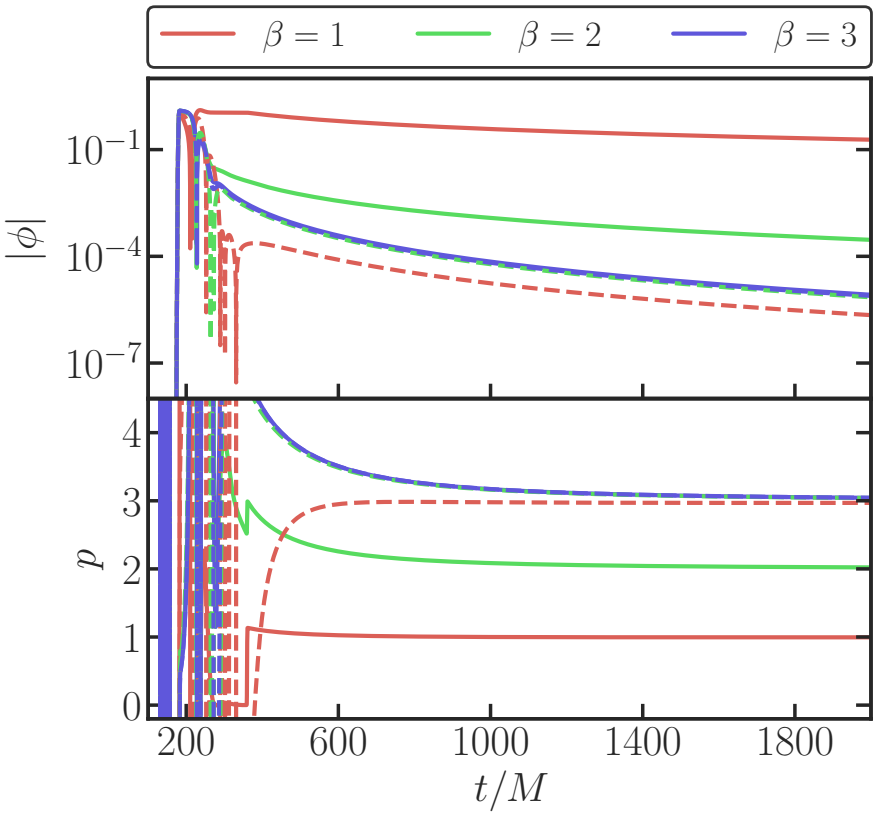

Figure 8.1: Scattering of a scalar field ($\ell = 0$) in a Schwarzschild background, Eq. (8.20) with $U_s = \pm 0.5$ and non-static initial data $\partial_t \Phi \neq 0$ (see Section 8.4). Source is initialized at $x_s = 20M$, ϕ is extracted at $x_{\rm ext} = 200M$. Solid (dashed) lines denote outward (inward) motion. The power-law is independent on initial data for $U_s < 1$, and agrees with prediction (8.12). Throughout this work, the exponent p is calculated via $p = -t\partial_t \ln |\phi|$. Steep jumps in outward motion occur after source passage (see Section 8.4).

in perfect agreement with the analytical predictions (8.12). All the results we discuss were also measured at null infinity to obey the relation in footnote 2. For $\beta \geq \ell + 3$, SoDTs are also excited (according to our analytical results) but are subdominant with respect to IDTs. In agreement with analytical predictions, we find that inwards-directed sources only excite IDTs. It is worth mentioning that *before* the particle passes the observer, for some regimes—specially low U_s—we find still a power-law behavior, but now of the form, $\Phi \sim t^{1-\beta+\ell}$, for $t < (x - x_s)/U_s$.

The above results are independent of velocity, for $|U_s| < 1$, and of initial conditions. For an *inwards* travelling source with $U_s = -1$, we find Price tails in all cases, i.e. $\Phi \sim t^{-3-2\ell}$. On the other hand, for an *outwards* travelling source ($U_s = 1$) [295]

$$\begin{aligned} \Phi &\sim t^{-\beta-\ell}, \quad \text{for} \quad \beta = 0, 1\,, \\ \Phi &\sim t^{-2-2\ell}, \quad \text{for} \quad 2 \leq \beta \leq \ell + 2\,, \\ \Phi &\sim t^{-3-2\ell}, \quad \text{otherwise}\,. \end{aligned} \tag{8.22}$$

(the power p at intermediate times is sensitive to the initial location x_s of the source and to its width; we start the particle close to the BH ($x_s < 0$) to suppress "junk radiation" which could excite IDTs stronger than SoDTs).

The empirical, numerical result disagrees with analytical predictions (8.13)–(8.14) for $2 \leq \beta \leq \ell+2$. We attribute this to the fact that $\Phi^{(0,1)}$ relies on the perturbative expansion (8.9), not the exact problem (8.20), missing some properties of Φ.

We can repeat the numerical experiment with a realistic setup: a pointlike mass following a radial geodesic on Schwarzschild background. The particle sources GWs which are governed by the Zerilli equation (Section 8.2, Section 8.4 and Refs. [292, 296, 297]). We use vanishing initial data. Therefore, we expect to recover—and we do—the results of the previous section for $\beta = 0$ for massive particles (8.21), and $\beta = 2, U_s = 1$ (8.22) for massless particles. The precise signal and power is shown for outward null motion in Fig. 8.2. Inward motion yields the expected IDTs.

Having examined linear effects with point sources, we now turn to nonlinear effects arising from second-order perturbations.

8.6 SECOND ORDER PERTURBATIONS

For the numerical simulation of the second order equation (15), we use the hyperboloidal coordinates $\{\tau, \rho, \theta, \varphi\}$ with minimal gauge [298–300], where the coordinate transformation from standard coordinates is given by

$$\frac{t}{4M} = \tau - \frac{1}{2}\left(\ln\rho + \ln(1-\rho) - \frac{1}{\rho}\right)\,, \tag{8.23}$$

$$\frac{x}{4M} = \frac{1}{2}\left(\frac{1}{\rho} + \ln(1-\rho) - \ln\rho\right)\,. \tag{8.24}$$

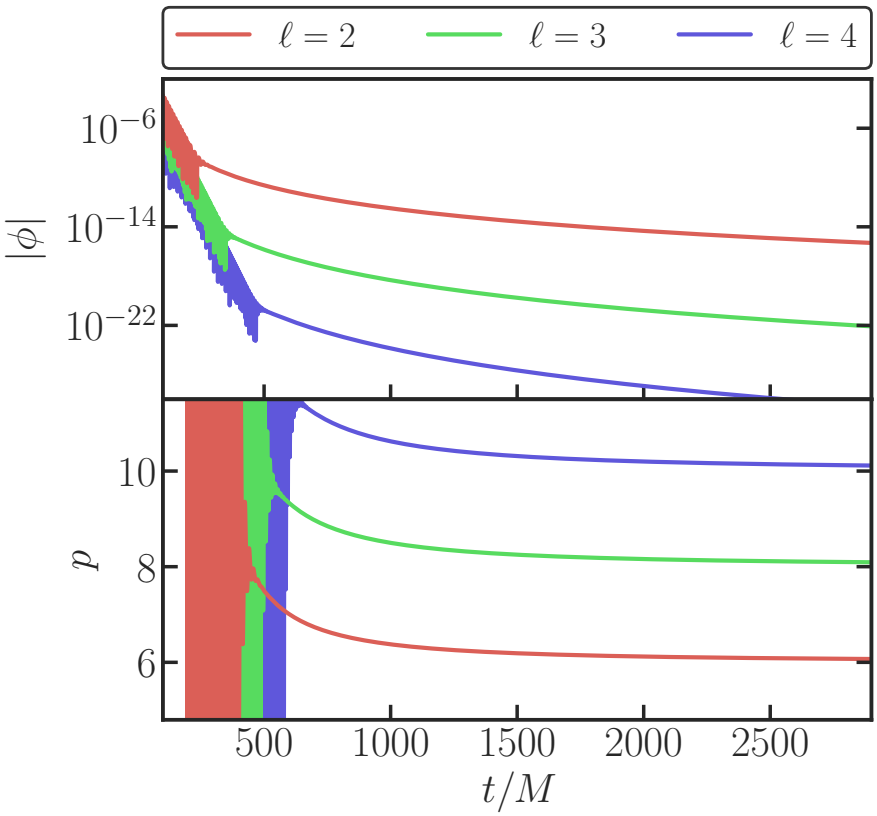

Figure 8.2: Tails for massless particle on outgoing radial geodesics on a Schwarzschild background. We use $\Phi(0,x) = \partial_t\Phi(0,x) = 0$. Particle is initialized at $x_s = -20M$, ϕ extracted at $x_{\rm ext} = 200M$. The asymptotic behavior agrees with (8.22) for $\beta = 2$.

We will use $p = -\tau\partial_\tau \ln|\Psi|$ in this section. To allow a stable evolution with larger time-steps, we introduce a new momentum variable ${}^{\{n\}}\Pi = \partial_\tau {}^{\{n\}}\Psi - (\rho-1)\partial_\rho {}^{\{n\}}\Psi$. We use the following types of initial data for first order polar perturbation with parameters $\rho_0 = 0.6$ and $\sigma^2 = 1/1000$: Approximately Ingoing:

$$ {}^{\{1\}}\Psi(\tau = 0, \rho) = \exp\left(-\frac{(\rho-\rho_0)^2}{2\sigma^2}\right), \tag{8.25} $$

$$ {}^{\{1\}}\Pi(\tau = 0, \rho) = (\rho+1)^{-1}\partial_\rho {}^{\{1\}}\Psi(\tau = 0, \rho)\,. \tag{8.26} $$

Approximately Outgoing:

$$ {}^{\{1\}}\Psi(\tau = 0, \rho) = \exp\left(-\frac{(\rho-\rho_0)^2}{2\sigma^2}\right), \tag{8.27} $$

$$ {}^{\{1\}}\Pi(\tau = 0, \rho) = 0\,. \tag{8.28} $$

For simplicity, we set the initial data of the second-order polar perturbation to zero, but we checked that its power law doesn't depend on the initial data.

$$ {}^{\{2\}}\Psi(\tau = 0, \rho) = 0\,, \qquad {}^{\{2\}}\Pi(\tau = 0, \rho) = 0\,. \tag{8.29} $$

To resolve the late-time tails, high-accuracy spatial discretization methods such as high-order finite differences or the pseudospectral method are required. Here, we use the Chebyshev pseudo-spectral methods for spatial discretization and the canonical Runge-Kutta 4th order method for time integration. High-precision floating-point numbers are also required to achieve the necessary precision for the study of late-time tails of second-order perturbation. For the final results in this section, we use $N = 450$ for Chebyshev pseudo-spectral methods, and integrate the equation using a fixed step $\Delta\tau = 0.0005$, with the numerical precision being around 210 bits.

8.7 NUMERICAL RESULTS II: SECOND ORDER TAILS

Consider now the full nonlinear Einstein equations. A perturbative expansion of the field equations around a background metric can be written as $\tilde{g}_{\mu\nu} = g_{\mu\nu} + \sum_{n=1}^{\infty} \frac{\varepsilon^n}{n!} {}^{\{n\}}h_{\mu\nu}$ [276–280, 302–304]. For a vacuum Schwarzschild background spacetime, ${}^{\{n\}}h_{\mu\nu}$ can be reconstructed from the gauge-invariant generalisation of the Zerilli and Regge-Wheeler master variables [302–306]. We focus on the Zerilli sector, governed by,

$$ -\partial_t^2 {}^{\{2\}}\Psi + \partial_x^2 {}^{\{2\}}\Psi - V_Z {}^{\{2\}}\Psi = {}^{\{2\}}\mathcal{S}_\Psi\,, \tag{8.30} $$

with the potentials given in Equation (8.3).

The source term of order n, ${}^{\{n\}}\mathcal{S}_\Psi$, depends on the metric perturbations up to order $n-1$, with the first order sources being identically zero [304–306]. We focus on the expansion up to and including second order, $n = 2$. Source terms decay as $\mathcal{O}(1)/r^2$ at infinity [304, 306].

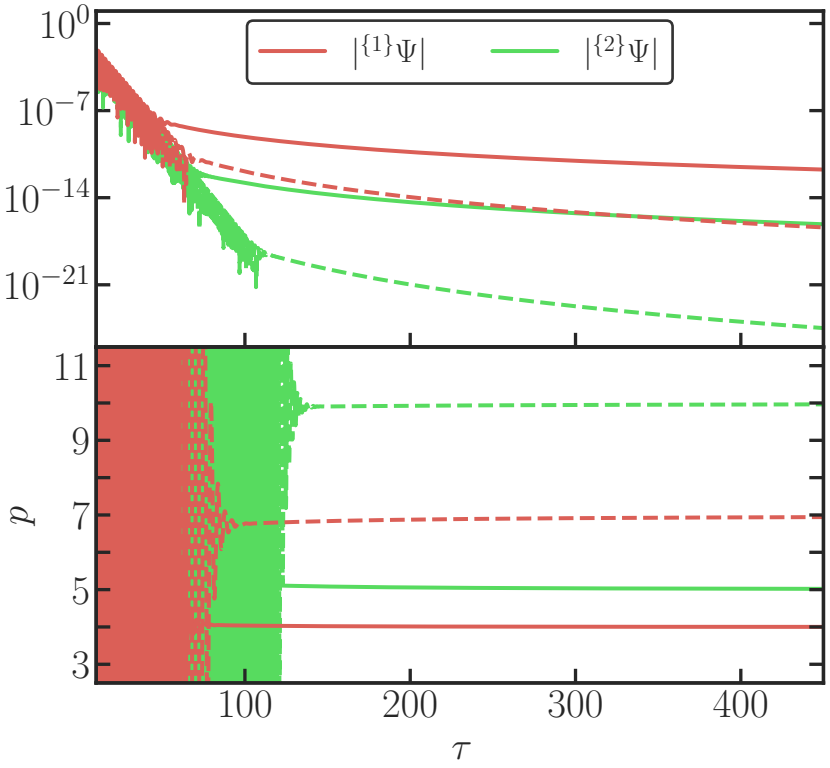

Figure 8.3: First-order ($\ell = m = 2$) (red line) and second-order polar gravitational perturbations ($\ell = m = 4$) (green line) sourced by self-coupling of the former. We use sources in Ref. [301] and evolve the equations with approximately ingoing initial data for first order perturbations, and zero initial data for second order quantities. Solid and dashed lines are extracted at future null infinity $\mathcal{I}^+$ and at $\rho_{\rm ext} \approx 0.1$, respectively. First order decays as Price tail, second order as (8.22).

Evolutions of second-order perturbations were carried out in the past [307], with a different purpose. We use a pseudospectral code, with hyperboloidal coordinates $\{\tau, \rho, \theta, \varphi\}$ in the minimal gauge [298–300]. Details on the numerical procedure and initial conditions for first order quantities are given in the Section 8.6.

Results for the evolution of Eq. (8.30) are shown in Fig. 8.3 for a $\ell = m = 4$ second order perturbation driven by the self-coupling of $\ell = m = 2$ quantities. With Prony methods [104], we find two families of QNMs [306, 308–310]. The first family belongs to potential-driven modes and are also part of the spectrum of first-order quantities. Our results are compatible with the linearized prediction (to 14 decimal digits or more). The second family are source-driven, whose frequencies are twice that of the first-order perturbations [305, 306, 308–313].

We find a power $p = 10$ for the decay at fixed spatial distance for this particular mode, which, given the fall-off of the source term ${}^{\{2\}}\mathcal{S}_\Psi$ at infinity ($\propto r^{-2}$), is consistent with the SoDT (8.22) [295]. These results are to the best of our knowledge the first accurate simulations of second order gravitational modes including late-time tails. The source term in Ref. [306] yields a power p which is consistently one unity less than that for the source in Ref. [304], since the master wavefunction of the former is, up to irrelevant factors, the time derivative of the latter. We show in the Section 8.8 that for this reason there must be special classes of initial data for which the late-time decay is consistently faster than that predicted by Price's law.

Our findings are consistent with those from nonlinear, spherically symmetric collapse simulations [285, 314, 315] (there are a few studies of dynamical spacetimes with no symmetries, but it is unclear whether they apply to GR [316–318]). Our results are in tension with claims in Ref. [275] (also Ref. [312]), which reports a decay t^{-2}. To further investigate this issue without being limited by the numerical accuracy of first-order quantities, we solved the following problem with an independent numerical routine,

$$\nabla^a \nabla_a \Phi = \sum_{\ell m} \frac{e^{-i\omega(t\pm x)} H(t \pm x)}{r^{\beta+1}} Y_{\ell m} \,, \tag{8.31}$$

with H the Heaviside function and $\omega = 0.5 - 0.1i$ (arbitrarily chosen). This source mimics a first-order ringdown waveform. Numerical results are again consistent with our previous findings: there are two distinct tails, depending on the sign in the exponent. For $\beta < 3$, we find results (8.22) for outward-moving sources and Price's law $\Phi \sim t^{-3-2\ell}$ for inward-moving sources (again, the analytical approach fails to capture all the features, we suspect because some properties of Φ are missing in $\Phi^{(0,1)}$).

Predictions [275, 312] of source-driven and nonlinear tails assumed that the effective potential decays asymptotically faster than the centrifugal barrier and using a (1+1)-dimensional Green's function. Such studies predicts a $1/t^2$ decay, slower than any IDT [275, 312]. Our results are consistent with this prediction only for $\ell = 0$ modes, where

the centrifugal barrier is absent and indeed the Green's function is 1+1 dimensional. In such toy models, the source term decays slower than the effective potential at large distances [275, 312]. We conjecture that this determines the asymptotic time behavior and that $p = \beta + \ell$ in such cases.

8.8 TAILS OF TIME DERIVATIVES

As previously stated, we explore special classes of initial data for which the late-time decay is consistently faster than that predicted by Price's law.

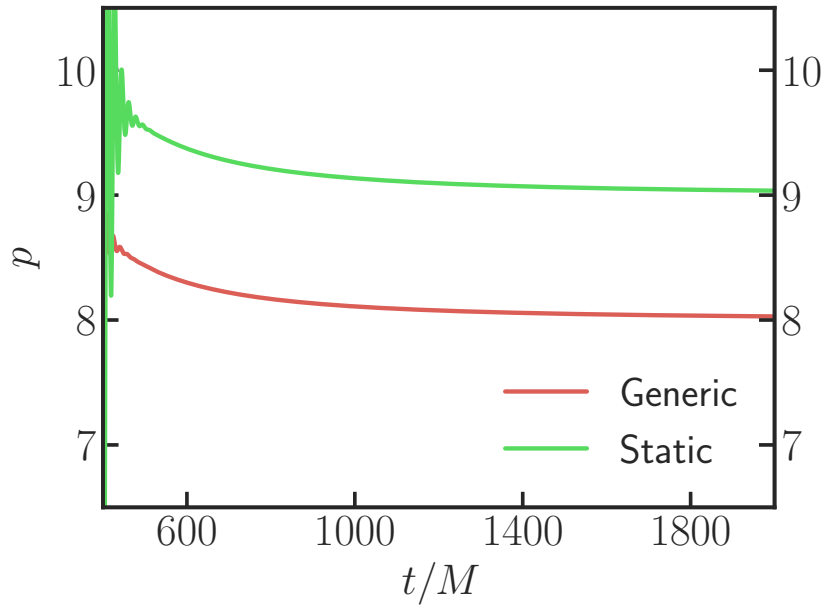

Figure 8.4: Power-law for the $\ell = 2$ solution of Eq. (8.32) with ${}^{\{2\}}\dot{\mathcal{S}}_\Psi = 0$, using initial data from Eq. (8.35). Red line corresponds to using Ψ_0 as defined in Eq. (8.17), green line to Ψ_0 as defined in Eq. (8.16). Data is extracted at $x = 100M$.

Suppose Ψ is the Zerilli wavefunction, obeying Zerilli's equation (15). Take a time derivative of that, to get

$$-\partial_t^2 X + \partial_x^2 X - V_Z X = {}^{\{2\}}\dot{\mathcal{S}}_\Psi \,, \tag{8.32}$$

where we defined $X = {}^{\{2\}}\dot{\Psi}$; dot is a time derivative. This can be done an arbitrary number of times, i.e., the $n-$th time derivative of the Zerilli wavefunction obeys the Zerilli equation. This looks like a contradiction: the n-th order derivative of the Zerilli wavefunction obeys the Zerilli equation, hence should have the same tails. However, the initial data is now

$$\begin{aligned} {}^{\{2\}}\Psi(t=0) &= \Psi_0(r)\,, \; {}^{\{2\}}\dot{\Psi}(t=0) = \dot{\Psi}_0\,, & (8.33)\\ X(t=0) &= \dot{\Psi}_0\,, \dot{X}(t=0) = \ddot{\Psi}_0\,. & (8.34) \end{aligned}$$

Thus, there are constraints that need to be satisfied if X is indeed the time derivative of the original master function. In particular, using the Zerilli equation we find

$$X(t=0) = \dot{\Psi}_0\,, \qquad \dot{X}(t=0) = \partial_x^2\Psi_0 - V_Z\Psi_0\,. \tag{8.35}$$

Our numerical results confirm that initial conditions (8.35) are indeed "special". Based on Price's results one would expect naively that they would produce tails with power $p = 2\ell + 3$ for generic initial data and $2\ell + 4$ for initially static data. We find, however—Fig. 8.4—that $p = 2\ell + 4$ and $p = 2\ell + 5$ respectively. Thus, there *are* special classes of initial data that escape Price's description, as had to be the case for consistency.

8.9 DISCUSSION

We have shown that distributional sources, such as those appropriate to describe pointlike objects, or even extended coherent sources, give rise to late-time power-law tails which can dominate over IDTs. These results are important as a point of principle, but could play a role in observations in the linearized context, for example for extreme-mass-ratio systems. For second-order corrections, our results establish the existence of tails which can dominate over linear ones, but which decay much faster than over-simplified toy models suggest [275, 312].

Nonlinear corrections to extreme-mass-ratio systems will also occur, but are suppressed by the mass ratio. However, there are consequences at *linear* order, due to the distributional character of the source. The high-amplitude post-ringdown signal observed in extreme-mass-ratio systems and for which there is evidence in numerical evolutions of binary mergers [273, 274] then begs the question of their origin. Since they are apparent in eccentric binaries only, we have also looked for imprints in toy models attempting to mimic eccentric binaries, such as $\nabla^a\nabla_a\Phi = \delta(x - x_s - U_s t - A\cos\Omega t)/r^{\beta+1}$, but for all plunging motions the asymptotic behavior of radiation at late times is governed by the IDT $t^{-(2\ell+3)}$. We were thus unable to reproduce the behavior reported in the literature, which requires a more specialised analysis.

Our results, summarized in Figs. 8.1–8.3 also suggest that the on-set of the tail occurs long after the start time of ringdown for plunging particles, and that in this case their magnitudes are suppressed by orders of magnitude relative to the main burst. However, for outgoing sources, tail magnitudes are not negligible, raising questions about detectability. We also note that our results are consistent with the literature. Timelike scattering of pointlike particles was predicted to give rise to a $1/u$ leading tail [319]. This result is consistent with our own numerical result for scattered particles. For ingoing sources, our results predict that the tail is suppressed, in line also with Ref. [319], which shows that if the final state is a single massive object and radiation – as in our ingoing or outgoing massless sources – the $1/u$ piece cancels out. This also provides consistency with Price's results and explains why tails for second

order perturbations decay faster than $1/u$, because these are massless sources, for which one would expect the cancellations to occur.

In classical mechanics and GR, the future is dictated by initial conditions. The reader might then wonder why we find an asymptotic behavior different from that derived from the evolution of generic initial conditions, for linearized equations. The reason is that compact sources, such as the ones we consider, arise as the evolution of initial data only if one includes extra, nonlinear interactions, in the theory. These have not been dealt with in Price's analysis.

Finally, the existence of SoDTs is not fundamentally tied to the existence of horizons nor to the asymptotic structure of the spacetime. Hence, one might suspect they exist in cosmological backgrounds of interest, like asymptotic de Sitter spacetimes. Our results show they exist in toy models with Pöschl-Teller effective potentials, which have no IDTs and which are a good proxy for Schwarzschild de Sitter spacetimes [320]. It would be an intriguing resolution to cosmic censorship violations if the very existence of matter would restore it [120, 272].

Beyond the intrinsic features of the gravitational waveform itself, the dynamic spacetime distortions during events like BH relaxation can also influence other messengers, such as light. The subsequent chapter explores this phenomenon through the lens of gravitational lensing.

9

DYNAMICAL LENSING DURING BLACK HOLE RINGDOWN

As discussed in the previous chapter, the relaxation of BHs following a merger generates a complex gravitational wave signal, including characteristic late-time tails. Complementary to studying the waveform itself, the dynamic spacetime curvature associated with these gravitational waves provides another observational probe: the lensing of light. One of the foundational tests of GR concerns the deflection of light by massive bodies [321–324], where the path of light rays is "bent" by mass-energy distorting the spacetime fabric. Similarly, travelling spacetime distortions like GWs can also bend light paths.

This chapter focuses specifically on the prospect of detecting *light* bending by the GWs emitted during the ringdown phase of a black hole, which would add an extra information channel on strong gravity, particularly in highly dynamic scenarios. This possibility was raised and studied by different authors in the weak field regime [325–329]. Our purpose here is to study light deflection near compact objects in highly dynamic spacetimes. In particular, we will study the appearance of a BH which is approaching a quiescent state via relaxation in its characteristic modes of oscillation, called QNMs. The relaxation stage is also referred to as ringdown stage, and is a generic late-time description of the coalescence of compact objects [88, 330]. Our results could describe stars on the background of a binary BH merger, or the appearance of a circumbinary accretion disk surrounding two merging compact objects.

9.1 RAY TRACING TOWARDS A RELAXING BLACK HOLE

A relaxing BH is well described by general relativistic first-order perturbation theory, where spacetime is expressed by small fluctuations away from the final, stationary state. Uniqueness results in GR suggest that the final state, to a good approximation, is a Kerr BH [264, 331, 332]. We thus take our relaxing BH spacetime, of mass M and angular momentum aM to be given by

$$g_{\mu\nu} = g^{(0)}_{\mu\nu} + h_{\mu\nu}\,, \tag{9.1}$$

where $g^{(0)}_{\mu\nu}$ is the Kerr metric (we will use Boyer-Lindquist (t, r, θ, ϕ) coordinates throughout [333]). The term $h_{\mu\nu}$ denotes first-order perturbations.

Instead of working directly with the metric perturbations $h_{\mu\nu}$, we consider instead curvature perturbations [47, 334]. These can be separated and decoupled and all the relevant information about radiative degrees of freedom is encapsulated in a master variable

$$\psi_s(t,r,\theta,\phi) = \frac{{}_sZ}{\sqrt{2\pi}}\,{}_sS(\theta)\,{}_sR(r)e^{-i\omega t+im\phi}\,. \tag{9.2}$$

The gravitational quantity of interest is $\Psi_4^{(1)} = \psi_{-2}(t,r,\theta,\phi)(r-ia\cos\theta)^{-4}$, the first-order perturbation of one of the Weyl scalars, which is directly related to the amplitude of GWs far from the source. Notation and conventions are shown in Section A.1. The function ${}_sS(\theta)$ is a spin-weighted spheroidal harmonic, while the radial Teukolsky function ${}_sR(r)$ obeys a homogeneous second-order differential equation. We fix its normalization by calculating energy fluxes at infinity, and comparing to numerical relativity results. Then, ${}_sZ$ controls the amplitude of the GW, by matching the ringdown stage to some physically generated process. The characteristic modes are found by imposing proper boundary conditions on ${}_sR(r)$, which selects only a discrete set of frequencies ω, the ringdown frequencies [88]. All the functions and quantities carry a dependence on angular numbers ℓ, m and a possible overtone number n [47, 88, 334]. For simplicity, we do not include these indices in the subscripts. A GW signal comprises a superposition of various modes, but the $\ell = |m| = 2$ dominates (so far it is the only one detected beyond any doubt). Additionally, we exclusively address the $n = 0$ mode, which lasts longer compared to the more rapidly decaying higher overtones. For similar reasons we neglect nonlinearities, which are of much smaller amplitude even for equal-mass mergers, and of shorter duration [308, 310]. For QNMs characterized by frequency ω and labeled by (ℓ, m, n), there exists a corresponding "mirror" mode with frequency $-\bar{\omega}$ and $(\ell, -m, n)$. In the final spin frame, these paired modes primarily represent GW emissions propagating in opposite directions along the spin axis [91, 335–337]. The observed waveform typically manifests as a superposition of these two distinct sets of modes. However, one of the paired modes may be less prominent due to weaker excitation [336, 338]. In the following analysis, we primarily focus on the $m = 2$ mode with $\mathrm{Re}(\omega) > 0$, which predominantly emits toward the southern hemisphere, as more general cases exhibit similar features, as discussed in Section 9.4.

Once ${}_{-2}R(r)$ is known, we reconstruct the metric fluctuation $h_{\mu\nu}$ following well-known prescriptions [339–341], summarized in Section A.2. We initiate the ringdown at $t = r_*$, where r_* denotes the tortoise radial coordinate, by applying a Heaviside-like filter to the perturbation, $h_{\mu\nu} \to H(t - r_*)\, h_{\mu\nu}$, along the light cone, with

$$H(t-r_*) = \frac{1}{2}\left(\tanh\frac{t-r_*}{\chi} + 1\right)\,. \tag{9.3}$$

In the following, we employ a relatively sharp truncation in the filter function $H(t - r_*)$, with $-\chi\mathrm{Im}(\omega) = 0.1$.

During the ringdown phase, a photon trajectory is influenced by the metric perturbations encountered along its path, governed by the geodesic equation:

$$\frac{\mathrm{d}^2 x^\mu}{\mathrm{d}\tau^2} + \Gamma^\mu{}_{\nu\rho} \frac{\mathrm{d}x^\nu}{\mathrm{d}\tau} \frac{\mathrm{d}x^\rho}{\mathrm{d}\tau} = 0\,, \tag{9.4}$$

where Γ denotes the Levi-Civita connection, and τ represents the proper time.

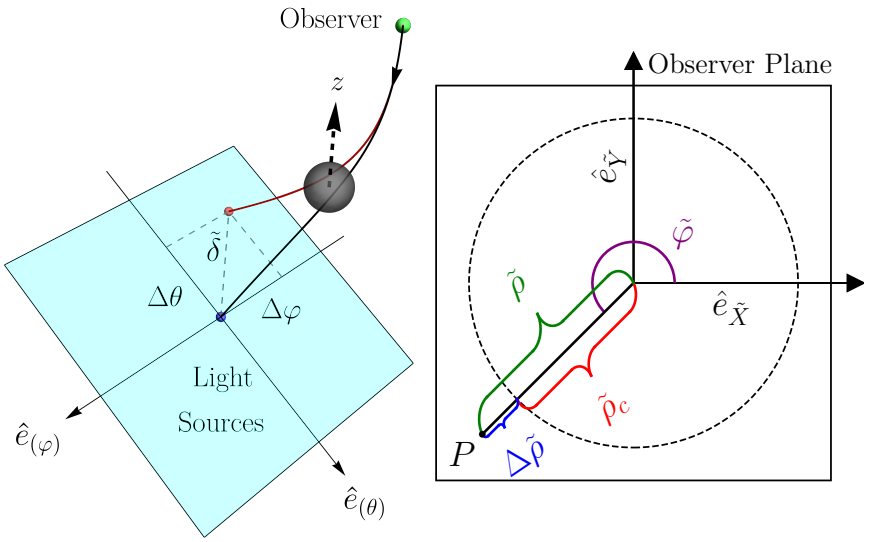

Figure 9.1: Schematic diagram of the coordinate system. **Left:** Illustration of a light ray originating from the observer (green point) and traced backward (black arrow) toward the BH, terminating at the celestial sphere plane at infinity (blue plane). The black and red lines represent the geodesics in unperturbed Kerr spacetime and those deflected by metric perturbations, respectively. The grand arc difference is denoted by $\tilde{\delta}$, with angular variations in the azimuthal and polar directions labeled as $\Delta\phi$ and $\Delta\theta$. **Right:** Diagram of the observer plane with polar coordinates $(\tilde{\rho}, \tilde{\varphi})$. The critical curve $\tilde{\rho}_c(\tilde{\varphi})$ is shown as a black contour, and the relative impact parameter is defined as $\Delta\tilde{\rho} \equiv \tilde{\rho} - \tilde{\rho}_c$.

To characterize the observable effects, it is essential to define the observer frame. In an unperturbed Kerr BH scenario, a zero angular momentum observer (ZAMO) frame is typically used [342]. However, in a dynamic spacetime, the ZAMO tetrads are neither orthogonal nor normalized. To rectify this, we apply a Gram-Schmidt orthogonalization process to establish a normalized, orthogonal tetrad basis derived from the ZAMO tetrads, as detailed in Section 9.2.1. Using this newly defined observer frame, we initiate geodesics towards the BH employ-

ing backward ray tracing. Here, each pixel on the observer plane, represented by coordinates $(\tilde{X}, \tilde{Y})$ [55, 343, 344], corresponds to photon momentum in this frame. The photon's 4-momentum in the dynamic spacetime $p^\mu \equiv \mathrm{d}x^\mu/\mathrm{d}\tau$ is then constructed from this orthogonal tetrad basis, similar to the procedure established in Kerr spacetime [345]. For convenience, we also introduce polar coordinates for the observer plane centered on the direction directly facing the BH in Kerr spacetime, denoted as $(\tilde{\rho}, \tilde{\varphi})$, where $\tilde{\rho}$ is the impact parameter and $\tilde{\varphi}$ is the angle.

Photon geodesics in the relaxing Kerr spacetime are then computed. We position an observer at $r_o = 10^9\, M$, confirming convergence of results at large r_o due to the decay of $h_{\mu\nu}$ amplitude as $1/r$ at greater distances. Notice that even though we employ backward ray tracing, photon propagation in the $+t$ direction still aims towards the observer, aligning with the GWs that co-propagate in the same direction upon departure from the BH.

The following section details the technical implementation of this backward ray tracing approach. We first define the observer's local reference frame in the perturbed spacetime and then discuss the coordinate systems and parameters used to trace the photon paths.

9.2 BACKWARD RAY TRACING

9.2.1 *Local oberver basis*

The observation of photons at any given point is dependent on the observer. For the case of a pure Kerr BH, ZAMOs are typically employed. In this section, we extend them to dynamically perturbed Kerr spacetime.

Within the Boyer-Lindquist coordinate system, a ZAMO frame can be chosen and expressed in terms of the coordinate basis $\{\partial_t, \partial_r, \partial_\theta, \partial_\phi\}$ [55, 342, 345, 346] as

$$\vec{z}^{\,\mu}_{(t)} = \frac{g_{\phi\phi}\partial_t - g_{\phi t}\partial_\phi}{\sqrt{g_{\phi\phi}\left(g_{\phi t}^2 - g_{\phi\phi}g_{tt}\right)}}\,,\ \vec{z}^{\,\mu}_{(r)} = \frac{\partial_r}{\sqrt{g_{rr}}}\,,\ \vec{z}^{\,\mu}_{(\theta)} = \frac{\partial_\theta}{\sqrt{g_{\theta\theta}}}\,,\ \vec{z}^{\,\mu}_{(\phi)} = \frac{\partial_\phi}{\sqrt{g_{\phi\phi}}}\,. \tag{9.5}$$

The observer basis $\vec{z}^{\,\nu}_{(\sigma)}$ has a Minkowski normalization

$$g^{(0)}_{\mu\nu}\vec{z}^{\,\mu}_{(\rho)}\vec{z}^{\,\nu}_{(\sigma)} = \eta_{(\rho)(\sigma)}\,, \tag{9.6}$$

with $\eta_{(\rho)(\sigma)} = \mathrm{diag}\{-1, 1, 1, 1\}$. Unlike the unperturbed case, Eq. (9.6) no longer holds when the unperturbed metric $g^{(0)}_{\mu\nu}$ is replaced by the perturbed metric $g_{\mu\nu}$. To address this issue, we employ a Gram-Schmidt orthogonalization process, using the chosen ZAMO tetrad $\vec{v}_\rho = \vec{z}^{\,\mu}_{(\rho)}$ as

the initial set of vectors. The Gram-Schmidt process can be expressed as

$$\begin{aligned}
\vec{u}_0 &= \vec{v}_0\,, \\
\vec{u}_1 &= \vec{v}_1 - \mathrm{proj}_{\vec{u}_0}(\vec{v}_1)\,, \\
\vec{u}_2 &= \vec{v}_2 - \mathrm{proj}_{\vec{u}_0}(\vec{v}_2) - \mathrm{proj}_{\vec{u}_1}(\vec{v}_2)\,, \\
\vec{u}_3 &= \vec{v}_3 - \mathrm{proj}_{\vec{u}_0}(\vec{v}_3) - \mathrm{proj}_{\vec{u}_1}(\vec{v}_3) - \mathrm{proj}_{\vec{u}_2}(\vec{v}_3)\,,
\end{aligned} \tag{9.7}$$

where the projection operator is defined as

$$\mathrm{proj}_{\vec{u}}\,\vec{v} = \frac{\langle \vec{u}, \vec{v} \rangle}{\langle \vec{u}, \vec{u} \rangle}\vec{u}\,, \tag{9.8}$$

with the inner product evaluated using the metric $g_{\mu\nu}$. The resulting orthonormalized tetrad, denoted as

$$\tilde{\vec{e}}^{\,\mu}_{(\rho)} = \frac{\vec{u}_\rho}{\sqrt{|\langle \vec{u}_\rho\,, \vec{u}_\rho \rangle|}} \tag{9.9}$$

satisfies the following condition

$$g_{\mu\nu}\tilde{\vec{e}}^{\,\mu}_{(\rho)}\tilde{\vec{e}}^{\,\nu}_{(\sigma)} = \eta_{(\rho)(\sigma)}\,. \tag{9.10}$$

9.2.2 *Impact Parameters*

In the image plane of the observer defined above, each photon is assigned Cartesian coordinates $(\tilde{X}, \tilde{Y})$, which represent its impact parameters. These coordinates are proportional to the photon's observation angles $(\tilde{\alpha}, \tilde{\beta})$. Here we follow a convention similar to Ref. [345], and define them as:

$$\tilde{X} \equiv -r\tilde{\beta}, \quad \tilde{Y} \equiv r\tilde{\alpha}\,. \tag{9.11}$$

Considering the geometry of photon detection, we can express the photon's 4-momentum in the observer's reference frame as follows (refer to Fig. 1 in Ref. [345]):

$$p^{(\phi)} = |\vec{P}|\sin\tilde{\beta}\cos\tilde{\alpha}\,,\; p^{(\theta)} = |\vec{P}|\sin\tilde{\alpha}\,,\; p^{(r)} = |\vec{P}|\cos\tilde{\beta}\cos\tilde{\alpha}\,, \tag{9.12}$$

where $|\vec{P}| = p^{(t)}$. From this, we can derive the photon's momentum using

$$p^{\mu} = \tilde{\vec{e}}^{\,\mu}_{(\sigma)}p^{(\sigma)}\,. \tag{9.13}$$

9.2.3 *Kerr–Schild coordinates*

To avoid the numerical problem when a photon gets too close to the pole in the BL coordinate system, we perform ray tracing in the Cartesian Kerr–Schild (KS) coordinate system $\{t_{\mathrm{KS}}, x, y, z\}$. The coordinate

transformations, which can be found in Ref. [347–349], are also reviewed in the following.

The Kerr metric in KS coordinates $\{t_{\rm KS}, x, y, z\}$ can be expressed as

$$\begin{aligned} g^{(0)}_{\mu\nu} &= \eta_{\mu\nu} + f k_\mu k_\nu \,, \\ f &= \frac{2Mr^3}{r^4 + a^2 z^2} \,, \; k_\mu = \left(1, \frac{rx + ay}{r^2 + a^2}, \frac{ry - ax}{r^2 + a^2}, \frac{z}{r}\right) \,, \end{aligned} \tag{9.14}$$

where r is the same as the radial coordinate in the BL coordinates. The radial coordinate r can be defined in terms of the Cartesian KS coordinates as

$$\frac{x^2 + y^2}{r^2 + a^2} + \frac{z^2}{r^2} = 1 \,. \tag{9.15}$$

Then the coordinates $\{r, \theta, \phi_{\rm KS}\}$ can be written explicitly in terms of Cartesian KS as

$$\begin{aligned} r &= \left[\frac{R^2 - a^2 + \sqrt{(R^2 - a^2)^2 + 4a^2 z^2}}{2}\right]^{1/2} \,, \\ \theta &= \arccos\frac{z}{r} \,, \; \phi_{\rm KS} = \tan^{-1}(-ay - rx, ax - ry) + \pi \,. \end{aligned} \tag{9.16}$$

where

$$R = \sqrt{x^2 + y^2 + z^2} \,. \tag{9.17}$$

The function $\tan^{-1}(x, y)$, also known as the two-argument arctangent function, calculates the arctangent of y/x while considering the quadrant in which the point (x, y) lies.

The coordinate transformation from BL coordinates can be written as

$$\begin{aligned} t_{\rm KS} &= t + \int \frac{2Mr}{\Delta_{\rm BL}} dr \,, \\ x &= \sqrt{r^2 + a^2} \sin\theta \cos\left[\phi_{\rm KS} + \arctan(a/r)\right] \,, \\ y &= \sqrt{r^2 + a^2} \sin\theta \sin\left[\phi_{\rm KS} + \arctan(a/r)\right] \,, \\ z &= r\cos\theta \,, \end{aligned} \tag{9.18}$$

where

$$\phi_{\rm KS} = \phi + a \int \frac{dr}{\Delta_{\rm BL}} \,. \tag{9.19}$$

Following Ref. [347], we fix the integration constant is fixed by letting $t_{\rm KS} = t$ and $\phi_{\rm KS} = \phi$ at the initial radius r_o, so we have

$$\begin{aligned} t_{\rm KS} &= t + \frac{M}{\sqrt{M^2 - a^2}} \left[r_+ \ln\left(\frac{r - r_+}{r_o - r_+}\right) - r_- \ln\left(\frac{r - r_-}{r_o - r_-}\right)\right] \,, \\ \phi_{\rm KS} &= \phi + \frac{a}{2\sqrt{M^2 - a^2}} \left[\ln\left(\frac{r - r_+}{r_o - r_+}\right) - \ln\left(\frac{r - r_-}{r_o - r_-}\right)\right] \,. \end{aligned} \tag{9.20}$$

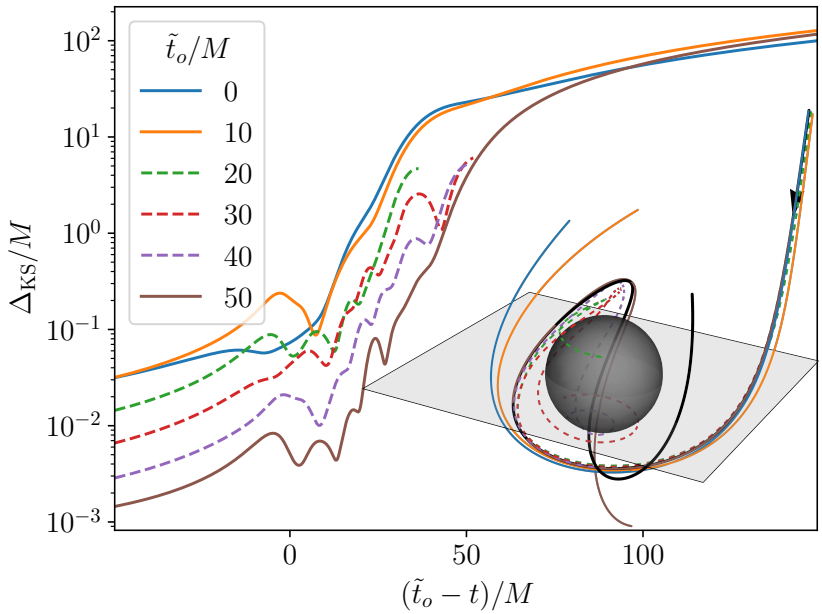

Figure 9.2: Growth of geodesic deviation $\Delta_{\rm KS}$, representing the distance between unperturbed and deflected geodesics at the same backward-propagating time $\tilde{t}_o - t$, in a relaxing Kerr BH spacetime with spin $a = 0.7M$, viewed from a face-on observer with $\theta_0 \approx \pi$, is shown in Cartesian KS coordinates. Different colors represent geodesics launched at various observation times $\tilde{t}_o$, as detailed in the accompanying inset panel. The dashed line marks a trajectory terminating on the BH, whereas the others extend towards infinity. The metric perturbation is modeled using the $n = 0$ and $\ell = m = 2$ mode, with the magnitude normalized to $|{}_{-2}Z| = 0.24$. The initial impact parameters are set at $\tilde{\rho} = 5.041M$, slightly exceeding the critical curve $\tilde{\rho}_c = 5.04M$ in Kerr spacetime. **Inset:** Illustration of the corresponding photon trajectories. The black line represents unperturbed geodesics in Kerr spacetime, with an arrow indicating the direction from the observer to the BH to depict the backward ray-tracing method used. The gray plane indicates the BH equator.

9.3 LENSING TOMOGRAPHY

We explore geodesics in a relaxing Kerr spacetime, particularly focusing on the merger events of supermassive black hole binaries (SMBHBs) with equal mass ratios. The remnant BH from each mass ratio merger events typically characterized by an angular momentum parameter $a \sim 0.7\,M$ [350], a value consistent with numerous observations [8, 351] and considered as our fiducial value. The GW signal from these mergers is dominated by the $\ell = |m| = 2$ mode [88, 212, 336, 352], with the $n = 0$ mode persisting the longest. This fundamental mode is characterized by $M\omega = 0.5326 - 0.08079i$ [88, 353].

The radiated energy determines the amplitude of the metric perturbation. Here, we estimate the radiated energy of a single mode after truncation. The energy flux is given by [212]

$$\frac{\mathrm{d}E}{\mathrm{d}t} = \lim_{r\to\infty}\left[\frac{r^2}{16\pi}\int_\Omega \left|\int_{+\infty}^{t} \Psi_4^{(1)} d\tilde{t}\right|^2 \mathrm{d}\Omega\right] , \tag{9.21}$$

The total energy emitted can then be calculated as

$$E_{\rm tot} = \int_{t_0}^{\infty} \frac{\mathrm{d}E}{\mathrm{d}t}\,\mathrm{d}t \ , \tag{9.22}$$

where $t_0 = r_*(r_o)$. This total energy satisfies the condition $E_{\rm tot}/M \lessapprox 3\%$ [212]. Assuming that only the $\ell = m = 2$ mode dominates the radiated energy, this relationship leads to

$$|{}_sZ| \lessapprox 0.24\,. \tag{9.23}$$

It is important to note that this approach differs slightly from truncating the metric using $H(t - r_*)$. However, it should provide a sufficiently accurate estimate for our purposes.

In the vicinity of the BH, the metric perturbation amplitude can reach up to $M^2\Psi_4^{(1)} \sim 0.1$ [212]. The total radiated energy during the ringdown, $E_{\rm tot}$, is limited to approximately 3% of the remnant BH's mass [212], setting an upper limit on the magnitude of $|{}_{-2}Z|$ for the $\ell = m = 2$ mode at about 0.24. We adopt this upper bound as the fiducial value for our analyses, our results can be trivially re-scaled for generic amplitudes.

We first consider a face-on observer with $\theta_o \approx \pi$. Figure 9.2 illustrates backward photon trajectories, all launched from the same direction, using identical backward impact parameters relative to the observer positioned at $r_0 = 10^9 M$. These trajectories are depicted using the Cartesian KS coordinate system (x, y, z). The black line represents a geodesic in an unperturbed Kerr spacetime, while the various colors indicate different observation times $\tilde{t}_o \equiv t_o - r_*(r_o)$, where $\tilde{t}_o = 0$ is approximately the time when the GW ringdown initially reaches the observer. The bottom panel displays the growth of deviations between unperturbed and deflected geodesics, defined as $\Delta_{\rm KS} \equiv (\Delta x^2 + \Delta y^2 + \Delta z^2)^{1/2}$, representing the distance between the two trajectories at the same backward

propagating time $\tilde{t}_o - t$, colors corresponding to trajectory lines in the inset panel.

In Fig. 9.2, we select $\tilde{\rho} = 5.041M$ as the (backward) impact parameter, which is close to the critical curve $\tilde{\rho}_c \approx 5.04M$ for this BH spin. This curve, defined in Kerr spacetime, represents the geodesics that can propagate around the BH indefinitely. Some of the perturbed geodesics, shown in dashed lines, terminate on the BH instead of propagating towards infinity, indicating a distortion of the critical curve during the ringdown.

The evolution of geodesic deviations, launched at different observer times, initially shows a weak increase after departing from the observer. Geodesics launched later exhibit deviations exponentially smaller than those launched earlier, reflecting the exponential decay of GW amplitude near the BH during the ringdown phase. Closer to the BH, all deviations begin to exhibit exponential growth due to the instability of the radial potential in the light ring region [56, 114, 344, 354–362]. Here, the interplay between light ring instability and GW induces additional oscillation features in the exponential growth. The geodesics that depart from the light ring region begin to develop deviations that increase linearly with time.

To quantify the lensing during ringdown, we analyze backward photons that ultimately reach infinity, corresponding to far-away sources. We assess the angular difference between the asymptotic direction for Kerr geodesic and the deflected geodesic as observables, including the grand arc difference $\tilde{\delta}$, and variations in the azimuthal angle $\Delta\phi$ and polar angle $\Delta\theta$.

Figure 9.3 displays the deflected angles in polar ($\Delta\theta$) and azimuthal ($\Delta\phi$) components as a function of observer frame time, $\tilde{t}_o$, for trajectories initially launched from various polar coordinate angles $\tilde{\varphi}$ on the observer plane. The impact parameters are fixed at $\tilde{\rho} = 6M$. Due to ringdown metric perturbations, axial symmetry is not preserved even in face-on observations. Notably, both $\Delta\phi$ and $\Delta\theta$ show identical variations for values of $\tilde{\varphi}$ separated by π. This pattern is precisely attributable to the $m = 2$ mode of the metric perturbations, akin to those generated by vector or tensor superradiant clouds [362], demonstrating that the deflected angles can effectively dissect the polarization pattern of the GWs around the BH.

In the top panel of Fig. 9.4, we depict the evolution of the deflection angle $\tilde{\delta}$ for different relative impact parameters $\Delta\tilde{\rho} \equiv \tilde{\rho} - \tilde{\rho}_c$, where $\tilde{\rho}_c \approx 5.04M$ is defined as the critical curve in Kerr spacetime (for $a = 0.7M$). The early time evolutions of $\tilde{\delta}$ consistently exhibit a pattern of exponential decay and oscillation that aligns with the time-dependence of the gravitational waveform shown in the bottom panel. This alignment suggests that these observables effectively capture key characteristics of the BH ringdown. We fit the envelope of the $\Delta\tilde{\rho}/M = 0.5$ case using the ringdown decay rate, specifically, $\tilde{\delta} \sim A_{\tilde{\delta}} \exp(\mathrm{Im}(\omega)\, \tilde{t}_o)$, as shown in the dot-dashed line. This demon-

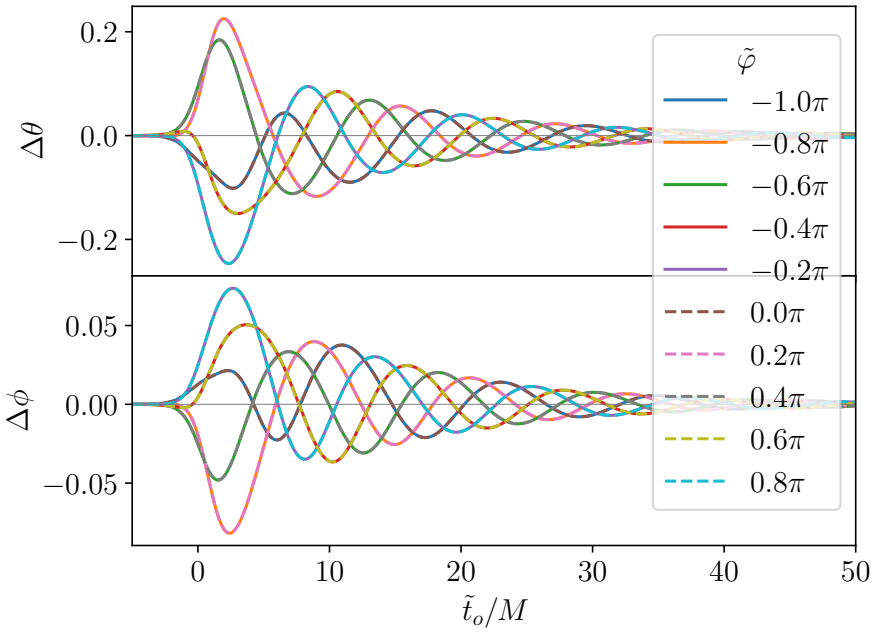

Figure 9.3: Evolutions of the deflected angles in the azimuthal ($\Delta\phi$) and polar ($\Delta\theta$) components for geodesics terminating at infinity, plotted as a function of observation time $\tilde{t}_o$. The configuration of the BH, observer, and ringdown is consistent with the setup described in Fig. 9.2. Different colors illustrate geodesics launched from various angles on the polar coordinate of the observer's plane $\tilde{\varphi}$, all with fixed impact parameters of $\tilde{\rho} = 6M$. The symmetrical patterns observed in cases separated by π in $\tilde{\varphi}$ highlight the $m = 2$ symmetry of the BH ringdown.

strates a clear overlap in the early stages. The amplitude of the deflection angle $A_{\tilde{\delta}}$ is well described at large $\Delta\tilde{\rho}$ by

$$A_{\tilde{\delta}} \sim \frac{1.2\sqrt{E_{\rm tot}/M}}{\Delta\tilde{\rho}/M}\,, \tag{9.24}$$

with $E_{\rm tot}/M = 0.03$ in our fiducial case.

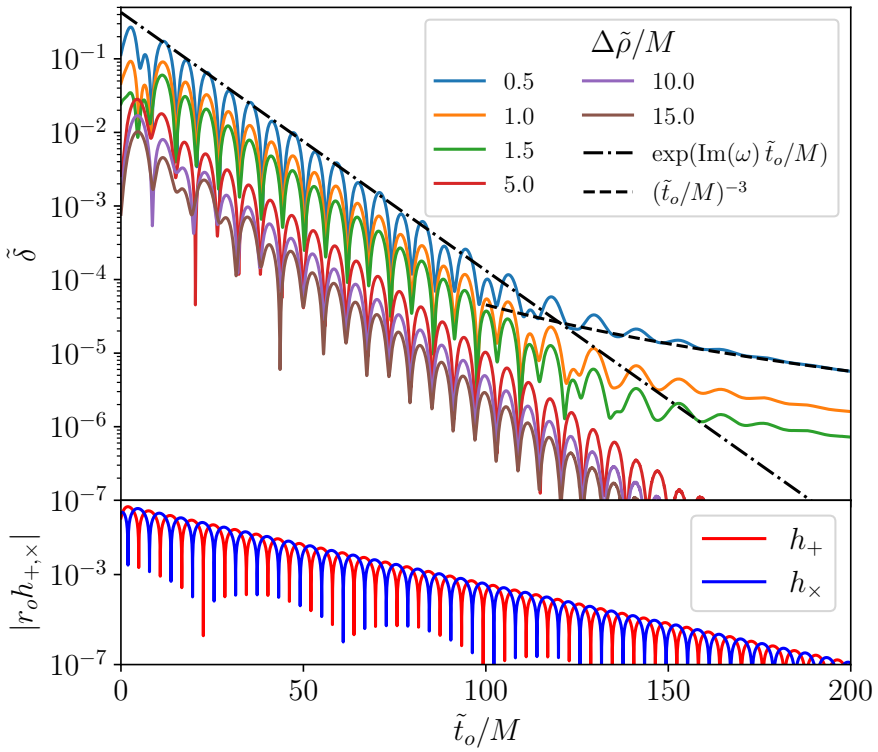

Figure 9.4: **Top:** Deflection angle of geodesics terminating at infinity, $\tilde{\delta}$, defined as the grand arc difference from the unperturbed direction, plotted as a function of observation time $\tilde{t}_o$. Different colors represent geodesics launched with varying relative impact parameters $\Delta\tilde{\rho}$ along the $+\tilde{X}$-axis. The BH, observer, and ringdown configuration are consistent with the setup described in Fig. 9.2. Early stages show a dominant exponential decay and oscillation behavior, in very good agreement with the GW ringdown depicted in the bottom panel. The envelope of the $\Delta\tilde{\rho}/M = 0.5$ curve is fitted by $\tilde{\delta} \sim A_{\tilde{\delta}} \exp\big(\mathrm{Im}(\omega)\,\tilde{t}_o\big)$, illustrated by the dot-dashed line. At later times, a slow decay appears, fitted by $\tilde{\delta} \propto \tilde{t}_o^{-3}$, shown by the dashed line. **Bottom:** Amplitudes of the GWs in the two polarizations, h_+ and $h_\times$, in transverse traceless gauge, as observed by an observer at $\theta_o/\pi = 1 - 10^{-4}$.

Note that the scaling $A_{\tilde{\delta}} \propto 1/\Delta\tilde{\rho}$ differs from the inverse-cubic dependence reported in Refs. [329, 363–365]. This distinction arises because, in our case, the dominant deflection occurs locally when the photon first encounters the ringdown perturbation near $t \approx r_*$ – close to the BH and at early times – when the photon and GW propagation directions are not yet fully aligned. As a result, the deflection, which is proportional

to the contraction $h_{\mu\nu}p^\mu p^\nu$, is primarily governed by the $1/r$ component of the metric perturbation, rather than the $1/r^3$ contribution. In contrast, the inverse-cubic scaling in Refs. [329, 363–365] assumes a source that emits GWs continuously and nearly isotropically long before the photon arrives, such that only the component of the GW field with momentum aligned with the photon direction contributes appreciably to the net deflection.

Furthermore, as the impact parameter approaches the critical curve, specifically when $\Delta\tilde{\rho} \ll M$, there is a noticeable increase in the overall amplitude of $\tilde{\delta}$. This enhancement can be attributed to the instability of the BH light ring region, which causes an exponential growth in the perturbed deviation during propagation around the BH [56, 114, 344, 354–360, 362].

On the other hand, at late times, the evolution exhibits a power-law decay. This distinction arises from deflections developing in two distinct regions. During the early stages, the photon encounters the GW field close to the BH, where the $1/r$ component of the perturbation dominates and induces a deflection that decays locally in an exponential fashion—reflecting the ringdown behavior of the GW itself. At late times, the encounter occurs farther from the BH, where the photon and GW propagate nearly anti-parallel. In this regime, the deflection effect receives non-vanishing contributions only from the $1/r^3$ component of the metric perturbations. Indeed, our results are consistent with a power-law scaling, $\tilde{\delta} \propto \tilde{t}_o^{-3}$, as shown by the dot-dashed fit in Fig. 9.4, following the behavior predicted in Refs. [329, 363–365].

We also present cases with different observer inclination angles θ_o in Fig. 9.5, with the impact parameters fixed at $\tilde{\rho}/M = 10$ along the $+\tilde{X}$-axis. Similar to the observations in Fig. 9.4, the evolutions exhibit two distinct types of behavior: a ringdown-like exponential decay with oscillations, and a subsequent power-law decay proportional to $\tilde{t}_o^{-3}$. The power-law tail becomes more pronounced at smaller θ_o. This effect is due to the polar angle θ of photon geodesics at $t \approx r_*$ being closer to π, where the metric perturbation of the $\ell = m = 2$ mode is most dominant, as shown in the angular distribution of the GW ringdown in the inset panel. For $\theta_o = \pi(1 - 10^{-4})$, the deflection angle is predominantly characterized by ringdown behavior, with oscillation frequency mimics the ringdown frequency to one part in 10^{10}.

Furthermore, we consider the effect of incorporating the QNM's mirror mode with equal energy, reflecting a more realistic scenario where the SMBHB was in a quasi-circular orbit before the merger. This setup also exhibits the two previously discussed characteristics: an initial rapid decay during the ringdown phase, followed by a late-time power-law tail, as shown in Section 9.4.

9.4 RESULTS OF MIRROR MODE

We consider the effect of incorporating the QNM's mirror mode with equal energy, reflecting a more realistic scenario where the SMBHB

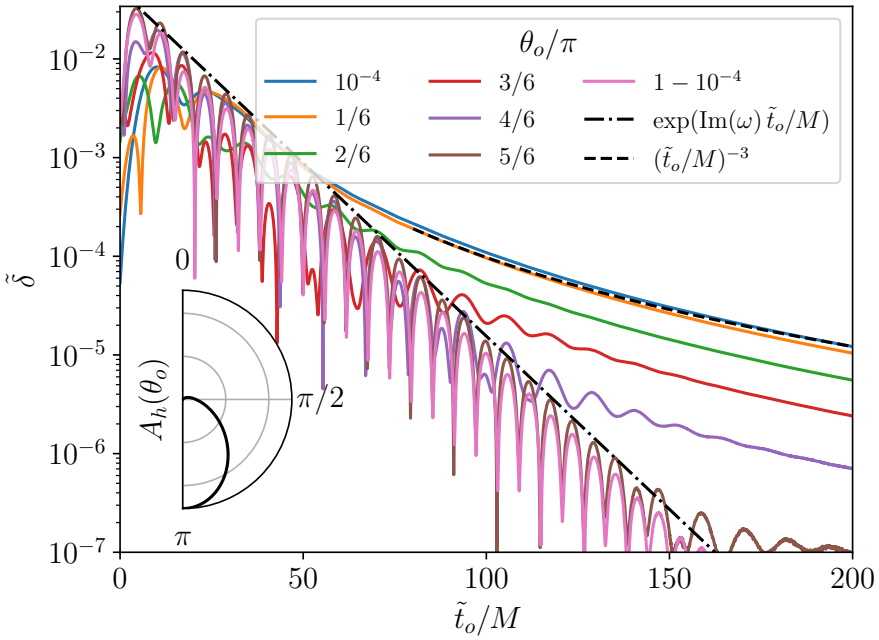

Figure 9.5: Evolutions of the deflection angles of geodesics terminating at infinity, observed from various inclination angles θ_0 and plotted against observation time $\tilde{t}_o$. The impact parameter is consistently set at $\tilde{\rho}/M = 10$ along the $+\tilde{X}$ axis. The dashed black line indicates that $\tilde{\delta}$ scales proportionally to $\tilde{t}_o^{-3}$. **Inset:** The relative strain amplitudes of the GWs, A_h, defined as $h \equiv (h_+^2 + h_\times^2)^{1/2} \sim A_h \exp\big(\mathrm{Im}(\omega)\tilde{t}_o\big)$, are plotted as a function of the θ_o. The amplitude is most prominent at $\theta_o = \pi$.

was in a quasi-circular orbit before the merger. In Fig. 9.6, we show the evolution of $\tilde{\delta}$ for different values of $\Delta\tilde{\rho}$ and θ_o. Compared to the results of Figs. 9.4 and 9.5, this setup also exhibits the two previously discussed characteristics: exhibit the same two key features: an initial rapid decay during the ringdown phase, followed by a late-time power-law tail. Due to the mirror mode's symmetry across the equatorial plane, the dependence on θ_o becomes less pronounced.

9.5 DISCUSSION

This study explored the dynamic lensing of photons during the ringdown phase after SMBHB mergers. By calculating photon trajectories around a relaxing Kerr BH using backward ray tracing, we demonstrate how metric perturbations during the ringdown significantly influence photon paths. In most cases, the evolutions of photon deflection angles initially exhibit behavior akin to GW ringdown, providing insights into the fascinating dynamics of spacetime.

The visualization of ringdown through photon lensing opens a new avenue for multi-messenger astronomy. While pulsar timing arrays (PTAs) [32, 366–368], astrometry [369–371], binary orbits [372, 373], and fast radio burst timing [374] may directly detect ringdown GWs from SMBHB mergers, observations from the EHT [4, 375] and future upgrades [376], could provide visualizations of a 'Waltz' between GWs and photon co-propagation. Each pixel on the observer plane could reveal additional insights by dissecting the metric perturbations in the vicinity of the relaxing BH.

A critical question is the feasibility of observing ringdown in electromagnetic channels. This requires the telescope's Gaussian kernel, represented by $\theta_{\rm res}/2.4$ (where $\theta_{\rm res}$ is the angular resolution), to be finer than the changes in the impact parameter on the observer plane, scaling as $\tilde{\delta} \times r_s/r_o$ with r_s being the distance to the BH. Substituting from Eq. (9.24) and using $E_{\rm tot} \sim 0.27Mq^2/(1+q)^4$, where q is the mass ratio [212], we derive the requirement:

$$\frac{M}{r_o} > 0.67\,\theta_{\rm res}\beta\left(2+q+\frac{1}{q}\right), \tag{9.25}$$

where $\beta \equiv \Delta\tilde{\rho}/r_s < 1$ is a geometric factor dependent on the configuration of the light source, the BH, and the observer. The current angular resolution achievable by the EHT is 20μas, anticipated to improve to 3μas with space-based missions like the Black Hole Explorer (BHEX) [377–380]. Further enhancements in resolution can be achieved by extending the baselines to locations such as the Moon or the second Sun-Earth Lagrange point [360].

For a merger involving BHs with comparable mass ratios, assuming $M = 10^{10}\,M_\odot$ as suggested by PTA observations [381], BHEX could detect lensing signatures from distant sources out to $r_o \sim 12$ Mpc$/\beta$. For well-monitored supermassive black holes (SMBHs) such as Sgr A* and M87*, even mergers with smaller mass ratios become observable,

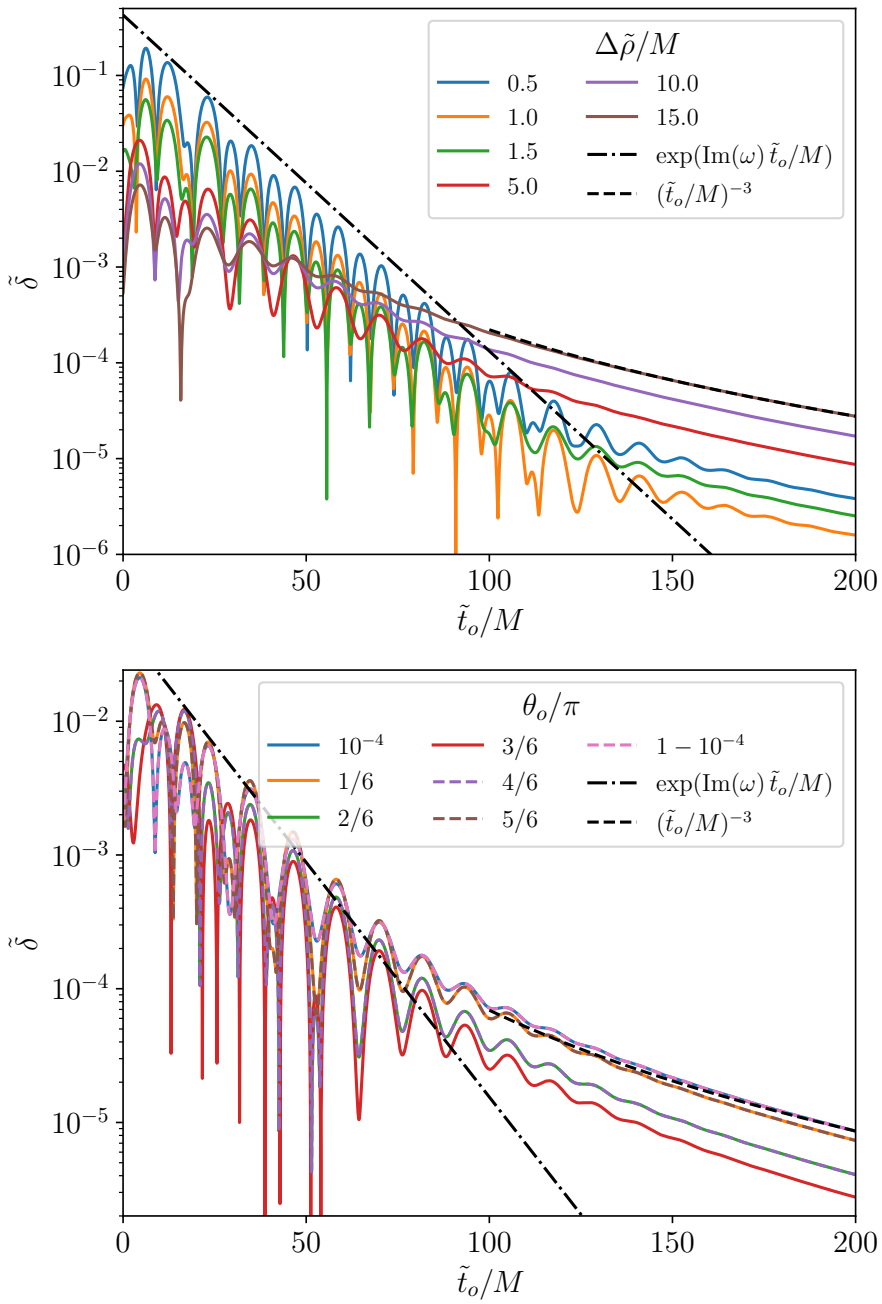

Figure 9.6: Evolution of the deflection angles of geodesics terminating at infinity, plotted as a function of observation time $\tilde{t}_o$, for the case incorporating the QNM's mirror mode with equal energy. **Left:** Results for various impact parameters $\Delta\tilde{\rho}/M$ with $\theta_o/\pi = 1-10^{-4}$. **Right:** Results for various initial inclination angles θ_0 with $\tilde{\rho}/M = 10$ along the $+\tilde{X}$ axis.

enabling detection of events with $q \sim 0.5\beta$. A source with a small β—typically located on the far side of the BH, such as a jet feature, an accretion flow near the light ring, or a background star—can therefore significantly enhance the detection prospects.

In the case of background stars lensed by Sgr A*, Ref. [382] predicts that upcoming telescopes like Extremely Large Telescope (ELT), Thirty Meter Telescope (TMT), and Giant Magellan Telescope (GMT) will detect $\mathcal{O}(100)$ stars with angular separations of $\sim$1 mas and distances of $\sim$1 pc behind the BH, corresponding to $\beta \sim 10^{-5}$. Given their mas-level angular resolution, these telescopes could detect lensing signatures from intermediate-mass BHs merging into Sgr A* with mass ratios as small as $q \sim 10^{-3}$.

While our focus here is on ringdown, the underlying formalism applies more broadly to dynamic metric perturbations. For instance, a single SMBH surrounded by a bosonic superradiant cloud could generate sustained periodic perturbations, potentially observable by EHT-class instruments as time-dependent lensing signatures in the accretion flow near the photon ring [362]. Moreover, our approach is applicable to the long-lasting inspiral stage of a binary system, where the accumulation of signal-to-noise ratio could make such searches feasible. A more precise prediction of the apparent position shift of a point source would require generalizing forward ray tracing [383] in perturbed spacetime.

Part V

CONCLUSION

10

CONCLUDING REMARKS

This thesis embarked on an exploration of the intricate dynamics, stability properties, and potential observational signatures associated with compact objects within the framework of GR. Structured into several parts focusing on foundational theory, stability and energy extraction, interactions, and observational probes, we leveraged advanced numerical relativity techniques alongside analytical and perturbative methods to investigate fundamental questions at the intersection of strong gravity, DM physics, and the burgeoning field of gravitational wave astronomy.

10.1 DISCUSSION OF KEY FINDINGS AND INTERCONNECTIONS

Our investigations, following the thematic progression of the thesis, revealed several key physical phenomena.

First, exploring **stability and energy extraction mechanisms** (Part II) provided crucial insights into the behavior of compact objects beyond standard BHs. We precisely mapped the threshold for the ergoregion instability in truncated Kerr spacetimes to the equatorial ergosurface for large multipoles (Chapter 3). Importantly, outside the ergoregion, we found no evidence for linear instabilities driven solely by light rings on astrophysically relevant timescales ($\tau \lesssim 10^5 M$), suggesting that rotation and trapping alone might not destabilize horizonless objects linearly. Complementing this stability analysis, we uncovered potent energy extraction mechanisms beyond standard superradiance. Dynamic bouncing geometries mimicking evaporating BHs exhibit a blueshift instability near the inner apparent horizon capable of enormous energy amplification (Chapter 4). Similarly, time-periodic fundamental solitons like Q-balls amplify scattered waves via mode-mixing, a potentially generic mechanism for such structures (Chapter 5).

Second, the study of **interactions and dynamics between BSs and BHs** (Part III) highlighted the dramatic consequences of encounters between these objects. A central theme emerged from simulating a BH piercing through mini-BSs (Chapter 6) and SBSs (Chapter 7). We discovered a surprisingly dominant role for tidal capture, leading to the near-total accretion of the BS by the BH across a wide range of parameters, even for significant scale disparities. This extreme tidal capture, robust even for self-interacting SBSs, suggests such encounters are highly disruptive. A consistent outcome was the formation of quasi-bound scalar field remnants—"gravitational atoms"—around the

final BH, linking interaction dynamics to the fundamental properties of scalar fields in strong gravity.

Third, our work on **observational probes of gravitational waves** (Part IV) revealed deviations from previous theoretical expectations in late-time signals and offered new multi-messenger avenues. We identified source-driven tails (SoDTs) in gravitational perturbations, generated by point-like matter or nonlinearities, which can dominate over the canonical Price's law decay (IDTs) for outgoing sources (Chapter 8). This alters our understanding of the late-time behaviour of gravitational signals. We also demonstrated that dynamical gravitational lensing during BH ringdown encodes quasinormal mode oscillations in the light deflection angle, offering a novel multi-messenger probe (Chapter 9).

These findings interconnect, showing how stability properties (ergoregion, trapping), fundamental field characteristics (scalar potentials, time-periodicity), and interaction dynamics (BH-BS encounters) manifest in potentially observable phenomena like energy extraction signatures, gravitational wave tails, and lensing effects.

10.2 SIGNIFICANCE AND BROADER IMPLICATIONS

The results presented carry significant implications across several domains. For DM physics, the prevalence of tidal capture and disruption in BH-BS interactions poses challenges for the survival of extended scalar DM structures in dense environments, potentially constraining models where BSs constitute a significant fraction of DM. The formation of gravitational atoms, however, offers a potential signature if such remnants can be detected.

In the context of testing GR, our findings offer new avenues. The characterization of SoDTs provides a more nuanced picture of late-time gravitational wave signals, potentially requiring modifications to waveform models used in data analysis, especially for sources involving matter or significant nonlinearities. Dynamical lensing during ringdown presents a conceptually new way to probe the strong-field dynamics near merging BHs using electromagnetic observations, offering tests complementary to direct gravitational wave detection.

Regarding quantum gravity phenomenology, the stability analysis of horizonless UCOs helps delineate the parameter space where such exotic objects could potentially exist, refining constraints derived from the ergoregion instability. The investigation of energy extraction from bouncing geometries and Q-balls touches upon fundamental questions about energy conservation and extraction in scenarios potentially motivated by quantum gravity effects (e.g., singularity resolution, fundamental solitons), offering glimpses into physics beyond classical BHs.

Observationally, this work points towards new targets and methods. The potential for high-energy bursts from bouncing geometries, the specific gravitational wave signatures from BH-BS interactions, the subtle effects of SoDTs on late-time signals, and the prospect of observing dy-

namical lensing with next-generation telescopes (like next generation Event Horizon Telescope (ngEHT) or space-based very long baseline interferometry (VLBI)) all represent concrete, albeit challenging, observational goals. These studies underscore the power of multi-messenger astronomy in probing fundamental physics in the strong gravity regime.

10.3 OPEN QUESTIONS AND FUTURE RESEARCH

Despite the progress made, several limitations and open questions remain, paving the way for future research.

- **Extreme Scale Separation:** Our BH-BS simulations were limited by computational resources to moderate mass and length ratios. Exploring astrophysically relevant scenarios, such as a astrophysical BH interacting with a galactic-scale DM halo ($\mathcal{L} \sim 10^6$), requires new approaches.
- **Diverse Objects and Physics:** We focused primarily on scalar fields. Extending stability and interaction studies to other types of compact objects (e.g., Proca stars, fermion stars) or including additional physics (e.g., magnetic fields, different scalar potentials, vector fields) would broaden our understanding. The stability of UCOs with different equations of state or boundary conditions also requires further investigation.
- **Backreaction and Nonlinearities:** Our analysis of SoDTs included second-order gravitational perturbations, but a full understanding requires exploring higher orders and potentially nonperturbative effects. Similarly, the energy extraction mechanisms studied (e.g., bouncing geometry blueshift, Q-ball mode-mixing) largely assumed negligible backreaction; incorporating this self-consistently, especially for the potentially explosive bouncing geometry scenario, is a significant theoretical challenge.
- **Observational Signatures and Realistic Scenarios:** Connecting theoretical models to concrete observational predictions needs refinement. This includes generating more realistic gravitational waveforms for BH-BS encounters across a wider parameter space and quantifying the detectability of potential signatures like gravitational atoms. For SoDTs, assessing their detectability amidst detector noise and astrophysical foregrounds, particularly in sources like EMRIs, is crucial. Detailed feasibility studies for observing dynamical lensing during ringdown (and potentially during inspiral or from superradiant clouds) require further work. Furthermore, exploring the potential for testing energy extraction mechanisms in analogue gravity experiments could provide complementary insights.
- **Connections to Fundamental Theory:** Linking the phenomenological models used (e.g., bouncing metrics, specific scalar potentials) more directly to candidate theories of quantum gravity

or specific DM models would strengthen the physical motivation and allow for more direct constraints on fundamental parameters. Additionally, investigating the implications of phenomena like SoDTs for fundamental principles such as strong cosmic censorship, particularly in de Sitter spacetime, is an important theoretical direction.

Addressing these open questions through continued theoretical modelling, advanced numerical simulations, and synergistic analysis of gravitational wave and electromagnetic observations promises to further unravel the mysteries of compact objects and the fundamental laws governing our Universe.

Part VI

APPENDIX

A

METRIC PERTURBATIONS DURING RINGDOWN

A.1 NEWMAN-PENROSE FORMALISM

In this appendix, we review the Newman-Penrose (NP) formalism, adopting the convention from Refs. [384–386]. Note the overall sign difference in some NP quantities compared to the common convention, as seen, for example, in Ref. [47]. This ensures that the background values remain consistent with cases where the metric signature is $(+,-,-,-)$. In the NP formalism, four null vectors $e^a_{(\mu)}$ are defined as

$$e^a_{(\mu)} = \left\{e^a_{(0)}, e^a_{(1)}, e^a_{(2)}, e^a_{(3)}\right\} \equiv \{l^a, n^a, m^a, \bar{m}^a\} \,, \tag{A.1}$$

where l^a and n^a are real null vectors, and m^a and $\bar{m}^a$ are complex null vectors, satisfying

$$l^a n_a = -1 \quad \text{and} \quad m^a \bar{m}_a = 1 \,. \tag{A.2}$$

The metric can be obtained via

$$g_{ab} = -2 l_{(a} n_{b)} + 2 m_{(a} \bar{m}_{b)} \,. \tag{A.3}$$

The directional covariant derivatives are defined as

$$\hat{D} \equiv l^a \nabla_a, \; \hat{\Delta} \equiv n^a \nabla_a, \; \hat{\delta} \equiv m^a \nabla_a, \; \hat{\bar{\delta}} \equiv \bar{m}^a \nabla_a \,. \tag{A.4}$$

The Ricci rotation coefficients are given by

$$\gamma_{(a)(b)(c)} \equiv g_{\mu\lambda} e^\mu_{(a)} e^\nu_{(c)} \nabla_\nu e^\lambda_{(b)} \,, \tag{A.5}$$

which can be explicitly written as

$$\begin{aligned}
&\kappa \equiv -\gamma_{(3)(1)(1)} \,, \; \varpi \equiv -\gamma_{(2)(4)(1)} \,, \; \epsilon \equiv -\frac{1}{2}\left(\gamma_{(2)(1)(1)} + \gamma_{(3)(4)(1)}\right) , \\
&\tau \equiv -\gamma_{(3)(1)(2)} \,, \; \nu \equiv -\gamma_{(2)(4)(2)} \,, \; \gamma \equiv -\frac{1}{2}\left(\gamma_{(2)(1)(2)} + \gamma_{(3)(4)(2)}\right) , \\
&\sigma \equiv -\gamma_{(3)(1)(3)} \,, \; \mu \equiv -\gamma_{(2)(4)(3)} \,, \; \beta \equiv -\frac{1}{2}\left(\gamma_{(2)(1)(3)} + \gamma_{(3)(4)(3)}\right) , \\
&\rho \equiv -\gamma_{(3)(1)(4)} \,, \; \lambda \equiv -\gamma_{(2)(4)(4)} \,, \; \alpha \equiv -\frac{1}{2}\left(\gamma_{(2)(1)(4)} + \gamma_{(3)(4)(4)}\right) .
\end{aligned} \tag{A.6}$$

The formal adjoint $\mathcal{L}^\dagger$ of an operator

$$\mathcal{L} = e^a_{(\mu)} \nabla_a \tag{A.7}$$

can be written as [387–389]

$$\mathcal{L}^\dagger = -\mathcal{L} - \nabla_a e^a_{(\mu)} \,. \tag{A.8}$$

Therefore, the formal adjoint directional derivative operators are

$$\begin{aligned} \hat{D}^\dagger &= -(\hat{D} + \varepsilon + \bar{\varepsilon} - \rho - \bar{\rho}) \,, \; \hat{\Delta}^\dagger = -(\hat{\Delta} - \gamma - \bar{\gamma} + \mu + \bar{\mu}) \,, \\ \hat{\delta}^\dagger &= -(\hat{\delta} + \beta - \bar{\alpha} - \tau + \bar{\varpi}) \,, \; \hat{\bar{\delta}}^\dagger = -(\hat{\bar{\delta}} + \bar{\beta} - \alpha - \bar{\tau} + \varpi) \,. \end{aligned} \tag{A.9}$$

In the Kerr background, we use the Kinnersley tetrad as follows

$$\begin{aligned} e^\mu_{(1)} = l^\mu = \frac{1}{\Delta_{\rm BL}} \left(r^2 + a^2, \Delta_{\rm BL}, 0, a\right) \,, \quad e^\mu_{(2)} = n^\mu = \frac{1}{2\Sigma_{\rm BL}} \left(r^2 + a^2, -\Delta_{\rm BL}, 0, a\right) \,, \\ e^\mu_{(3)} = m^\mu = -\frac{\bar{\rho}}{\sqrt{2}} \left(ia \sin\theta, 0, 1, \frac{i}{\sin\theta}\right) \,, \quad e^\mu_{(4)} = \bar{m}^\mu = \frac{\rho}{\sqrt{2}} \left(ia \sin\theta, 0, -1, \frac{i}{\sin\theta}\right) \,, \end{aligned} \tag{A.10}$$

where $\rho = -1/(r - ia\cos\theta)$ and the overbar denotes complex conjugation. $\Delta_{\rm BL}$ and $\Sigma_{\rm BL}$ are defined as

$$\Delta_{\rm BL} \equiv r^2 - 2Mr + a^2 \,, \quad \Sigma_{\rm BL} \equiv r^2 + a^2 \cos^2\theta \,. \tag{A.11}$$

The Ricci rotation coefficients can be written explicitly as

$$\kappa = \lambda = \nu = \sigma = \epsilon = 0 \,, \tag{A.12}$$

and

$$\begin{aligned} &\rho = -1/(r - ia\cos\theta) \,, \; \beta = -\bar{\rho}\cot\theta/(2\sqrt{2}) \,, \; \varpi = ia\rho^2 \sin\theta/\sqrt{2} \,, \\ &\tau = -ia\rho\bar{\rho}\sin\theta/\sqrt{2} \,, \; \mu = \rho^2\bar{\rho}\Delta/2 \,, \; \gamma = \mu + \rho\bar{\rho}(r - M)/2 \,, \; \alpha = \varpi - \bar{\beta} \,. \end{aligned} \tag{A.13}$$

The Weyl scalars are defined as

$$\begin{aligned} &\Psi_0 \equiv C_{(1)(3)(1)(3)} = C_{\mu\nu\rho\sigma} l^\mu m^\nu l^\rho m^\sigma \,, \; \Psi_1 \equiv C_{(1)(2)(1)(3)} = C_{\mu\nu\rho\sigma} l^\mu n^\nu l^\rho m^\sigma \,, \\ &\Psi_2 \equiv C_{(1)(3)(4)(2)} = C_{\mu\nu\rho\sigma} l^\mu m^\nu \bar{m}^\rho n^\sigma \,, \; \Psi_3 \equiv C_{(1)(2)(4)(2)} = C_{\mu\nu\rho\sigma} l^\mu n^\nu \bar{m}^\rho n^\sigma \,, \\ &\Psi_4 \equiv C_{(2)(4)(2)(4)} = C_{\mu\nu\rho\sigma} n^\mu \bar{m}^\nu n^\rho \bar{m}^\sigma \,, \end{aligned} \tag{A.14}$$

where $C_{\mu\nu\rho\sigma}$ is the Weyl tensor. In the Kerr background, we have $\Psi_0 = \Psi_1 = \Psi_3 = \Psi_4 = 0$ and

$$\Psi_2 = \rho^3 M \,. \tag{A.15}$$

Other useful equations derived from the Bianchi identities are

$$\hat{D}\Psi_2 = 3\rho\Psi_2 \,, \; \hat{\Delta}\Psi_2 = -3\mu\Psi_2 \,, \; \hat{\delta}\Psi_2 = 3\tau\Psi_2 \,, \; \hat{\bar{\delta}}\Psi_2 = -3\varpi\Psi_2 \,. \tag{A.16}$$

A.2 METRIC RECONSTRUCTION

Cohen, Chrzanowski, and Kegeles (CCK) formulated a method for reconstructing vacuum metric perturbations within a radiation gauge [339–341]. Here, we briefly review the procedure of CCK reconstruction, which is detailed in Ref. [385, 390–394]. Many of our calculations heavily depend on the NP formalism, adhering to the conventions outlined in Appendix A.1.

We begin by introducing four operators: $\hat{\mathcal{E}}$, $\hat{\mathcal{O}}$, $\hat{\mathcal{S}}$, and $\hat{\mathcal{T}}$, each with their respective formal adjoints

- The linearized Einstein operator $\hat{\mathcal{E}}$, which is defined as

$$\hat{\mathcal{E}}_{ab}(h) = \frac{1}{2}\left[-\nabla^c\nabla_c h_{ab} - \nabla_a\nabla_b h_c{}^c + 2\nabla^c\nabla_{(a}h_{b)c} + g_{ab}\left(\nabla^c\nabla_c h_d{}^d - \nabla^c\nabla^d h_{cd}\right)\right] . \tag{A.17}$$

  The operator $\hat{\mathcal{E}}$ is self-adjoint, as indicated by $\hat{\mathcal{E}} = \hat{\mathcal{E}}^\dagger$, and it maps a metric perturbation to its corresponding linearized Einstein tensor.

- The Teukolsky operator $\hat{\mathcal{O}}$, which can be written as [47]

$$\begin{aligned}\hat{\mathcal{O}}_0 &= \left(\hat{D} - 3\epsilon + \bar{\epsilon} - 4\rho - \bar{\rho}\right)\left(\hat{\Delta} - 4\gamma + \mu\right) - \left(\hat{\delta} + \bar{\varpi} - \bar{\alpha} - 3\beta - 4\tau\right)\left(\hat{\bar{\delta}} + \varpi - 4\alpha\right) - 3\Psi_2 ,\\ \hat{\mathcal{O}}_4 &= \left(\hat{\Delta} + 3\gamma - \bar{\gamma} + 4\mu + \bar{\mu}\right)\left(\hat{D} + 4\epsilon - \rho\right) - \left(\hat{\bar{\delta}} - \bar{\tau} + \bar{\beta} + 3\alpha + 4\varpi\right)\left(\hat{\delta} - \tau + 4\beta\right) - 3\Psi_2 .\end{aligned} \tag{A.18}$$

  Then the Teukolsky equation with spin ± 2 can be expressed as

$$\hat{\mathcal{O}}_0\Psi_0^{(1)} = 8\pi T_0 , \hat{\mathcal{O}}_4\Psi_4^{(1)} = 8\pi T_4 . \tag{A.19}$$

  Their separable form, the Teukolsky master equation, can be written as

$$\hat{\mathcal{O}}_s\psi_s = 8\pi\Sigma T_s , \tag{A.20}$$

  where the spin s is designated as either ± 2. For $s = -2$

$$\psi_{-2} = \rho^{-4}\Psi_4^{(1)} , \hat{\mathcal{O}}_{-2} = 2\Sigma\rho^{-4}\hat{\mathcal{O}}_4\rho^4 , T_{-2} = 2\rho^{-4}T_4 ; \tag{A.21}$$

  conversely, when $s = +2$

$$\psi_{+2} = \Psi_0^{(1)} , \hat{\mathcal{O}}_{+2} = 2\Sigma\hat{\mathcal{O}}_0 , T_{+2} = 2T_0 . \tag{A.22}$$

- The operator $\hat{\mathcal{S}}$, which acts on an energy-momentum tensor T_{ab} to yield the source T_4 of the Teukolsky equation (Eq. (2.15) in Ref. [47])

$$\begin{aligned}\hat{\mathcal{S}}^{ab} = &\left(\hat{\Delta} + 3\gamma - \bar{\gamma} + 4\mu + \bar{\mu}\right)\left[(\hat{\bar{\delta}} - 2\bar{\tau} + 2\alpha)n^{(a}\bar{m}^{b)} - (\hat{\Delta} + 2\gamma - 2\bar{\gamma} + \bar{\mu})\bar{m}^a\bar{m}^b\right]\\ &+ \left(\hat{\bar{\delta}} - \bar{\tau} + \bar{\beta} + 3\alpha + 4\varpi\right)\left[\left(\hat{\Delta} + 2\gamma + 2\bar{\mu}\right)n^{(a}\bar{m}^{b)} - \left(\hat{\bar{\delta}} - \bar{\tau} + 2\bar{\beta} + 2\alpha\right)n^a n^b\right] ,\end{aligned} \tag{A.23}$$

- The operator $\hat{\mathcal{T}}$, which acts on a metric perturbation h_{ab} to yield the perturbed Weyl scalar $\Psi_4^{(1)}$

$$\begin{aligned}\hat{\mathcal{T}}^{ab} = &-\frac{1}{2}\Big\{\Big(\hat{\bar{\delta}} - \bar{\tau} + 3\alpha + \bar{\beta}\Big)\Big(\hat{\bar{\delta}} - \bar{\tau} + 2\alpha + 2\bar{\beta}\Big)\, n^a n^b \\ &+ \Big(\hat{\Delta} + \bar{\mu} + 3\gamma - \bar{\gamma}\Big)\Big(\hat{\Delta} + \bar{\mu} + 2\gamma - 2\bar{\gamma}\Big)\, \bar{m}^a \bar{m}^b \\ &- \Big[\Big(\hat{\Delta} + \bar{\mu} + 3\gamma - \bar{\gamma}\Big)\Big(\hat{\bar{\delta}} - 2\bar{\tau} + 2\alpha\Big) \\ &+ \Big(\hat{\bar{\delta}} - \bar{\tau} + 3\alpha + \bar{\beta}\Big)\Big(\hat{\Delta} + 2\bar{\mu} + 2\gamma\Big)\Big]\, n^{(a}\bar{m}^{b)}\Big\}\,.\end{aligned} \tag{A.24}$$

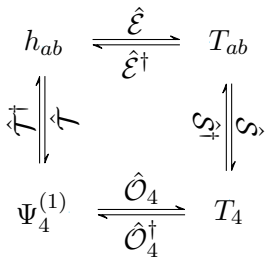

Figure A.1: Relation of operators for $s = -2$.

As pointed out by Wald [387], one can find the following operator identity

$$\hat{\mathcal{O}}_4\hat{\mathcal{T}} = \hat{\mathcal{S}}\hat{\mathcal{E}}\,, \tag{A.25}$$

and its formal adjoint, $\hat{\mathcal{T}}^\dagger\hat{\mathcal{O}}_4^\dagger = \hat{\mathcal{E}}\hat{\mathcal{S}}^\dagger$, is also valid. Then, assuming a complex potential Φ, also known as the Hertz potential, satisfies the adjoint Teukolsky equation $\hat{\mathcal{O}}_4^\dagger\Phi = 0$, we can consequently have

$$\hat{\mathcal{E}}_{ab}(h) = 2\,\mathrm{Re}(\hat{\mathcal{T}}_{ab}^\dagger\hat{\mathcal{O}}_4^\dagger\Phi) = 0\,. \tag{A.26}$$

Therefore, under the assumption, h_{ab} provides a solution to the linearized Einstein equation, and can be expressed as

$$h_{ab} = 2\,\mathrm{Re}\left(\hat{\mathcal{S}}_{ab}^\dagger\Phi\right)\,. \tag{A.27}$$

Chrzanowski introduced two radiation gauges: the *ingoing radiation gauge (IRG)* and the *outgoing radiation gauge (ORG)* [339]. In this paper, we choose ORG, which can be written as

$$h_{ab}n^b = 0 = g^{ab}h_{ab}\,. \tag{A.28}$$

Under this gauge condition, the metric satisfies

$$h_{nn} = 0 = h_{ln} = 0 = h_{nm} = 0 = h_{n\bar{m}} = 0 = h_{m\bar{m}}\,. \tag{A.29}$$

The Hertz potential Φ_{ORG} fulfills the adjoint Teukolsky equation $\mathcal{O}_4^\dagger\Phi_{\mathrm{ORG}} = 0$, where

$$\mathcal{O}_4^\dagger = \Big(\hat{D} - 3\epsilon + \bar{\epsilon} - \bar{\rho}\Big)\Big(\hat{\Delta} - 4\gamma - 3\mu\Big) - \Big(\hat{\delta} - 3\beta - \bar{\alpha} + \bar{\varpi}\Big)\Big(\hat{\bar{\delta}} - 4\alpha - 3\varpi\Big) - 3\Psi_2\,.$$

(A.30)

One can verify $\mathcal{O}_4^\dagger \Phi_{\rm ORG} = 0$ is equivalent to the homogeneous Teukolsky equation for a field with $s = +2$, that is,

$$\hat{\mathcal{O}}_4^\dagger \Phi_{\rm ORG} = \rho^{-4} \mathcal{O}_0 \left(\rho^4 \Phi_{\rm ORG}\right) = 0\,, \tag{A.31}$$

and the metric component can be written as [388]

$$\begin{aligned} h_{ab} = \Big\{ & n_{(a}\bar{m}_{b)} \Big[\left(\hat{\bar{\delta}} + \bar{\beta} - 3\alpha + \bar{\tau} + \varpi\right) \left(\hat{\Delta} - 4\gamma - 3\mu\right) \\ & + \left(\hat{\Delta} - 3\gamma - \bar{\gamma} + \mu - \bar{\mu}\right) \left(\hat{\bar{\delta}} - 4\alpha - 3\varpi\right) \Big] \\ & - n_a n_b \left(\hat{\bar{\delta}} - \bar{\beta} - 3\alpha + \varpi\right) \left(\hat{\bar{\delta}} - 4\alpha - 3\varpi\right) \\ & - \bar{m}_a \bar{m}_b \left(\hat{\Delta} - 3\gamma + \bar{\gamma} + \mu\right) \left(\hat{\Delta} - 4\gamma - 3\mu\right) \Big\} \Phi_{\rm ORG} + \text{c.c.}\,, \end{aligned} \tag{A.32}$$

where "c.c." stands for the complex conjugate part of the whole object. If we define $\mathring{\Phi}_{\rm ORG} = \rho^4 \Phi_{\rm ORG}$, then the non-zero metric component can be written as [395, 396]

$$\begin{aligned} & h_{ll} \equiv h_{\mu\nu} l^\mu l^\nu = \hat{\mathcal{H}}_{ll}^\dagger \mathring{\Phi}_{\rm ORG} + \text{c.c.}\,,\ h_{lm} \equiv h_{\mu\nu} l^\mu m^\nu = \hat{\mathcal{H}}_{lm}^\dagger \mathring{\Phi}_{\rm ORG}\,, \\ & h_{l\bar{m}} \equiv \bar{h}_{lm}\,,\ h_{mm} \equiv h_{\mu\nu} m^\mu m^\nu = \hat{\mathcal{H}}_{mm}^\dagger \mathring{\Phi}_{\rm ORG}\,, \end{aligned} \tag{A.33}$$

where

$$\begin{aligned} \hat{\mathcal{H}}_{ll}^\dagger &= -\rho^{-4} \left(\hat{\bar{\delta}} - 3\alpha - \bar{\beta} + 5\varpi\right) \left(\hat{\bar{\delta}} - 4\alpha + \varpi\right)\,, \\ \hat{\mathcal{H}}_{lm}^\dagger &= -\frac{\rho^{-4}}{2} \Big\{ \left(\hat{\bar{\delta}} - 3\alpha + \bar{\beta} + 5\varpi + \bar{\tau}\right) \left(\hat{\Delta} + \mu - 4\gamma\right) \\ &\quad + \left(\hat{\Delta} + 5\mu - \bar{\mu} - 3\gamma - \bar{\gamma}\right) \left(\hat{\bar{\delta}} - 4\alpha + \varpi\right) \Big\}\,, \\ \hat{\mathcal{H}}_{mm}^\dagger &= -\rho^{-4} \left(\hat{\Delta} + 5\mu - 3\gamma + \bar{\gamma}\right) \left(\hat{\Delta} + \mu - 4\gamma\right)\,. \end{aligned} \tag{A.34}$$

While $\mathring{\Phi}_{\rm ORG}$ does indeed satisfy the vacuum Teukolsky equation with $s = +2$, the field does not correspond to either the Weyl scalar $\Psi_0^{(1)}$ or $\Psi_4^{(1)}$ originating from the reconstructed metric h_{ab}. From Fig. A.1, it is clear that $\Psi_4^{(1)}$ can be obtained via a fourth-order ordinary differential equation (ODE) along ingoing null rays [385, 396, 397]

$$\Psi_4^{(1)} = \hat{\mathcal{T}}^{ab} h_{ab}\,. \tag{A.35}$$

We can reduce this circularity condition to what is known as a radial inversion relation [385, 386, 398–400]

$$\Psi_4^{(1)} = \frac{1}{2} \left(\hat{\Delta} + 3\gamma - \bar{\gamma}\right) \left(\hat{\Delta} + 2\gamma - 2\bar{\gamma}\right) \left(\hat{\Delta} + \gamma - 3\bar{\gamma}\right) \left(\hat{\Delta} - 4\bar{\gamma}\right) \bar{\Phi}_{\rm ORG}\,, \tag{A.36}$$

which can be solved in vacuum algebraically by applying the separation of variables in the next section.

A.2.1 *QNM to Hertz potential*

In Boyer-Lindquist (BL) coordinates, the Teukolsky operator $\hat{\mathcal{O}}_s$ with spin s in Eq. (A.20) can be written as [47]

$$\begin{aligned}\hat{\mathcal{O}}_s\psi_s = &\left[\frac{\left(r^2+a^2\right)^2}{\Delta_{\rm BL}} - a^2\sin^2\theta\right]\frac{\partial^2\psi_s}{\partial t^2} + \frac{4Mar}{\Delta_{\rm BL}}\frac{\partial^2\psi_s}{\partial t\partial\phi} + \left[\frac{a^2}{\Delta} - \frac{1}{\sin^2\theta}\right]\frac{\partial^2\psi_s}{\partial\phi^2} \\ &- \Delta_{\rm BL}^{-s}\frac{\partial}{\partial r}\left(\Delta_{\rm BL}^{s+1}\frac{\partial\psi_s}{\partial r}\right) - \frac{1}{\sin\theta}\frac{\partial}{\partial\theta}\left(\sin\theta\frac{\partial\psi_s}{\partial\theta}\right) - 2s\left[\frac{a(r-M)}{\Delta_{\rm BL}} + \frac{i\cos\theta}{\sin^2\theta}\right]\frac{\partial\psi_s}{\partial\phi} \\ &- 2s\left[\frac{M\left(r^2-a^2\right)}{\Delta_{\rm BL}} - r - ia\cos\theta\right]\frac{\partial\psi_s}{\partial t} + \left(s^2\cot^2\theta - s\right)\psi_s\,.\end{aligned} \tag{A.37}$$

where ψ_s is a field with spin s. In the vacuum case $T_s = 0$, we can apply the separation of variables by letting

$$\psi_s(t,r,\theta,\phi) = \frac{1}{\sqrt{2\pi}}\sum_{l,m,n} {}_sZ_{\ell mn}\,{}_sS_{\ell mn}(\theta)\,{}_sR_{\ell mn}(r)e^{-i\omega_{mn}t+im\phi}\,, \tag{A.38}$$

With $z = \cos\theta$, ${}_sS_{\ell mn}(\theta)$ satisfy

$$\partial_z\left[\left(1-z^2\right)\partial_z\left[{}_sS_{\ell mn}(\theta)\right]\right] + \left[(cz)^2 - 2csz + s + A_s^{\ell mn}(c) - \frac{(m+sz)^2}{1-z^2}\right]{}_sS_{\ell mn}(\theta) = 0\,. \tag{A.39}$$

where $c = a\omega$, and ${}_sS_{\ell mn}(\theta)e^{im\phi}$ represents the spin-weighted spheroidal harmonics, with their phase is consistent with Ref. [91]. To normalize the spin-weighted spheroidal harmonics, we apply the following normalization condition

$$\int_0^\pi {}_sS_{\ell mn}(\theta)\bar{S}_{\ell mn}(\theta)\sin\theta\,{\rm d}\theta = 1\,. \tag{A.40}$$

The radial function $R(r)$ is required to fulfill

$$\Delta_{\rm BL}^{-s}\frac{d}{dr}\left[\Delta_{\rm BL}^{s+1}\frac{{\rm d}_sR_{\ell mn}(r)}{{\rm d}r}\right] + \left[\frac{K^2 - 2is(r-M)K}{\Delta_{\rm BL}} + 4is\omega r - \lambda_{\ell mn}\right]{}_sR_{\ell mn}(r) = 0\,. \tag{A.41}$$

where

$$K_{mn} \equiv \left(r^2+a^2\right)\omega_{mn} - am\,,\ {}_s\lambda_{\ell mn} \equiv {}_sA_{\ell mn} + a^2\omega_{mn}^2 - 2am\omega_{mn}\,. \tag{A.42}$$

Here ${}_sA_{\ell mn}$ is the angular separation constant.

In the following, we will revisit the procedure for obtaining the Hertz potential corresponding to specific Weyl scalar $\Psi_0^{(1)}$ or $\Psi_4^{(1)}$, which is discussed in Ref. [396, 397]. According to the previously mentioned condition, $\hat{\mathcal{O}}_{+2}\mathring{\Phi}_{\rm ORG} = 0$, we can expand $\mathring{\Phi}_{\rm ORG}$ in modes

$$\mathring{\Phi}_{\rm ORG} = \frac{1}{\sqrt{2\pi}}\sum_{\ell,m,n} C_{\ell mn}\,{}_{+2}R_{\ell mn}(r)\,{}_{+2}S_{\ell mn}(\theta)e^{im\phi-i\omega_{mn}t}\,, \tag{A.43}$$

where $C_{\ell mn}$ are constant coefficients. In addition, the Hertz potential $\mathring{\Phi}_{\rm ORG}$ also satisfies Eq. (A.36), which can be simplified using the following relationship

$$\left(\hat{\Delta} - m\bar{\gamma} + n\gamma\right) f = \Delta_{\rm BL}^{(n-m)/2} \bar{\rho}^{-m} \rho^{n} \hat{\Delta} \left[\Delta_{\rm BL}^{(m-n)/2} \bar{\rho}^{m} \rho^{-n} f\right] . \tag{A.44}$$

In this equation, $f = f(t, r, \theta, \phi)$ can represent any function. Then Eq. (A.36) can be written as [386, 395–397]

$$\frac{1}{32}\Delta_{\rm BL}^2 \left(\hat{\mathcal{D}}_0^\dagger\right)^4 \left[\Delta_{\rm BL}^2 \bar{\mathring{\Phi}}_{\rm ORG}\right] = \rho^{-4}\Psi_4^{(1)} . \tag{A.45}$$

Here, the operator $\hat{\mathcal{D}}_0^\dagger$ is defined as

$$\hat{\mathcal{D}}_0^\dagger = \partial_r - \frac{\left(r^2 + a^2\right)\partial_t + a\partial_\phi}{\Delta_{\rm BL}} . \tag{A.46}$$

Note that Eq. (A.45) can be solved easily on the mode basis given by Eq. (A.43), using the operator

$$\hat{\mathcal{D}}_{mn}^\dagger = \partial_r + i\frac{K_{mn}}{\Delta_{\rm BL}} = \partial_r + i\frac{\omega_{mn}\left(r^2 + a^2\right) - ma}{\Delta_{\rm BL}} , \tag{A.47}$$

which acts on radial modes. The coefficient can be fixed by considering the asymptotic limit approaching infinity and the horizon. This analysis was previously carried out in Ref. [396, 397] for real ω. Due to our choice of gauge (ORG), the results are similar to those in Section III.C of Ref. [396]. Here, we briefly review and extend the procedure to complex ω

$$\frac{1}{32}\Delta_{\rm BL}^2 \left(\hat{\mathcal{D}}_0^\dagger\right)^4 \left[\Delta_{\rm BL}^2 \bar{\mathring{\Phi}}_{\rm ORG}\right] = \sum_{\ell,m,n} \frac{\bar{C}_{\ell mn}}{32\sqrt{2\pi}} \Delta_{\rm BL}^2 \left(\partial_r - i\frac{\bar{K}_{mn}}{\Delta_{\rm BL}}\right)^4 \left[\Delta_{\rm BL}^2 \, {}_{+2}\bar{R}_{\ell mn}(r) \, {}_{+2}S_{\ell mn}(\theta) e^{-im\phi + i\bar{\omega}_{mn}t}\right] . \tag{A.48}$$

By relabelling (m, n) to $(-m, -n)$ and employing the identities ${}_sS_{\ell mn}(\theta) = (-1)^{s+m} {}_{-s}S_{l-m-n}(\theta)$, ${}_s\bar{R}_{\ell mn} = {}_sR_{l-m-n}$, $\bar{K}_{mn} = -K_{-m-ns}$ and $\bar{\omega}_{mn} = -\omega_{-m-n}$, the equation transforms into

$$\frac{1}{32}\Delta_{\rm BL}^2 \left(\hat{\mathcal{D}}_0^\dagger\right)^4 \left[\Delta_{\rm BL}^2 \bar{\mathring{\Phi}}_{\rm ORG}\right] = \sum_{\ell,m,n} (-1)^m \frac{\bar{C}_{\ell-m-n}}{32\sqrt{2\pi}} \Delta_{\rm BL}^2 \left(\hat{\mathcal{D}}_{mn}^\dagger\right)^4 \left[\Delta_{\rm BL}^2 \, {}_{+2}\bar{R}_{\ell mn}(r) \, {}_{-2}S_{\ell mn}(\theta) e^{im\phi - i\omega_{mn}t}\right] . \tag{A.49}$$

When considering Eq. (A.38), we obtain

$${}_{-2}Z_{\ell mn} \, {}_{-2}R_{\ell mn}(r) = \frac{(-1)^m}{32} \bar{C}_{\ell-m-n} \Delta_{\rm BL}^2 \left(\hat{\mathcal{D}}_{mn}^\dagger\right)^4 \left[\Delta_{\rm BL}^2 \, {}_{+2}R_{\ell mn}(r)\right] . \tag{A.50}$$

The asymptotic behavior of ${}_sR_{\ell mn}$ is as follows [91, 401]

$$\lim_{r^* \to \infty} {}_sR_{\ell mn}(r^*) \sim \begin{cases} \frac{e^{-i\omega r^*}}{r} & : \text{ ingoing wave} \\ \frac{e^{i\omega r^*}}{r^{2s+1}} & : \text{ outgoing wave.} \end{cases} \tag{A.51}$$

$$\lim_{r^*\to-\infty} {}_sR_{\ell mn}\left(r^*\right) \sim \begin{cases} e^{ik_{mn}r^*} & : \text{ ingoing (out of BH)} \\ \Delta_{\rm BL}^{-s} e^{-ik_{mn}r^*} & : \text{ outgoing (into BH).} \end{cases} \tag{A.52}$$

where $k_{mn} = \omega_{mn} - \frac{ma}{2Mr_+}$, and r^* is the tortoise coordinate, which is given by

$$r^* = r + \frac{2M}{r_+ - r_-}\left[r_+ \ln\left(\frac{r-r_+}{2M}\right) - r_- \ln\left(\frac{r-r_-}{2M}\right)\right] . \tag{A.53}$$

If $f(r)$ is a solution to the radial Teukolsky equation Eq. (A.41) with spin s, then $\Delta_{\rm BL}^s \bar{f}(r)$ is a solution to the radial Teukolsky equation with spin $-s$. For generic modes with $\omega_{mn} \neq 0$, the asymptotic behavior suggests that this relation swaps physical (retarded) boundary conditions with unphysical (advanced) ones. We denote the relationship as

$${}_{-s}R^{\#}_{\ell mn} \equiv \Delta^s_{\rm BL}\, {}_s\bar{R}_{\ell mn} . \tag{A.54}$$

With this in mind, we have

$${}_{-2}Z_{\ell mn}\, {}_{-2}R_{\ell mn}(r) = \frac{(-1)^m}{32}\bar{C}_{\ell -m -n}\Delta^2_{\rm BL}\left(\hat{\mathcal{D}}^\dagger_{mn}\right)^4\left[{}_{-2}R^{\#}_{\ell mn}\right] . \tag{A.55}$$

Inserting the asymptotic behavior into Eq. (A.55), we find

$$C_{\ell mn} = \frac{2}{\omega^4_{mn}}(-1)^{\ell+m}\, {}_{-2}Z_{\ell mn} . \tag{A.56}$$

Here, we used the following relationship

$${}_{-2}\bar{Z}_{lmn} = (-1)^l\, {}_{-2}Z_{l-m-n} . \tag{A.57}$$

Consequently, once we have the solution set $\{\omega, \Psi_4^{(1)}\}$ for the Teukolsky equation with $s = -2$, we are able to reconstruct the first-order metric perturbation h_{ab}. After reconstructing the metric, we verify its validity by substituting it into the linearized Einstein equation $\hat{\mathcal{E}}_{ab}(h) = 0$.

We calculate the quasinormal mode using the `qnm` package [353], which employs Leaver's method for the radial equation and the Cook-Zalutskiy spectral approach for the angular sector [90, 91]. Furthermore, we use the pseudospectral method to obtain solutions to the radial Teukolsky equation. Here, we briefly illustrate our steps. We convert the asymptotic behavior into coordinate r [91]

$$\lim_{r\to\infty} {}_sR_{\ell mn}(r) \sim r^{-1-2s+2i\omega_{mn}M} e^{i\omega_{mn}r} . \tag{A.58}$$

$$\lim_{r\to r_+} {}_sR_{\ell mn}(r) \sim (r-r_+)^{-s-i\sigma_+} . \tag{A.59}$$

where $\sigma_+ = \frac{2\omega_{mn}Mr_+ - ma}{r_+ - r_-}$. Then we can define a new radial function ${}_s\tilde{R}_{\ell mn}(r)$ by

$${}_sR_{\ell mn}(r) = (r-r_+)^{-s-i\sigma_+}\, r^{-1-s+2i\omega_{mn}M+i\sigma_+} e^{i\omega_{mn}r}\, {}_s\tilde{R}_{\ell mn}(r) , \tag{A.60}$$

where ${}_s\tilde{R}_{\ell mn}(r)$ is regular at the BH horizon and infinity, and we normalize it by applying

$$\lim_{r\to\infty} {}_s\tilde{R}_{\ell mn}(r) = 1\,. \tag{A.61}$$

We can expand ${}_s\tilde{R}_{\ell mn}(r)$ as a series of Chebyshev polynomials and obtain ${}_sS_{\ell mn}(\theta)$ in terms of spin-weighted spherical functions as in Ref. [91]. As a result, we can use our numerical results and evaluate them at any point (t, r, θ, ϕ) of spacetime in the subsequent ray tracing section. To ensure the perturbation metric is flawless, we also verified $\hat{\mathcal{E}}_{ab}(h) = 0$ numerically.

A.3 RADIATED ENERGY

In this section, we estimate the radiated energy of a single mode after truncation. The energy flux is given by [212]

$$\frac{\mathrm{d}E}{\mathrm{d}t} = \lim_{r\to\infty}\left[\frac{r^2}{16\pi}\int_\Omega \left|\int_{+\infty}^{t} \Psi_4^{(1)} d\tilde{t}\right|^2 \mathrm{d}\Omega\right]\,, \tag{A.62}$$

Then the total energy emitted can be calculated as

$$E_{\rm tot} = \int_{t_0}^{\infty} \frac{\mathrm{d}E}{\mathrm{d}t}\,\mathrm{d}t\,. \tag{A.63}$$

where $t_0 = r_*(r_o)$. This total energy satisfies the condition $E_{\rm tot}/M \lessapprox 3\%$ [212]. Assuming that only the $\ell = m = 2$ mode dominates the radiated energy, this relationship leads to

$$|{}_sZ| \lessapprox 0.24\,. \tag{A.64}$$

It is important to note that this approach differs slightly from truncating the metric using $H(t - r_*)$. However, it should provide a sufficiently accurate estimation for our purposes.

BIBLIOGRAPHY

[1] Robert M. Wald. *General Relativity*. Chicago, USA: Chicago Univ. Pr., 1984. DOI: 10.7208/chicago/9780226870373.001.0001.

[2] Roy P. Kerr. "Gravitational field of a spinning mass as an example of algebraically special metrics." In: *Phys. Rev. Lett.* 11 (1963), pp. 237–238. DOI: 10.1103/PhysRevLett.11.237.

[3] B. P. Abbott et al. "Observation of Gravitational Waves from a Binary Black Hole Merger." In: *Phys. Rev. Lett.* 116.6 (2016), p. 061102. DOI: 10.1103/PhysRevLett.116.061102. arXiv: 1602.03837 [gr-qc].

[4] Kazunori Akiyama et al. "First M87 Event Horizon Telescope Results. I. The Shadow of the Supermassive Black Hole." In: *Astrophys. J. Lett.* 875 (2019), p. L1. DOI: 10.3847/2041-8213/ab0ec7. arXiv: 1906.11238 [astro-ph.GA].

[5] B. P. Abbott et al. "Prospects for observing and localizing gravitational-wave transients with Advanced LIGO, Advanced Virgo and KAGRA." In: *Living Rev. Rel.* 19 (2016), p. 1. DOI: 10.1007/s41114-020-00026-9. arXiv: 1304.0670 [gr-qc].

[6] S.D. Mathur. "What Exactly is the Information Paradox?" In: *Physics of Black Holes: A Guided Tour*. Ed. by Eleftherios Papantonopoulos. Berlin, Heidelberg: Springer Berlin Heidelberg, 2009, pp. 3–48. ISBN: 978-3-540-88460-6. DOI: 10.1007/978-3-540-88460-6_1. URL: https://doi.org/10.1007/978-3-540-88460-6_1.

[7] David Wallace. "Why Black Hole Information Loss is Paradoxical." In: *Beyond Spacetime*. Ed. by Nick Huggett, Keizo Matsubara, and Christian Wüthrich. Apr. 2020, pp. 209–236. DOI: 10.1017/9781108655705.013. arXiv: 1710.03783 [gr-qc].

[8] B. P. Abbott et al. "GWTC-1: A Gravitational-Wave Transient Catalog of Compact Binary Mergers Observed by LIGO and Virgo during the First and Second Observing Runs." In: *Phys. Rev. X* 9.3 (2019), p. 031040. DOI: 10.1103/PhysRevX.9.031040. arXiv: 1811.12907 [astro-ph.HE].

[9] Kazunori Akiyama et al. "First Sagittarius A* Event Horizon Telescope Results. I. The Shadow of the Supermassive Black Hole in the Center of the Milky Way." In: *Astrophys. J. Lett.* 930.2 (2022), p. L12. DOI: 10.3847/2041-8213/ac6674. arXiv: 2311.08680 [astro-ph.HE].

[10] Samir D. Mathur. "The Information paradox: A Pedagogical introduction." In: *Class. Quant. Grav.* 26 (2009). Ed. by A. M. Uranga, p. 224001. DOI: 10.1088/0264-9381/26/22/224001. arXiv: 0909.1038 [hep-th].

[11] Vitor Cardoso and Paolo Pani. "Testing the nature of dark compact objects: a status report." In: *Living Rev. Rel.* 22.1 (2019), p. 4. DOI: 10.1007/s41114-019-0020-4. arXiv: 1904.05363 [gr-qc].

[12] Mateja Bošković and Enrico Barausse. "Soliton boson stars, Q-balls and the causal Buchdahl bound." In: *JCAP* 02.02 (2022), p. 032. DOI: 10.1088/1475-7516/2022/02/032. arXiv: 2111.03870 [gr-qc].

[13] Burkhard Kleihaus, Jutta Kunz, and Meike List. "Rotating boson stars and Q-balls." In: *Phys. Rev. D* 72 (2005), p. 064002. DOI: 10.1103/PhysRevD.72.064002. arXiv: gr-qc/0505143.

[14] Burkhard Kleihaus, Jutta Kunz, Meike List, and Isabell Schaffer. "Rotating Boson Stars and Q-Balls. II. Negative Parity and Ergoregions." In: *Phys. Rev. D* 77 (2008), p. 064025. DOI: 10.1103/PhysRevD.77.064025. arXiv: 0712.3742 [gr-qc].

[15] Vitor Cardoso, Edgardo Franzin, and Paolo Pani. "Is the gravitational-wave ringdown a probe of the event horizon?" In: *Phys. Rev. Lett.* 116.17 (2016). [Erratum: Phys.Rev.Lett. 117, 089902 (2016)], p. 171101. DOI: 10.1103/PhysRevLett.116.171101. arXiv: 1602.07309 [gr-qc].

[16] Enrico Barausse, Richard Brito, Vitor Cardoso, Irina Dvorkin, and Paolo Pani. "The stochastic gravitational-wave background in the absence of horizons." In: *Class. Quant. Grav.* 35.20 (2018), 20LT01. DOI: 10.1088/1361-6382/aae1de. arXiv: 1805.08229 [gr-qc].

[17] Gianfranco Bertone and Tim Tait M. P. "A new era in the search for dark matter." In: *Nature* 562.7725 (2018), pp. 51–56. DOI: 10.1038/s41586-018-0542-z. arXiv: 1810.01668 [astro-ph.CO].

[18] R. D. Peccei and Helen R. Quinn. "CP Conservation in the Presence of Pseudoparticles." In: *Phys. Rev. Lett.* 38 (1977), pp. 1440–1443. DOI: 10.1103/PhysRevLett.38.1440.

[19] C. B. Adams et al. "Axion Dark Matter." In: *Snowmass 2021*. Mar. 2022. arXiv: 2203.14923 [hep-ex].

[20] Steven L. Liebling and Carlos Palenzuela. "Dynamical Boson Stars." In: *Living Rev. Rel.* 15 (2012). [Living Rev. Rel.20,no.1,5(2017)], p. 6. DOI: 10.12942/lrr-2012-6,10.1007/s41114-017-0007-y. arXiv: 1202.5809 [gr-qc].

[21] Richard Brito, Vitor Cardoso, Carlos A. R. Herdeiro, and Eugen Radu. "Proca stars: Gravitating Bose–Einstein condensates of massive spin 1 particles." In: *Phys. Lett. B* 752 (2016), pp. 291–295. DOI: 10.1016/j.physletb.2015.11.051. arXiv: 1508.05395 [gr-qc].

[22] Nils Siemonsen. "Bosonic fields in strong-field gravity." PhD thesis. U. Waterloo (main), 2023.

[23] Sidney R. Coleman. "Q Balls." In: *Nucl. Phys. B* 262 (1985). [Erratum: Nucl.Phys.B 269, 744 (1986)], p. 263. DOI: 10.1016/0550-3213(86)90520-1.

[24] B. P. Abbott et al. "Properties of the Binary Black Hole Merger GW150914." In: *Phys. Rev. Lett.* 116.24 (2016), p. 241102. DOI: 10.1103/PhysRevLett.116.241102. arXiv: 1602.03840 [gr-qc].

[25] B. P. Abbott et al. "GW170817: Observation of Gravitational Waves from a Binary Neutron Star Inspiral." In: *Phys. Rev. Lett.* 119.16 (2017), p. 161101. DOI: 10.1103/PhysRevLett.119.161101. arXiv: 1710.05832 [gr-qc].

[26] R. Abbott et al. "Observation of Gravitational Waves from Two Neutron Star–Black Hole Coalescences." In: *Astrophys. J. Lett.* 915.1 (2021), p. L5. DOI: 10.3847/2041-8213/ac082e. arXiv: 2106.15163 [astro-ph.HE].

[27] R. Abbott et al. "GW190521: A Binary Black Hole Merger with a Total Mass of $150M_{\odot}$." In: *Phys. Rev. Lett.* 125.10 (2020), p. 101102. DOI: 10.1103/PhysRevLett.125.101102. arXiv: 2009.01075 [gr-qc].

[28] R. Abbott et al. "Tests of General Relativity with GWTC-3." In: (Dec. 2021). arXiv: 2112.06861 [gr-qc].

[29] Michele Maggiore et al. "Science Case for the Einstein Telescope." In: *JCAP* 03 (2020), p. 050. DOI: 10.1088/1475-7516/2020/03/050. arXiv: 1912.02622 [astro-ph.CO].

[30] Matthew Evans et al. "A Horizon Study for Cosmic Explorer: Science, Observatories, and Community." In: (Sept. 2021). arXiv: 2109.09882 [astro-ph.IM].

[31] Pau Amaro-Seoane et al. "Laser Interferometer Space Antenna." In: (Feb. 2017). arXiv: 1702.00786 [astro-ph.IM].

[32] Gabriella Agazie et al. "The NANOGrav 15 yr Data Set: Evidence for a Gravitational-wave Background." In: *Astrophys. J. Lett.* 951.1 (2023), p. L8. DOI: 10.3847/2041-8213/acdac6. arXiv: 2306.16213 [astro-ph.HE].

[33] Zhen Zhong, Vitor Cardoso, and Elisa Maggio. "Instability of ultracompact horizonless spacetimes." In: *Phys. Rev. D* 107.4 (2023), p. 044035. DOI: 10.1103/PhysRevD.107.044035. arXiv: 2211.16526 [gr-qc].

[34] John L. Friedman. "Generic instability of rotating relativistic stars." In: *Commun. Math. Phys.* 62.3 (1978), pp. 247–278. DOI: 10.1007/BF01202527.

[35] Vitor Cardoso, Paolo Pani, Mariano Cadoni, and Marco Cavaglia. "Instability of hyper-compact Kerr-like objects." In: *Class. Quant. Grav.* 25 (2008), p. 195010. DOI: 10.1088/0264-9381/25/19/195010. arXiv: 0808.1615 [gr-qc].

[36] Richard Brito, Vitor Cardoso, and Paolo Pani. "Superradiance: New Frontiers in Black Hole Physics." In: *Lect. Notes Phys.* 906 (2015), pp.1–237. DOI: 10.1007/978-3-319-19000-6. arXiv: 1501.06570 [gr-qc].

[37] Sean A. Hayward. "Formation and evaporation of regular black holes." In: *Phys. Rev. Lett.* 96 (2006), p. 031103. DOI: 10.1103/PhysRevLett.96.031103. arXiv: gr-qc/0506126.

[38] Vitor Cardoso, João L. Costa, José Natário, and Zhen Zhong. "Energy extraction from bouncing geometries." In: *Phys. Rev. D* 108.2 (2023), p. 024071. DOI: 10.1103/PhysRevD.108.024071. arXiv: 2304.08520 [gr-qc].

[39] Vitor Cardoso, Rodrigo Vicente, and Zhen Zhong. "Energy Extraction from Q-balls and Other Fundamental Solitons." In: *Phys. Rev. Lett.* 131.11 (2023), p. 111602. DOI: 10.1103/PhysRevLett.131.111602. arXiv: 2307.13734 [hep-th].

[40] Vitor Cardoso, Taishi Ikeda, Zhen Zhong, and Miguel Zilhão. "Piercing of a boson star by a black hole." In: *Phys. Rev. D* 106.4 (2022), p. 044030. DOI: 10.1103/PhysRevD.106.044030. arXiv: 2206.00021 [gr-qc].

[41] Zhen Zhong, Vitor Cardoso, Taishi Ikeda, and Miguel Zilhão. "Piercing of a solitonic boson star by a black hole." In: *Phys. Rev. D* 108.8 (2023), p. 084051. DOI: 10.1103/PhysRevD.108.084051. arXiv: 2307.02548 [gr-qc].

[42] Steven L. Detweiler. "KLEIN-GORDON EQUATION AND ROTATING BLACK HOLES." In: *Phys. Rev.* D22 (1980), pp. 2323–2326. DOI: 10.1103/PhysRevD.22.2323.

[43] Daniel Baumann, Horng Sheng Chia, John Stout, and Lotte ter Haar. "The Spectra of Gravitational Atoms." In: *JCAP* 12 (2019), p. 006. DOI: 10.1088/1475-7516/2019/12/006. arXiv: 1908.10370 [gr-qc].

[44] Richard H. Price. "Nonspherical perturbations of relativistic gravitational collapse. 1. Scalar and gravitational perturbations." In: *Phys. Rev. D* 5 (1972), pp. 2419–2438. DOI: 10.1103/PhysRevD.5.2419.

[45] Carsten Gundlach, Richard H. Price, and Jorge Pullin. "Late time behavior of stellar collapse and explosions: 1. Linearized perturbations." In: *Phys. Rev. D* 49 (1994), pp. 883–889. DOI: 10.1103/PhysRevD.49.883. arXiv: gr-qc/9307009.

[46] Vitor Cardoso, Gregorio Carullo, Marina De Amicis, Francisco Duque, Takuya Katagiri, David Pereniguez, Jaime Redondo-Yuste, Thomas F. M. Spieksma, and Zhen Zhong. "Hushing black holes: Tails in dynamical spacetimes." In: *Phys. Rev. D* 109.12 (2024), p. L121502. DOI: 10.1103/PhysRevD.109.L121502. arXiv: 2405.12290 [gr-qc].

[47] Saul A. Teukolsky. "Perturbations of a rotating black hole. 1. Fundamental equations for gravitational electromagnetic and neutrino field perturbations." In: *Astrophys. J.* 185 (1973), pp. 635–647. DOI: 10.1086/152444.

[48] Zhen Zhong, Vitor Cardoso, and Yifan Chen. *Dynamical Lensing Tomography of Black Hole Ringdown*. Aug. 2024. arXiv: 2408.10303 [gr-qc].

[49] Matt Visser. "The Kerr spacetime: A Brief introduction." In: *Kerr Fest: Black Holes in Astrophysics, General Relativity and Quantum Gravity*. June 2007. arXiv: 0706.0622 [gr-qc].

[50] R. Penrose. "Gravitational collapse: The role of general relativity." In: *Riv. Nuovo Cim.* 1 (1969), pp. 252–276. DOI: 10.1023/A:1016578408204.

[51] Robert H. Boyer and Richard W. Lindquist. "Maximal analytic extension of the Kerr metric." In: *J. Math. Phys.* 8 (1967), p. 265. DOI: 10.1063/1.1705193.

[52] Charles W. Misner, K. S. Thorne, and J. A. Wheeler. *Gravitation*. San Francisco: W. H. Freeman, 1973. ISBN: 978-0-7167-0344-0, 978-0-691-17779-3.

[53] Eric Poisson and W. Israel. "Inner-horizon instability and mass inflation in black holes." In: *Phys. Rev. Lett.* 63 (1989), pp. 1663–1666. DOI: 10.1103/PhysRevLett.63.1663.

[54] Amos Ori. "Inner structure of a charged black hole: An exact mass-inflation solution." In: *Phys. Rev. Lett.* 67 (1991), pp. 789–792. DOI: 10.1103/PhysRevLett.67.789.

[55] J. M. Bardeen. "Timelike and null geodesics in the Kerr metric." In: *Proceedings, Ecole d'Eté de Physique Théorique: Les Astres Occlus : Les Houches, France, August, 1972, 215-240* (1973). Ed. by Cécile DeWitt and Bryce Seligman DeWitt, pp. 215–240.

[56] J.-P. Luminet. "Image of a spherical black hole with thin accretion disk." In: *Astron. Astrophys.* 75 (1979), pp. 228–235.

[57] Marek A. Abramowicz, Wlodek Kluzniak, and Jean-Pierre Lasota. "No observational proof of the black hole event-horizon." In: *Astron. Astrophys.* 396 (2002), pp. L31–L34. DOI: 10.1051/0004-6361:20021645. arXiv: astro-ph/0207270.

[58] J. H. Jeans. "The Stability of a Spherical Nebula." In: *Phil. Trans. A. Math. Phys. Eng. Sci.* 199.312-320 (1902), pp. 1–53. DOI: 10.1098/rsta.1902.0012.

[59] Subrahmanyan Chandrasekhar. *Hydrodynamic and hydromagnetic instability*. Dover, 1981. DOI: 10.1063/1.3058072.

[60] R. Penrose and R. M. Floyd. "Extraction of rotational energy from a black hole." In: *Nature* 229 (1971), pp. 177–179. DOI: 10.1038/physci229177a0.

[61] Ya. B. Zel'dovich. In: *Pis'ma Zh. Eksp. Teor. Fiz.* 14 (1971), 270 [JETP Lett. **14**, 180 (1971)].

[62] Ya. B. Zel'dovich. In: *Zh. Eksp. Teor. Fiz* 62 (1972), 2076 [Sov.Phys. JETP **35**, 1085 (1972)].

[63] R.D. Blandford and R.L. Znajek. "Electromagnetic extractions of energy from Kerr black holes." In: *Mon.Not.Roy.Astron.Soc.* 179 (1977), pp. 433–456.

[64] J. L. Friedman. "Ergosphere instability." In: *Communications in Mathematical Physics* 63 (1978), pp. 243–255.

[65] N. Comins and B. F. Schutz. "On the Ergoregion Instability." In: *Proceedings of the Royal Society of London. Series A, Mathematical and Physical Sciences* 364.1717 (1978), pp. 211–226. ISSN: 00804630. URL: http://www.jstor.org/stable/79759.

[66] Georgios Moschidis. "A Proof of Friedman's Ergosphere Instability for Scalar Waves." In: *Commun. Math. Phys.* 358.2 (2018), pp. 437–520. DOI: 10.1007/s00220-017-3010-y. arXiv: 1608.02035 [math.AP].

[67] Rodrigo Vicente, Vitor Cardoso, and Jorge C. Lopes. "Penrose process, superradiance, and ergoregion instabilities." In: *Phys. Rev. D* 97.8 (2018), p. 084032. DOI: 10.1103/PhysRevD.97.084032. arXiv: 1803.08060 [gr-qc].

[68] S. Yoshida and Y. Eriguchi. "Ergoregion instability revisited - a new and general method for numerical analysis of stability." In: *Mon.Not.Roy.Astron.Soc.* 282 (1996), pp. 580–586.

[69] Kostas D. Kokkotas, J. Ruoff, and N. Andersson. "The w-mode instability of ultracompact relativistic stars." In: *Phys. Rev. D* 70 (2004), p. 043003. DOI: 10.1103/PhysRevD.70.043003. arXiv: astro-ph/0212429.

[70] Vitor Cardoso, Oscar J. C. Dias, Jordan L. Hovdebo, and Robert C. Myers. "Instability of non-supersymmetric smooth geometries." In: *Phys. Rev. D* 73 (2006), p. 064031. DOI: 10.1103/PhysRevD.73.064031. arXiv: hep-th/0512277.

[71] Vitor Cardoso, Paolo Pani, Mariano Cadoni, and Marco Cavaglia. "Ergoregion instability of ultracompact astrophysical objects." In: *Phys. Rev. D* 77 (2008), p. 124044. DOI: 10.1103/PhysRevD.77.124044. arXiv: 0709.0532 [gr-qc].

[72] Cecilia B.M.H. Chirenti and Luciano Rezzolla. "On the ergoregion instability in rotating gravastars." In: *Phys.Rev.* D78 (2008), p. 084011. DOI: 10.1103/PhysRevD.78.084011. arXiv: 0808.4080 [gr-qc].

[73] Paolo Pani, Enrico Barausse, Emanuele Berti, and Vitor Cardoso. "Gravitational instabilities of superspinars." In: *Phys. Rev. D* 82 (2010), p. 044009. DOI: 10.1103/PhysRevD.82.044009. arXiv: 1006.1863 [gr-qc].

[74] Shahar Hod. "Ultra-spinning exotic compact objects supporting static massless scalar field configurations." In: *Phys. Lett. B* 774 (2017), p. 582. DOI: 10.1016/j.physletb.2017.10.022. arXiv: 1708.09399 [hep-th].

[75] Elisa Maggio, Paolo Pani, and Valeria Ferrari. "Exotic Compact Objects and How to Quench their Ergoregion Instability." In: *Phys. Rev. D* 96.10 (2017), p. 104047. DOI: 10.1103/PhysRevD.96.104047. arXiv: 1703.03696 [gr-qc].

[76] Elisa Maggio, Vitor Cardoso, Sam R. Dolan, and Paolo Pani. "Ergoregion instability of exotic compact objects: electromagnetic and gravitational perturbations and the role of absorption." In: *Phys. Rev. D* 99.6 (2019), p. 064007. DOI: 10.1103/PhysRevD.99.064007. arXiv: 1807.08840 [gr-qc].

[77] Joe Keir. "Slowly decaying waves on spherically symmetric spacetimes and ultracompact neutron stars." In: *Class. Quant. Grav.* 33.13 (2016), p. 135009. DOI: 10.1088/0264-9381/33/13/135009. arXiv: 1404.7036 [gr-qc].

[78] Vitor Cardoso, Luís C. B. Crispino, Caio F. B. Macedo, Hirotada Okawa, and Paolo Pani. "Light rings as observational evidence for event horizons: long-lived modes, ergoregions and nonlinear instabilities of ultracompact objects." In: *Phys. Rev. D* 90.4 (2014), p. 044069. DOI: 10.1103/PhysRevD.90.044069. arXiv: 1406.5510 [gr-qc].

[79] Pedro V. P. Cunha, Emanuele Berti, and Carlos A. R. Herdeiro. "Light-Ring Stability for Ultracompact Objects." In: *Phys. Rev. Lett.* 119.25 (2017), p. 251102. DOI: 10.1103/PhysRevLett.119.251102. arXiv: 1708.04211 [gr-qc].

[80] Pedro V. P. Cunha, Carlos Herdeiro, Eugen Radu, and Nicolas Sanchis-Gual. *The fate of the light-ring instability.* July 2022. arXiv: 2207.13713 [gr-qc].

[81] Leandro A. Oliveira, Vitor Cardoso, and Luís C. B. Crispino. "Ergoregion instability: The hydrodynamic vortex." In: *Phys. Rev. D* 89.12 (2014), p. 124008. DOI: 10.1103/PhysRevD.89.124008. arXiv: 1405.4038 [gr-qc].

[82] Shahar Hod. "Stationary bound-state scalar configurations supported by rapidly-spinning exotic compact objects." In: *Phys. Lett. B* 770 (2017), pp. 186–192. DOI: 10.1016/j.physletb.2017.04.065. arXiv: 1803.07093 [gr-qc].

[83] Rajes Ghosh and Sudipta Sarkar. "Light rings of stationary spacetimes." In: *Phys. Rev. D* 104.4 (2021), p. 044019. DOI: 10.1103/PhysRevD.104.044019. arXiv: 2107.07370 [gr-qc].

[84] Justin L. Ripley. "Computing the quasinormal modes and eigenfunctions for the Teukolsky equation using horizon penetrating, hyperboloidally compactified coordinates." In: *Class. Quant. Grav.* 39.14 (2022), p. 145009. DOI: 10.1088/1361-6382/ac776d. arXiv: 2202.03837 [gr-qc].

[85] Anil Zenginoglu. "A Geometric framework for black hole perturbations." In: *Phys. Rev. D* 83 (2011), p. 127502. DOI: 10.1103/PhysRevD.83.127502. arXiv: 1102.2451 [gr-qc].

[86] Emanuele Berti, Vitor Cardoso, and Marc Casals. "Eigenvalues and eigenfunctions of spin-weighted spheroidal harmonics in four and higher dimensions." In: *Phys. Rev. D* 73 (2006). [Erratum: Phys.Rev.D 73, 109902 (2006)], p. 024013. DOI: 10.1103/PhysRevD.73.109902. arXiv: gr-qc/0511111.

[87] John David Jackson. *Classical Electrodynamics*. Wiley, 1998. ISBN: 978-0-471-30932-1.

[88] Emanuele Berti, Vitor Cardoso, and Andrei O. Starinets. "Quasinormal modes of black holes and black branes." In: *Class. Quant. Grav.* 26 (2009), p. 163001. DOI: 10.1088/0264-9381/26/16/163001. arXiv: 0905.2975 [gr-qc].

[89] E. W. Leaver. "An Analytic representation for the quasi normal modes of Kerr black holes." In: *Proc. Roy. Soc. Lond. A* 402 (1985), pp. 285–298. DOI: 10.1098/rspa.1985.0119.

[90] Edward W Leaver. "Solutions to a generalized spheroidal wave equation: Teukolsky's equations in general relativity, and the two-center problem in molecular quantum mechanics." In: *Journal of mathematical physics* 27.5 (1986), pp. 1238–1265.

[91] Gregory B. Cook and Maxim Zalutskiy. "Gravitational perturbations of the Kerr geometry: High-accuracy study." In: *Phys. Rev. D* 90.12 (2014), p. 124021. DOI: 10.1103/PhysRevD.90.124021. arXiv: 1410.7698 [gr-qc].

[92] C. Flammer. *Spheroidal Wave Functions*. Stanford University Press.

[93] Tomohiro Oguchi. "Eigenvalues of Spheroidal Wave Functions and Their Branch Points for Complex Values of Propagation Constants." In: *Radio Science* 5.8-9 (1970), pp. 1207–1214. DOI: https://doi.org/10.1029/RS005i008p01207.

[94] Benjamin E. Barrowes, Kevin O'Neill, Tomasz M. Grzegorczyk, and Jin A. Kong. "On the Asymptotic Expansion of the Spheroidal Wave Function and Its Eigenvalues for Complex Size Parameter." In: *Studies in Applied Mathematics* 113.3 (2004), pp. 271–301. DOI: https://doi.org/10.1111/j.0022-2526.2004.01526.x. eprint: https://onlinelibrary.wiley.com/doi/pdf/10.1111/j.0022-2526.2004.01526.x. URL: https://onlinelibrary.wiley.com/doi/abs/10.1111/j.0022-2526.2004.01526.x.

[95] Sheehan Olver and Alex Townsend. "A fast and well-conditioned spectral method." In: *siam REVIEW* 55.3 (2013), pp. 462–489. DOI: https://doi.org/10.1137/120865458. arXiv: 1202.1347 [math.NA].

[96] T. A Driscoll, N. Hale, and L. N. Trefethen. *Chebfun Guide*. Pafnuty Publications, 2014. URL: http://www.chebfun.org/docs/guide/.

[97] Sheehan Olver and Alex Townsend. "A practical framework for infinite-dimensional linear algebra." In: *Proceedings of the 1st Workshop for High Performance Technical Computing in Dynamic Languages – HPTCDL '14*. IEEE, 2014.

[98] Piotr Kowalczyk. "Complex Root Finding Algorithm Based on Delaunay Triangulation." In: *ACM Trans. Math. Softw.* 41.3 (June 2015). ISSN: 0098-3500. DOI: 10.1145/2699457. URL: https://doi.org/10.1145/2699457.

[99] Piotr Kowalczyk. "Global Complex Roots and Poles Finding Algorithm Based on Phase Analysis for Propagation and Radiation Problems." In: *IEEE Transactions on Antennas and Propagation* 66.12 (2018), pp. 7198–7205. DOI: 10.1109/TAP.2018.2869213.

[100] Forrest Gasdia. *RootsAndPoles.jl: Global complex Roots and Poles Finding in the Julia programming language*. 2019. DOI: 10.5281/zenodo.3525387. URL: https://github.com/fgasdia/RootsAndPoles.jl.

[101] Bas Nijholt, Joseph Weston, Jorn Hoofwijk, and Anton Akhmerov. *Adaptive: parallel active learning of mathematical functions*. 2019. DOI: 10.5281/zenodo.1182437.

[102] Sam R. Dolan. "Superradiant instabilities of rotating black holes in the time domain." In: *Phys. Rev. D* 87.12 (2013), p. 124026. DOI: 10.1103/PhysRevD.87.124026. arXiv: 1212.1477 [gr-qc].

[103] Alexandru Dima and Enrico Barausse. "Numerical investigation of plasma-driven superradiant instabilities." In: *Class. Quant. Grav.* 37.17 (2020), p. 175006. DOI: 10.1088/1361-6382/ab9ce0. arXiv: 2001.11484 [gr-qc].

[104] Emanuele Berti, Vitor Cardoso, Jose A. Gonzalez, and Ulrich Sperhake. "Mining information from binary black hole mergers: A Comparison of estimation methods for complex exponentials in noise." In: *Phys. Rev. D* 75 (2007), p. 124017. DOI: 10.1103/PhysRevD.75.124017. arXiv: gr-qc/0701086.

[105] John Denholm Lambert et al. *Numerical methods for ordinary differential systems*. Vol. 146. Wiley New York, 1991.

[106] Shahar Hod. "Onset of superradiant instabilities in rotating spacetimes of exotic compact objects." In: *JHEP* 06 (2017), p. 132. DOI: 10.1007/JHEP06(2017)132. arXiv: 1704.05856 [hep-th].

[107] Milton Abramowitz and Irene A. Stegun. *Handbook of Mathematical Functions*. GPO, 1964.

[108] R. B. Paris. *Asymptotics of a Gauss hypergeometric function with large parameters, III: Application to the Legendre functions of large imaginary order and real degree*. 2016. DOI: 10.48550/ARXIV.1609.08365. URL: https://arxiv.org/abs/1609.08365.

[109] S. W. Hawking. "Black hole explosions." In: *Nature* 248 (1974), pp. 30–31. DOI: 10.1038/248030a0.

[110] Abhay Ashtekar, Javier Olmedo, and Parampreet Singh. "Regular Black Holes from Loop Quantum Gravity." In: *Regular Black Holes: Towards a New Paradigm of Gravitational Collapse*. Ed. by Cosimo Bambi. Singapore: Springer Nature Singapore, 2023, pp. 235–282. ISBN: 978-981-99-1596-5. DOI: 10.1007/978-981-99-1596-5_7. URL: https://doi.org/10.1007/978-981-99-1596-5%5C_7.

[111] Valeri P. Frolov and Andrei Zelnikov. "Quantum radiation from an evaporating nonsingular black hole." In: *Phys. Rev. D* 95.12 (2017), p. 124028. DOI: 10.1103/PhysRevD.95.124028. arXiv: 1704.03043 [hep-th].

[112] Denis Pollney, Christian Reisswig, Erik Schnetter, Nils Dorband, and Peter Diener. "High accuracy binary black hole simulations with an extended wave zone." In: *Phys. Rev. D* 83 (2011), p. 044045. DOI: 10.1103/PhysRevD.83.044045. arXiv: 0910.3803 [gr-qc].

[113] Valeria Ferrari and Bahram Mashhoon. "New approach to the quasinormal modes of a black hole." In: *Phys. Rev.* D30 (1984), pp. 295–304. DOI: 10.1103/PhysRevD.30.295.

[114] Vitor Cardoso, Alex S. Miranda, Emanuele Berti, Helvi Witek, and Vilson T. Zanchin. "Geodesic stability, Lyapunov exponents and quasinormal modes." In: *Phys. Rev. D* 79 (2009), p. 064016. DOI: 10.1103/PhysRevD.79.064016. arXiv: 0812.1806 [hep-th].

[115] Roger Penrose. "Structure of space-time." In: *Battelle Rencontres*. 1968, pp. 121–235.

[116] Mihalis Dafermos. "The Interior of charged black holes and the problem of uniqueness in general relativity." In: *Commun. Pure Appl. Math.* 58 (2005), pp. 0445–0504. arXiv: gr-qc/0307013.

[117] Jonathan Luk and Sung-Jin Oh. "Proof of linear instability of the Reissner–Nordström Cauchy horizon under scalar perturbations." In: *Duke Math. J.* 166.3 (2017), pp. 437–493. DOI: 10.1215/00127094-3715189. arXiv: 1501.04598 [gr-qc].

[118] Jonathan Luk and Jan Sbierski. "Instability results for the wave equation in the interior of Kerr black holes." In: (Dec. 2015). arXiv: 1512.08259 [gr-qc].

[119] J. L. Costa, Pedro M. Girão, José Natário, and Jorge Drumond Silva. "On the Occurrence of Mass Inflation for the Einstein–Maxwell-Scalar Field System with a Cosmological Constant and an Exponential Price Law." In: *Commun. Math. Phys.* 361.1 (2018), pp. 289–341. DOI: 10.1007/s00220-018-3122-z. arXiv: 1707.08975 [gr-qc].

[120] Vitor Cardoso, J. L. Costa, Kyriakos Destounis, Peter Hintz, and Aron Jansen. "Quasinormal modes and Strong Cosmic Censorship." In: *Phys. Rev. Lett.* 120.3 (2018), p. 031103. DOI: 10.1103/PhysRevLett.120.031103. arXiv: 1711.10502 [gr-qc].

[121] Jonathan Luk and Sung-Jin Oh. "Strong cosmic censorship in spherical symmetry for two-ended asymptotically flat initial data I. The interior of the black hole region." In: (Feb. 2017). arXiv: 1702.05715 [gr-qc].

[122] J. L. Costa and Pedro M. Girão. "Higher order linear stability and instability of Reissner–Nordström's Cauchy horizon." In: *Anal. Math. Phys.* 10.3 (2020), p. 40. DOI: 10.1007/s13324-020-00380-5. arXiv: 1902.10726 [gr-qc].

[123] Stefan Hollands, Robert M. Wald, and Jochen Zahn. "Quantum instability of the Cauchy horizon in Reissner–Nordström–deSitter spacetime." In: *Class. Quant. Grav.* 37.11 (2020), p. 115009. DOI: 10.1088/1361-6382/ab8052. arXiv: 1912.06047 [gr-qc].

[124] Noa Zilberman, Marc Casals, Amos Ori, and Adrian C. Ottewill. "Quantum Fluxes at the Inner Horizon of a Spinning Black Hole." In: *Phys. Rev. Lett.* 129.26 (2022), p. 261102. DOI: 10.1103/PhysRevLett.129.261102. arXiv: 2203.08502 [gr-qc].

[125] Eric G. Brown, Robert B. Mann, and Leonardo Modesto. "Mass Inflation in the Loop Black Hole." In: *Phys. Rev. D* 84 (2011), p. 104041. DOI: 10.1103/PhysRevD.84.104041. arXiv: 1104.3126 [gr-qc].

[126] Raúl Carballo-Rubio, Francesco Di Filippo, Stefano Liberati, Costantino Pacilio, and Matt Visser. "Inner horizon instability and the unstable cores of regular black holes." In: *JHEP* 05 (2021), p. 132. DOI: 10.1007/JHEP05(2021)132. arXiv: 2101.05006 [gr-qc].

[127] Alfio Bonanno, Amir-Pouyan Khosravi, and Frank Saueressig. "Regular evaporating black holes with stable cores." In: *Phys. Rev. D* 107.2 (2023), p. 024005. DOI: 10.1103/PhysRevD.107.024005. arXiv: 2209.10612 [gr-qc].

[128] Don N. Page. "Particle Emission Rates from a Black Hole: Massless Particles from an Uncharged, Nonrotating Hole." In: *Phys. Rev. D* 13 (1976), pp. 198–206. DOI: 10.1103/PhysRevD.13.198.

[129] Fabbri Alessandro and José Navarro-Salas. *Modeling Black Hole Evaporation*. World Scientific, 2005.

[130] Martin Bojowald, Rituparno Goswami, Roy Maartens, and Parampreet Singh. "A Black hole mass threshold from non-singular quantum gravitational collapse." In: *Phys. Rev. Lett.* 95 (2005), p. 091302. DOI: 10.1103/PhysRevLett.95.091302. arXiv: gr-qc/0503041.

[131] Yaser Tavakoli, J. Marto, and Andrea Dapor. "Semiclassical dynamics of horizons in spherically symmetric collapse." In: *Int. J. Mod. Phys. D* 23.7 (2014), p. 1450061. DOI: 10.1142/S0218271814500618. arXiv: 1303.6157 [gr-qc].

[132] Cosimo Bambi, Daniele Malafarina, and Leonardo Modesto. "Non-singular quantum-inspired gravitational collapse." In: *Phys. Rev. D* 88 (2013), p. 044009. DOI: 10.1103/PhysRevD.88.044009. arXiv: 1305.4790 [gr-qc].

[133] Carlos Barceló, Valentin Boyanov, Raúl Carballo-Rubio, and Luis J. Garay. "Black hole inner horizon evaporation in semiclassical gravity." In: *Class. Quant. Grav.* 38.12 (2021), p. 125003. DOI: 10.1088/1361-6382/abf89c. arXiv: 2011.07331 [gr-qc].

[134] Carlos Barceló, Valentin Boyanov, Raúl Carballo-Rubio, and Luis J. Garay. "Classical mass inflation versus semiclassical inner horizon inflation." In: *Phys. Rev. D* 106.12 (2022), p. 124006. DOI: 10.1103/PhysRevD.106.124006. arXiv: 2203.13539 [gr-qc].

[135] Florencia Benitez, Rodolfo Gambini, Luis Lehner, Steve Liebling, and Jorge Pullin. "Critical collapse of a scalar field in semiclassical loop quantum gravity." In: *Phys. Rev. Lett.* 124.7 (2020), p. 071301. DOI: 10.1103/PhysRevLett.124.071301. arXiv: 2002.04044 [gr-qc].

[136] Vitor Cardoso and Paolo Pani. "Tests for the existence of black holes through gravitational wave echoes." In: *Nature Astron.* 1.9 (2017), pp. 586–591. DOI: 10.1038/s41550-017-0225-y. arXiv: 1709.01525 [gr-qc].

[137] V. Moncrief. "Stability of stationary, spherical accretion onto a Schwarzschild black hole." In: *ApJ* 235 (Feb. 1980), pp. 1038–1046. DOI: 10.1086/157707.

[138] W. G. Unruh. "Experimental black hole evaporation." In: *Phys. Rev. Lett.* 46 (1981), pp. 1351–1353. DOI: 10.1103/PhysRevLett.46.1351.

[139] Matt Visser. "Acoustic black holes: Horizons, ergospheres, and Hawking radiation." In: *Class. Quant. Grav.* 15 (1998), pp. 1767–1791. DOI: 10.1088/0264-9381/15/6/024. arXiv: gr-qc/9712010.

[140] Carlos Barcelo, Stefano Liberati, and Matt Visser. "Analogue gravity." In: *Living Rev. Rel.* 8 (2005), p. 12. DOI: 10.12942/lrr-2005-12. arXiv: gr-qc/0505065.

[141] Ju-Fu Lu, K. N. Yu, Feng Yuan, and E. C. M. Young. "Multi-Sonic Points and Possible Shocks in Relativistic Adiabatic Flows." In: *Astrophysical Letters and Communications* 35 (Jan. 1997), p. 389.

[142] G. H. Schnerr and P. Leidner. "Internal flows with multiple sonic points." In: *Fluid- and Gasdynamics*. Ed. by G. H. Schnerr, R. Bohning, W. Frank, and K. Bühler. Vienna: Springer Vienna, 1994, pp. 147–154. ISBN: 978-3-7091-9310-5. DOI: 10.1007/978-3-7091-9310-5_17. URL: https://doi.org/10.1007/978-3-7091-9310-5_17.

[143] Michael P. Brenner, Sascha Hilgenfeldt, and Detlef Lohse. "Single-bubble sonoluminescence." In: *Rev. Mod. Phys.* 74 (2002), pp. 425–484. DOI: 10.1103/RevModPhys.74.425.

[144] Jacob D. Bekenstein and Marcelo Schiffer. "The Many faces of superradiance." In: *Phys.Rev.* D58 (1998), p. 064014. DOI: 10.1103/PhysRevD.58.064014. arXiv: gr-qc/9803033 [gr-qc].

[145] J Dittrich, P Duclos, and P. Seba. "Instability in a classical periodically driven string." In: *Phys. Rev. E* 49 (1994), p. 3535. DOI: 10.1103/PhysRevE.49.3535.

[146] J Cooper. "Long-time behavior and energy growth for electromagnetic waves reflected by a moving boundary." In: *IEEE Transactions on Antennas and Propagation* 41 (1993). [Erratum: Phys.Rev.D 70, 049903 (2004)], p. 1365. DOI: 10.1109/8.247776.

[147] C. K. Law. "Resonance Response of the Quantum Vacuum to an Oscillating Boundary." In: *Phys. Rev. Lett.* 73 (14 Oct. 1994), pp. 1931–1934. DOI: 10.1103/PhysRevLett.73.1931. URL: https://link.aps.org/doi/10.1103/PhysRevLett.73.1931.

[148] Taishi Ikeda, Vitor Cardoso, and Miguel Zilhão. "Instabilities of Scalar Fields around Oscillating Stars." In: *Phys. Rev. Lett.* 127.19 (2021), p. 191101. DOI: 10.1103/PhysRevLett.127.191101. arXiv: 2110.06937 [gr-qc].

[149] Vitor Cardoso and Rodrigo Vicente. "Moving black holes: energy extraction, absorption cross-section and the ring of fire." In: *Phys. Rev. D* 100.8 (2019), p. 084001. DOI: 10.1103/PhysRevD.100.084001. arXiv: 1906.10140 [gr-qc].

[150] Mitsuo I. Tsumagari. "The Physics of Q-Balls." Ph.D. thesis, U. Nottingham. Oct. 2009. arXiv: 0910.3845 [hep-th].

[151] Paul M. Saffin, Qi-Xin Xie, and Shuang-Yong Zhou. "Q-ball Superradiance." In: *Phys. Rev. Lett.* 131.11 (2023), p. 111601. DOI: 10.1103/PhysRevLett.131.111601. arXiv: 2212.03269 [hep-th].

[152] G. H. Derrick. "Comments on nonlinear wave equations as models for elementary particles." In: *J. Math. Phys.* 5 (1964), pp. 1252–1254. DOI: 10.1063/1.1704233.

[153] Tuomas Multamaki and Iiro Vilja. "Analytical and numerical properties of Q balls." In: *Nucl. Phys. B* 574 (2000), pp. 130–152. DOI: 10.1016/S0550-3213(99)00827-5. arXiv: hep-ph/9908446.

[154] D. Christodoulou and R. Ruffini. "Reversible transformations of a charged black hole." In: *Phys. Rev. D* 4 (1971), pp. 3552–3555. DOI: 10.1103/PhysRevD.4.3552.

[155] Lorenzo Annulli, Vitor Cardoso, and Rodrigo Vicente. "Response of ultralight dark matter to supermassive black holes and binaries." In: *Phys. Rev. D* 102.6 (2020), p. 063022. DOI: 10.1103/PhysRevD.102.063022. arXiv: 2009.00012 [gr-qc].

[156] Caio F.B. Macedo, Paolo Pani, Vitor Cardoso, and Luís C. B. Crispino. "Astrophysical signatures of boson stars: quasinormal modes and inspiral resonances." In: *Phys. Rev. D* 88.6 (2013), p. 064046. DOI: 10.1103/PhysRevD.88.064046. arXiv: 1307.4812 [gr-qc].

[157] Vitor Cardoso, Oscar J. C. Dias, Jose P. S. Lemos, and Shijun Yoshida. "The Black hole bomb and superradiant instabilities." In: *Phys. Rev. D* 70 (2004). [Erratum: Phys.Rev.D 70, 049903 (2004)], p. 044039. DOI: 10.1103/PhysRevD.70.049903. arXiv: hep-th/0404096.

[158] Vitor Cardoso and Oscar J. C. Dias. "Small Kerr-anti-de Sitter black holes are unstable." In: *Phys. Rev. D* 70 (2004), p. 084011. DOI: 10.1103/PhysRevD.70.084011. arXiv: hep-th/0405006.

[159] Katherine Freese. "Review of Observational Evidence for Dark Matter in the Universe and in upcoming searches for Dark Stars." In: *EAS Publ. Ser.* 36 (2009). Ed. by E. Pécontal, T. Buchert, Ph. Di Stefano, and Y. Copin, pp. 113–126. DOI: 10.1051/eas/0936016. arXiv: 0812.4005 [astro-ph].

[160] Julio F. Navarro, Carlos S. Frenk, and Simon D. M. White. "The Structure of cold dark matter halos." In: *Astrophys. J.* 462 (1996), pp. 563–575. DOI: 10.1086/177173. arXiv: astro-ph/9508025.

[161] Douglas Clowe, Marusa Bradac, Anthony H. Gonzalez, Maxim Markevitch, Scott W. Randall, Christine Jones, and Dennis Zaritsky. "A direct empirical proof of the existence of dark matter." In: *Astrophys. J. Lett.* 648 (2006), pp. L109–L113. DOI: 10.1086/508162. arXiv: astro-ph/0608407.

[162] Gianfranco Bertone, Dan Hooper, and Joseph Silk. "Particle dark matter: Evidence, candidates and constraints." In: *Phys. Rept.* 405 (2005), pp. 279–390. DOI: 10.1016/j.physrep.2004.08.031. arXiv: hep-ph/0404175.

[163] Felix Kahlhoefer. "Review of LHC Dark Matter Searches." In: *Int. J. Mod. Phys. A* 32.13 (2017), p. 1730006. DOI: 10.1142/S0217751X1730006X. arXiv: 1702.02430 [hep-ph].

[164] Carlos Pérez de los Heros. "Status, Challenges and Directions in Indirect Dark Matter Searches." In: *Symmetry* 12.10 (2020), p. 1648. DOI: 10.3390/sym12101648. arXiv: 2008.11561 [astro-ph.HE].

[165] David J. Kaup. "Klein-Gordon Geon." In: *Phys.Rev.* 172 (1968), pp. 1331–1342. DOI: 10.1103/PhysRev.172.1331.

[166] Remo Ruffini and Silvano Bonazzola. "Systems of selfgravitating particles in general relativity and the concept of an equation of state." In: *Phys.Rev.* 187 (1969), pp. 1767–1783. DOI: 10.1103/PhysRev.187.1767.

[167] Hirotada Okawa, Vitor Cardoso, and Paolo Pani. "Collapse of self-interacting fields in asymptotically flat spacetimes: do self-interactions render Minkowski spacetime unstable?" In: *Phys. Rev. D* 89.4 (2014), p. 041502. DOI: 10.1103/PhysRevD.89.041502. arXiv: 1311.1235 [gr-qc].

[168] Richard Brito, Vitor Cardoso, and Hirotada Okawa. "Accretion of dark matter by stars." In: *Phys. Rev. Lett.* 115.11 (2015), p. 111301. DOI: 10.1103/PhysRevLett.115.111301. arXiv: 1508.04773 [gr-qc].

[169] Richard Brito, Vitor Cardoso, Caio F. B. Macedo, Hirotada Okawa, and Carlos Palenzuela. "Interaction between bosonic dark matter and stars." In: *Phys. Rev. D* 93.4 (2016), p. 044045. DOI: 10.1103/PhysRevD.93.044045. arXiv: 1512.00466 [astro-ph.SR].

[170] Edward Seidel and Wai-Mo Suen. "Dynamical Evolution of Boson Stars. 1. Perturbing the Ground State." In: *Phys. Rev. D* 42 (1990), pp. 384–403. DOI: 10.1103/PhysRevD.42.384.

[171] Victor H. Robles and Tonatiuh Matos. "Flat Central Density Profile and Constant DM Surface Density in Galaxies from Scalar Field Dark Matter." In: *Mon. Not. Roy. Astron. Soc.* 422 (2012), pp. 282–289. DOI: 10.1111/j.1365-2966.2012.20603.x. arXiv: 1201.3032 [astro-ph.CO].

[172] Lam Hui, Jeremiah P. Ostriker, Scott Tremaine, and Edward Witten. "Ultralight scalars as cosmological dark matter." In: *Phys. Rev. D* 95.4 (2017), p. 043541. DOI: 10.1103/PhysRevD.95.043541. arXiv: 1610.08297 [astro-ph.CO].

[173] Nitsan Bar, Kfir Blum, Joshua Eby, and Ryosuke Sato. "Ultralight dark matter in disk galaxies." In: *Phys. Rev.* D99.10 (2019), p. 103020. DOI: 10.1103/PhysRevD.99.103020. arXiv: 1903.03402 [astro-ph.CO].

[174] Nitsan Bar, Diego Blas, Kfir Blum, and Sergey Sibiryakov. "Galactic rotation curves versus ultralight dark matter: Implications of the soliton-host halo relation." In: *Phys. Rev.* D98.8 (2018), p. 083027. DOI: 10.1103/PhysRevD.98.083027. arXiv: 1805.00122 [astro-ph.CO].

[175] Vincent Desjacques and Adi Nusser. "Axion core–halo mass and the black hole–halo mass relation: constraints on a few parsec scales." In: *Mon. Not. Roy. Astron. Soc.* 488.4 (2019), pp. 4497–4503. DOI: 10.1093/mnras/stz1978. arXiv: 1905.03450 [astro-ph.CO].

[176] Hooman Davoudiasl and Peter B Denton. "Ultralight Boson Dark Matter and Event Horizon Telescope Observations of M87*." In: *Phys. Rev. Lett.* 123.2 (2019), p. 021102. DOI: 10.1103/PhysRevLett.123.021102. arXiv: 1904.09242 [astro-ph.CO].

[177] Hsi-Yu Schive, Tzihong Chiueh, and Tom Broadhurst. "Cosmic Structure as the Quantum Interference of a Coherent Dark Wave." In: *Nature Phys.* 10 (2014), pp. 496–499. DOI: 10.1038/nphys2996. arXiv: 1406.6586 [astro-ph.GA].

[178] Leor Barack et al. "Black holes, gravitational waves and fundamental physics: a roadmap." In: *Class. Quant. Grav.* 36.14 (2019), p. 143001. DOI: 10.1088/1361-6382/ab0587. arXiv: 1806.05195 [gr-qc].

[179] Gian F. Giudice, Matthew McCullough, and Alfredo Urbano. "Hunting for Dark Particles with Gravitational Waves." In: *JCAP* 10 (2016), p. 001. DOI: 10.1088/1475-7516/2016/10/001. arXiv: 1605.01209 [hep-ph].

[180] John Ellis, Andi Hektor, Gert Hütsi, Kristjan Kannike, Luca Marzola, Martti Raidal, and Ville Vaskonen. "Search for Dark Matter Effects on Gravitational Signals from Neutron Star Mergers." In: *Phys. Lett.* B781 (2018), pp. 607–610. DOI: 10.1016/j.physletb.2018.04.048. arXiv: 1710.05540 [astro-ph.CO].

[181] Kazunari Eda, Yousuke Itoh, Sachiko Kuroyanagi, and Joseph Silk. "A new probe of dark matter properties: gravitational waves from an intermediate mass black hole embedded in a dark matter mini-spike." In: *Phys.Rev.Lett.* 110 (2013), p. 221101. DOI: 10.1103/PhysRevLett.110.221101. arXiv: 1301.5971 [gr-qc].

[182] Caio F. B. Macedo, Paolo Pani, Vitor Cardoso, and Luís C. B. Crispino. "Into the lair: gravitational-wave signatures of dark matter." In: *Astrophys. J.* 774 (2013), p. 48. DOI: 10.1088/0004-637X/774/1/48. arXiv: 1302.2646 [gr-qc].

[183] Enrico Barausse, Vitor Cardoso, and Paolo Pani. "Can environmental effects spoil precision gravitational-wave astrophysics?" In: *Phys. Rev.* D89.10 (2014), p. 104059. DOI: 10.1103/PhysRevD.89.104059. arXiv: 1404.7149 [gr-qc].

[184] Otto A. Hannuksela, Kaze W.K. Wong, Richard Brito, Emanuele Berti, and Tjonnie G.F. Li. "Probing the existence of ultralight bosons with a single gravitational-wave measurement." In: *Nature Astron.* 3.5 (2019), pp. 447–451. DOI: 10.1038/s41550-019-0712-4. arXiv: 1804.09659 [astro-ph.HE].

[185] Vitor Cardoso and Andrea Maselli. "Constraints on the astrophysical environment of binaries with gravitational-wave observations." In: *Astron. Astrophys.* 644 (2020), A147. DOI: 10.1051/0004-6361/202037654. arXiv: 1909.05870 [astro-ph.HE].

[186] Daniel Baumann, Horng Sheng Chia, Rafael A. Porto, and John Stout. "Gravitational Collider Physics." In: *Phys. Rev. D* 101.8 (2020), p. 083019. DOI: 10.1103/PhysRevD.101.083019. arXiv: 1912.04932 [gr-qc].

[187] Bradley J. Kavanagh, David A. Nichols, Gianfranco Bertone, and Daniele Gaggero. "Detecting dark matter around black holes with gravitational waves: Effects of dark-matter dynamics on the gravitational waveform." In: (Feb. 2020). arXiv: 2002.12811 [gr-qc].

[188] Lorenz Zwick, Andrea Derdzinski, Mudit Garg, Pedro R. Capelo, and Lucio Mayer. "Dirty waveforms: multiband harmonic content of gas-embedded gravitational wave sources." In: (Oct. 2021). arXiv: 2110.09097 [astro-ph.HE].

[189] Rodrigo Vicente and Vitor Cardoso. "Dynamical friction of black holes in ultralight dark matter." In: *Phys. Rev. D* 105.8 (2022), p. 083008. DOI: 10.1103/PhysRevD.105.083008. arXiv: 2201.08854 [gr-qc].

[190] Carlos Palenzuela, Paolo Pani, Miguel Bezares, Vitor Cardoso, Luis Lehner, and Steven Liebling. "Gravitational Wave Signatures of Highly Compact Boson Star Binaries." In: *Phys. Rev.* D96.10 (2017), p. 104058. DOI: 10.1103/PhysRevD.96.104058. arXiv: 1710.09432 [gr-qc].

[191] Juan Calderón Bustillo, Nicolas Sanchis-Gual, Alejandro Torres-Forné, José A. Font, Avi Vajpeyi, Rory Smith, Carlos Herdeiro, Eugen Radu, and Samson H. W. Leong. "GW190521 as a Merger of Proca Stars: A Potential New Vector Boson of 8.7×10^{-13} eV." In: *Phys. Rev. Lett.* 126.8 (2021), p. 081101. DOI: 10.1103/PhysRevLett.126.081101. arXiv: 2009.05376 [gr-qc].

[192] Miguel Bezares, Mateja Bošković, Steven Liebling, Carlos Palenzuela, Paolo Pani, and Enrico Barausse. "Gravitational waves and kicks from the merger of unequal mass, highly compact boson stars." In: (Jan. 2022). arXiv: 2201.06113 [gr-qc].

[193] Vitor Cardoso, Leonardo Gualtieri, Carlos Herdeiro, and Ulrich Sperhake. "Exploring New Physics Frontiers Through Numerical Relativity." In: *Living Rev. Relativity* 18 (2015), p. 1. DOI: 10.1007/lrr-2015-1. arXiv: 1409.0014 [gr-qc].

[194] Vitor Cardoso, Edgardo Franzin, Andrea Maselli, Paolo Pani, and Guilherme Raposo. "Testing strong-field gravity with tidal Love numbers." In: *Phys. Rev. D* 95.8 (2017). [Addendum: Phys.Rev.D 95, 089901 (2017)], p. 084014. DOI: 10.1103/PhysRevD.95.084014. arXiv: 1701.01116 [gr-qc].

[195] Noah Sennett, Tanja Hinderer, Jan Steinhoff, Alessandra Buonanno, and Serguei Ossokine. "Distinguishing Boson Stars from Black Holes and Neutron Stars from Tidal Interactions in Inspiraling Binary Systems." In: *Phys. Rev. D* 96.2 (2017), p. 024002. DOI: 10.1103/PhysRevD.96.024002. arXiv: 1704.08651 [gr-qc].

[196] Dina Traykova, Katy Clough, Thomas Helfer, Pedro G. Ferreira, Emanuele Berti, and Lam Hui. "Dynamical friction from scalar dark matter in the relativistic regime." In: (June 2021). arXiv: 2106.08280 [gr-qc].

[197] Pierre-Henri Chavanis. "Mass-radius relation of Newtonian self-gravitating Bose-Einstein condensates with short-range interactions. I. Analytical results." In: *Physical Review D* 84.4 (Aug. 2011). ISSN: 1550-2368. DOI: 10.1103/physrevd.84.043531. URL: http://dx.doi.org/10.1103/PhysRevD.84.043531.

[198] Eric Gourgoulhon. "3+1 Formalism and Bases of Numerical Relativity." In: (2007). arXiv: gr-qc/0703035.

[199] Miguel Alcubierre. *Introduction to 3+1 Numerical Relativity*. Oxford University Press, Apr. 2008. ISBN: 9780199205677. DOI: 10.1093/acprof:oso/9780199205677.001.0001. URL: https://doi.org/10.1093/acprof:oso/9780199205677.001.0001.

[200] Takashi Nakamura, Kenichi Oohara, and Yasufumi Kojima. "General Relativistic Collapse to Black Holes and Gravitational Waves from Black Holes." In: *Prog. Theor. Phys. Suppl.* 3 (1987), pp. 1–218.

[201] Masaru Shibata and Takashi Nakamura. "Evolution of three-dimensional gravitational waves: Harmonic slicing case." In: *Phys. Rev. D* 52 (1995), pp. 5428–5444. DOI: 10.1103/PhysRevD.52.5428.

[202] Thomas W. Baumgarte and Stuart L. Shapiro. "On the numerical integration of Einstein's field equations." In: *Phys.Rev.* D59 (1999), p. 024007. DOI: 10.1103/PhysRevD.59.024007. arXiv: gr-qc/9810065 [gr-qc].

[203] Pedro V. P. Cunha, José A. Font, Carlos Herdeiro, Eugen Radu, Nicolas Sanchis-Gual, and Miguel Zilhão. "Lensing and dynamics of ultracompact bosonic stars." In: *Phys. Rev. D* 96.10 (2017), p. 104040. DOI: 10.1103/PhysRevD.96.104040. arXiv: 1709.06118 [gr-qc].

[204] Frank Löffler et al. "The Einstein Toolkit: A Community Computational Infrastructure for Relativistic Astrophysics." In: *Class. Quantum Grav.* 29.11 (2012), p. 115001. DOI: doi:10.1088/0264-9381/29/11/115001. eprint: arXiv:1111.3344[gr-qc].

[205] Miguel Zilhão and Frank Löffler. "An Introduction to the Einstein Toolkit." In: *Int. J. Mod. Phys.* A28 (2013), p. 1340014. DOI: 10.1142/S0217751X13400149. arXiv: 1305.5299 [gr-qc].

[206] Maria Babiuc-Hamilton et al. "The Einstein Toolkit." Version The "Mayer" release, ET_2019_10. In: (Oct. 2019). http://einsteintoolkit.org. DOI: 10.5281/zenodo.3522086. URL: https://doi.org/10.5281/zenodo.3522086.

[207] Erik Schnetter, Scott H. Hawley, and Ian Hawke. "Evolutions in 3-D numerical relativity using fixed mesh refinement." In: *Class. Quant. Grav.* 21 (2004), pp. 1465–1488. DOI: 10.1088/0264-9381/21/6/014. arXiv: gr-qc/0310042 [gr-qc].

[208] Jonathan Thornburg. "Finding apparent horizons in numerical relativity." In: *Phys. Rev.* D54 (1996), pp. 4899–4918. DOI: 10.1103/PhysRevD.54.4899. arXiv: gr-qc/9508014.

[209] Jonathan Thornburg. "A Fast apparent horizon finder for three-dimensional Cartesian grids in numerical relativity." In: *Class. Quant. Grav.* 21 (2004), pp. 743–766. DOI: 10.1088/0264-9381/21/2/026. arXiv: gr-qc/0306056 [gr-qc].

[210] Olaf Dreyer, Badri Krishnan, Deirdre Shoemaker, and Erik Schnetter. "Introduction to isolated horizons in numerical relativity." In: *Phys. Rev.* D67 (2003), p. 024018. DOI: 10.1103/PhysRevD.67.024018. arXiv: gr-qc/0206008 [gr-qc].

[211] Helvi Witek, Miguel Zilhao, Gabriele Bozzola, Matthew Elley, Giuseppe Ficarra, Taishi Ikeda, Nicolas Sanchis-Gual, and Hector Silva. *Canuda: a public numerical relativity library to probe fundamental physics*. Oct. 2021. DOI: 10.5281/zenodo.3565474. URL: https://doi.org/10.5281/zenodo.3565474.

[212] Emanuele Berti, Vitor Cardoso, Jose A. Gonzalez, Ulrich Sperhake, Mark Hannam, Sascha Husa, and Bernd Bruegmann. "Inspiral, merger and ringdown of unequal mass black hole binaries: A Multipolar analysis." In: *Phys. Rev. D* 76 (2007), p. 064034. DOI: 10.1103/PhysRevD.76.064034. arXiv: gr-qc/0703053.

[213] Ulrich Sperhake. "Binary black-hole evolutions of excision and puncture data." In: *Phys. Rev. D* 76 (2007), p. 104015. DOI: 10.1103/PhysRevD.76.104015. arXiv: gr-qc/0606079.

[214] William E. East. "Superradiant instability of massive vector fields around spinning black holes in the relativistic regime." In: *Phys. Rev. D* 96.2 (2017), p. 024004. DOI: 10.1103/PhysRevD.96.024004. arXiv: 1705.01544 [gr-qc].

[215] Masaru Shibata, Hirotada Okawa, and Tetsuro Yamamoto. "High-velocity collision of two black holes." In: *Phys. Rev. D* 78 (10 Nov. 2008), p. 101501. DOI: 10.1103/PhysRevD.78.101501. URL: https://link.aps.org/doi/10.1103/PhysRevD.78.101501.

[216] Nicolas Sanchis-Gual, Carlos Herdeiro, José A. Font, Eugen Radu, and Fabrizio Di Giovanni. "Head-on collisions and orbital mergers of Proca stars." In: *Phys. Rev. D* 99.2 (2019), p. 024017. DOI: 10.1103/PhysRevD.99.024017. arXiv: 1806.07779 [gr-qc].

[217] Nicolas Sanchis-Gual, Miguel Zilhão, Carlos Herdeiro, Fabrizio Di Giovanni, José A. Font, and Eugen Radu. "Synchronized gravitational atoms from mergers of bosonic stars." In: *Phys. Rev. D* 102.10 (2020), p. 101504. DOI: 10.1103/PhysRevD.102.101504. arXiv: 2007.11584 [gr-qc].

[218] Víctor Jaramillo, Nicolas Sanchis-Gual, Juan Barranco, Argelia Bernal, Juan Carlos Degollado, Carlos Herdeiro, Miguel Megevand, and Darío Núñez. "Head-on collisions of ℓ-boson stars." In: *Phys. Rev. D* 105.10 (2022), p. 104057. DOI: 10.1103/PhysRevD.105.104057. arXiv: 2202.00696 [gr-qc].

[219] See movies at https://centra.tecnico.ulisboa.pt/network/grit/files/movies/, shows animations of the collision between a black hole and a boson star.

[220] Raissa F. P. Mendes and Huan Yang. "Tidal deformability of boson stars and dark matter clumps." In: *Class. Quant. Grav.* 34.18 (2017), p. 185001. DOI: 10.1088/1361-6382/aa842d. arXiv: 1606.03035 [astro-ph.CO].

[221] Vitor Cardoso, Taishi Ikeda, Rodrigo Vicente, Zhen Zhong, and Miguel Zilhao. "Accretion onto boson stars." In: (Feb. 2022). arXiv: inpreparation [gr-qc].

[222] W.G. Unruh. "Absorption Cross-Section of Small Black Holes." In: *Phys. Rev. D* 14 (1976), pp. 3251–3259. DOI: 10.1103/PhysRevD.14.3251.

[223] A. C. Fabian, J. E. Pringle, and M. J. Rees. "Tidal Capture Formation of Binary Systems and X-ray Sources in Globular Clusters." In: *Monthly Notices of the Royal Astronomical Society* 172.1 (July 1975), 15P–18P. ISSN: 0035-8711. DOI: 10.1093/mnras/172.1.15P. URL: https://academic.oup.com/mnras/article-pdf/172/1/15P/3217198/mnras172-015P.pdf.

[224] W. H. Press and S. A. Teukolsky. "On formation of close binaries by two-body tidal capture." In: *ApJ* 213 (Apr. 1977), pp. 183–192. DOI: 10.1086/155143.

[225] Lachlan Lancaster, Cara Giovanetti, Philip Mocz, Yonatan Kahn, Mariangela Lisanti, and David N. Spergel. "Dynamical Friction in a Fuzzy Dark Matter Universe." In: *JCAP* 01 (2020), p. 001. DOI: 10.1088/1475-7516/2020/01/001. arXiv: 1909.06381 [astro-ph.CO].

[226] Ulrich Sperhake, Vitor Cardoso, Frans Pretorius, Emanuele Berti, and Jose A. Gonzalez. "The High-energy collision of two black holes." In: *Phys. Rev. Lett.* 101 (2008), p. 161101. DOI: 10.1103/PhysRevLett.101.161101. arXiv: 0806.1738 [gr-qc].

[227] Hiroko Koyama and Akira Tomimatsu. "Asymptotic tails of massive scalar fields in Schwarzschild background." In: *Phys. Rev. D* 64 (2001), p. 044014. DOI: 10.1103/PhysRevD.64.044014. arXiv: gr-qc/0103086.

[228] Helvi Witek, Vitor Cardoso, Akihiro Ishibashi, and Ulrich Sperhake. "Superradiant instabilities in astrophysical systems." In: *Physical Review D* 87.4 (Feb. 2013). ISSN: 1550-2368. DOI: 10.1103/physrevd.87.043513. URL: http://dx.doi.org/10.1103/PhysRevD.87.043513.

[229] Thomas Helfer, Ulrich Sperhake, Robin Croft, Miren Radia, Bo-Xuan Ge, and Eugene A. Lim. "Malaise and remedy of binary boson-star initial data." In: *Class. Quant. Grav.* 39.7 (2022), p. 074001. DOI: 10.1088/1361-6382/ac53b7. arXiv: 2108.11995 [gr-qc].

[230] Jae-Weon Lee. "Brief History of Ultra-light Scalar Dark Matter Models." In: *EPJ Web Conf.* 168 (2018). Ed. by B. Gwak, G. Kang, C. Kim, H. C. Kim, C. H. Lee, J. Lee, S. Lee, and W. Lee, p. 06005. DOI: 10.1051/epjconf/201816806005. arXiv: 1704.05057 [astro-ph.CO].

[231] Carlos A. R. Herdeiro and Eugen Radu. "On the classicality of bosonic stars." In: *Int. J. Mod. Phys. D* 31.14 (2022), p. 2242022. DOI: 10.1142/S0218271822420226. arXiv: 2205.05395 [gr-qc].

[232] Katherine Freese. "Status of Dark Matter in the Universe." In: *Int. J. Mod. Phys.* 1.06 (2017). Ed. by Massimo Bianchi, Robert T. Jantzen, and Remo Ruffini, pp. 325–355. DOI: 10.1142/S0218271817300129. arXiv: 1701.01840 [astro-ph.CO].

[233] Eckehard W. Mielke and Franz E. Schunck. "Boson stars: Early history and recent prospects." In: *8th Marcel Grossmann Meeting on Recent Developments in Theoretical and Experimental General Relativity, Gravitation and Relativistic Field Theories (MG 8)*. June 1997, pp. 1607–1626. arXiv: gr-qc/9801063.

[234] Vitor Cardoso, Caio F. B. Macedo, Kei-ichi Maeda, and Hirotada Okawa. "ECO-spotting: looking for extremely compact objects with bosonic fields." In: *Class. Quant. Grav.* 39.3 (2022), p. 034001. DOI: 10.1088/1361-6382/ac41e7. arXiv: 2112.05750 [gr-qc].

[235] Fangzhou Jiang and Frank C. van den Bosch. "Statistics of dark matter substructure – III. Halo-to-halo variance." In: *Mon. Not. Roy. Astron. Soc.* 472.1 (2017), pp. 657–674. DOI: 10.1093/mnras/stx1979. arXiv: 1610.02399 [astro-ph.CO].

[236] Hsi-Yu Schive, Ming-Hsuan Liao, Tak-Pong Woo, Shing-Kwong Wong, Tzihong Chiueh, Tom Broadhurst, and W. -Y. Pauchy Hwang. "Understanding the Core-Halo Relation of Quantum Wave Dark Matter from 3D Simulations." In: *Phys. Rev. Lett.* 113.26 (2014), p. 261302. DOI: 10.1103/PhysRevLett.113.261302. arXiv: 1407.7762 [astro-ph.GA].

[237] Elisa G. M. Ferreira. "Ultra-light dark matter." In: *Astron. Astrophys. Rev.* 29.1 (2021), p. 7. DOI: 10.1007/s00159-021-00135-6. arXiv: 2005.03254 [astro-ph.CO].

[238] Philip Mocz, Mark Vogelsberger, Victor H. Robles, Jesús Zavala, Michael Boylan-Kolchin, Anastasia Fialkov, and Lars Hernquist. "Galaxy formation with BECDM – I. Turbulence and relaxation of idealized haloes." In: *Mon. Not. Roy. Astron. Soc.* 471.4 (2017), pp. 4559–4570. DOI: 10.1093/mnras/stx1887. arXiv: 1705.05845 [astro-ph.CO].

[239] Bodo Schwabe, Jens C. Niemeyer, and Jan F. Engels. "Simulations of solitonic core mergers in ultralight axion dark matter cosmologies." In: *Phys. Rev. D* 94.4 (2016), p. 043513. DOI: 10.1103/PhysRevD.94.043513. arXiv: 1606.05151 [astro-ph.CO].

[240] T. Harko. "Bose-Einstein condensation of dark matter solves the core/cusp problem." In: *JCAP* 05 (2011), p. 022. DOI: 10.1088/1475-7516/2011/05/022. arXiv: 1105.2996 [astro-ph.CO].

[241] Heling Deng, Mark P. Hertzberg, Mohammad Hossein Namjoo, and Ali Masoumi. "Can Light Dark Matter Solve the Core-Cusp Problem?" In: *Phys. Rev. D* 98.2 (2018), p. 023513. DOI: 10.1103/PhysRevD.98.023513. arXiv: 1804.05921 [astro-ph.CO].

[242] A. M. Gavrilik, M. V. Khelashvili, and A. V. Nazarenko. "Bose-Einstein condensate dark matter model with three-particle interaction and two-phase structure." In: *Phys. Rev. D* 102.8 (2020), p. 083510. DOI: 10.1103/PhysRevD.102.083510. arXiv: 2007.04832 [astro-ph.GA].

[243] Alexandre M. Gavrilik and Andriy V. Nazarenko. "Phases of the Bose–Einstein Condensate Dark Matter Model with Both Two- and Three-Particle Interactions." In: *Universe* 7.10 (2021), p. 359. DOI: 10.3390/universe7100359. arXiv: 2109.00252 [astro-ph.GA].

[244] Ohad Shemmer, H. Netzer, R. Maiolino, E. Oliva, S. Croom, E. Corbett, and L. di Fabrizio. "Near infrared spectroscopy of high redshift active galactic nuclei. 1. A Metallicity-accretion rate relationship." In: *Astrophys. J.* 614 (2004), pp. 547–557. DOI: 10.1086/423607. arXiv: astro-ph/0406559.

[245] Miguel Bezares, Carlos Palenzuela, and Carles Bona. "Final fate of compact boson star mergers." In: *Phys. Rev. D* 95.12 (2017), p. 124005. DOI: 10.1103/PhysRevD.95.124005. arXiv: 1705.01071 [gr-qc].

[246] R. Becerril, A. Bernal, F.S. Guzmán, and U. Nucamendi. "Stability properties of Q-stars." In: *Physics Letters B* 657.4 (2007), pp. 263–268. ISSN: 0370-2693. DOI: https://doi.org/10.1016/j.physletb.2007.07.077. URL: https://www.sciencedirect.com/science/article/pii/S0370269307009227.

[247] Nils Siemonsen and William E. East. "Stability of rotating scalar boson stars with nonlinear interactions." In: *Phys. Rev. D* 103.4 (2021), p. 044022. DOI: 10.1103/PhysRevD.103.044022. arXiv: 2011.08247 [gr-qc].

[248] Lucas G. Collodel and Daniela D. Doneva. "Solitonic boson stars: Numerical solutions beyond the thin-wall approximation." In: *Phys. Rev. D* 106.8 (2022), p. 084057. DOI: 10.1103/PhysRevD.106.084057. arXiv: 2203.08203 [gr-qc].

[249] Burkhard Kleihaus, Jutta Kunz, and Stefanie Schneider. "Stable Phases of Boson Stars." In: *Phys. Rev. D* 85 (2012), p. 024045. DOI: 10.1103/PhysRevD.85.024045. arXiv: 1109.5858 [gr-qc].

[250] Takashi Tamaki and Nobuyuki Sakai. "How does gravity save or kill Q-balls?" In: *Phys. Rev. D* 83 (2011), p. 044027. DOI: 10.1103/PhysRevD.83.044027. arXiv: 1105.2932 [gr-qc].

[251] Roland Haas et al. *The Einstein Toolkit*. Version The "Sophie Kowalevski" release, ET_2022_11. To find out more, visit http://einsteintoolkit.org. Oct. 2022. DOI: 10.5281/zenodo.7245853. URL: https://doi.org/10.5281/zenodo.7245853.

[252] Gabriele Bozzola. "kuibit: Analyzing Einstein Toolkit simulations with Python." In: *The Journal of Open Source Software* 6.60, 3099 (Apr. 2021), p. 3099. DOI: 10.21105/joss.03099. arXiv: 2104.06376 [gr-qc].

[253] E. W. Leaver. "Solutions to a generalized spheroidal wave equation: Teukolsky's equations in general relativity, and the two-center problem in molecular quantum mechanics." In: *Journal of Mathematical Physics* 27.5 (May 1986), pp. 1238–1265. DOI: 10.1063/1.527130.

[254] Edward W. Leaver. "Spectral decomposition of the perturbation response of the Schwarzschild geometry." In: *Phys. Rev. D* 34 (2 July 1986), pp. 384–408. DOI: 10.1103/PhysRevD.34.384. URL: https://link.aps.org/doi/10.1103/PhysRevD.34.384.

[255] F. S. Guzman and F. D. Lora-Clavijo. "Spherical non-linear absorption of cosmological scalar fields onto a black hole." In: *Phys. Rev. D* 85 (2012), p. 024036. DOI: 10.1103/PhysRevD.85.024036. arXiv: 1201.3598 [astro-ph.CO].

[256] F. Siddhartha Guzman. "Evolving spherical boson stars on a 3-D Cartesian grid." In: *Phys. Rev. D* 70 (2004), p. 044033. DOI: 10.1103/PhysRevD.70.044033. arXiv: gr-qc/0407054.

[257] Niklas G. Nielsen, Andrea Palessandro, and Martin S. Sloth. "Gravitational Atoms." In: *Phys. Rev. D* 99.12 (2019), p. 123011. DOI: 10.1103/PhysRevD.99.123011. arXiv: 1903.12168 [hep-ph].

[258] F. S. Guzmán and L. Arturo Ureña-López. "Gravitational atoms: General framework for the construction of multistate axially symmetric solutions of the Schrödinger-Poisson system." In: *Phys. Rev. D* 101.8 (2020), p. 081302. DOI: 10.1103/PhysRevD.101.081302. arXiv: 1912.10585 [astro-ph.GA].

[259] Francisco S. Guzman. "Possible formation mechanism of multistate gravitational atoms." In: *Phys. Rev. D* 105.12 (2022), p. 123535. DOI: 10.1103/PhysRevD.105.123535. arXiv: 2206.03407 [gr-qc].

[260] S. W. Hawking and W. Israel, eds. *THREE HUNDRED YEARS OF GRAVITATION*. Cambridge University Press, 1987.

[261] Subrahmanyan Chandrasekhar. *The mathematical theory of black holes*. 1985. ISBN: 978-0-19-850370-5.

[262] B. Carter. "Axisymmetric Black Hole Has Only Two Degrees of Freedom." In: *Phys. Rev. Lett.* 26 (1971), pp. 331–333. DOI: 10.1103/PhysRevLett.26.331.

[263] D. C. Robinson. "Uniqueness of the Kerr black hole." In: *Phys. Rev. Lett.* 34 (1975), pp. 905–906. DOI: 10.1103/PhysRevLett.34.905.

[264] Piotr T. Chrusciel, Joao Lopes Costa, and Markus Heusler. "Stationary Black Holes: Uniqueness and Beyond." In: *Living Rev. Rel.* 15 (2012), p. 7. DOI: 10.12942/lrr-2012-7. arXiv: 1205.6112 [gr-qc].

[265] Roger Penrose. "Gravitational collapse and space-time singularities." In: *Phys. Rev. Lett.* 14 (1965), pp. 57–59. DOI: 10.1103/PhysRevLett.14.57.

[266] Edward W. Leaver. "Spectral decomposition of the perturbation response of the Schwarzschild geometry." In: *Phys. Rev. D* 34 (1986), pp. 384–408. DOI: 10.1103/PhysRevD.34.384.

[267] Peter Hintz. "A Sharp Version of Price's Law for Wave Decay on Asymptotically Flat Spacetimes." In: *Commun. Math. Phys.* 389.1 (2022), pp. 491–542. DOI: 10.1007/s00220-021-04276-8. arXiv: 2004.01664 [math.AP].

[268] Vitor Cardoso, Shijun Yoshida, Oscar J. C. Dias, and Jose P. S. Lemos. "Late time tails of wave propagation in higher dimensional space-times." In: *Phys. Rev. D* 68 (2003), p. 061503. DOI: 10.1103/PhysRevD.68.061503. arXiv: hep-th/0307122.

[269] Enno Harms, Sebastiano Bernuzzi, Alessandro Nagar, and An Zenginoglu. "A new gravitational wave generation algorithm for particle perturbations of the Kerr spacetime." In: *Class. Quant. Grav.* 31.24 (2014), p. 245004. DOI: 10.1088/0264-9381/31/24/245004. arXiv: 1406.5983 [gr-qc].

[270] Shahar Hod. "Strong cosmic censorship in charged black-hole spacetimes: As strong as ever." In: *Nucl. Phys. B* 941 (2019), pp. 636–645. DOI: 10.1016/j.nuclphysb.2019.03.003. arXiv: 1801.07261 [gr-qc].

[271] Vitor Cardoso, Joao L. Costa, Kyriakos Destounis, Peter Hintz, and Aron Jansen. "Strong cosmic censorship in charged black-hole spacetimes: still subtle." In: *Phys. Rev. D* 98.10 (2018), p. 104007. DOI: 10.1103/PhysRevD.98.104007. arXiv: 1808.03631 [gr-qc].

[272] Harvey Reall. "Viewpoint: A Possible Failure of Determinism in General Relativity." In: *Physics* 11 (2018), p. 6.

[273] Simone Albanesi, Sebastiano Bernuzzi, Thibault Damour, Alessandro Nagar, and Andrea Placidi. "Faithful effective-one-body waveform of small-mass-ratio coalescing black hole binaries: The eccentric, nonspinning case." In: *Phys. Rev. D* 108.8 (2023), p. 084037. DOI: 10.1103/PhysRevD.108.084037. arXiv: 2305.19336 [gr-qc].

[274] Gregorio Carullo and Marina De Amicis. "Late-time tails in nonlinear evolutions of merging black hole binaries." In: (Oct. 2023). arXiv: 2310.12968 [gr-qc].

[275] Satoshi Okuzumi, Kunihito Ioka, and Masa-aki Sakagami. "Possible Discovery of Nonlinear Tail and Quasinormal Modes in Black Hole Ringdown." In: *Phys. Rev. D* 77 (2008), p. 124018. DOI: 10.1103/PhysRevD.77.124018. arXiv: 0803.0501 [gr-qc].

[276] Tullio Regge and John A. Wheeler. "Stability of a Schwarzschild singularity." In: *Phys.Rev.* 108 (1957), pp. 1063–1069. DOI: 10.1103/PhysRev.108.1063.

[277] Frank J. Zerilli. "Effective potential for even parity Regge-Wheeler gravitational perturbation equations." In: *Phys.Rev.Lett.* 24 (1970), pp. 737–738. DOI: 10.1103/PhysRevLett.24.737.

[278] Ulrich H. Gerlach and Uday K. Sengupta. "Gauge-invariant perturbations on most general spherically symmetric space-times." In: *Phys. Rev. D* 19 (8 Apr. 1979), pp. 2268–2272. DOI: 10.1103/PhysRevD.19.2268. URL: https://link.aps.org/doi/10.1103/PhysRevD.19.2268.

[279] Ulrich H. Gerlach and Uday K. Sengupta. "Gauge-invariant coupled gravitational, acoustical, and electromagnetic modes on most general spherical space-times." In: *Phys. Rev. D* 22 (6 Sept. 1980), pp. 1300–1312. DOI: 10.1103/PhysRevD.22.1300. URL: https://link.aps.org/doi/10.1103/PhysRevD.22.1300.

[280] Karl Martel and Eric Poisson. "Gravitational perturbations of the Schwarzschild spacetime: A Practical covariant and gauge-invariant formalism." In: *Phys. Rev. D* 71 (2005), p. 104003. DOI: 10.1103/PhysRevD.71.104003. arXiv: gr-qc/0502028.

[281] E. S. C. Ching, P. T. Leung, W. M. Suen, and K. Young. "Late time tail of wave propagation on curved space-time." In: *Phys. Rev. Lett.* 74 (1995), pp. 2414–2417. DOI: 10.1103/PhysRevLett.74.2414. arXiv: gr-qc/9410044.

[282] E. S. C. Ching, P. T. Leung, W. M. Suen, and K. Young. "Wave propagation in gravitational systems: Late time behavior." In: *Phys. Rev. D* 52 (1995), pp. 2118–2132. DOI: 10.1103/PhysRevD.52.2118. arXiv: gr-qc/9507035.

[283] Janusz Karkowski, Zdobyslaw Swierczynski, and Edward Malec. "Comments on tails in Schwarzschild space-times." In: *Class. Quant. Grav.* 21 (2004), pp. 1303–1310. DOI: 10.1088/0264-9381/21/6/002. arXiv: gr-qc/0303101.

[284] Richard H. Price and Lior M. Burko. "Late time tails from momentarily stationary, compact initial data in Schwarzschild spacetimes." In: *Phys. Rev. D* 70 (2004), p. 084039. DOI: 10.1103/PhysRevD.70.084039. arXiv: gr-qc/0408077.

[285] Mihalis Dafermos and Igor Rodnianski. "A Proof of Price's law for the collapse of a selfgravitating scalar field." In: *Invent. Math.* 162 (2005), pp. 381–457. DOI: 10.1007/s00222-005-0450-3. arXiv: gr-qc/0309115.

[286] Leor Barack. "Late time dynamics of scalar perturbations outside black holes. 2. Schwarzschild geometry." In: *Phys. Rev. D* 59 (1999), p. 044017. DOI: 10.1103/PhysRevD.59.044017. arXiv: gr-qc/9811028.

[287] Ofek Birnholtz and Tsvi Piran. "Gravitational wave memory from gamma ray bursts' jets." In: *Phys. Rev. D* 87.12 (2013), p. 123007. DOI: 10.1103/PhysRevD.87.123007. arXiv: 1302.5713 [astro-ph.HE].

[288] William Krivan, Pablo Laguna, Philippos Papadopoulos, and Nils Andersson. "Dynamics of perturbations of rotating black holes." In: *Physical Review D* 56.6 (Sept. 1997), pp. 3395–3404. ISSN: 1089-4918. DOI: 10.1103/physrevd.56.3395. URL: http://dx.doi.org/10.1103/PhysRevD.56.3395.

[289] Enrique Pazos-Ávalos and Carlos O. Lousto. "Numerical integration of the Teukolsky equation in the time domain." In: *Physical Review D* 72.8 (Oct. 2005). ISSN: 1550-2368. DOI: 10.1103/physrevd.72.084022. URL: http://dx.doi.org/10.1103/PhysRevD.72.084022.

[290] Anil Zenginoglu and Gaurav Khanna. "Null infinity waveforms from extreme-mass-ratio inspirals in Kerr spacetime." In: *Phys. Rev. X* 1 (2011), p. 021017. DOI: 10.1103/PhysRevX.1.021017. arXiv: 1108.1816 [gr-qc].

[291] Anil Zenginoğlu, Gaurav Khanna, and Lior M. Burko. "Intermediate behavior of Kerr tails." In: *Gen. Rel. Grav.* 46 (2014), p. 1672. DOI: 10.1007/s10714-014-1672-8. arXiv: 1208.5839 [gr-qc].

[292] Vitor Cardoso, Francisco Duque, and Gaurav Khanna. "Gravitational tuning forks and hierarchical triple systems." In: *Phys. Rev. D* 103.8 (2021), p. L081501. DOI: 10.1103/PhysRevD.103.L081501. arXiv: 2101.01186 [gr-qc].

[293] Gioel Calabrese and Carsten Gundlach. "Discrete boundary treatment for the shifted wave equation." In: *Class. Quant. Grav.* 23 (2006), S343–S368. DOI: 10.1088/0264-9381/23/16/S04. arXiv: gr-qc/0509119.

[294] Ramon Lopez-Aleman, Gaurav Khanna, and Jorge Pullin. "Perturbative evolution of particle orbits around Kerr black holes: Time domain calculation." In: *Class. Quant. Grav.* 20 (2003), pp. 3259–3268. DOI: 10.1088/0264-9381/20/14/320. arXiv: gr-qc/0303054.

[295] We find two curious exceptions to the empirical numerical results quoted. The first, for $U_s < 1$, concerns $\ell = 1$, $\beta = 3$ for which we find the power $p = 5$, not 4 as the empirical rule quoted suggests. The second concerns $U_s = 1$ and refers to $\ell = 0$, $\beta = 3$ for which our numerics give $p = 4$, rather than the empirical rule (8.22). These are the only known exceptions for $\ell \leq 4$ and $\beta \leq 7$. Similarly, not all second order quantities seem to follow (8.22) (in particular, the coupling of $\ell = m = 2$ to $\ell = -m = 2$).

[296] M. Davis, R. Ruffini, W.H. Press, and R.H. Price. "Gravitational radiation from a particle falling radially into a schwarzschild black hole." In: *Phys. Rev. Lett.* 27 (1971), pp. 1466–1469. DOI: 10.1103/PhysRevLett.27.1466.

[297] Vitor Cardoso and Jose' P. S. Lemos. "Gravitational radiation from collisions at the speed of light: A Massless particle falling into a Schwarzschild black hole." In: *Phys. Lett. B* 538 (2002), pp. 1–5. DOI: 10.1016/S0370-2693(02)01961-5. arXiv: gr-qc/0202019.

[298] Marcus Ansorg and Rodrigo Panosso Macedo. "Spectral decomposition of black-hole perturbations on hyperboloidal slices." In: *Phys. Rev. D* 93.12 (2016), p. 124016. DOI: 10.1103/PhysRevD.93.124016. arXiv: 1604.02261 [gr-qc].

[299] Rodrigo Panosso Macedo, José Luis Jaramillo, and Marcus Ansorg. "Hyperboloidal slicing approach to quasi-normal mode expansions: the Reissner-Nordström case." In: *Phys. Rev. D* 98.12 (2018), p. 124005. DOI: 10.1103/PhysRevD.98.124005. arXiv: 1809.02837 [gr-qc].

[300] Rodrigo Panosso Macedo. "Comment on "Some exact quasinormal frequencies of a massless scalar field in Schwarzschild spacetime"." In: *Phys. Rev. D* 99.8 (2019), p. 088501. DOI: 10.1103/PhysRevD.99.088501. arXiv: 1807.05940 [gr-qc].

[301] David Brizuela, Jose M. Martin-Garcia, and Manuel Tiglio. "A Complete gauge-invariant formalism for arbitrary second-order perturbations of a Schwarzschild black hole." In: *Phys. Rev. D* 80 (2009), p. 024021. DOI: 10.1103/PhysRevD.80.024021. arXiv: 0903.1134 [gr-qc].

[302] Reinaldo J. Gleiser, Carlos O. Nicasio, Richard H. Price, and Jorge Pullin. "Second order perturbations of a Schwarzschild black hole." In: *Class. Quant. Grav.* 13 (1996), pp. L117–L124. DOI: 10.1088/0264-9381/13/10/001. arXiv: gr-qc/9510049.

[303] Reinaldo J. Gleiser, Carlos O. Nicasio, Richard H. Price, and Jorge Pullin. "Gravitational radiation from Schwarzschild black holes: The Second order perturbation formalism." In: *Phys. Rept.* 325 (2000), pp. 41–81. DOI: 10.1016/S0370-1573(99)00048-4. arXiv: gr-qc/9807077.

[304] David Brizuela, Jose M. Martin-Garcia, and Guillermo A. Mena Marugan. "Second and higher-order perturbations of a spherical spacetime." In: *Phys. Rev. D* 74 (2006), p. 044039. DOI: 10.1103/PhysRevD.74.044039. arXiv: gr-qc/0607025.

[305] Kunihito Ioka and Hiroyuki Nakano. "Second and higher-order quasi-normal modes in binary black hole mergers." In: *Phys. Rev. D* 76 (2007), p. 061503. DOI: 10.1103/PhysRevD.76.061503. arXiv: 0704.3467 [astro-ph].

[306] Hiroyuki Nakano and Kunihito Ioka. "Second Order Quasi-Normal Mode of the Schwarzschild Black Hole." In: *Phys. Rev. D* 76 (2007), p. 084007. DOI: 10.1103/PhysRevD.76.084007. arXiv: 0708.0450 [gr-qc].

[307] Enrique Pazos, David Brizuela, Jose M. Martin-Garcia, and Manuel Tiglio. "Mode coupling of Schwarzschild perturbations: Ringdown frequencies." In: *Phys. Rev. D* 82 (2010), p. 104028. DOI: 10.1103/PhysRevD.82.104028. arXiv: 1009.4665 [gr-qc].

[308] Mark Ho-Yeuk Cheung et al. "Nonlinear Effects in Black Hole Ringdown." In: *Phys. Rev. Lett.* 130.8 (2023), p. 081401. DOI: 10.1103/PhysRevLett.130.081401. arXiv: 2208.07374 [gr-qc].

[309] Keefe Mitman et al. "Nonlinearities in black hole ringdowns." In: (Aug. 2022). arXiv: 2208.07380 [gr-qc].

[310] Jaime Redondo-Yuste, Gregorio Carullo, Justin L. Ripley, Emanuele Berti, and Vitor Cardoso. "Spin dependence of black hole ringdown nonlinearities." In: *Phys. Rev. D* 109.10 (2024), p. L101503. DOI: 10.1103/PhysRevD.109.L101503. arXiv: 2308.14796 [gr-qc].

[311] Lionel London, Deirdre Shoemaker, and James Healy. "Modeling ringdown: Beyond the fundamental quasinormal modes." In: *Phys. Rev. D* 90.12 (2014). [Erratum: Phys.Rev.D 94, 069902 (2016)], p. 124032. DOI: 10.1103/PhysRevD.90.124032. arXiv: 1404.3197 [gr-qc].

[312] Macarena Lagos and Lam Hui. "Generation and propagation of nonlinear quasi-normal modes of a Schwarzschild black hole." In: (Aug. 2022). arXiv: 2208.07379 [gr-qc].

[313] Neev Khera, Ariadna Ribes Metidieri, Béatrice Bonga, Xisco Jiménez Forteza, Badri Krishnan, Eric Poisson, Daniel Pook-Kolb, Erik Schnetter, and Huan Yang. "Nonlinear Ringdown at the Black Hole Horizon." In: *Phys. Rev. Lett.* 131.23 (2023), p. 231401. DOI: 10.1103/PhysRevLett.131.231401. arXiv: 2306.11142 [gr-qc].

[314] Carsten Gundlach, Richard H. Price, and Jorge Pullin. "Late time behavior of stellar collapse and explosions: 2. Nonlinear evolution." In: *Phys. Rev. D* 49 (1994), pp. 890–899. DOI: 10.1103/PhysRevD.49.890. arXiv: gr-qc/9307010.

[315] Piotr Bizon, Tadeusz Chmaj, and Andrzej Rostworowski. "Late-time tails of a self-gravitating massless scalar field revisited." In: *Class. Quant. Grav.* 26 (2009), p. 175006. DOI: 10.1088/0264-9381/26/17/175006. arXiv: 0812.4333 [gr-qc].

[316] Nikodem Szpak, Piotr Bizon, Tadeusz Chmaj, and Andrzej Rostworowski. "Linear and nonlinear tails II: Exact decay rates in spherical symmetry." In: *J. Hyperbol. Diff. Equat.* 6.01 (2009), pp. 107–125. DOI: 10.1142/S0219891609001782. arXiv: 0712.0493 [math-ph].

[317] Jonathan Luk. "The null condition and global existence for nonlinear wave equations on slowly rotating Kerr spacetimes." In: *J. Eur. Math. Soc.* 15.5 (2013), pp. 1629–1700. DOI: 10.4171/jems/400. arXiv: 1009.4109 [gr-qc].

[318] Hans Lindblad and Mihai Tohaneanu. "The weak null condition on Kerr backgrounds." In: *Analysis & PDE* 17.8 (2024), pp. 2971–2996.

[319] Arnab Priya Saha, Biswajit Sahoo, and Ashoke Sen. "Proof of the classical soft graviton theorem in $D = 4$." In: *JHEP* 06 (2020), p. 153. DOI: 10.1007/JHEP06(2020)153. arXiv: 1912.06413 [hep-th].

[320] Vitor Cardoso and Jose P. S. Lemos. "Quasinormal modes of the near extremal Schwarzschild-de Sitter black hole." In: *Phys. Rev. D* 67 (2003), p. 084020. DOI: 10.1103/PhysRevD.67.084020. arXiv: gr-qc/0301078.

[321] Clifford M. Will. "The Confrontation between General Relativity and Experiment." In: *Living Rev. Rel.* 17 (2014), p. 4. DOI: 10.12942/lrr-2014-4. arXiv: 1403.7377 [gr-qc].

[322] José P. S. Lemos, Carlos A. R. Herdeiro, and Vitor Cardoso. "Einstein and Eddington and the eclipse in Principe: Celebration and science 100 years after." In: (Dec. 2019). arXiv: 1912.08354 [physics.hist-ph].

[323] Matthias Bartelmann and Peter Schneider. "Weak gravitational lensing." In: *Phys. Rept.* 340 (2001), pp. 291–472. DOI: 10.1016/S0370-1573(00)00082-X. arXiv: astro-ph/9912508.

[324] Matthias Bartelmann. "Gravitational Lensing." In: *Class. Quant. Grav.* 27 (2010), p. 233001. DOI: 10.1088/0264-9381/27/23/233001. arXiv: 1010.3829 [astro-ph.CO].

[325] A. Labeyrie. "Lensing effects of gravitational radiation near celestial sources." In: *Astronomy and Astrophysics* 268 (Feb. 1993), pp. 823–828.

[326] Redouane Fakir. "Gravity Wave Watching." In: *ApJ* 426 (May 1994), p. 74. DOI: 10.1086/174040. arXiv: gr-qc/9304003 [gr-qc].

[327] Ruth Durrer. "Light deflection in perturbed Friedmann universes." In: *Phys. Rev. Lett.* 72 (21 May 1994), pp. 3301–3304. DOI: 10.1103/PhysRevLett.72.3301. URL: https://link.aps.org/doi/10.1103/PhysRevLett.72.3301.

[328] Nick Kaiser and Andrew H. Jaffe. "Bending of light by gravity waves." In: *Astrophys. J.* 484 (1997), pp. 545–554. DOI: 10.1086/304357. arXiv: astro-ph/9609043.

[329] Thibault Damour and Gilles Esposito-Farese. "Light deflection by gravitational waves from localized sources." In: *Phys. Rev. D* 58 (1998), p. 044003. DOI: 10.1103/PhysRevD.58.044003. arXiv: gr-qc/9802019.

[330] Vishal Baibhav, Mark Ho-Yeuk Cheung, Emanuele Berti, Vitor Cardoso, Gregorio Carullo, Roberto Cotesta, Walter Del Pozzo, and Francisco Duque. "Agnostic black hole spectroscopy: Quasinormal mode content of numerical relativity waveforms and limits of validity of linear perturbation theory." In: *Phys. Rev. D* 108.10 (2023), p. 104020. DOI: 10.1103/PhysRevD.108.104020. arXiv: 2302.03050 [gr-qc].

[331] Vitor Cardoso and Leonardo Gualtieri. "Testing the black hole 'no-hair' hypothesis." In: *Class. Quant. Grav.* 33.17 (2016), p. 174001. DOI: 10.1088/0264-9381/33/17/174001. arXiv: 1607.03133 [gr-qc].

[332] Vitor Cardoso, Kyriakos Destounis, Francisco Duque, Rodrigo Panosso Macedo, and Andrea Maselli. "Black holes in galaxies: Environmental impact on gravitational-wave generation and propagation." In: *Phys. Rev. D* 105.6 (2022), p. L061501. DOI: 10.1103/PhysRevD.105.L061501. arXiv: 2109.00005 [gr-qc].

[333] James M. Bardeen, William H. Press, and Saul A Teukolsky. "Rotating black holes: Locally nonrotating frames, energy extraction, and scalar synchrotron radiation." In: *Astrophys. J.* 178 (1972), p. 347. DOI: 10.1086/151796.

[334] S. A. Teukolsky. "Rotating black holes - separable wave equations for gravitational and electromagnetic perturbations." In: *Phys. Rev. Lett.* 29 (1972), pp. 1114–1118. DOI: 10.1103/PhysRevLett.29.1114.

[335] Xiang Li, Ling Sun, Rico Ka Lok Lo, Ethan Payne, and Yanbei Chen. "Angular emission patterns of remnant black holes." In: *Phys. Rev. D* 105.2 (2022), p. 024016. DOI: 10.1103/PhysRevD.105.024016. arXiv: 2110.03116 [gr-qc].

[336] Emanuele Berti, Vitor Cardoso, and Clifford M. Will. "On gravitational-wave spectroscopy of massive black holes with the space interferometer LISA." In: *Phys. Rev. D* 73 (2006), p. 064030. DOI: 10.1103/PhysRevD.73.064030. arXiv: gr-qc/0512160.

[337] William Krivan, Pablo Laguna, Philippos Papadopoulos, and Nils Andersson. "Dynamics of perturbations of rotating black holes." In: *Phys. Rev. D* 56 (1997), pp. 3395–3404. DOI: 10.1103/PhysRevD.56.3395. arXiv: gr-qc/9702048.

[338] Eleanor Hamilton, Lionel London, and Mark Hannam. "Ringdown frequencies in black holes formed from precessing black-hole binaries." In: *Phys. Rev. D* 107.10 (2023), p. 104035. DOI: 10.1103/PhysRevD.107.104035. arXiv: 2301.06558 [gr-qc].

[339] P. L. Chrzanowski. "Vector Potential and Metric Perturbations of a Rotating Black Hole." In: *Phys. Rev. D* 11 (1975), pp. 2042–2062. DOI: 10.1103/PhysRevD.11.2042.

[340] J. M. Cohen and L. S. Kegeles. "Electromagnetic fields in curved spaces - a constructive procedure." In: *Phys. Rev. D* 10 (1974), pp. 1070–1084. DOI: 10.1103/PhysRevD.10.1070.

[341] L. S. Kegeles and J. M. Cohen. "CONSTRUCTIVE PROCEDURE FOR PERTURBATIONS OF SPACE-TIMES." In: *Phys. Rev. D* 19 (1979), pp. 1641–1664. DOI: 10.1103/PhysRevD.19.1641.

[342] V. P. Frolov and I. D. Novikov, eds. *Black hole physics: Basic concepts and new developments*. 1998. DOI: 10.1007/978-94-011-5139-9.

[343] Samuel E. Gralla, Alexandru Lupsasca, and Andrew Strominger. "Observational Signature of High Spin at the Event Horizon Telescope." In: *Mon. Not. Roy. Astron. Soc.* 475.3 (2018), pp. 3829–3853. DOI: 10.1093/mnras/sty039. arXiv: 1710.11112 [astro-ph.HE].

[344] Samuel E. Gralla and Alexandru Lupsasca. "Lensing by Kerr Black Holes." In: *Phys. Rev. D* 101.4 (2020), p. 044031. DOI: 10.1103/PhysRevD.101.044031. arXiv: 1910.12873 [gr-qc].

[345] Pedro V. P. Cunha, Carlos A. R. Herdeiro, Eugen Radu, and Helgi F. Runarsson. "Shadows of Kerr black holes with and without scalar hair." In: *Int. J. Mod. Phys. D* 25.09 (2016). Ed. by Carlos A. R. Herdeiro, Emanuele Berti, Vitor Cardoso, Luis C. B. Crispino, Leonardo Gualtieri, and Ulrich Sperhake, p. 1641021. DOI: 10.1142/S0218271816410212. arXiv: 1605.08293 [gr-qc].

[346] Tim Johannsen. "Photon Rings around Kerr and Kerr-like Black Holes." In: *Astrophys. J.* 777 (2013), p. 170. DOI: 10.1088/0004-637X/777/2/170. arXiv: 1501.02814 [astro-ph.HE].

[347] Pierre Christian and Chi-Kwan Chan. "FANTASY: User-Friendly Symplectic Geodesic Integrator for Arbitrary Metrics with Automatic Differentiation." In: *Astrophys. J.* 909.1 (2021), p. 67. DOI: 10.3847/1538-4357/abdc28. arXiv: 2010.02237 [gr-qc].

[348] Thomas Mädler and Jeffrey Winicour. "Kerr Black Holes and Nonlinear Radiation Memory." In: *Class. Quant. Grav.* 36.9 (2019), p. 095009. DOI: 10.1088/1361-6382/ab1187. arXiv: 1811.04711 [gr-qc].

[349] José A. Font, José Maria Ibáñez, and Philippos Papadopoulos. "Non-axisymmetric relativistic Bondi-Hoyle accretion on to a Kerr black hole." In: *Monthly Notices of the Royal Astronomical Society* 305.4 (May 1999), pp. 920–936. ISSN: 0035-8711. DOI: 10.1046/j.1365-8711.1999.02459.x. eprint: https://academic.oup.com/mnras/article-pdf/305/4/920/18634678/305-4-920.pdf. URL: https://doi.org/10.1046/j.1365-8711.1999.02459.x.

[350] Alessandra Buonanno, Gregory B. Cook, and Frans Pretorius. "Inspiral, merger and ring-down of equal-mass black-hole binaries." In: *Phys. Rev. D* 75 (2007), p. 124018. DOI: 10.1103/PhysRevD.75.124018. arXiv: gr-qc/0610122.

[351] Alexander H. Nitz, Collin Capano, Alex B. Nielsen, Steven Reyes, Rebecca White, Duncan A. Brown, and Badri Krishnan. "1-OGC: The first open gravitational-wave catalog of binary mergers from analysis of public Advanced LIGO data." In: *Astrophys. J.* 872.2 (2019), p. 195. DOI: 10.3847/1538-4357/ab0108. arXiv: 1811.01921 [gr-qc].

[352] Michele Maggiore. *Gravitational Waves: Volume 2: Astrophysics and Cosmology*. Oxford University Press, 2018.

[353] Leo C. Stein. "qnm: A Python package for calculating Kerr quasinormal modes, separation constants, and spherical-spheroidal mixing coefficients." In: *J. Open Source Softw.* 4.42 (2019), p. 1683. DOI: 10.21105/joss.01683. arXiv: 1908.10377 [gr-qc].

[354] M. A. Podurets. "Asymptotic Behavior of the Optical Luminosity of a Star in Gravitational Collapse." In: *Soviet Ast.* 8 (June 1965), p. 868.

[355] William L. Ames and Kip S. Thorne. "The Optical Appearance of a Star that is Collapsing Through its Gravitational Radius." In: *ApJ* 151 (Feb. 1968), p. 659. DOI: 10.1086/149465.

[356] G.A. Campbell and R.A. Matzner. "A model for peaking of galactic gravitational radiation." In: *J. Math. Phys.* 14 (1973), pp. 1–6. DOI: 10.1063/1.1666159.

[357] C. T. Cunningham and J. M. Bardeen. "The Optical Appearance of a Star Orbiting an Extreme Kerr Black Hole." In: *Astrophys. J. Lett.* 173 (May 1972), p. L137. DOI: 10.1086/180933.

[358] Heino Falcke, Fulvio Melia, and Eric Agol. "Viewing the shadow of the black hole at the galactic center." In: *Astrophys. J. Lett.* 528 (2000), p. L13. DOI: 10.1086/312423. arXiv: astro-ph/9912263.

[359] S. Chandrasekhar. *The Mathematical Theory of Black Holes*. New York: Oxford University Press, 1983.

[360] Michael D. Johnson et al. "Universal interferometric signatures of a black hole's photon ring." In: *Sci. Adv.* 6.12 (2020), eaaz1310. DOI: 10.1126/sciadv.aaz1310. arXiv: 1907.04329 [astro-ph.IM].

[361] Vitor Cardoso, Francisco Duque, and Arianna Foschi. "Light ring and the appearance of matter accreted by black holes." In: *Phys. Rev. D* 103.10 (2021), p. 104044. DOI: 10.1103/PhysRevD.103.104044. arXiv: 2102.07784 [gr-qc].

[362] Yifan Chen, Xiao Xue, Richard Brito, and Vitor Cardoso. "Photon Ring Astrometry for Superradiant Clouds." In: *Phys. Rev. Lett.* 130.11 (2023), p. 111401. DOI: 10.1103/PhysRevLett.130.111401. arXiv: 2211.03794 [gr-qc].

[363] Sergei M. Kopeikin, Gerhard Schaefer, Carl R. Gwinn, and T. Marshall Eubanks. "Astrometric and timing effects of gravitational waves from localized sources." In: *Phys. Rev. D* 59 (1999), p. 084023. DOI: 10.1103/PhysRevD.59.084023. arXiv: gr-qc/9811003.

[364] Sergei M. Kopeikin and Gerhard Schaefer. "Lorentz covariant theory of light propagation in gravitational fields of arbitrary moving bodies." In: *Phys. Rev. D* 60 (1999), p. 124002. DOI: 10.1103/PhysRevD.60.124002. arXiv: gr-qc/9902030.

[365] Sergei Kopeikin, Pavel Korobkov, and Alexander Polnarev. "Propagation of light in the field of stationary and radiative gravitational multipoles." In: *Class. Quant. Grav.* 23 (2006), pp. 4299–4322. DOI: 10.1088/0264-9381/23/13/001. arXiv: gr-qc/0603064.

[366] J. Antoniadis et al. "The second data release from the European Pulsar Timing Array - III. Search for gravitational wave signals." In: *Astron. Astrophys.* 678 (2023), A50. DOI: 10.1051/0004-6361/202346844. arXiv: 2306.16214 [astro-ph.HE].

[367] Daniel J. Reardon et al. "Search for an Isotropic Gravitational-wave Background with the Parkes Pulsar Timing Array." In: *Astrophys. J. Lett.* 951.1 (2023), p. L6. DOI: 10.3847/2041-8213/acdd02. arXiv: 2306.16215 [astro-ph.HE].

[368] Heng Xu et al. "Searching for the Nano-Hertz Stochastic Gravitational Wave Background with the Chinese Pulsar Timing Array Data Release I." In: *Res. Astron. Astrophys.* 23.7 (2023), p. 075024. DOI: 10.1088/1674-4527/acdfa5. arXiv: 2306.16216 [astro-ph.HE].

[369] V. B. Braginsky, N. S. Kardashev, I. D. Novikov, and A. G. Polnarev. "Propagation of electromagnetic radiation in a random field of gravitational waves and space radio interferometry." In: *Nuovo Cim. B* 105 (1990), pp. 1141–1158.

[370] Laura G. Book and Eanna E. Flanagan. "Astrometric Effects of a Stochastic Gravitational Wave Background." In: *Phys. Rev. D* 83 (2011), p. 024024. DOI: 10.1103/PhysRevD.83.024024. arXiv: 1009.4192 [astro-ph.CO].

[371] Christopher J. Moore, Deyan P. Mihaylov, Anthony Lasenby, and Gerard Gilmore. "Astrometric Search Method for Individually Resolvable Gravitational Wave Sources with Gaia." In: *Phys. Rev. Lett.* 119.26 (2017), p. 261102. DOI: 10.1103/PhysRevLett.119.261102. arXiv: 1707.06239 [astro-ph.IM].

[372] Diego Blas and Alexander C. Jenkins. "Detecting stochastic gravitational waves with binary resonance." In: *Phys. Rev. D* 105.6 (2022), p. 064021. DOI: 10.1103/PhysRevD.105.064021. arXiv: 2107.04063 [gr-qc].

[373] Diego Blas and Alexander C. Jenkins. "Bridging the μHz Gap in the Gravitational-Wave Landscape with Binary Resonances." In: *Phys. Rev. Lett.* 128.10 (2022), p. 101103. DOI: 10.1103/PhysRevLett.128.101103. arXiv: 2107.04601 [astro-ph.CO].

[374] Zhiyao Lu, Lian-Tao Wang, and Huangyu Xiao. *A New Probe of μHz Gravitational Waves with FRB Timing*. July 2024. arXiv: 2407.12920 [gr-qc].

[375] Kazunori Akiyama et al. "First Sagittarius A* Event Horizon Telescope Results. I. The Shadow of the Supermassive Black Hole in the Center of the Milky Way." In: *Astrophys. J. Lett.* 930.2 (2022), p. L12. DOI: 10.3847/2041-8213/ac6674. arXiv: 2311.08680 [astro-ph.HE].

[376] D. Ayzenberg et al. *Fundamental Physics Opportunities with the Next-Generation Event Horizon Telescope*. Dec. 2023. arXiv: 2312.02130 [astro-ph.HE].

[377] Michael D. Johnson et al. "The Black Hole Explorer: Motivation and Vision." In: June 2024. arXiv: 2406.12917 [astro-ph.IM].

[378] Daniel P. Marrone et al. *The Black Hole Explorer: Instrument System Overview*. 2024. arXiv: 2406.10143 [astro-ph.IM]. URL: https://arxiv.org/abs/2406.10143.

[379] Sara Issaoun et al. "The Black Hole Explorer: operating a hybrid observatory." In: *Space Telescopes and Instrumentation 2024: Optical, Infrared, and Millimeter Wave*. Ed. by Laura E. Coyle, Marshall D. Perrin, and Shuji Matsuura. SPIE, Aug. 2024, p. 193. DOI: 10.1117/12.3020041. URL: http://dx.doi.org/10.1117/12.3020041.

[380] Kari Haworth et al. *Studying black holes on horizon scales with space-VLBI*. Sept. 2019. arXiv: 1909.01405 [astro-ph.IM].

[381] Gabriella Agazie et al. "The NANOGrav 15 yr Data Set: Constraints on Supermassive Black Hole Binaries from the Gravitational-wave Background." In: *Astrophys. J. Lett.* 952.2 (2023), p. L37. DOI: 10.3847/2041-8213/ace18b. arXiv: 2306.16220 [astro-ph.HE].

[382] Michał J. Michałowski and Przemek Mróz. "Stars Lensed by the Supermassive Black Hole in the Center of the Milky Way: Predictions for ELT, TMT, GMT, and JWST." In: *Astrophys. J. Lett.* 915.2 (2021), p. L33. DOI: 10.3847/2041-8213/ac0f81. arXiv: 2107.00659 [astro-ph.GA].

[383] Lihang Zhou, Zhen Zhong, Yifan Chen, and Vitor Cardoso. "Forward ray tracing and hot spots in Kerr spacetime." In: *Phys. Rev. D* 111.6 (2025), p. 064075. DOI: 10.1103/PhysRevD.111.064075. arXiv: 2408.16049 [gr-qc].

[384] Maarten van de Meent. "Gravitational self-force on eccentric equatorial orbits around a Kerr black hole." In: *Phys. Rev. D* 94.4 (2016), p. 044034. DOI: 10.1103/PhysRevD.94.044034. arXiv: 1606.06297 [gr-qc].

[385] Andrew Spiers, Adam Pound, and Jordan Moxon. "Second-order Teukolsky formalism in Kerr spacetime: Formulation and nonlinear source." In: *Phys. Rev. D* 108.6 (2023), p. 064002. DOI: 10.1103/PhysRevD.108.064002. arXiv: 2305.19332 [gr-qc].

[386] Adam Pound and Barry Wardell. "Black Hole Perturbation Theory and Gravitational Self-Force." In: *Handbook of Gravitational Wave Astronomy*. Ed. by Cosimo Bambi, Stavros Katsanevas, and Konstantinos D. Kokkotas. Singapore: Springer Singapore, 2020, pp. 1–119. ISBN: 978-981-15-4702-7. DOI: 10.1007/978-981-15-4702-7_38-1. URL: https://doi.org/10.1007/978-981-15-4702-7%5C_38-1.

[387] Robert M. Wald. "Construction of Solutions of Gravitational, Electromagnetic, Or Other Perturbation Equations from Solutions of Decoupled Equations." In: *Phys. Rev. Lett.* 41 (1978), pp. 203–206. DOI: 10.1103/PhysRevLett.41.203.

[388] Oscar J. C. Dias, Harvey S. Reall, and Jorge E. Santos. "Kerr-CFT and gravitational perturbations." In: *JHEP* 08 (2009), p. 101. DOI: 10.1088/1126-6708/2009/08/101. arXiv: 0906.2380 [hep-th].

[389] R. Cartas-Fuentevilla. "Perturbations of Einstein-Maxwell dilaton fields." In: *Phys. Rev. D* 56 (1997), pp. 7700–7707. DOI: 10.1103/PhysRevD.56.7700.

[390] Vahid Toomani, Peter Zimmerman, Andrew Spiers, Stefan Hollands, Adam Pound, and Stephen R. Green. "New metric reconstruction scheme for gravitational self-force calculations." In: *Class. Quant. Grav.* 39.1 (2022), p. 015019. DOI: 10.1088/1361-6382/ac37a5. arXiv: 2108.04273 [gr-qc].

[391] Stephen R. Green, Stefan Hollands, and Peter Zimmerman. "Teukolsky formalism for nonlinear Kerr perturbations." In: *Class. Quant. Grav.* 37.7 (2020), p. 075001. DOI: 10.1088/1361-6382/ab7075. arXiv: 1908.09095 [gr-qc].

[392] Manuela Campanelli and Carlos O. Lousto. "Second order gauge invariant gravitational perturbations of a Kerr black hole." In: *Phys. Rev. D* 59 (1999), p. 124022. DOI: 10.1103/PhysRevD.59.124022. arXiv: gr-qc/9811019.

[393] B. F. Whiting and L. R. Price. "Metric reconstruction from Weyl scalars." In: *Class. Quant. Grav.* 22 (2005), S589–S604. DOI: 10.1088/0264-9381/22/15/003.

[394] John M. Stewart. "Hertz-Bromwich-Debye-Whittaker-Penrose Potentials in General Relativity." In: *Proc. Roy. Soc. Lond. A* 367 (1979), pp. 527–538. DOI: 10.1098/rspa.1979.0101.

[395] Carlos O. Lousto and Bernard F. Whiting. "Reconstruction of black hole metric perturbations from Weyl curvature." In: *Phys. Rev. D* 66 (2002), p. 024026. DOI: 10.1103/PhysRevD.66.024026. arXiv: gr-qc/0203061.

[396] Maarten van de Meent and Abhay G. Shah. "Metric perturbations produced by eccentric equatorial orbits around a Kerr black hole." In: *Phys. Rev. D* 92.6 (2015), p. 064025. DOI: 10.1103/PhysRevD.92.064025. arXiv: 1506.04755 [gr-qc].

[397] Amos Ori. "Reconstruction of inhomogeneous metric perturbations and electromagnetic four potential in Kerr space-time." In: *Phys. Rev. D* 67 (2003), p. 124010. DOI: 10.1103/PhysRevD.67.124010. arXiv: gr-qc/0207045.

[398] David Kofroň. "Point particles and Appell's solutions on the axis of a Kerr black hole for an arbitrary spin in terms of the Debye potentials." In: *Phys. Rev. D* 101.6 (2020), p. 064027. DOI: 10.1103/PhysRevD.101.064027. arXiv: 2003.10969 [gr-qc].

[399] Steffen Aksteiner and Thomas Bäckdahl. "Symmetries of linearized gravity from adjoint operators." In: *J. Math. Phys.* 60.8 (2019), p. 082501. DOI: 10.1063/1.5092587. arXiv: 1609.04584 [gr-qc].

[400] E Deadman and J M Stewart. "Linearized perturbations of the Kerr spacetime and outer boundary conditions in numerical relativity." In: *Classical and Quantum Gravity* 28.1 (Dec. 2010), p. 015003. DOI: 10.1088/0264-9381/28/1/015003. URL: https://dx.doi.org/10.1088/0264-9381/28/1/015003.

[401] S. A. Teukolsky and W. H. Press. "Perturbations of a rotating black hole. III - Interaction of the hole with gravitational and electromagnet ic radiation." In: *Astrophys. J.* 193 (1974), pp. 443–461. DOI: 10.1086/153180.

DECLARATION

I declare that this document is an original work of my own and that it fulfills all the requirements of the Code of Conduct and Good Practices of the Universidade de Lisboa.

Name: Zhen Zhong
Student number: 102031

Lisbon, July 2025

Zhen Zhong

COLOPHON

This document was typeset using the typographical look-and-feel `classicthesis` developed by André Miede and Ivo Pletikosić. The style was inspired by Robert Bringhurst's seminal book on typography "*The Elements of Typographic Style*".

Final Version as of May 7, 2025 (draft v1).